Beam Transfer Function measurements and transverse beam stability studies for the Large Hadron Collider and its High Luminosity upgrade

THÈSE N^{O} 7867 (2017)

PRÉSENTÉE LE 31 AOÛT 2017
À LA FACULTÉ DES SCIENCES DE BASE
LABORATOIRE DE PHYSIQUE DES ACCÉLÉRATEURS DE PARTICULES
PROGRAMME DOCTORAL EN PHYSIQUE

ÉCOLE POLYTECHNIQUE FÉDÉRALE DE LAUSANNE

POUR L'OBTENTION DU GRADE DE DOCTEUR ÈS SCIENCES

PAR

Claudia TAMBASCO

acceptée sur proposition du jury:

Prof. H. M. Rønnow, président du jury
Prof. L. Rivkin, Dr T. Pieloni, directeurs de thèse
Prof. O. Boine-Frankenheim, rapporteur
Dr W. Fischer, rapporteur
Prof. M. Q. Tran, rapporteur

ÉCOLE POLYTECHNIQUE
FÉDÉRALE DE LAUSANNE

Suisse
2017

It always seems
impossible until it is done
— Nelson Mandela

To my family and Vincenzo…

Acknowledgements

These past years of PhD work have been intense and characterized by an important personal and professional growth. It has been a long and difficult journey that fortunately I have not faced all alone. It is also thanks to the people who have been close to me that I managed to reach the destination and such an important professional achievement. In these lines I would like to thank all the people who walked with me through this path.

First of all I want to express my sincere gratitude to my CERN supervisor and thesis director Tatiana Pieloni. Her enthusiasm and her positivity were always accompanying me during the work, motivating me and spurring me to do my best to reach my goals; she always encouraged me to face new work experiences. I want also to thank her for the several teachings received in the field of accelerator physics. I warmly thank Tatiana, not only for her concrete contribution to this work but also for having supported me in the difficult moments.

I would like to address a special thank to Prof. Leonid Rivkin that gave me the possibility to work on this thesis project and enrich both my professional and human experience involving me on teaching assistant activities. He has been a constant and reliable reference point on which I could always rely on. I thank him for actively believing in me grating the support to participate to the accelerator schools and for giving me the possibility to exploit important resources as the EPFL's High Performance Computing machines.

I'm extremely grateful to my section leader Elias Métral for the constant support and for the great challenges he helped me to face during these years. I particularly appreciated his lively interest in these studies and the useful insights he provided me with.

I wish to express my gratitude to Dr. Werner Herr for the inestimable teachings received during these years that were fundamental for helping me understand this field. Moreover, his constant advices on this thesis work were enlightening.

I sincerely thank Dr. Xavier Buffat for the valuable advices and the fruitful discussions which shed light on several results presented in this thesis. He was always ready to help me with a smile and cordiality.

I thank Dr. Javier Barranco for the collaboration at work and for the help he provided me, in particular with the particle tracking simulations and the extension of simulation tools.

A constant work with the instrumentation team made possible the development of the trans-

verse BTF system in the LHC for the experimental studies presented in this thesis. I extend my thanks to Tom Levens, Thibaut Lefevre, Andrea Boccardi, Marek Gasior and Manoel Barros Martin for the efforts made to install and improve the system as well as for the assistance provided during the data taking.

The collaborations with the operation team of the LHC were crucial for the success of experimental activities, for this I really thank Belen Salvachua, Mirko Pojer, Matteo Solfaroli, Roberto Giachino, Jorg Wenninger, Giulia Papotti, Kajetan Fuchsberger and all the OP crews on shift during measurements and Georges Trad for BSRT measurements.

I wish to address a great thank to all the colleagues of the HSC section in particular: Lee Carver, Nicoló Biancacci, Giovanni Rumolo, Gianni Iadarola, Kevin Li, Adrian Öftiger, Micheal Schenk and Bonoit Salvant and to the optics team in particular to Rogelio Tomás Garcia, Ewen Hamish Maclean and Tobias Hakan Bjorn Persson for the discussions on the linear coupling.

I would like also to thank my office mate Alessandra Valloni, for her constant help, in particular with the presentation speeches at the beginning of my PhD work. Her support was never missing and she has been a constant reference point for me over these years.

No achievement would be ever possible without my family and my friends. My first special thought goes to my parents Amelia and Lorenzo for the unconditional love and the support they surrounded me with for all my life. Thanks to them I have become the person I am today. I thank my lovely brother Diego and his wife Sara for their love and for the pleasant time together when coming back home. Voglio ringraziare i miei nonni, Rossana e Roberto, per essere constantemente dei punti di riferimento nella mia vita.

I warmly thank my dearest and best friends Romina and Manlio not only for the good time spent together in Rome but also here in Geneva. Even if we have been living far away from each other, they have never made me feel alone. True friends are priceless and I can always count on them.

A special thank to the friends always present in good and bad moments, Roberto and Raluca for all the pleasant time spent together which helped me to escape my bad moments. I thank Elena, trustworthy friend, and lovely housemate who shared with me this journey since the beginning. I also thank Annalisa and Letizia for the chat during every morning coffee and for fun nights out in Geneva.

Last but not least, I want to lovingly thank Vincenzo, for being always by my side and for all the help and the advices given to me during this journey. I never felt alone when coming back home thanks to the love and affection from him and my dearest Leo and Luna. Few lines will be not enough to describe everything he did for me to reassure me and comfort in the dark moments when I was about to give up on. *"Il futuro appartiene a coloro che credono nella bellezza dei propri sogni" (E. Roosevelt).*

Geneva, 19 May 2017 C. T.

Abstract

The motion of high energetic particle beams in accelerators is influenced by their interactions with the accelerator environment through electromagnetic fields induced by the particle passages. Traveling with a speed close to the speed of light, the particles induce image charge and currents in the surroundings generating wake-fields that act back on the beams. Destabilizing effects may arise from the coupled motion between the circulating particles and the induced wake fields compromising the accelerator performances. The stability of the beams is ensured by the Landau damping of coherent motions generated by the diversity of oscillation frequencies of the particles in the beams. Under the effect of non linear forces produced by machine non linearities or beam-beam interactions the particles oscillate with slightly different frequencies depending on their amplitudes in the beams (tune spread). At the Large Hadron Collider (LHC) transverse instability thresholds are evaluated via the computation of the dispersion integral that depends on the tune spread in the beams as well as on the particle distribution. A large tune spread is beneficial for the Landau damping as long as no diffusive mechanism is present. In the presence of diffusive mechanisms, caused by resonance excitations or noise, the stability diagram can be deformed due to the modification of the particle distribution inside the beam leading to a possible lack of Landau damping of the impedance coherent modes previously damped by lying within the unperturbed stability area. This work aims to experimentally explore the transverse stability of the beams by means of Beam Transfer Function measurements at the LHC. They provide direct measurements of the stability diagrams and are sensitive to particle distribution changes. First measurements of the Landau stability diagrams at the LHC are presented and compared to model expectations. Experimental studies have been carried out in the presence of different sources of non linear effects such as octupole magnets and beam-beam interactions and compared to the model expectations. Limitations deriving from transverse coherent instabilities in the LHC are analysed and possible explanations for the observed LHC instabilities are discussed. In the perspective of the High-Luminosity LHC upgrade (HL-LHC), transverse stability studies for different beam-beam interactions and machine configurations are presented together with possible solutions to compensate reductions of the Landau damping during the operational phases of the HL-LHC.

Key words: Beam Transfer Function, Transverse stability, Particle accelerator, Collider, Beam-beam interaction, Beam stability, Landau damping, Stability diagram, multi-particle tracking simulation, LHC

Riassunto

Durante il loro moto nell’acceleratore le particelle di alta energia interagiscono con l’ambiente circostante e viaggiando ad una velocità prossima a quella della luce inducono cariche immagine e correnti generando campi elettromagnetici che influenzano il moto delle particelle durante il loro passaggio. Effetti destabilizzanti possono derivare dal moto accoppiato tra le particelle circolanti e i campi elettromagnetici indotti, compromettendo le prestazioni dell’acceleratore.

La stabilità dei fasci di particelle è garantita dallo smorzamento di Landau dei modi coerenti d’impedenza. Questo meccanismo stabilizzante è generato dalla diversità delle frequenze di oscillazione delle particelle nei fasci. Sotto l’effetto di forze non lineari, prodotte dalle non linearità dei campi magnetici dell’acceleratore o dalle collisioni dei fasci stessi, le particelle oscillano con frequenze leggermente diverse tra di loro a seconda della loro ampiezza nei fasci. Al Large Hadron Collider (LHC) le soglie di instabilità trasversale vengono valutate mediante il calcolo dell’integrale di dispersione, che dipende non solo dalla diversità delle frequenze di oscillazione delle particelle, ma anche dalle distribuzioni delle particelle nei fasci. Una maggiore diversificazione delle frequenze di oscillazione apporta una maggiore stabilità aumentando l’effetto di smorzamento di Landau fintanto che non s’instaurino meccanismi diffusivi. In presenza di meccanismi diffusivi, causati dall’ eccitazione di risonanze o rumore, il diagramma di stabilità determinato dall’integrale di dispersione può essere ridotto o deformato a causa delle modifiche nella distribuzione di particelle. Questi meccanismi possono a loro volta generare una possibile mancanza di smorzamento di Landau dei modi coerenti d’impedenza precedentemente smorzati giacendo all’interno del diagramma di stabilità imperturbato. Il presente lavoro è finalizzato all’ esplorazione sperimentalmente della stabilità trasversale dei fasci di particelle tramite misurazioni delle Funzioni di Trasferimento dei Fasci che forniscono una misura diretta dei diagrammi di stabilità e che sono sensibili alle modifiche delle distribuzioni di particelle. Le prime misure dei diagrammi di stabilità a LHC sono presentate e confrontate con i modelli teorici. Studi sperimentali sono stati condotti in presenza di diverse fonti di effetti non lineari prodotti dai magneti ottupolari e dalle interazioni generate dalle collisioni dei fasci e confrontate con le predizioni del modello teorico. Le limitazioni derivanti dalle instabilità trasversali coerenti sono state analizzate e le possibili spiegazioni vengono discusse per le alcune delle instabilità osservate in LHC. In vista dell’aggiornamento di LHC per l’alta luminosità (HL-LHC), vengono presentati studi di stabilità trasversale per diverse configurazioni di collisione insieme alle possibili soluzioni per compensare le riduzioni di smorzamento di Landau durante le diverse fasi operative di HL-LHC.

Parole chiave : Funzioni di Trasferimento del Fascio, stabilità transversa, acceleratore di particelle, collisore, collisioni fascio-fascio, stabilità del fascio, diagrammi di stabilità, simulazioni di tracciamento multi-particelle, LHC

Contents

Acknowledgements i

Abstract iii

List of figures ix

List of tables xvii

Introduction 1

1 Beam Dynamics 3
- 1.1 Single Particle Dynamics 3
  - 1.1.1 Transverse Beam Dynamics 4
  - 1.1.2 Working point and tune diagram 8
  - 1.1.3 Linear coupling 9
  - 1.1.4 Longitudinal Beam Dynamics 10
  - 1.1.5 Beam-Beam interaction 11
- 1.2 Collective effects 15
  - 1.2.1 Beam coupling impedance 16
  - 1.2.2 Coherent beam-beam effects 17
  - 1.2.3 Landau damping mechanisms 18
- 1.3 Luminosity 20

2 Physical model simulations 23
- 2.1 Particle tracking 23
  - 2.1.1 COherent Multi Bunch Interaction (COMBI) 23
  - 2.1.2 BTF module in COMBI 24
  - 2.1.3 Effects of chromaticity on simulated BTF response 26
  - 2.1.4 Normalization of the BTF amplitude response 30
  - 2.1.5 SixTrack simulations 33
- 2.2 Computation of the stability diagram: the PySSD code 33
  - 2.2.1 Effects of particle distribution on the stability diagram 35
- 2.3 Summary 39

3 Transverse beam stability at the Large Hadron Collider 41

3.1 The LHC injection complex . . . 41

3.2 LHC machine operations . . . 42

3.3 Landau damping in the LHC . . . 46

3.3.1 Transverse stability at the end of the betatron squeeze . . . 49

3.3.2 Transverse stability during the adjust process . . . 50

3.3.3 Instability during OP scans in the 2015 physics Run . . . 52

3.3.4 Beam stability during luminosity leveling with a transverse beam offset . 57

3.3.5 Set up of the collisions for the 2015 and 2016 physics runs . . . 58

3.4 Summary . . . 64

4 Transverse beam stability studies for the High-Luminosity LHC upgrade 67

4.1 Collision configurations and optics . . . 67

4.1.1 Luminosity leveling . . . 67

4.1.2 The Achromatic Telescopic Squeezing optics . . . 68

4.1.3 Crossing angle and crab cavities . . . 69

4.2 Transverse beam stability during the HL-LHC operational cycle . . . 70

4.2.1 Stability diagram with single beam . . . 70

4.2.2 Effects of non linearities induced by ATS optics . . . 71

4.2.3 Stability diagram during the Betatron squeeze . . . 73

4.2.4 Stability diagram during the adjust beam process . . . 78

4.2.5 Analysis of the stability minima . . . 79

4.3 Collision beam process . . . 83

4.4 Summary . . . 84

5 Beam based experimental study of Landau damping at the LHC 87

5.1 The transverse BTF system in the LHC . . . 87

5.1.1 Fitting function for the BTF data analysis . . . 89

5.2 LHC stability at injection energy . . . 92

5.2.1 Effect of chromaticity on the reconstructed stability diagram . . . 99

5.3 Beam stability in presence of beam-beam interactions . . . 101

5.3.1 Measurements with head-on collision . . . 101

5.3.2 Separation scan at the IPs . . . 103

5.3.3 Crossing angle scan at the end of the betatron squeeze . . . 106

5.3.4 Observations with linear coupling . . . 116

5.3.5 BTF limitations and improvements . . . 128

5.4 Summary . . . 128

6 Conclusions 131

Bibliography 139

List of Figures

1.1 Coordinate system with respect to the beam direction 3

1.2 Particle trajectory in the trace space (x, x'). 5

1.3 Particle trajectory in the phase space (x, p_x). 7

1.4 LHC tune diagram (fractional tunes) with resonance lines up to the 13th order. 9

1.5 Normalized transverse beam-beam kick as a function of the particle amplitude in the bunch for head-on collisions (blue line), long range interactions (red line) and with a transverse offset between the two beams (green line). 11

1.6 Different detuning with amplitude (tune footprints) in the presence of head-on collisions only (blue line), long range interactions (red line) and with a small transverse offset at the IP between the two colliding beams. 12

1.7 Schematic view of the beam crossing scheme with finite crossing angle α_c at the LHC IRs. 14

1.8 Tune footprints for two head-on collisions (blue line), long range interactions with horizontal separation (green line) and vertical separation (red line) together with the combined beam-beam head-on and long range interaction footprint (pink line). 15

1.9 Tune footprints for PACMAN and nominal bunches in the presence of long range beam-beam interactions (red and green line respectively) and in the presence of beam-beam head-on and long range interactions (pink and blue line respectively). 16

2.1 Simulated amplitude and phase BTF response as a function of different number of macro particles and turns. 26

2.2 Standard deviation between model and simulated amplitude and phase responses as a function of the number of macro particle used in COMBI simulations. The red shadow in the plots represents the calculated standard deviation from the model. Simulations have been carried out for an amplitude detuning produced by octupole magnets. 27

2.3 Emittance growth for different BTF excitation amplitudes and frequency resolution steps in COMBI. 28

2.4 Simulated BTF response in COMBI with chromaticity set to 4 units. 29

2.5 Stability diagram from simulated BTF response in COMBI with chromaticity set to 4 units. 29

2.6 Stability diagram from simulated BTF response in COMBI with chromaticity set to 4 units for a frequency sweep from higher to lower frequency. 30

2.7 Simulated BTF amplitude response for different octupole currents. 30

2.8 Maximum of the the dispersion integral amplitude and simulated BTF amplitude as a function of the octupole current. 31

2.9 Maximum of the simulated BTF amplitude as a function of the octupole current, for different chromaticity values and synchrotron tunes Q_s. 32

2.10 Uniform particle distribution generated at the first turn in IP1. 34

2.11 SixTrack particle distribution after 10^6 turns (left) at injection energy in the presence of linear detuning with amplitude for different octupole current together with the corresponding computed stability (right). The black lines represent the stability diagram for a Gaussian distribution, the blue and red lines are the computed stability diagrams in the horizontal and vertical plane respectively for the tracked particle distribution. The red shadow represents the computational error with respect to the stability diagram for a Gaussian distribution and linear detuning with amplitude. 37

2.12 Standard deviation from expectations of the stability diagram computed with the tracked particle distribution (quasi uniform case) as a function of the total number of particles in the distribution. 38

2.13 Frequency distribution at injection energy for an octupole current of 35A up to 4 σ particles. 38

3.1 Accelerator complex at CERN 42

3.2 Typical operational cycle in the LHC during a physics run of the 2016. 43

3.3 Long range separations at the long range beam-beam encounters in IP1 and IP5 for the 2012, 2015 and 2016 LHC physics runs considering nominal beam parameters. 44

3.4 Tune footprints in the presence of negative and positive octupole polarity ($I_{oct} \pm$ 550 A) at flat top energy $E_b = 4$ TeV as during the operations of the 2012 physics run (pink line) and at flat top energy of $E_b = 6.5$ TeV as during the operations of the 2016 and 2015 physics runs (blue line). 46

3.5 Tune footprints in the presence of negative and positive octupole polarity ($I_{oct} \pm$ 550 A) at the end of the betatron squeeze for the 2012 machine configurations, with and without long range beam-beam interactions. 47

3.6 Stability diagram at the end of the betatron squeeze for the LHC 2012 configuration with $\beta^* = 60$ cm for nominal (blue line) and PACMAN bunches (red line) as compared to the stability diagram at flat top (black lines) in the presence of negative and positive octupole polarity. 48

3.7 Stability diagram at the end of the betatron squeeze for the LHC 2012 configuration with $\beta^* = 60$ cm (on the left) for negative (red line) and positive octupole polarity (blue line) as compared to the corresponding stability diagram for the 2015 LHC nominal machine configurations (on the right). 48

3.8 Summary of the stability diagrams at the end of squeeze for the 2015 physics run compared to the stability diagrams at flat top for negative (solid black line) and positive (dashed black line) octupole polarities. 50
3.9 Stability diagram evolution during the LHC collapse of the beam separation bumps in the presence of positive octupole polarity for the LHC 2015 and 2016 physics runs. 51
3.10 Summary of the stability diagrams at the minimum of stability during the adjust process for the 2015 physics run. 51
3.11 Bunch by bunch emittance evolution during the Physics fill 4363. 53
3.12 Oscillation amplitude in the horizontal plane for Beam 1 and Beam 2 together with the parallel separations in IP1 and IP5 during the OP scan. 54
3.13 Tune footprints (up to 10 σ amplitude particles) for different parallel separations in IP1 (left plot) and in IP5 (right plot). 54
3.14 Computed stability diagrams for different parallel separations between the beams c in IP1 (top) and in IP5 (bottom) 55
3.15 Stability diagrams at the minimum of stability with a parallel separation $d \approx 2\,\sigma$ in the horizontal and vertical plane of IP1 (blue line and green line respectively) and in the horizontal and vertical plane of IP5 (red line and light blue line respectively) compared to the stability diagram expected at flat top with positive octupole polarity ($I_{oct} = 550$A). 56
3.16 Normalized luminosity in IP1 and IP5 during luminosity leveling with a transverse beam offset in IP1 and IP5 together with the corresponding beam parallel separation in IP1 and IP5. 57
3.17 Measured luminosity reduction with a transverse offset in IP1(red dotted line) and IP5 (blue dotted line) compared to model expectations (black solid line). . 58
3.18 Long range separations in IP8 at the end the betatron squeeze for positive (left) and negative (right) polarity of the LHCb spectrometer. 59
3.19 Long range separations in IP2 at the end of the betatron squeeze for the ALICE spectrometer switched off (left) and for the ALICE spectrometer switched on (right). 59
3.20 Horizontal and vertical tune shifts induced by long range beam-beam interactions at the end of the betatron squeeze as a function of the crossing angle in IP8. 60
3.21 Horizontal and vertical tune shifts induced by long range beam-beam interactions at the end of the betatron squeeze as a function of the crossing angle in IP2. 61
3.22 Tune footprints for the 2015 configuration with beams in collision in IP1 and IP5 with $\beta^* = 0.80$ m and crossing angle $\alpha_c = 290$ μrad (light blue line). The long range beam-beam contributions at the end of the betatron squeeze configuration is added in IP2 with a crossing angle $\alpha_c = 240$ μrad (blue line) and in IP8 with a crossing angle $\alpha_c = 500$ μrad (red line). 61

3.23 Footprint in collision for the 2015 Run and 2016 Run with nominal beam parameters. 62
3.24 Stability diagram evolution during the LHC adjust process in the presence of positive octupole polarity for the 2016 physics run configuration, for the first part of the year with a normalized beam emittance $\epsilon = 3.5\,\mu\text{m}$ and a nominal crossing angle of $\alpha_c = 370\,\mu\text{rad}$ and for the second part of the year with a normalized beam emittance $\epsilon = 2.5\,\mu\text{m}$ and a reduced crossing angle of $\alpha_c = 280\,\mu\text{rad}$. . . . 63
3.25 Long range separations in IR2 at the end of the betatron squeeze for the ALICE spectrometer with swapped polarity. 64
3.26 Long range beam-beam tune shifts as a function of the crossing angle in IP2 for the 2016 LHC configuration with beams in collision in all the IPs. 64
3.27 Long range beam-beam tune spread as a function of the crossing angle in IP2 for the 2016 LHC configuration with beams in collision in all the IPs. 65

4.1 HL-LHC luminosity evolution during a physics fill 69
4.2 β-functions in the arcs beside IP1 and IP5 for the ATS optics with $\beta^* = 15\,\text{cm}$ compared to the LHC optics with $\beta^* = 80\,\text{cm}$. 70
4.3 Schematic view of collisions with the crab cavities rotation of the bunches at the IP 70
4.4 Stability diagrams at flat top for the HL-LHC 71
4.5 Tune footprint comparison between the nominal LHC 2015 optics with $\beta^* = 80\,\text{cm}$ (blue line) and the ATS optics with $\beta^* = 15\,\text{cm}$ (red line). 72
4.6 Stability diagrams with nominal LHC 2015 optics with $\beta^* = 80\,\text{cm}$ (red line) and ATS optics ($\beta^* = 15\,\text{cm}$) (blue line). 72
4.7 Tune footprint with negative and octupole polarities and corresponding stability diagram for the ATS optics with $\beta^* = 15\,\text{cm}$. 73
4.8 Tune footprint produced by the tune spread due to machine non linearities with squeezed ATS optics ($\beta^* = 15\,\text{cm}$)). 73
4.9 Tune footprint with negative and octupole polarities and associated stability diagram for the ATS optics ($\beta^* = 15\,\text{cm}$) without non linearities contribution in the tune spread. 74
4.10 Stability diagram evolution during the HL-LHC betatron squeeze for both negative and positive octupole polarities 74
4.11 Stability diagrams at the end of the betatron squeeze for the Ultimate and Baseline scenario of the HL-LHC 75
4.12 Comparison between the stability diagram at flat top with negative octupole polarity ($I_{oct} = -570\,\text{A}$) and the stability diagrams during the squeeze with negative (blue line) and positive (red line) octupole polarity. 76
4.13 Comparison between the stability diagram at flat top with negative octupole polarity ($I_{oct} = -570\,\text{A}$) and the stability diagrams during the squeeze with negative (blue line) and positive (red line) octupole polarity. 77
4.14 Evolution of the stability diagrams during adjust beam process for the HL-LHC case with crab crossing turned off (Baseline scenario) 78

4.15 Evolution of the stability diagrams during the adjust beam process for the HL-LHC case with full crab-crossing turned on (Baseline scenario) 79
4.16 Stability diagrams at the reduction of $d = 6\,\sigma$ during the adjust beam process . 80
4.17 Stability diagrams at the reduction of $d = 1.5\,\sigma$ during the adjust beam process 80
4.18 Stability diagrams at the minima of stability during the adjust beam process together with the impedance coherent modes expected at the end of the squeeze for the HL-LHC Baseline scenario. 81
4.19 Beam separation in IP1 and IP5 during the adjust beam process compared to the current of some corrector magnets of the beam orbit in IP1 and IP5. 82
4.20 HL-LHC Stability diagrams with beam in collisions and crab-crossing with Landau octupole switched off. 84

5.1 Schematic view of the BTF system. The beam is excited by the ADT kickers with a sinusoidal wave, the complex response of the beam is given by the BBQ BPM. 88
5.2 Example of a BTF a measurement: amplitude and phase response for B1 at the LHC injection energy. 89
5.3 Normalized beam emittance in the vertical of Beam 1 while scanning the excitation amplitude of the BTF. 90
5.4 Measured amplitude and phase response of the beam during a BTF measurement (blue line) in presence of detuning with amplitude given by octupole magnets at injection energy ($I_{oct} = 6.5$A) compared to analytical expectations (black line). The green shadow represent the data points excluded from the fit because of the artifact signal in the BTF response for the frequency above the betatron tune. 91
5.5 Reconstructed stability diagram from measured BTF (blue crosses) in presence of detuning with amplitude given by octupole magnets at injection energy ($I_{oct} = 6.5$A), compared to analytical estimation (black line) and with the semi-analytical model (red line). The green shadow represent data points excluded from the fit because of the artifact signal in the BTF response for frequencies above the betatron tune. 92
5.6 Measured BTF amplitude and phase for Beam 1 for different octupole currents at injection energy. 93
5.7 Vertical and horizontal BTF amplitude at injection energy in presence of 26A octupole current. 94
5.8 Measured B1 losses at the primary collimators in IR7 during the octupole current scan at injection energy. 95
5.9 Two dimensional detuning with amplitude (tune footprint) due to octupole magnets powered with a current of 26A at injection energy (450 GeV) and a normalized beam emittance of $\epsilon = 2.0\,\mu$m rad. Machine fractional tunes are set to ($Q_x = 0.312, Q_y = 0.318$) as experimental conditions during the octupole scan at injection energy. 95

5.10 Two dimensional detuning with amplitude (up to 6 σ particles) due to octupole magnets powered with 26 A. Projections of the vertical and horizontal plane are shown. The dashed red lines display the extremum betatron frequencies up to 3 σ particles. 96

5.11 Cross amplitude between the horizontal and the vertical BTF at injection in presence of 26 A octupole current. 96

5.12 Two dimensional detuning with amplitude (up to 6 σ particles) due to octupole magnets powered with 26 A and linear coupling ($C^{-} \approx 1.5 \times 10^{-3}$). Projections of the vertical and horizontal plane are shown. The dashed red lines display the extremum betatron frequencies up to 3 σ particles. 97

5.13 Particle distribution tracked for 10^{6} turns in presence of linear coupling and octupole detuning with amplitude, the color bar represents the particle density. 97

5.14 Amplitude of the complex dispersion integral as a function of the frequency obtained by tracked distributions in presence of linear coupling ($C^{-} \approx 1.5 \times 10^{-3}$) and octupole magnets powered with 26 A at injection energy. 98

5.15 Tune spread factors evaluated from the fitting function applied to the BTF measurements at injection energy for different octupole currents. The blue dots represent the BTF measurements in the horizontal plane while the green dots are the measurements in the vertical plane. The solid black line represents the factors expected from the model with respect to the reference case with an octupole current of $I_{oct} = 6.5$ A. The red shadow represents the model expectations where an additional spread of ≈ 5.5 A (corresponding to the case for an octupole current of 0 A), was applied with an uncertainty of ±10% on the emittance value. 99

5.16 Measured amplitude and phase (blue line) and simulated BTF (green line) at injection energy in presence of 6.5 A octupole current and a chromaticity $Q' \approx 5$ units. 100

5.17 Reconstructed stability diagram from BTF measurements (blue crosses) compared to semi-analytical 2D dispersion integral (black line) and multi-particle 3D model (green line) at injection energy in presence of 6.5 A octupole current and a chromaticity $Q' \approx 5$ units. 100

5.18 Measured BTF amplitude in the vertical plane of Beam 1 with colliding beams. The coherent beam-beam σ and π modes are visible in the amplitude response. 101

5.19 BBQ spectrogram for Beam 1 in the horizontal plane with beams in collisions. The BTF excitations correspond to the diagonal red lines in the spectrogram. . 102

5.20 Normalized luminosity recorded by ATLAS and CMS during the separation scan in IP1 and IP5. 104

5.21 Measured BTF for Beam 2 for different parallel separations in IP1 and IP5. . . . 104

5.22 Measured tune shifts from BTF measurements during the parallel separation scan in IP1 and IP5. The tune shifts are normalized to the maximum tune shift observed in each plane. 105

5.23 Stability diagrams reconstructed from BTF measurements in the horizontal plane with beams in collision with full head-on collision (blue crosses) and with a parallel separation of 3.69 σ (red crosses). 106

5.24 Measured amplitude and phase in the horizontal plane with full head-on collision (blue line) and with a parallel separation of 3.69 σ (red line). The corresponding stability diagrams are presented in Fig. 5.23 where the Savitzky-Golay filter was applied to the data to remove signal noise from measurements (black solid line). 107

5.25 Measured BTF for Beam 1 for different crossing angles in IP1 and IP5 simultaneously changed in both the IPs. 108

5.26 Measured BTF amplitude and phase response for Beam 1 at the end of the squeeze ($\alpha_c = 370\,\mu\text{m}$) and for a reduced crossing angle ($\alpha_c = 270\,\mu\text{m}$) in IP1 and IP5. The BTF response is compared to the model expectations (black and pink lines) for both the angles used. 109

5.27 BTF response in the vertical plane of B1 for a crossing angle of 230µrad for different vertical tune values. The blue line corresponds to the first acquisition of the BTF while the green line corresponds to the BTF amplitude with a shift of the vertical tune of $\Delta Q = -0.001$. The initial BTF amplitude shape is fully recovered by restoring the initial vertical tune value (red line). 110

5.28 Measured BTF for Beam 1 at the end of the betatron squeeze in the horizontal plane. 111

5.29 Measured BTF for Beam 1 at the end of the betatron squeeze in the vertical plane. 111

5.30 Horizontal and vertical tune spread and tune shifts during the crossing angle scan at the end of squeeze for Beam 1 from fitted BTF data. 112

5.31 Measured long range beam-beam contribution to the stability diagram as function of the crossing angle (blue line) compared to the model expectations (black line). The long range beam-beam contribution is expressed (as a percentage) as the ratio between the half height of the stability diagram for each angle and the half height of the stability diagram at the end of the betatron squeeze. 113

5.32 Particle distribution from SixTrack tracking and corresponding stability diagrams for different crossing angles in IP1 and IP5 at the end of the betatron squeeze. . 114

5.33 Particle distribution from SixTrack tracking and corresponding stability diagrams at the end of the betatron squeeze for asymmetric crossing angles in IP1 (reduced crossing angle) and IP5. 115

5.34 Measured BTF amplitude response for Beam 1 before and after linear coupling correction. 116

5.35 Tune footprints at the end of the betatron squeeze for different linear coupling ($|C^-|$) values. 117

5.36 Stability diagrams at the end of the betatron squeeze for a Gaussian particle distribution without linear coupling and with linear coupling. 118

5.37 Particle and frequency distributions after long particle tracking at end of the betatron squeeze (LHC 2016 configuration), with positive octupole polarity (current of 470 A) for different values of linear coupling. 119
5.38 Stability diagrams from tracked particle distribution for different value of $|C^-|$. 120
5.39 Particle distribution after SixTrack tracking at end of the betatron squeeze, with positive octupole polarity (current of 470 A) without linear coupling and with linear coupling ($|C^-| = 0.0035$) introduced in the model by using positive and negative skew quadrupole knobs. 121
5.40 Tracked particle distribution and corresponding stability diagrams at end of the betatron squeeze with positive octupole polarity (current of 470 A) and linear coupling $|C^-| = 0.0035$ (positive skew quadrupole knobs) for different crossing angle in IP1 and IP5. 122
5.41 Tracked particle distribution and corresponding stability diagrams at end of the betatron squeeze with positive octupole polarity (current of 470 A) and linear coupling, $|C^-| = 0.0035$ (negative skew quadrupole knobs) for different crossing angle in IP1 and IP5. 124
5.42 Tune footprint at the end of the betatron squeeze (2012 configuration) with positive and negative octupole polarity ($I_{oct} = 550$A) in presence of linear coupling (red line) and without linear coupling (blue line). 125
5.43 Particle distribution from SixTrack tracking and corresponding stability diagrams at end of the betatron squeeze (2012 configuration) for positive octupole polarity (current of 550 A) with linear coupling ($|C^-| = 0.0035$ and positive coupling knobs) and without linear coupling, and for a reduced vertical tune ($\Delta Q_y = 3 \times 10^{-3}$). 126
5.44 Stability diagrams from tracked particle distribution in presence of long range beam-beam interactions at end of the betatron squeeze for the 2012 configuration, positive octupole polarity ($I_{oct} = 550$A) with transverse linear coupling, $|C^-| = 0.0035$ (positive skew quadrupole knobs). 127

List of Tables

2.1 Amplitude ratio from fitting function between the COMBI BTF amplitude and the semi-analytical dispersion integral as a function of the octupole current for different chromaticity value Q', and synchrotron tunes Q_s 33

3.1 Main LHC machine parameters during the 2012, the 2015 and the 2016 physics runs. 44
3.2 LHC machine configurations for different operational phases. 45

4.1 Beam parameters for the HL-LHC compared to the LHC nominal parameters. . 68
4.2 Time spent while crossing the minimum of Landau damping during the adjust beam process in IP1 and IP5 for several physics fills of the 2015 LHC physics run. 83

5.1 Tune spread factors for different octupole currents at injection energy. The tune spread factors are evaluated with respect to the semi-analytical reference case with an octupole current of $I_{oct} = 6.5\,\text{A}$. 99
5.2 Beam parameters during BTF measurements on colliding beams at injection energy. 102
5.3 Normalized full parallel separation in IP1 and IP5 during parallel separation scan with beams in collision. 103
5.4 Normalized beam emittances at the end of squeeze for Fill 1 and Fill 2 103
5.5 Normalized long range beam-beam separation at the first encounter in units of the rms beam size for different crossing angles at the IPs during the experiment. Normalized beam emittance $\epsilon \approx 1.8\,\mu\text{m}\,\text{rad}$ in both planes. 107

Introduction

The discovery of the Higgs boson in the 2012, one of the most important results in physics of the last decade, was possible thanks to the high collision rate of the proton beams colliding at the CERN Large Hadron Collider (LHC). Together with the beam energy, one of the most important parameters to quantify the performance of a particle collider is the luminosity, which defines the production rate of a certain physics process. For increasingly rare processes, higher luminosity is required for discovery. The luminosity is determined by the collision frequency and the beam brightness that is defined as the number of particles in the beam divided by the beam emittance. The higher the beam brightness, the greater is the risk of triggering mechanisms that may compromise the stability of the particle motion in the accelerator deteriorating the beam quality, and hence its performance. The particles in the same beam interact electromagnetically among each other (space charge effect) and also interact with the particles of the opposite beam (beam-beam interaction). Positively charged beams traveling through the accelerator beam pipe can generate the so-called electron cloud effect. In addition, particles passing through the vacuum chamber induce electromagnetic fields (wake fields). The wake fields can lead to beam instabilities that cause a deterioration of the beam quality. The impedance, that is the Fourier transformation of the wake fields, affects both the transverse and the longitudinal beam motion. Several theories have been developed to model the coherent modes of oscillation of a single beam due to the impedance. The coherent modes can be damped by the so called Landau damping, which depends on both the tune spread in the beam and on the particle distribution in the phase space.

Since 2012 the beams of the LHC have shown transverse instabilities at top energy during different phases of the operational cycle which are not yet fully understood. In 2012, the instabilities led to a beam emittance blow-up of a factor ≈ 2 with corresponding luminosity loss. Several studies were carried out to explain these instabilities. Models to predict the instability thresholds in the LHC have been extended to include the beam-beam interaction, which has strong impact on the particle frequency spread modifying the strength of the Landau damping. Despite these studies, the mechanisms of the observed instabilities are still unclear. On this basis, the studies reported in this thesis aim to experimentally explore the transverse Landau damping of the beams by means of Beam Transfer Function (BTF) measurements.

These measurements were performed for the first time in the LHC in order to investigate possible explanations for the observed loss of Landau damping. The BTF represents the complex response of the beam, characterized by an amplitude and a phase as a function of the excitation frequency. It is sensitive to changes of the particle distribution in the beams as well as to changes of the tune spread. The latter may be caused by several effects present in the LHC such as beam-beam interaction, magnet non linearities, chromaticity and linearly coupled motion between the horizontal and the vertical planes. Therefore, BTF measurements are powerful tools to experimentally investigate the limitations of the models by comparing the measured Landau damping with the expected stability diagram. In addition to the experimental studies, analytical models have been extended to include the effects of the particle distribution changes due to diffusive mechanisms.

The understanding of the limitations due to coherent instabilities in the LHC becomes more crucial in the perspective of the future projects aiming to increase the performance of the LHC, such as the High-Luminosity upgrade of the LHC (HL-LHC). This major upgrade relies on increased beam brightness (twice the intensity) and requires a careful monitoring and control of all the factors that can compromise the stability of the beams. The results of these studies apply to any collider where beam-beam effects are not negligible. The measurements of the first stability diagrams measured in the LHC are presented and compared with the analytical model. A parametric study of several effects (Landau octupole magnets, linear coupling and long range beam-beam interactions) was carried out together with a first estimate of the impact of long range beam-beam interactions on Landau damping.

In Chap. 1 the dynamics of charged particle beams in a circular collider is introduced, it is followed by a description of the extensions to the numerical models used for this study in Chap. 2. Chapter 3 outlines the analysis of transverse beam stability in the presence of beam-beam effects with the proposal adopted during operations in the LHC for improved performance. The results of the analysis of Landau damping in the presence of beam-beam effects for the HL-LHC together with extrapolations and a proposed operational scenario are presented in Chap. 4. The BTF experimental studies and comparisons with the model for the LHC are presented in Chap. 5 with parametric studies of the effects of Landau octupoles, linear coupling and long range beam-beam interactions. Finally, the conclusions of these studies are summarized in Chap. 6.

1 Beam Dynamics

1.1 Single Particle Dynamics

The charged particles are guided along the accelerators orbit under the effect of electric and magnetic fields. The particle motion is governed by the Lorentz force:

$$\frac{d\vec{p}}{dt} = q(\vec{E} + \vec{v} \times \vec{B}) \tag{1.1}$$

where $\vec{p}$ is the relativistic momentum of the particle, $\vec{v}$ is the velocity, q the charge, $\vec{E}$ the electric field and $\vec{B}$ the magnetic field, considering the particle traveling in a vacuum chamber. The magnetic field generates a change of the momentum direction with respect to the particle velocity vector acting on the trajectory of the particle to bend it. At the first order, the electric field provides a change of momentum in the same direction of the field in order to accelerate or decelerate the particle. To describe the particle motion it is convenient to use a right-handed

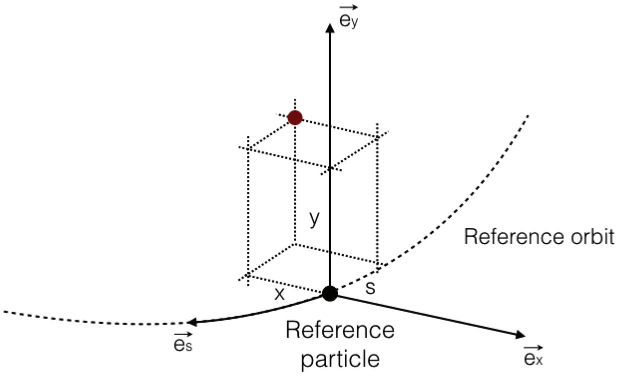

Figure 1.1 – Coordinate system respect to the beam direction.

orthogonal and moving system ($\vec{e}_x, \vec{e}_y, \vec{e}_s$) called Frenet-Serret system, it is illustrated in Fig. 1.1 . The reference particle moves on the reference closed orbit with the reference momentum $\vec{p}_0$. Another particle is moving on a different orbit characterized by the 6D coordinates $(x, x', y, y', s, \delta)$ where $x' = dx/ds$ and $y' = dy/ds$ are the transverse angular deviations while δ indicates the relative momentum deviation compared to the reference one.

1.1.1 Transverse Beam Dynamics

The equation of the transverse motion can be derived, in linear approximation, considering no longitudinal component of the magnetic field, i.e $\vec{B} = (B_x, B_y, B_s = 0)$. To the first order, it can be considered that only dipole and quadrupole magnets are acting on the particles of the beam. The dipoles produce uniform magnetic fields (without considering fringe errors) in the $\vec{e}_y$ direction to bend the particle in the horizontal plane. Ideally, a particle with reference momentum p_0 can move infinitely along the closed orbit of the accelerator. In the reality the particles diverge from the reference orbit and they need to be focused on the closed reference orbit. In synchrotron machines such as the LHC, the beam focusing is mainly provided by the quadrupole magnets acting as optical lenses. Focusing quadrupole magnets are used to provide focusing in the horizontal plane while defocusing magnets provide focusing in the vertical plane. In the presence of an uncoupled motion and for particles with no momentum deviation ($\delta = 0$), the transverse motion under the effect of periodic external fields is described, for synchrotron machines, by the so-called Hill equation [1, 2]:

$$x'' - k(s)x = 0 \tag{1.2}$$

with $k(s)$ the local quadrupole strength [1, 2] depending on the position s along the reference orbit. It is a periodic function such that $k(s) = k(s+C)$ with C being the circumference of the circular accelerator. The equation can be solved using Floquet theorem, using an ansatz of the form:

$$x(s) = A\,u(s)\,\cos(\varphi_x(s) + \phi) \tag{1.3}$$

where A and ϕ are constants of integration fixed by the initial conditions. The solution of Eq. 1.2 in the x-direction is [1, 2]:

$$x(s) = \sqrt{\epsilon_x \beta_x(s)}\,\sin(\varphi_x(s) + \phi) \tag{1.4}$$

and the angular deviation ($x' = dx/ds$):

$$x'(s) = -\sqrt{\frac{\epsilon_x}{\beta_x(s)}}\,[\alpha_x(s)\cos(\varphi_x(s) + \phi) + \sin(\varphi_x(s) + \phi)] \tag{1.5}$$

where $\beta_x(s)$ is the betatron function in the horizontal plane as a function of s along the accelerator reference orbit. It is a periodic function and it modulates the amplitude of the

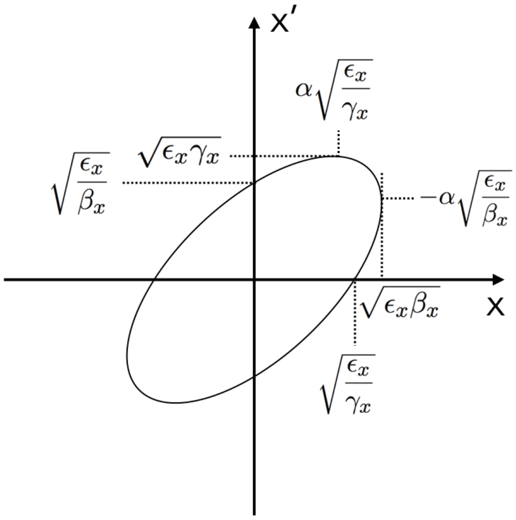
x'
$\alpha\sqrt{\frac{\epsilon_x}{\gamma_x}}$
$\sqrt{\epsilon_x\gamma_x}$
$\sqrt{\frac{\epsilon_x}{\beta_x}}$
$-\alpha\sqrt{\frac{\epsilon_x}{\beta_x}}$
$\sqrt{\epsilon_x\beta_x}$
x
$\sqrt{\frac{\epsilon_x}{\gamma_x}}$

Figure 1.2 – Particle trajectory in the trace space (x, x').

betatron oscillations $x(s)$ in the transverse plane. The phase ϕ is constant and depends on the initial conditions of the particle motion. The solution for the vertical motion gets the same form as in Eq. 1.4, characterized by the corresponding ϵ_y and $\beta_y(s)$. In the following only the horizontal plane will be considered for derivations that can be extended to the motion in the vertical plane (ignoring dipole focusing). The betatron phase advance $\varphi_x(s)$ is given by [1]:

$$\varphi_x(s) = \int_0^s \frac{\mathrm{ds}}{\beta_x(s)} \tag{1.6}$$

and it represents the fraction of betatron oscillation in the horizontal plane between two longitudinal positions in the accelerator orbit. The optical function $\alpha_x(s)$, that appears in Eq. 1.5, is defined as: $\alpha_x(s) = -\frac{\beta_x(s)'}{2}$ and together with $\beta_x(s)$ and $\gamma_x(s) = \frac{1+\alpha_x^2(s)}{\beta_x(s)}$ define the *Twiss parameters* that only depend on the lattice properties (i.e. the sequence of drifts and magnetic elements) of the accelerator. The number of betatron oscillations after one turn around the reference orbit defines the *betatron tune*:

$$Q_{x,y} = \frac{1}{2\pi}\int_0^C \frac{\mathrm{ds}}{\beta_{x,y}(s)} \tag{1.7}$$

that, as the other quantities related to betatron motion, can be expressed independently in x and y-direction in the case of uncoupled motion. The *off-momentum* particles generate a certain relative momentum spread $\Delta p/p_0$ in the beam leading to a dependency of the betatron tune to the so called *chromaticity*. The first order natural chromaticity is defined as:

$$Q'_{x,y} = \frac{\Delta Q_{x,y}}{\Delta p/p_0} \tag{1.8}$$

and it describes the tune perturbation at the first order due to quadrupolar errors for the off-momentum particles [2].

In the trace space (x, x'), the particle moves on an elliptical trajectory (Fig. 1.2) described by the following equation [2]:

$$\epsilon_x = \gamma_x(s)x^2(s) + 2\alpha_x(s)x(s)x'(s) + \beta_x(s)x'^2(s). \tag{1.9}$$

The shape of the ellipse depends on the longitudinal position s, while the area does not change in steady state conditions.

In the transverse plane, the particles distribution of the beam can be represented by a Gaussian distribution with $\sigma_x(s)$ (in the x-direction) that defines the beam size, and a divergence $\sigma'(s)$:

$$\sigma_x = \sqrt{\epsilon_x^{\mathrm{rms}}\beta(s)} \tag{1.10}$$

$$\sigma'_x = \sqrt{\epsilon_x^{\mathrm{rms}}\gamma(s)} \tag{1.11}$$

where $\epsilon_{\mathrm{x}}^{\mathrm{rms}}$ is the emittance root mean squared over all the particle trajectories in the trace space:

$$\epsilon_x^{\mathrm{rms}} = \sqrt{<x^2><x'^2> - <xx'>^2} \tag{1.12}$$

also called *geometric emittance* $\epsilon_x^{\mathrm{rms}} = \epsilon_x^{\mathrm{geo}}$. The corresponding geometric emittance $\epsilon_y^{\mathrm{geo}}$ can be defined in the $\vec{e}_y$ direction considering the trace space (y, y') .
In the trace space the geometric emittance $\epsilon_x^{\mathrm{geo}}$ is not an invariant of motion and during the acceleration (or deceleration) it reduces (or increases). To define an invariant of motion, it is possible to introduce more convenient variables to describe the dynamics of a particle moving along the beam orbit: the canonical action-angle variables. The advantage of action-angle variables is that, under symplectic transport, the action of a particle is constant [3]. The Cartesian x coordinate and the particle momentum along the $\vec{e}_x$ direction can be expressed as:

$$\begin{cases} x = \sqrt{2J_x\beta_x}\cos\Psi_x \\ p_x = -\sqrt{\dfrac{2J_x}{\beta_x}}(\sin\Psi_x + \alpha_x\cos\Psi_x) \end{cases} \tag{1.13}$$

the action J_x is now an invariant of motion:

$$J_x = \frac{1}{2}(\gamma_x x^2 + 2\alpha_x x p_x + \beta_x p_x^2). \tag{1.14}$$

In these new variables the ellipse in trace space is a circle in the phase space (x, p_x) of radius $R = \sqrt{2J_x}$ as illustrated in Fig. 1.3. The angular position Ψ_x along the ring became the inde-

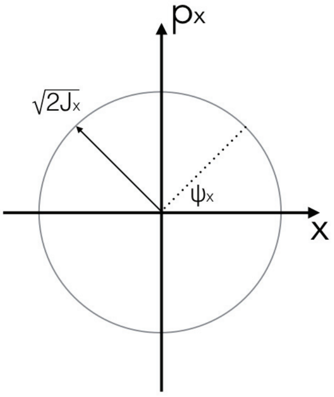

Figure 1.3 – Particle trajectory in the phase space (x, p_x).

pendent variable. The area in the phase space element $\Delta x\ \Delta p_x$ is now conserved.
The beam emittance is then defined as:

$$\epsilon_x = < J_x > \tag{1.15}$$

and it is an invariant of the motion. During acceleration, particles are accelerated only along the longitudinal direction $\vec{e}_s$ increasing their momentum p and the phase space element $\Delta x\ \Delta p_x$ is conserved because the transverse component of the momentum is constant. Since the momentum p is increasing (or reducing) the trace space element $\Delta x\ \Delta x'$ linked to the phase space through the relationship $\Delta x\ \Delta p_x = p \cdot \Delta x\ \Delta x'$ must be reduced (increased) to keep the product $\Delta x\ \Delta p_x$ constant. More precisely is $\Delta x'$ that must decrease during acceleration and as result the geometric emittance shrinks. It is therefore convenient to define a normalized emittance that does not vary with the particle energy:

$$\epsilon_x^{\text{norm}} = \gamma \beta_{rel} \epsilon_x^{\text{geo}} \tag{1.16}$$

where $\beta_{rel} = \frac{v}{c}$ is the relativistic factor, v is the particle velocity and c is the speed of light in the vacuum and $\gamma = \frac{1}{\sqrt{1-\beta_{rel}^2}}$. From here, each time we will refer to the emittance we will consider it as the normalized beam emittance $\epsilon_x^{\text{norm}} = \epsilon_x$. All these derivations can be applied to the vertical plane, and the related quantities will be specified by the corresponding index. If a particle is at a certain position s_1, it is possible to predict the evolution of the phase space coordinates downstream to a position s_2 by using the *transport matrix*:

$$\begin{pmatrix} x(s_2) \\ x'(s_2) \end{pmatrix} = M(s_1|s_2) \begin{pmatrix} x(s_1) \\ x'(s_1) \end{pmatrix} \tag{1.17}$$

where:

$$M(s_1|s_2) = \begin{pmatrix} \sqrt{\frac{\beta_1}{\beta_2}}(\cos\varphi_{21} + \alpha_1 \sin\varphi_{21}) & \sqrt{\beta_1\beta_2}\sin\varphi_{21} \\ -\frac{1+\alpha_1\alpha_2}{\sqrt{\beta_1\beta_2}}\sin\varphi_{21} + \frac{\alpha_1-\alpha_2}{\sqrt{\beta_1\beta_2}}\cos\varphi_{21} & \sqrt{\frac{\beta_1}{\beta_2}}(\cos\varphi_{21} - \alpha_2 \sin\varphi_{21} \end{pmatrix} \tag{1.18}$$

where φ_{21} is the phase advance between the two points. For *on-momentum* particles with reference momentum p_0, it is possible to use the transport matrix to calculate the coordinates x and x' in any point of the accelerator. After one turn, the transport matrix simplifies to the one-turn matrix (considering all linear elements):

$$M^{turn} = \begin{pmatrix} \cos(2\pi Q) + \alpha\sin(2\pi Q) & \beta\sin(2\pi Q) \\ -\frac{(1+\alpha^2)}{\beta}\sin(2\pi Q) & \cos(2\pi Q) - \alpha\sin(2\pi Q) \end{pmatrix}. \tag{1.19}$$

In general, for non-linear elements, the one-turn matrix will be replaced by a map $\mathscr{M}^{turn}$ that is obtained by concatenating in sequence around the ring all the N element individually described by a map. If we assume only linear elements, then all our maps are matrices.

1.1.2 Working point and tune diagram

Multiple fields induce higher resonances, for example an octupole field may produce a fourth order betatron oscillation resonance. Multipolar and misalignment errors in the real lattice always introduce multipole fields and as a result there are always resonances when mQ=p. In general every accelerator has two different betatron tune values Q_x in the horizontal plane and Q_y in the vertical plane. For higher multipole fields the strength in one plane depends on the beam position in the other. This leads to coupled betatron oscillations in the two planes, hence to coupled resonances. The tune diagram is defined by the (Q_x, Q_y)-space, where resonance lines appear when [1, 2]:

$$mQ_x + nQ_y = p \quad \text{(with m, n, and p integers)} \tag{1.20}$$

The resonance order is given by $|m| + |n|$. The strength of the resonance decreases rapidly with the order. For stable operation the working point (Q_x, Q_y) should be chosen far away from optical resonances. There are many constraints for choosing the working point: for example, it must not be an integer to avoid dipole error effects that can lead to closed orbit instability, it

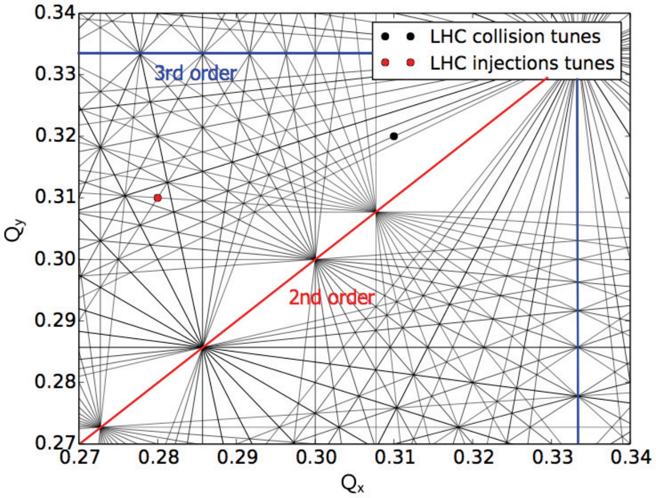

Figure 1.4 – LHC tune diagram (fractional tunes) with resonance lines up to the 13th order.

can not be half integer to avoid gradient error amplification that can lead to emittance blow up, it must not be at a sum resonance to avoid a coupled motion between the horizontal and the vertical plane. There are more constraints on the working point from collective instabilities, since the beam also spreads out in the tune diagram due to amplitude and momentum or due to beam-beam collisions (Fig. 1.6). The tune diagram with the LHC working points at flat top energy (black dot) and at injection energy (red dot) is shown in Fig. 1.4 with resonances up to the 13th order.

1.1.3 Linear coupling

The betatron motions in the horizontal and vertical plane are coupled through solenoidal fields placed in the detectors, skew quadrupole fields from quadrupole and feed-down effects arising from higher order multipoles. Following [4] the coupling betatron difference resonance occurs when:

$$Q_x - Q_y = p \tag{1.21}$$

with p integer and Q_x and Q_y the horizontal and vertical tunes respectively. When the above condition is satisfied the transverse motion in the two planes are on resonance and no longer independent. The strength of the linear coupling resonance can be quantify by a constant C^- that defines the minimum of the tune splitting between the horizontal and vertical tunes [5, 6]:

$$\Delta Q_{min} = |C^-| = \left| \frac{4\Delta}{2\pi R} \oint \mathrm{ds}\, \mathrm{f}_{1001} \mathrm{e}^{-\mathrm{i}(\phi_\mathrm{x}-\phi_\mathrm{y})+\mathrm{is}\Delta/\mathrm{R}} \right| \tag{1.22}$$

with R being the radius of the accelerator, ϕ_x and ϕ_y are the horizontal phase and vertical phase respectively, z is the longitudinal coordinate and f_{1001} the difference driving resonance term related to the Hamiltonian term [5]. The coupled motion between horizontal and vertical motions may lead to emittance blow up and deterioration of the beam lifetime. Therefore, it is important to minimize this effect and keep the coupling resonance strength under control.

1.1.4 Longitudinal Beam Dynamics

In the case of bunched beams, the particles are longitudinally grouped by the electric field in the *RF cavities* that consist of isolated gaps with a sinusoidal voltage applied. Passing through the RF, the particles are accelerated or decelerated depending on the synchronized arrival inside the RF.

During their motion the particle perform synchrotron oscillations around the reference particle's synchrotron phase Φ_s. The frequency ω_{RF} of the electric field is an integer multiple of the revolution frequency ω_0 in the ring:

$$\omega_{RF} = h\omega_0 \tag{1.23}$$

where h is the harmonic number.

The energy gain of the particles at each passage in the cavity is:

$$\Delta E = qV_0 \sin\varphi(t) \tag{1.24}$$

where q is the charge of the particle, V_0 is the amplitude of the potential of the cavity and φ is the phase of the particle compared to the RF phase. The derivation of the equation of the motion will be omitted here, it can be found in textbooks [1]. For small longitudinal amplitude, the synchrotron oscillations describe a stable motion following the equation:

$$\ddot{\varphi} + \Omega_s^2 \varphi = 0 \tag{1.25}$$

where

$$\Omega_s^2 = \omega_0^2 \frac{eV_0\eta h}{2\pi\beta_{rel}cp_0} \cos\Phi_s \tag{1.26}$$

with η being the slippage factor [1]. This is the equation of a harmonic oscillator and for stability the angular frequency must be a real positive number, therefore $\eta\cos\Phi_s > 0$. The stable particles oscillate on closed orbits within the area delimited by the separatrix [1]. This region of stability is called RF *bucket*. The particles that move on a trajectory outside become unstable and will be lost in the accelerator machine.

By analogy with the betatron motion it is possible to define a synchrotron tune Q_s:

$$Q_s = \frac{\Omega}{\omega_0} = \sqrt{\frac{eV_0\eta h}{2\pi\beta_{rel}cp_0} \cos\Phi_s}. \tag{1.27}$$

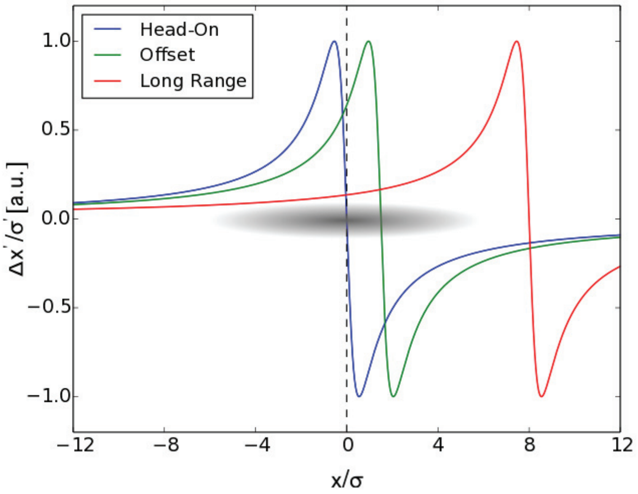

Figure 1.5 – Normalized transverse beam-beam kick as a function of the particle amplitude in the bunch for head-on collisions (blue line), long range interactions (red line) and with a transverse offset between the two beams (green line).

typically slower than the betatron tune, of the order of $Q_s \approx 10^{-3}$ in hadron machine. For the LHC, $Q_s \approx 5 \times 10^{-3}$ at injection energy and $Q_s \approx 2 \times 10^{-3}$ at flat top energy.

1.1.5 Beam-Beam interaction

In colliders, the two beams interact with each other at the Interaction Points (IPs) experiencing a force arising from the electromagnetic field produced by the particle distribution of the opposite beam, called the beam-beam force. The electromagnetic forces produced by the particle distributions are very non linear causing a wide spectrum of effects on the beam dynamics. These effects are classified in single particle effects and collective effects linked to a coherent motion of the whole beam [7, 8] discussed in the next section. Considering the opposite beam as a Gaussian distribution of particles with rms transverse beam sizes $\sigma = \sigma_x = \sigma_y$ and integrating the Poisson's equation [7, 8], the trajectory of a test particle at a position (x, y) with respect to the other beam's centroid will be deflected by a transverse beam-beam kick:

$$\Delta x' = -\frac{2r_0 N}{\gamma}\frac{x}{r^2}(1 - \mathrm{e}^{-\frac{\mathrm{r}^2}{2\sigma^2}}) \tag{1.28}$$

where N is the number of charges in the opposite beam, r_0 is the classical radius and $r = \sqrt{x^2 + y^2}$ is the radial distance from the beam axis. The transverse beam-beam kick is shown in Fig. 1.5 as a function of the transverse position x inside the bunch. The transverse beam-beam kick $\Delta x'$ was normalized to the r.m.s beam divergence σ' and the transverse position x to the rms transverse beam size σ. The blue line corresponds to the head-on collision for which

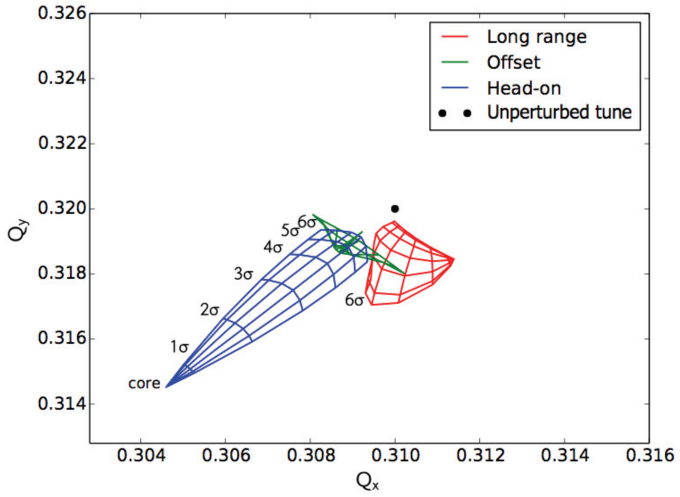

Figure 1.6 – Different detuning with amplitude (tune footprints) in the presence of head-on collisions only (blue line), long range interactions (red line) and with a small transverse offset at the IP between the two colliding beams.

the beams collide without any separation. For particles at very small amplitude, the force is approximately linear and a test particle in this range experiences a linear force. At larger radial distances, i.e. above ≈ 1σ in terms of transverse beam size units, the force strongly deviates from this linear behaviour, as it is also evident from the analytical formula in Eq. 1.28. This leads to a variation of the betatron tune $\Delta Q_{x,y}$ that depends on the particle's amplitude and it is related to the derivative of the beam-beam force. For a test particle in the core of the beam, the force can be considered approximately linear and from its derivative it is possible to derive a quantity ξ know as the beam-beam parameter [7, 8]:

$$\xi = \pm \frac{r_0 N}{4\pi\epsilon}. \tag{1.29}$$

The sign of the beam-beam parameter depends on the relative beam charges. For small values of ξ and a tune far away enough from linear resonances, the beam-beam parameter is equal to the linear tune shift $\Delta Q_{x,y}$ for the particles with vanishing amplitude. In this particular case the beam-beam interaction acts as an extra focusing (opposite charges) or defocusing (equal charges) quadrupolar component in the machine lattice. For the LHC, the beam-beam parameter is $\xi = 0.0037$ (per IP), considering the design beam parameters. The beam-beam parameter quantifies the strength of the beam-beam interaction but it does not evince the non linearity of the force. The non linear behaviour of the beam-beam force exhibits itself as an amplitude dependent tune shift. For a beam, that is a collection of particles oscillating with different amplitude, this results in a transverse tune spread.

In the presence of separated beams, the particles experience long range beam-beam interactions. The red line in Fig. 1.5 represent the beam-beam kick for a transverse displacement $d = 8\,\sigma$ between the two beams. The small amplitude particles will now experience a beam-

beam force proportional to $1/d$. With a small transverse offset, as shown in Fig. 1.5 (green line), for $d = 1.5\,\sigma$ between the two beams the small amplitude particles undergo to a strongly non-linear beam-beam force. The tune shift is proportional to the derivative of the beam-beam force. In the case of equal charged particles, as in the LHC with proton-proton collisions, the head-on produces negative tune shifts, in fact for zero amplitude particles the slope of the beam-beam force is negative (Fig. 1.5). Contrary to the head-on collisions, for long range interactions the slope of the beam-beam force is positive for the zero amplitude particles (Fig. 1.5) and the tune shift is hence positive in the separation plane. Figure 1.6 shows the transverse spread for different beam-beam interactions: head-on collisions (blue line), long range (red line) and long range and head-on collisions with a small transverse offset between the two colliding beams (green line) at the IPs. The black point represents the unperturbed tune. Typically the beam-beam force is very strong and a perturbative treatment, as usually done when considering multipolar magnets, is not adequate. The detuning with amplitude can be derived from the effective Hamiltonian by using Lie transforms [7, 8]. In complex configurations, including multiple beam-beam interactions or small transverse offsets at the IPs particle tracking is the most efficient way to compute and characterize the overall tune spread in the beams. Each plot in Fig. 1.6 is obtained by tracking the particles with different actions using the *DYNAP* module of the MAD-X code [9, 10]. The particles are tracked through the lattice element by element and their coordinates are computed turn by turn knowing the transfer map of each element. The oscillation frequencies in the transverse plane of each particle, i.e. the horizontal tune and the vertical tune, are evaluated by an interpolated FFT of the transverse positions and plotted in the tune diagram $(\mathrm{Q_x}, \mathrm{Q_y})$ as a tune *Footprint* [11]. As shown in Fig. 1.6, in the presence of head-on collision the particles in the core of the beams experience the largest tune shift with the maximum tune shift given by the beam-beam parameter ξ. The detuning in the presence of long range collisions is represented by the red line and the large amplitude particles are the most affected. In the presence of a small transverse offset at the IP the tune spread behaviour can be quite complicated (green line) and the use of numerical tools is the most effective way to characterize it.

The LHC collides particles of the same type traveling in separated beam pipes. The two beams are brought together at the IPs sharing the vacuum chamber for more than 120 m. The LHC beams are organized in trains of particle bunches according to the filling scheme used [12]. In the LHC the distance between the bunches is only 25 ns and therefore the bunches will meet in the interaction region. In order to avoid multiple head-on collisions, the beams collide quasi head-on at the IP with a small crossing angle α_c used to kept separated the other bunches [13]. Figure 1.7 shows a schematic view of a collision at the LHC. Since the bunches travel in a common beam pipe, the bunches still feel the electromagnetic forces from the bunches of the opposite beam experiencing long range beam-beam interactions.

From the bunch spacing and the length of the interaction region the bunches experience 30 of these long range encounters, i.e. in total 120 interactions for the four interaction regions at the LHC [12]. The normalized long range beam-beam separation in units of the transverse beam size at the IPs as a function of the crossing angle (without a transverse offset at IPs) is given by:

$$d_{bb} = \alpha_c \sqrt{\frac{\beta^*}{\epsilon^{geo}}} \tag{1.30}$$

where α_c is the crossing angle and it is only valid in the drift space. Typical separations at the first long range encounter are $d_{bb} = 7 - 12\ \sigma$ in units of the rms beam size of the opposing beam. The long-range interactions distort the beams much less than a head-on interaction, but their large number and some particular properties can cause several effects such as breaking the symmetry between planes. They mostly affect particles at large amplitudes causing tune shift with an opposite sign in the plane of separation compared to the head-on tune shift. At the LHC an alternating crossing scheme compensates the coherent tune shifts and PACMAN effects [13]. With this scheme the beams are separated in the horizontal plane in one interaction region and in the vertical plane in another one [14]. The tune footprints for two head-on collisions (blue line), long range interactions with horizontal separation (green line) and vertical separation (red line) are shown in Fig. 1.8. The different sign of the long range tune shift moves the footprints in opposite directions with respect to the original tune. The combined footprint for particles which experience two head-on collisions and long-range interactions with alternating crossing is also shown in Fig. 1.8 (pink line). A compensation of the beam-beam long range tune shifts is achieved and the tune footprint results to be symmetric in the horizontal and vertical plane, with the linear tune shifts of the central parts very well compensated [14]. The LHC beams are composed by bunches of particles organized

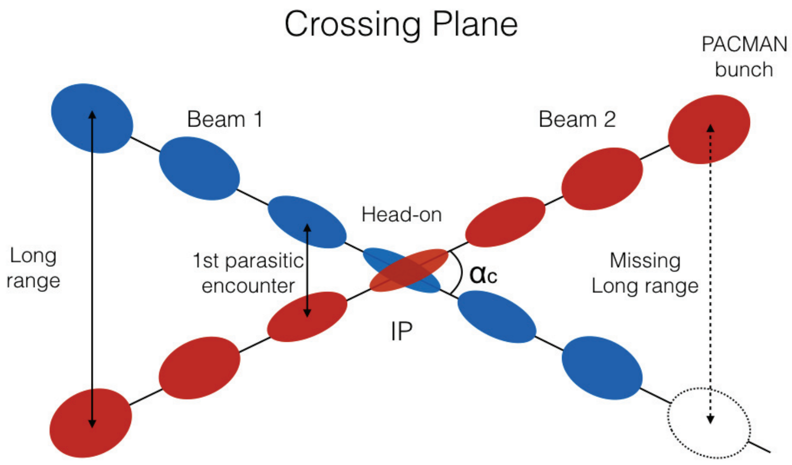

Figure 1.7 – Schematic view of the beam crossing scheme with finite crossing angle α_c at the LHC IRs.

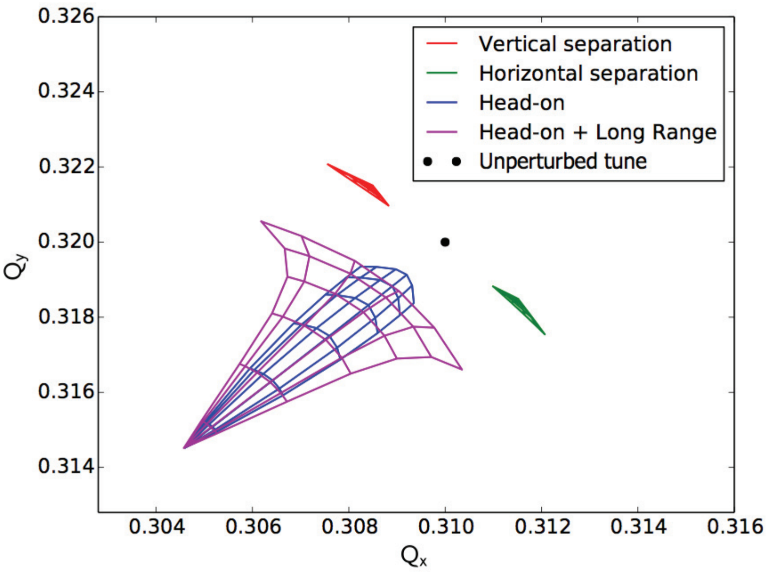

Figure 1.8 – Tune footprints for two head-on collisions (blue line), long range interactions with horizontal separation (green line) and vertical separation (red line) together with the combined beam-beam head-on and long range interaction footprint (pink line). The alternating crossing scheme compensates the tune shift caused by the beam-beam long range interactions.

in trains. The bunch spacing is not always uniform along the train since some time is needed to allow for the rise time of kickers for injection and extraction procedures of the beams. The specifications of the gaps and the number of bunches per batch are determined by the LHC injectors. According to the LHC filling scheme used [12], the bunches experience different number of head-on collisions and long range interactions leading to different families of bunches [15]. The so called PACMAN bunches are located in the head or in the tail of the batch, and they are characterized by missing head-on or long range interaction due to empty slots at the interaction points. As a result the PACMAN bunches experience fewer long range interactions than bunches from the middle of a batch (nominal bunches) leading to different beam-beam effects [15]. This is visible in Fig. 1.9 where the tune footprints are shown for PACMAN and nominal bunches in the presence of long range beam-beam interactions (red and green line respectively) and in the presence of beam-beam head-on and long range interactions (pink and blue line respectively). Due to the missing long range interactions for the PACMAN bunches, the tune spread due to the long range beam-beam interactions is smaller than the one for nominal bunches.

1.2 Collective effects

The electromagnetic fields induced by the particle passages in the accelerator environment (wake fields) act back on the beam, altering the beam dynamics. The interactions with the

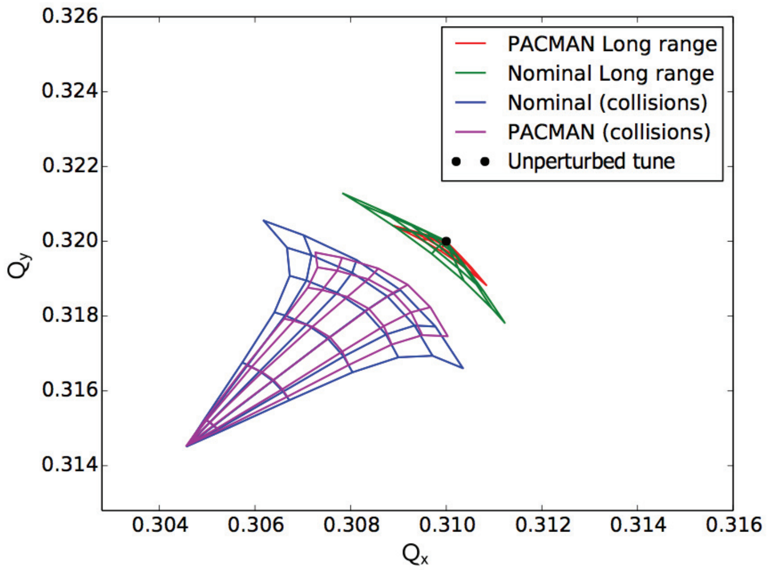

Figure 1.9 – Tune footprints for PACMAN and nominal bunches in the presence of long range beam-beam interactions (red and green line respectively) and in the presence of beam-beam head-on and long range interactions (pink and blue line respectively). The tune spread due to the beam-beam interactions for PACMAN bunches is smaller than the one for nominal bunches because of the missing long range collisions.

wake fields and the beam-beam interactions may result in coherent effects that can lead to an organized and collective motion of the particles inside the beam. In this section collective effects due to impedance and beam-beam interactions are shortly introduced.

1.2.1 Beam coupling impedance

Traveling in the accelerator environment, the charged particles induce image charges and currents in the surrounding structures creating electromagnetic fields called wake fields. The produced wake fields act back on the beam, altering the transverse and longitudinal beam dynamics. The impedance is defined as the Fourier transformation of the wake field and it is a complex function of frequency in the time domain [16].

Considering a test particle in the tail of the bunch with transverse and longitudinal coordinates $(\vec{x}_0, s_0)$ and a source particle of the wake field in the head off the bunch with transverse and longitudinal coordinates $(\vec{x}_s, s_s)$ separated by a constant (short) distance ds during the motion, the angular kicks due to the beam coupling impedance can be expressed as [17, 18]:

$$\begin{cases} dx' &= \vec{w}_{x,dip}(s_s, s_t)\vec{x}_s + \vec{w}_{x,quad}(s_s, s_t)\vec{x}_t \\ dy' &= \vec{w}_{y,dip}(s_s, s_t)\vec{x}_s + \vec{w}_{y,quad}(s_s, s_t)\vec{x}_t \\ d\delta &= \vec{w}_{s,dip}(s_s, s_t)\vec{x}_s + \vec{w}_{s,quad}(s_s, s_t)\vec{x}_t \end{cases} \tag{1.31}$$

where the beam oscillation amplitudes are assumed to be much smaller compared to the typical size of its surroundings and the beam coupling impedance is expressed as a Taylor expansion up to first order with ($\vec{w}_{x,dip}$) and ($\vec{w}_{x,dip}$) the dipolar and quadrupolar wake functions in the different degrees of freedom. The wake depends only on the distance between the two particles $ds = s_0 - s_s$ within the ultra relativistic approximation. The forces induced by the impedance can be considered small compared to the ones of other magnetic elements in one turn and it can be treated as a perturbation of the particle motion. Therefore it is possible to integrate their contributions over a full turn obtaining the total wake functions W and the change the total change of momentum in all degrees of freedom [17]:

$$\begin{cases} \Delta x' &= \vec{W}_{x,dip}(\Delta s)\vec{x}_s + \vec{W}_{x,quad}(\Delta s)\vec{x}_t \\ \Delta y' &= \vec{W}_{y,dip}(\Delta s)\vec{x}_s + \vec{W}_{y,quad}(\Delta s)\vec{x}_t \\ \Delta\delta &= \vec{W}_{s,dip}(\Delta s)\vec{x}_s + \vec{W}_{s,quad}(\Delta s)\vec{x}_t \end{cases} \tag{1.32}$$

a more complete treatment can be found in [18]. Extending the description of a single particle to the whole beam, the impedance kicks cause complex coherent tune shifts ΔQ_{coh} and may lead to beam instabilities under certain conditions [18]. The real part of the complex coherent tune shifts is linked to the real tune shifts induced by the machine impedance while the imaginary part is linked with the rise time of the instability and defines the stability of the impedance mode. The machine and beam parameters play an important role in the stability threshold of an accelerator such as chromaticity, beam intensity, bunch length and slippage factor. The coherent impedance modes can be computed using different impedance models such as DELPHI, an analytical code to compute transverse instability modes from beam-coupling impedance and transverse feedback [19], PyHEADTAIL [20] or BIM-BIM [17] to compute beam-beam and impedance coupled modes.

1.2.2 Coherent beam-beam effects

In the presence of the beam-beam interaction, the two beams can be strongly coupled to each other leading to a coherent oscillations between the bunches of the beams. In order to treat the coherent dynamics of the beams, different approaches can be used to calculate the electromagnetic field and describe the particle distribution inside the bunch. A full treatment

of the coupled system in terms of the Vlasov equation formalism can be found in [21].
In order to describe the beam-beam coupling of multi-bunches, a simplified linear model will be considered in this section. To describe the coherent motion of the bunches, it is needed to consider the beam as whole. In order to obtain the coherent beam-beam force, the single particle beam-beam transverse kick in Eq. 1.28 is integrated over the particle distribution of the bunch $\Psi(x, y)$:

$$\Delta x'_{coh}(x, y) = \int_{-\infty}^{\infty} \Delta x'(x, y)\Psi(x - \bar{x}, y - \bar{y})\mathrm{d}x\,\mathrm{d}y \tag{1.33}$$

where $\bar{x}$ and $\bar{y}$ are the mean value of displacement (dipole moment). Considering a round Gaussian distribution and following [22], the coherent beam-beam kick:

$$\Delta x' = -\frac{2r_0N}{\gamma}\frac{x}{r^2}(1 - \mathrm{e}^{-\frac{-\mathrm{r}^2}{4\sigma^2}}) \tag{1.34}$$

with $r = \sqrt{x^2 + y^2}$. Due to the factor $1/4$ in the exponential term, for the case of head-on interaction, i.e. for $r \to 0$, the coherent beam-beam kick felt by the whole bunch is half of the single particle kick. For long range, i.e. for large separation, the difference between coherent and incoherent effects vanishes.

As previously introduced, in circular accelerators, it is possible to determine the particle motion after one turn around the accelerator machine by the one-turn map. Including the non-linear elements of the beam-beam interaction in the one turn map, the beam-beam coherent modes from the head-on interactions can be analyzed by searching for the eigenvectors and the eigenvalues of the full one turn map [23]. In the case of two identical rigid bunches fully described by the centre of mass (rigid bunch approximation) and considering only one head-on collision, the eigenstates analysis reveals two frequencies (coherent tunes Q_{coh}) for two different coherent modes: in-phase oscillation of the two bunches (σ-mode): $Q_\sigma = Q_\beta$, with Q_β being the betatron tune, or out-of-phase oscillation (π-mode): $Q_\pi = Q_\sigma + \xi$ where the beam-beam interaction is linearized considering head-on collisions. Due to this approximation it is expected to have a difference with respect to the exact solution that can be quantified by the Yokoya factor Y for which $Q_\pi = Q_\sigma + Y \cdot \xi$. For round Gaussian beams $Y \approx 1.21$ [24].

1.2.3 Landau damping mechanisms

The derivation of the dispersion integral and the Beam Transfer Functions (BTFs) mainly follows [25, 26]. The Landau damping in plasma physics refers to the damping of collisionless oscillations predicted by L. Landau [27]. In accelerator physics the Landau damping concept can be applied to predict the stability of charged beams [28]. In particles beams, each particle oscillates with its own frequency in the horizontal and vertical plane $\omega_{x,y}(J_x, J_y)$ depending on its action variables. Therefore, the beam can be visualized as an ensemble of non linear oscillators under the effects of external non linear forces such as the sinusoidal RF wave in the longitudinal plane and octupolar or high multipolar field components in the transverse plane. Considering a driven oscillator under an infinitesimal force of frequency Ω, for instance in the horizontal plane:

$$F_x(t) = \epsilon A_x \mathrm{e}^{-\mathrm{i}\Omega \mathrm{t}} \tag{1.35}$$

with Ω close to the amplitude dependent betatron frequency $\omega_{x,y}(J_x, J_y)$. A perturbative solution of the Vlasov equation leads to a collective beam response in the same plane as the excitation frequency [25, 26]:

$$< x >= 2\pi^2 F_x(t) \int_0^\infty \mathrm{dJ_x} \int_0^\infty \frac{\mathrm{J_x} \frac{\partial \Psi(\mathrm{J_x},\mathrm{J_y})}{\partial \mathrm{J_x}}}{\Omega - \omega_{\mathrm{x,y}}(\mathrm{J_x}, \mathrm{J_y})} \mathrm{dJ_y} \tag{1.36}$$

with $\Psi(J_x, J_y)$ being the beam distribution function. The multiple integral is proportional to the BTF. If the driving terms are due to rigid dipole oscillations caused by the machine impedance, Eq. 1.36 relates with the coherent frequency tune shift ΔQ_{coh} through the dispersion relation [25]:

$$SD^{-1}(\Psi, \omega) = \frac{-1}{\Delta Q_{coh}} = \int_0^\infty \mathrm{dJ_x} \int_0^\infty \frac{\mathrm{J_x} \frac{\partial \Psi(\mathrm{J_x},\mathrm{J_y})}{\partial \mathrm{J_x}}}{\mathrm{q} - \omega_{\mathrm{x,y}}(\mathrm{J_x}, \mathrm{J_y})} \mathrm{dJ_y} \tag{1.37}$$

where $q \in \mathbb{R}$ is the unperturbed tunes where the imaginary part of the dispersion integral in Eq. 1.37 differs from zero and SD denotes the Stability Diagram that quantifies the Landau damping in the beams. It represents a stability area in the complex plane $(Im(\Delta Q_{coh}), Re(\Delta Q_{coh}))$ for which the coherent motion of the beam is stable in the presence of detuning, i.e. $Im(\Delta Q_{coh}) < 0$ [28]. The frequency spread $\omega_{x,y}(J_x, J_y)$ provides the size of the stability diagram while the particle distribution provides the shape. However, if the particle distribution changes, the term $\partial\Psi(J_x, J_y)/\partial J_{x,y}$ in Eq. 1.37, describes the change of tune with the amplitude. Several sources of tune spread can enlarge the beam frequency spread, and therefore the stability diagram, for example space charge, chromaticity, high-order multipole fields (as octupole magnets) and beam-beam interactions. As previously mentioned BTFs are proportional to the dispersion integral in Eq. 1.37 and provide direct measurements of the Landau damping in the beams. The response of the beam to a certain excitation frequency Ω of amplitude A_{exc} is defined as:

$$\frac{BTF(\Omega)}{A_{exc}(\Omega)} = C \cdot SD^{-1}(\Psi, \omega) = C \cdot \int_0^\infty \mathrm{dJ_x} \int_0^\infty \frac{\mathrm{J_x} \frac{\partial \Psi(\mathrm{J_x},\mathrm{J_y})}{\partial \mathrm{J_x}}}{\mathrm{q} - \omega_{\mathrm{x,y}}(\mathrm{J_x}, \mathrm{J_y})} \mathrm{dJ_y}. \tag{1.38}$$

Transverse BTF measurements in the LHC will be extensively discussed in Chapter 5.

1.3 Luminosity

To express and quantify the performance of a particle collider, the energy and the luminosity reach are key indicators of such parameter. The instantaneous luminosity quantifies the production rate R_t of a certain event of a cross section σ_{event} through the expression:

$$R_t = \frac{dN}{dt} = \mathscr{L} \cdot \sigma_{event} \tag{1.39}$$

the smaller is the event cross section (rare event), the higher is the required luminosity to detect it with a significant statistics. For example in the case of the Higgs Boson with a cross section $\sigma_{Higgs} \approx 57\,\mathrm{pb}$ (for the designed beam energy $E = 7\,\mathrm{TeV}$) the production rate is $R_t \approx 0.57\,\mathrm{s}^{-1}$ (considering the LHC designed instantaneous luminosity $\mathscr{L} = 1 \times 10^{34}\,\mathrm{cm}^{-2}\,\mathrm{s}^{-1}$ [29]). Considering round beams (i.e. $\sigma_x = \sigma_y = \sigma$) with a Gaussian particle distribution, when the beams collide with a full crossing angle α_c as shown in Fig. 1.7, the instantaneous luminosity $\mathscr{L}$ is defined as [30] :

$$\mathscr{L} = \frac{N_1 N_2 f_{rev} n_b}{4\pi\beta^* \epsilon^{\mathrm{geo}}} \cdot R; \quad R = \frac{1}{\sqrt{1 + \left(\frac{\alpha_c \sigma_z}{2\sigma}\right)^2}} \tag{1.40}$$

where R is called *luminosity geometrical reduction factor* and depends on the IP geometry, $N_{1,2}$ are the bunch intensities (number of particles per bunch), n_b is the number of bunches in the beam, f_{rev} is the revolution frequency (11.2 kHz in the LHC), σ is the rms transverse beam size at the IP, β^* is the betatron function at the collision point, ϵ^{geo} is the geometric emittance and σ_z is the r.m.s longitudinal beam size. The units to express the instantaneous luminosity are [$\mathrm{cm}^{-2}\mathrm{s}^{-1}$].

The instantaneous luminosity is not constant with time, indeed it degrades while the beams are kept in collisions. Different possibilities exist to model the time dependency [31]. In order to describe the decay an exponential behaviour with a given lifetime (τ) is assumed:

$$\mathscr{L}(t) = \mathscr{L}_0 \cdot \mathrm{e}^{\frac{-\mathrm{t}}{\tau}} \tag{1.41}$$

with $\mathscr{L}_0$, the maximum peak luminosity typically reached after the operational optimization of the IP at the beginning of collisions. The final figure of merit to calculate the total number of events produced over an amount of time T is the so-called integrated luminosity:

$$\mathscr{L}_{int} = \int_0^T \mathscr{L}(t)\mathrm{dt} = \mathscr{L}_0 \int_0^{\mathrm{T}} \mathrm{e}^{\frac{-\mathrm{t}}{\tau}}\,\mathrm{dt}. \tag{1.42}$$

High luminosity is required to produce rare events with a small production cross section σ. The design peak luminosity was reached in the LHC for the first time during the 2016 physics run thanks to high brightness beams injected into the LHC. In order to observe rare physics events with a significant statistics, the luminosity has to be maximized and with it also the event production. However, the detectors require some constraints on the luminosity value due to their detection efficiency [32] that depends both on the detector characteristics and the physics event to detect. One of the method to decrease the peak luminosity consists to collide the beams with a small transverse separation at the IP. This process is called *luminosity leveling* with an offset [30]. In the presence of a transverse separation d between the beams, the instantaneous luminosity is described by:

$$\mathscr{L}_d = \mathscr{L}_0 \cdot \mathrm{e}^{-\frac{\mathrm{d}^2}{4\sigma^2}} \tag{1.43}$$

where d is the separation at the IP between the two colliding beams and σ is the transverse rms beam size considering round beams.

2 Physical model simulations

The main features of the simulation tools used to carry out the Landau damping studies and the data analysis are presented in the next chapters.

2.1 Particle tracking

As previously presented, MAD-X [11] is used here to compute the detuning with amplitude, called also tune footprint, by tracking particles with different actions in the transverse plane. The particles are tracked turn by turn through the lattice elements described in MAD-X as transfer maps [9]. An interpolated FFT of the transverse coordinates x and y gives the amplitude detuning of the tracked particles. In particular, the amplitude detuning is used as an input for the semi-analytical computation of the stability diagram by using the PySSD code [17] presented in the next section. Particle tracking simulations are also carried out by using the SixTrack code [33] and the COMBI (COherent Multi Bunch Interation) code [34], more details will follow in the next sections.

2.1.1 COherent Multi Bunch Interaction (COMBI)

The COMBI code was developed by T. Pieloni in order to study the coherent beam-beam interaction of multiple bunches coupled by the head-on and long range interactions [8, 35–37]. Taking into account different collision patterns and schemes, the code allows to study in a self-consistent way the wide spectrum of modes expected for a collider with multiple interaction points such as the LHC [38, 39]. In the subsequent years, the code has been extended including a first level of parallelization with Message Passing Interface (MPI) [8] and a second one sharing several CPUs per node using OpenMPI [17, 40].

The particles of different bunches are tracked individually for many turns under the effects of several actions (e.g. beam-beam head-on and long range interactions, linear and non linear transfers, impedance, etc.). From the long term tracking the evolution of the beam parameters, e.g. emittances and barycentres, can be deduced treating the beam motion in a self-consistent manner to derive the coherent dynamics of the beam that is described as a set of macro particles. Each element is described by a linear or non linear map. The accelerator circumference is modeled by equally spaced number of slots that define the possible bunch positions. The number of available slots are defined in the beam filling schemes input file where the number of empty or occupied slots is specified. At each bunch position it is possible to assign an action that will be executed when a bunch is present. Beam-beam interactions (head-on or long range) require two bunches (i.e. one from each beam) in order to be performed. The full action sequence is described in a second text file read as input for the code. Each line is associated to an action, identified by a code number, specifying its position in the accelerator sequence and the arguments required by the action in order to be executed. The available actions are multiple, not only regarding the beam-beam interaction, but also non-linear elements, impedance and machine devices (transverse feedback, electron lens, BTF etc.). In the next paragraph a new implementation of the BTF module in COMBI will be described in detail.

2.1.2 BTF module in COMBI

A new dedicated module was implemented in the COMBI code to simulate the transverse BTF response of the beam characterized by an amplitude and a phase as a function of the excitation frequency. Each time a bunch occupies the position where the BTF action is defined, a sinusoidal excitation is applied to the particles under the following specific requirements given as arguments to the BTF action:

- Excitation amplitude of the kick applied in the horizontal or vertical plane;
- Initial and final excitation frequency;
- Resolution of the frequency sweep;
- Number of transient turns before starting the first BTF excitation;
- Number of turns for each step of the BTF excitation.

The BTF excitation is applied as a transverse kick (x' or y') in the chosen plane within the specified betatron frequency range over the selected number of turns N for each frequency step:

$$x' = A_x \cdot \sigma' \sin(2\pi Q) \tag{2.1a}$$

$$y' = A_y \cdot \sigma' \sin(2\pi Q) \tag{2.1b}$$

where $A_{x,y}$ is the excitation amplitude in the chosen plane in units of the beam divergence σ' and Q is the excitation frequency. The amplitude and the phase of the BTF are computed in the post processing by using the Fourier sums, for which the real part is:

$$\sum_{i-1}^{N} x_i \cos[2\pi Q\cdot(n-1)] \tag{2.2a}$$

and the imaginary part is:

$$\sum_{i-1}^{N} x_i \sin[2\pi Q\cdot(n-1)] \tag{2.3a}$$

where x_i is the transverse coordinate of the beam centroid at the $i-th$ turn, n is the number of turn and the sum extends over the total number of turns N during which the excitation frequency Q is applied. Usually the first 500 turns are discarded to avoid transient effects in between two consecutive BTF excitations. The longer the duration at the excitation the better is the signal to noise ratio in the BTF response. Figure 2.1 shows the simulated BTF response, as a function of different number of turns for each excitation frequency step (Fig. 2.1a) and for different number of macro particles (Fig. 2.1b). For each case, the amplitude response was normalized to the number of turns N and to the applied excitation amplitude. As expected, the signal response improves with N and with the number of macro particles both in the amplitude and in the phase. Figure 2.2 shows the standard deviation between model and the simulated amplitude (Fig. 2.2c) and phase response (Fig. 2.2d) as a function of the number of macro particle used. The black lines in the amplitude response (Fig . 2.2a) and in the phase (Fig . 2.2b) represent the model expectation in the presence of linear detuning with amplitude produced by octupole magnets, with a current of 6.5 A used at the LHC injection energy (450 TeV). The corresponding octupole strength can be quantified by the octupole linear coefficients given in Eq.2.6. The noise level, and therefore the comparison with the model improves by increasing the number of macro particle in the beams, usually 10^5-10^6 macro particles are used for the simulations presented here. The red shadow in the plots represents the calculated standard deviation from the model according to the number of macro particles used.

The excitation amplitude plays an important role in terms of signal to noise ratio, the larger it is the better is the BTF signal giving the possibility to reduce the number of turns N per step, hence the computing time of the simulations. However, if it is too large, it can affect the beam motion leading to an emittance blow up, especially after the excitation at the frequency of the coherent betatron tune. Figure 2.3 shows the emittance growth in the horizontal plane for different excitation amplitudes as a function of the number of turns during some BTF excitations in the same plane with a resolution of the frequency steps of 1.5×10^{-4}. Approaching the coherent response of the beam an emittance blow up is observed, negligible for a $\mathrm{A_x} = 2\sigma'\cdot10^{-5}$, and more important for $\mathrm{A_x} = 8\sigma'\cdot10^{-5}$ reaching a growth of the 6% ($\sigma' = 6.88\times10^{-6}$). Figure 2.3b shows the emittance growth for different frequency resolution steps with COMBI. The emittance growth becomes more important decreasing the frequency resolution steps. A key point to keep a good BTF signal to noise ratio without affecting the beam quality resides in the BTF simulation settings: an incorrect simulation setup may lead to a significant emittance blow-up during the particle tracking.

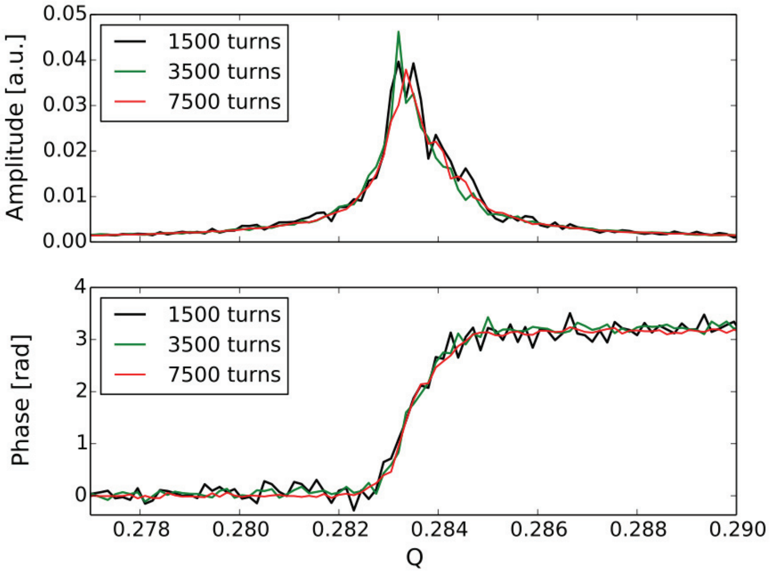

(a) BTF amplitude and phase response as a function of different number of turns for each BTF excitation.

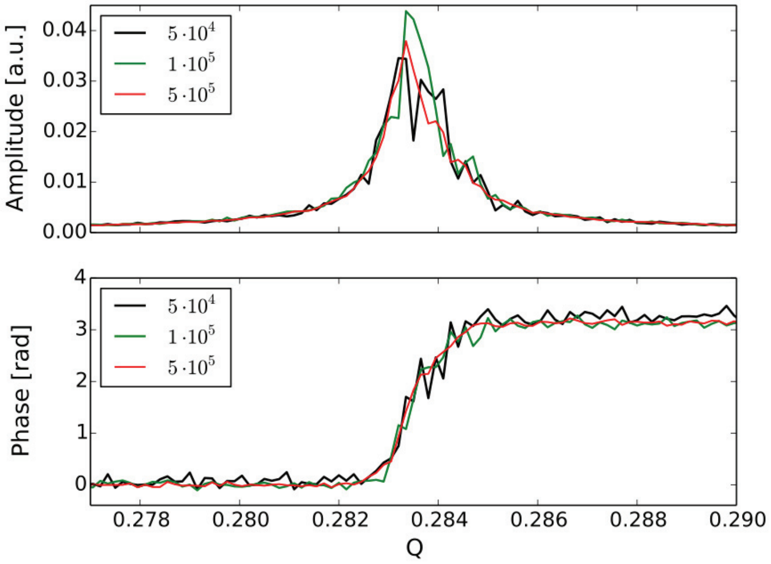

(b) BTF amplitude and phase as a function of different number of macro particles.

Figure 2.1 – Simulated amplitude and phase BTF response as a function of different number of macro particles and turns.

2.1.3 Effects of chromaticity on simulated BTF response

The chromaticity is included in COMBI by specifying the chromaticity value Q', the momentum spread δ_p and the synchrotron tune Q_s. The coupled synchro-betatron motion, under

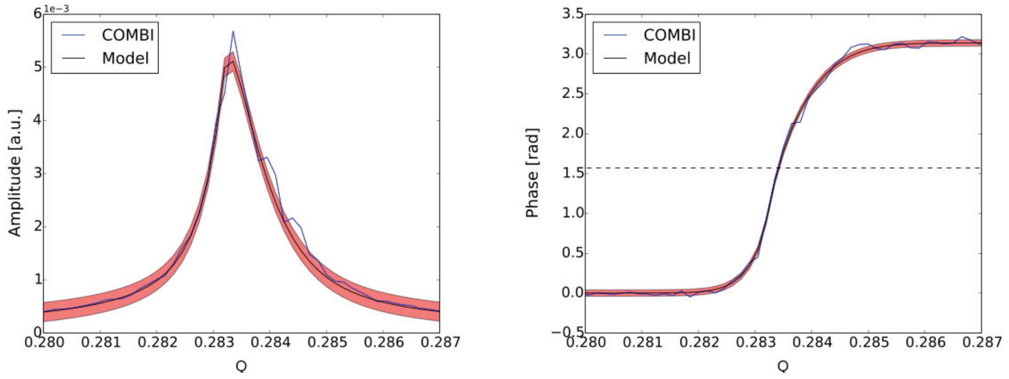

(a) Simulated BTF amplitude response compared to model.

(b) Simulated BTF phase response compared to model.

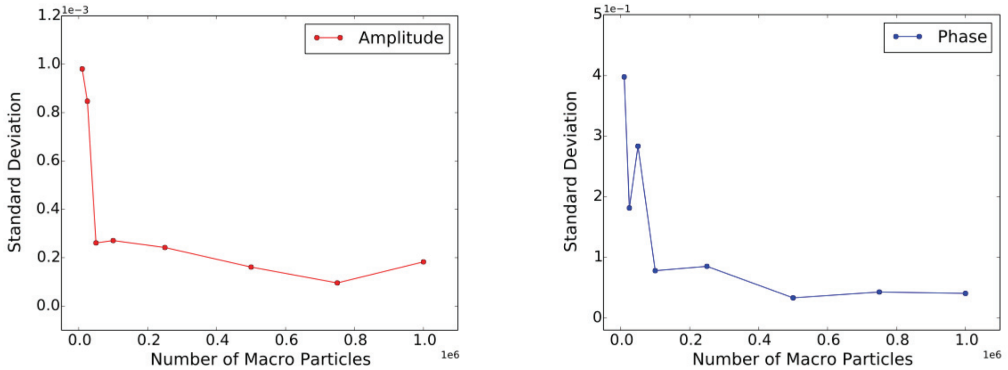

(c) Standard deviation of simulated BTF amplitude response as a function of the number of macro particles.

(d) Standard deviation of simulated BTF phase response as a function of the number of macro particle.

Figure 2.2 – Standard deviation between model and simulated amplitude and phase responses as a function of the number of macro particle used in COMBI simulations. The red shadow in the plots represents the calculated standard deviation from the model. Simulations have been carried out for an amplitude detuning produced by octupole magnets.

the effects of the BTF excitation produces sidebands at $n \cdot \pm Q_s$ from the bare betatron tune $Q_{x,y}$ in the amplitude response and jumps in the phase response. An example of a simulated BTF for a chromaticity value $Q' = 4$ (green line) is presented in Fig.2.4 for an excitation in the horizontal plane. A linear amplitude detuning was introduced in the simulations corresponding to an octupole current of 11.5 A (Eq. 2.6) for a beam energy of 450 GeV and a normalized beam emittance of $\epsilon = 2.0\,\mu\mathrm{m}$. The betatron tune was set to $\mathrm{Q_x} = 0.312$ and the synchrotron tune to $\mathrm{Q_s} = 0.005$, as a reference the black dashed lines are positioned at $\mathrm{Q_x} \pm \mathrm{Q_s}$. The red line corresponds to the same simulation case but without chromaticity. The corresponding stability diagrams for both cases are shown in Fig. 2.5 where close loops appear in the stability diagram only for the case with chromaticity. It has to be noticed that in this example the size of the stability diagram does not corresponds to the analytical one since arbitrary units were

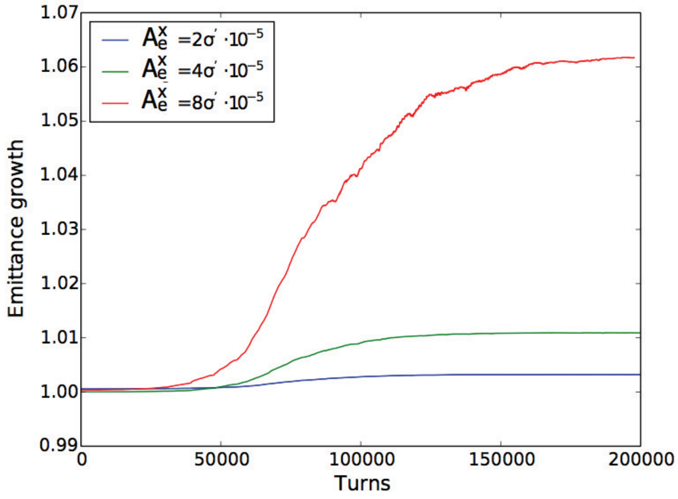

(a) Emittance growth for different excitation amplitudes.

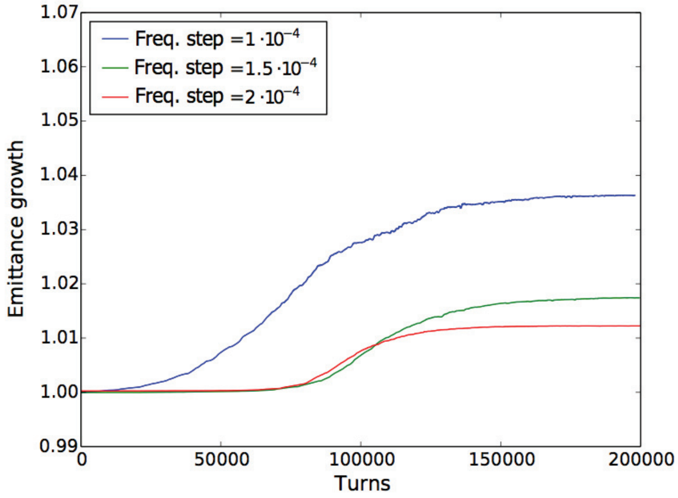

(b) Emittance growth for different frequency resolution steps.

Figure 2.3 – Emittance growth for different BTF excitation amplitudes and frequency resolution steps in COMBI.

used for the BTF amplitude response. The height of the BTF amplitude gives a rescaling factor of the stability diagram in the complex plane. Further details and analysis on this topic will be discussed in the next sections in order to address the correct size of the stability diagram derived from the simulated BTF response. The signal of the BTF response, and therefore the derived stability diagram is noisier on the right side of the frequencies with respect to the betatron tune. Usually the sweep in frequency for the BTF excitation is done from lower to higher frequencies during BTF measurements. By inverting the frequency sweep, the derived stability diagram becomes more distorted on the side of the negative real tune shifts. This

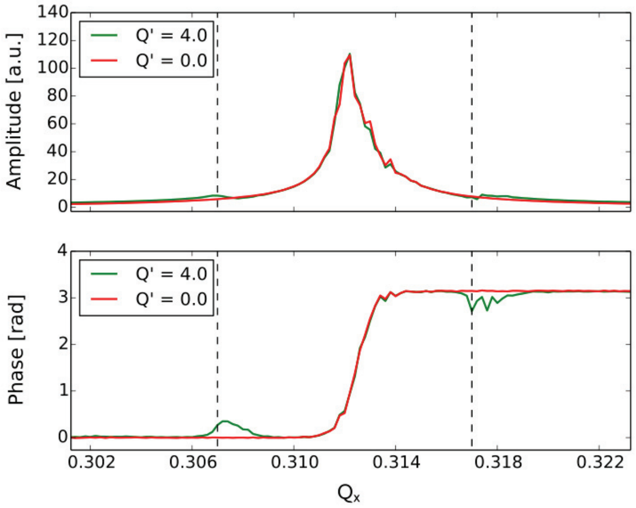

Figure 2.4 – Simulated BTF response in COMBI with chromaticity set to 4 units.

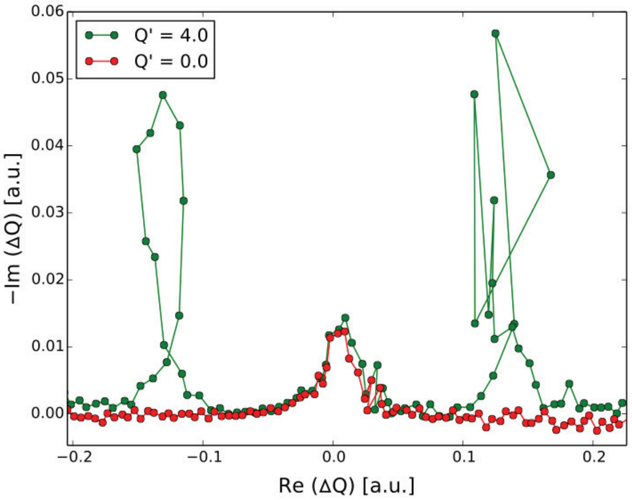

Figure 2.5 – Stability diagram from simulated BTF response in COMBI with chromaticity set to 4 units.

effect is visible in Fig. 2.6 where a cleaner loop appears on the right side with positive real tune shifts. Since the BTF excitation amplitude is fixed, the noise in the BTF signal can be due to a larger damping time required for the beam to damp the oscillations after the BTF excitation at the tune frequency. This effect will produce artifacts in the BTF signal according to the frequency sweep direction. This problem is also affecting the BTF measurements and it will be further discussed in Sec. 5.1.1.

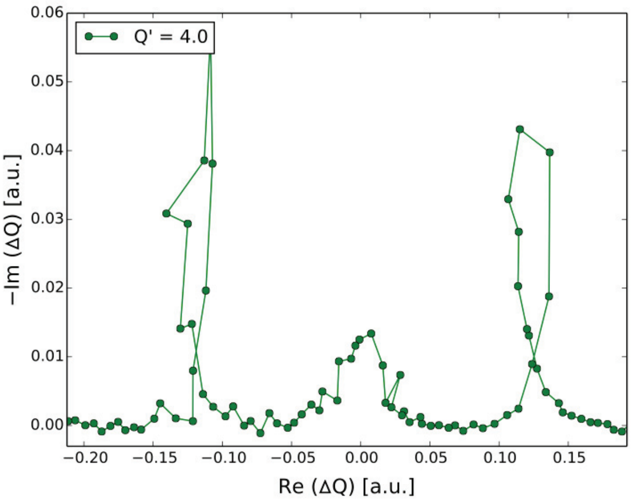

Figure 2.6 – Stability diagram from simulated BTF response in COMBI with chromaticity set to 4 units for a frequency sweep from higher to lower frequency.

2.1.4 Normalization of the BTF amplitude response

The BTF is proportional to the dispersion integral in Eq. 1.38. The constant *C*, is linked to the rescaling factor of the BTF amplitude that gives the correct size of the reconstructed stability diagram in the complex plane, allowing a comparison with the analytical expectations computed by the PySSD code presented in Sec. 2.2. Therefore, it is important to assess the value of the constant *C*, since this work focuses not only on the shape, mainly determined by the particle distribution, but also on the size of the stability diagram that quantifies the

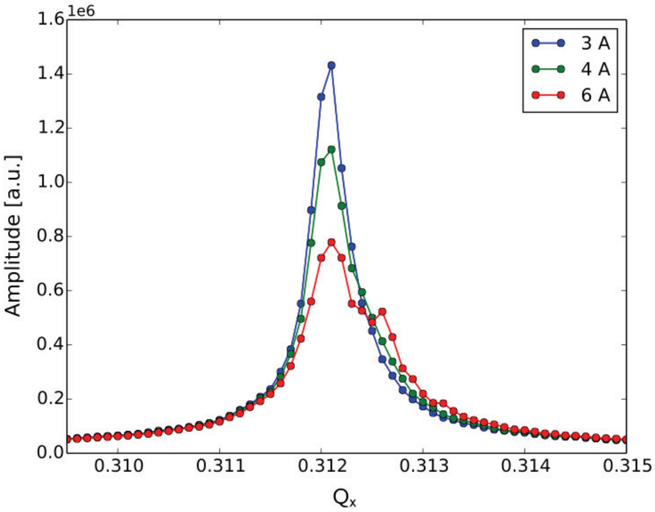

Figure 2.7 – Simulated BTF amplitude response for different octupole currents.

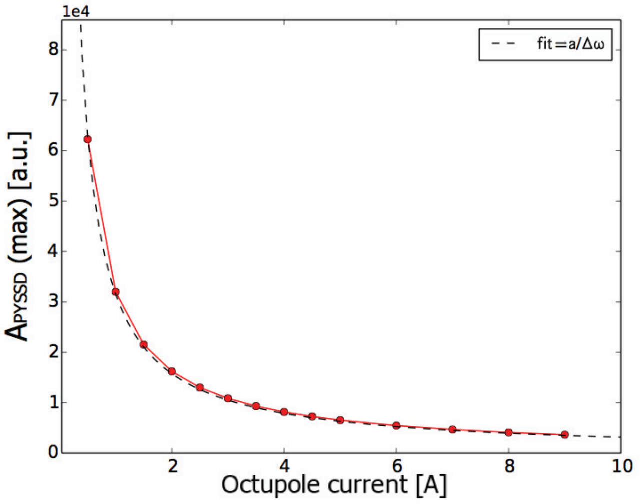

(a) Maximum of the dispersion integral amplitude.

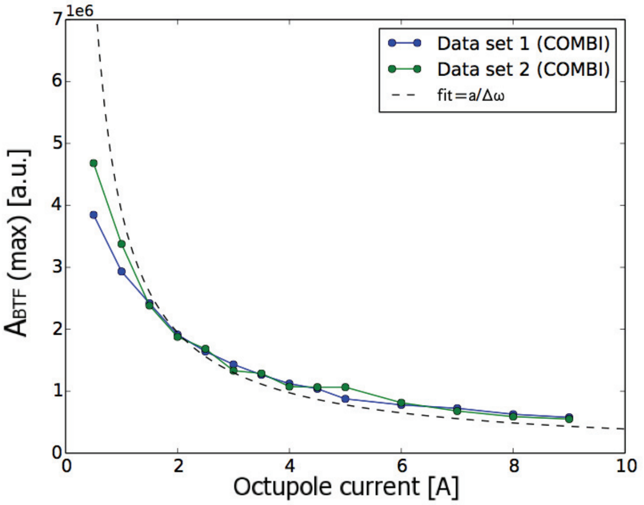

(b) Maximum of the simulated BTF amplitude.

Figure 2.8 – Maximum of the the dispersion integral amplitude and simulated BTF amplitude as a function of the octupole current.

Landau damping of the beams. However, the height of the BTF amplitude depends on the tune spread $\Delta\omega$ given by a certain source of frequency spread. For a linear amplitude detuning given by the octupole magnets, the height of the BTF amplitude reduces while increasing the octupole strength, hence by increasing the tune spread $\Delta\omega$. This is shown in Fig. 2.7 where the simulated BTF amplitude response in COMBI is plotted for different values of the octupole current. From the expectations, the amplitude of the dispersion integral is inversely proportional to the frequency spread $\Delta\omega$ as visible in Fig. 2.8 where the maximum height of the amplitude is plotted as a function of the octupole current. A function $f(\Delta\omega) = \dfrac{a}{\Delta\omega}$ was used for the fit showing a consistent agreement between the two curves. A similar analysis was made for the simulated BTF amplitude as function of the octuple current. The same fitting function was applied to the simulation data. By dividing the two fitting functions, one of the analytical amplitude and the other for the simulated BTF, a constant value was found that allows a direct comparison between the reconstructed stability diagram from the BTF response and the semi-analytical expectations. A similar analysis was carried out also for different chromaticity values (Fig. 2.9a) and different synchrotron tunes Q_s (Fig. 2.9b).

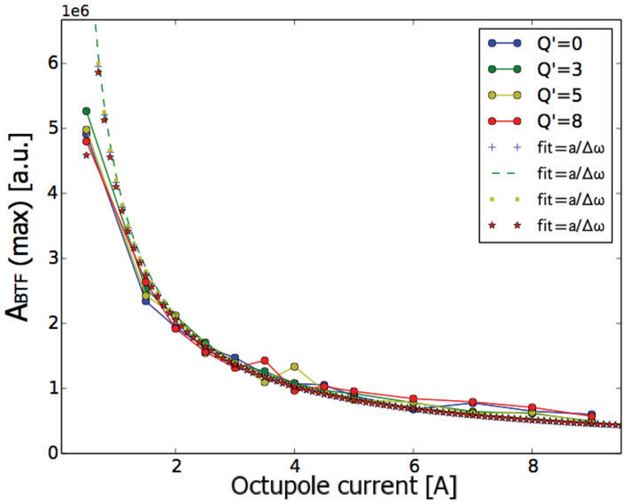

(a) Maximum of the simulated BTF amplitude for different chromaticity values.

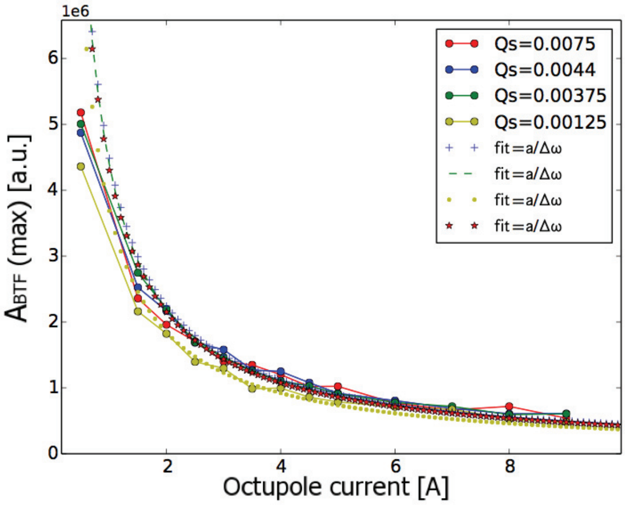

(b) Maximum of the simulated BTF amplitude for different synchrotron tunes Q_s

Figure 2.9 – Maximum of the simulated BTF amplitude as a function of the octupole current, for different chromaticity values and synchrotron tunes Q_s.

Table 2.1 – Amplitude ratio from fitting function between the COMBI BTF amplitude and the semi-analytical dispersion integral as a function of the octupole current for different chromaticity value Q', and synchrotron tunes Q_s

	Value	C
Q'	0	$0.0075 \pm 1.9 \times 10^{-4}$
	3	$0.0073 \pm 8.5 \times 10^{-5}$
	5	$0.0077 \pm 3.2 \times 10^{-4}$
	8	$0.0075 \pm 2.8 \times 10^{-4}$
Q_s	0.00125	$0.0085 \pm 1.8 \times 10^{-4}$
	0.00375	$0.0072 \pm 7.9 \times 10^{-5}$
	0.0044	$0.0070 \pm 1.6 \times 10^{-4}$
	0.0075	$0.0073 \pm 2.5 \times 10^{-4}$

The factor given by the fit will be applied when comparing the COMBI BTF response to the expectations and measurements. The values of the different fits are summarized in Table 2.1.

2.1.5 SixTrack simulations

The SixTrack code is a single particle 6D symplectic tracking code [33] initially written to carry out dynamic aperture studies [41]. The code was then extended and optimized for the long term tracking of a large number of particles to carry out dynamic aperture studies with non linearities, collimation beam cleaning studies, tune optimization and Frequency Map Analysis for high energy rings. The particles are tracked through the lattice by using a map derived from the electromagnetic field [42]. For a typical SixTrack run are required: specification of the magnetic strengths, sequence of the machine elements for the tracked beam (Beam 1 or Beam 2), collision configuration schemes at the IPs, beam parameters (emittance, intensity, energy) and type of tracked particles.

The SixTrack code was used for this work to track a large number of particles up to 10^6 turns in order to investigate the effects of the particle distribution changes on the computed dispersion integral in the presence of excited resonances due for instance to an interplay between Landau octupoles and beam-beam interactions.

2.2 Computation of the stability diagram: the PySSD code

The PySSD code is a Python Solver for the computation of the Stability Diagrams [17, 43, 44]. The code numerically solves the dispersion integral (Eq. 1.37) by using a trapezoidal integration for each relevant values $q \in \mathbb{R}$ where the imaginary part of the integral does not vanish. The dispersion relation in Eq. 1.37 is valid under specific approximations. Its derivation is based on perturbation theory, assuming small oscillation amplitudes and it does not include synchro-betatron coupling and coupling between the transverse planes [45]. In the presence of strong excited resonances the dispersion relation in Eq. 1.37 is not valid anymore, however,

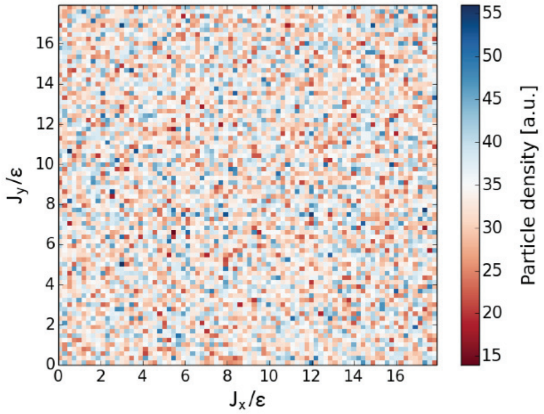

Figure 2.10 – Uniform particle distribution generated at the first turn in IP1.

these effects are always treated as a perturbation of the particle motion in order to investigate the limitations of the model.

In the absence of beam-beam interactions, the detuning with amplitude $Q_x(J_x, J_y)$ is dominated by the machine non linearities such as the ones introduced by octupole magnets giving a linear detuning with amplitude:

$$\begin{aligned} \Delta Q_x &= a \cdot I_x \, \epsilon + b \cdot I_y \, \epsilon \\ \Delta Q_y &= b \cdot I_x \, \epsilon + a \cdot I_y \, \epsilon \end{aligned} \tag{2.4}$$

where $I_{x,y} = J_{x,y}/\epsilon$, considering $\epsilon = \epsilon_x = \epsilon_y$ the rms normalized beam emittance. The detuning coefficients, specific for the LHC octupole magnets, are defined here as [28]:

$$a = 3.28 \cdot \frac{I_{oct}[\text{A}]}{E^2_{beam}[\text{TeV}^2]} \tag{2.5}$$

$$b = -2.32 \cdot \frac{I_{oct}[\text{A}]}{E^2_{beam}[\text{TeV}^2]} \tag{2.6}$$

and depend on the beam energy E_{beam}.

In the presence of beam-beam interactions the amplitude detuning from the lattice non linearities may be comparable or negligible. Therefore, to predict the Landau damping and quantify the stability threshold the amplitude detuning from the beam-beam interactions has to be taken into account. Due to the complexity of the collision scheme, as in the case of the LHC, the amplitude detuning in this case cannot be determined analytically. The PySSD code allows to take the detuning with amplitude as an input, reading an external file produced by the tracking module of MAD-X [11] and it solves the dispersion integral numerically considering Gaussian beam profiles that extends up to 6 σ in units of the rms beam size. However, any modification of the particle distribution may lead to a distortion of the resulting stability diagram provoking a lack of Landau damping.

For this work the PySSD code was extended in order to take into account the effects the particle distribution on the resulting stability diagram.

2.2.1 Effects of particle distribution on the stability diagram

The particle distribution contributes with its derivative $d\psi/dJ_{x,y}$ to the computation of the dispersion integral therefore any modifications of it may have a strong impact on the stability diagram shape causing a possible lack of Landau damping. In order to take into account these effects, the PySSD code was extended to take as an input the particle distribution from the long term SixTrack tracking. A uniform distribution is initially generated at a certain position in the accelerator machine, (usually IP1), according to the geometry of this point, in the given machine configuration, to avoid a mismatched initial distribution. In order to have enough statistics, especially when in the presence of significant beam losses at the end of the tracking, usually 10^6 particles are generated at the first turn and tracked for 10^6 turns. The initial generated distribution is uniform between 0-18 $J_{x,y}$. Before the integration, an exponential weight is applied to the tracked particle distribution. The initial uniform distribution is shown in Fig. 2.10. Figure 2.11 shows on the left the evolution of the particle distribution under the effects of different octupole current and the corresponding stability diagrams on the right. SixTrack simulations were performed considering the LHC injection optics with a normalized beam emittance of $\epsilon = 2.0\,\mu$m in both planes and a beam energy of 450 GeV. The linear detuning with amplitude given by the Landau octupole magnets was derived by using Eq. 2.4 and Eq. 2.6 for different values of the octupole current: 6.5 A, 26 A, and 35 A using the LHC collision tunes ($Q_x = 0.31$ and $Q_y = 0.32$). The black lines represent the stability diagram for a Gaussian distribution in the beams, the blue and red lines are the computed stability diagrams in the horizontal and vertical plane respectively for the tracked particle distribution. To determine the numerical error given by the computation the standard deviation from the expectations for a Gaussian distribution was calculated as a function of the number of particles used for the integration. The numerical error is represented by the red shadow in the plot. For the case of 6.5 A octupole current, the tracked distribution is almost uniform (Fig. 2.11a), corresponding to a Gaussian distribution case when the exponential weight is applied before the integration. From this case it is possible to evaluate the computational error as a function of the total number of particles in the distribution used for the integration. The standard deviation from the stability diagram computed from the tracked distribution in Fig. 2.11a and the expectations for a Gaussian particle distribution as a function of the number of particle is shown in Fig. 2.12. An error of $Im(\Delta Q_{coh}) \pm 1.5 \times 10^{-5}$ is expected for this case when the particles are $\approx 10^6$. Due to the linear detuning, it is possible to rescale linearly this error and apply it to the other octupole strengths. The smallest octupole strength does not produce any important effect on the particle distribution, few particles are lost during the tracking (≈ 2%) and no significant deformation is visible in the stability diagram shape. By increasing the octupole strength the distortions of the distribution become more important, producing particle losses of ≈ 34% and ≈ 57% for 26 A, and 35 A respectively.

For this last case the dynamic aperture, that defines the limit in the phase space beyond which particles are lost [1], corresponds to $\approx 3\ \sigma$ and a more important deformation is visible in the computed stability diagram compared to the case with a Gaussian distribution (black line). A cut in the horizontal plane (blue line) is produced while an increase of the stability area in the vertical plane (red line) is observed. The deformations in both planes exceed the computational error, validating the fact that it is due to the particle distribution modifications.

The corresponding frequency distribution up to $4\ \sigma$ particles is shown in Fig. 2.13 together with the projected histograms in the x and y-directions. The dashed red lines identify the frequencies for the particle in the beam core defined at $\pm 3\ \sigma$ in rms beam size.

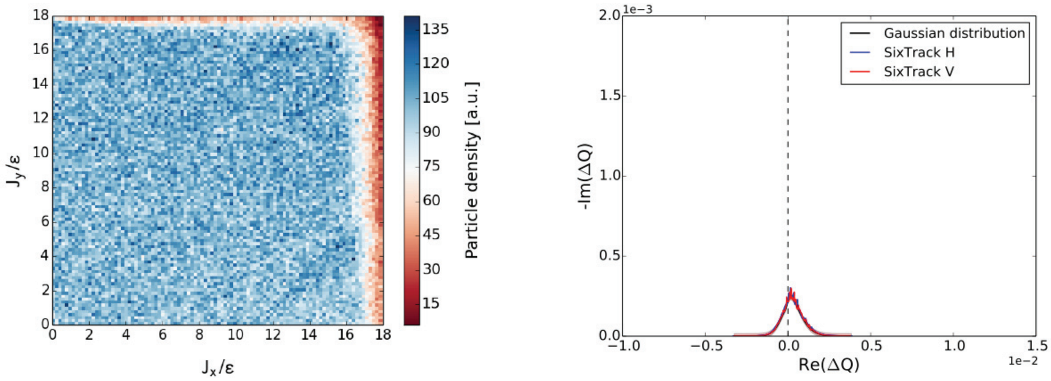

(a) Tracked distribution with an octupole current of 6.5 A in the machine lattice.

(b) Computed stability diagram for an octupole current of 6.5 A.

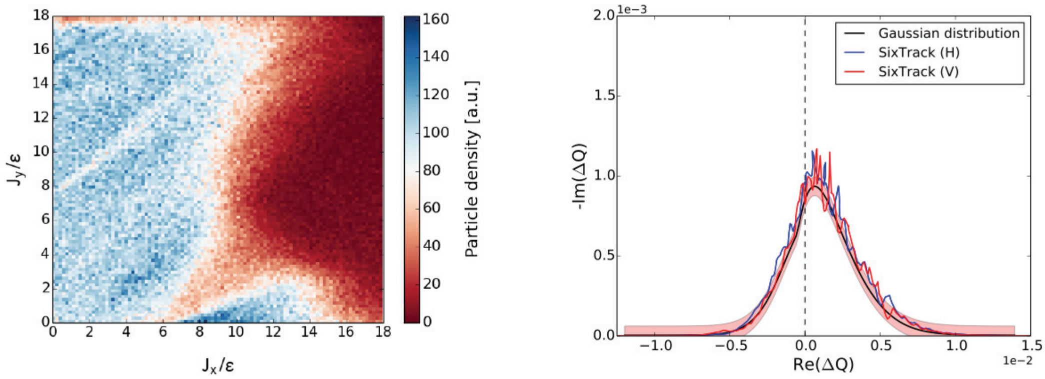

(c) Tracked distribution with an octupole current of 26 A in the machine lattice.

(d) Computed stability diagram for an octupole current of 26 A.

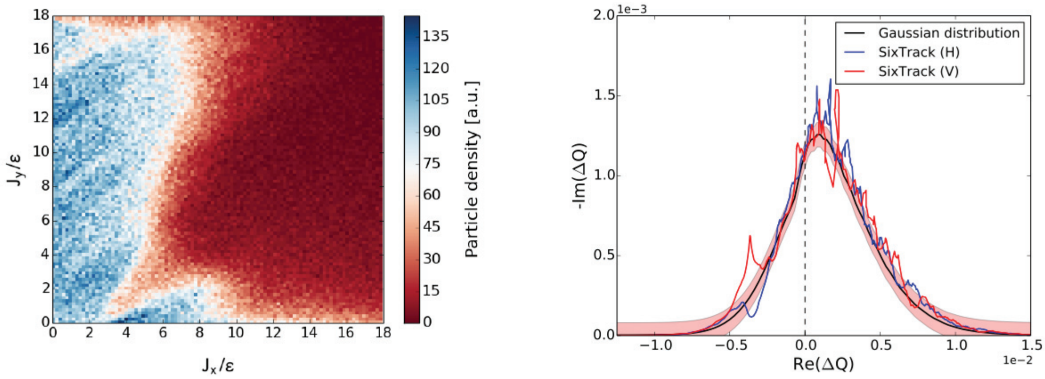

(e) Tracked distribution with an octupole current of 35 A in the machine lattice.

(f) Computed stability diagram for an octupole current of 35 A.

Figure 2.11 – SixTrack particle distribution after 10^6 turns (left) at injection energy in the presence of linear detuning with amplitude for different octupole current together with the corresponding computed stability (right). The black lines represent the stability diagram for a Gaussian distribution, the blue and red lines are the computed stability diagrams in the horizontal and vertical plane respectively for the tracked particle distribution. The red shadow represents the computational error with respect to the stability diagram for a Gaussian distribution and linear detuning with amplitude.

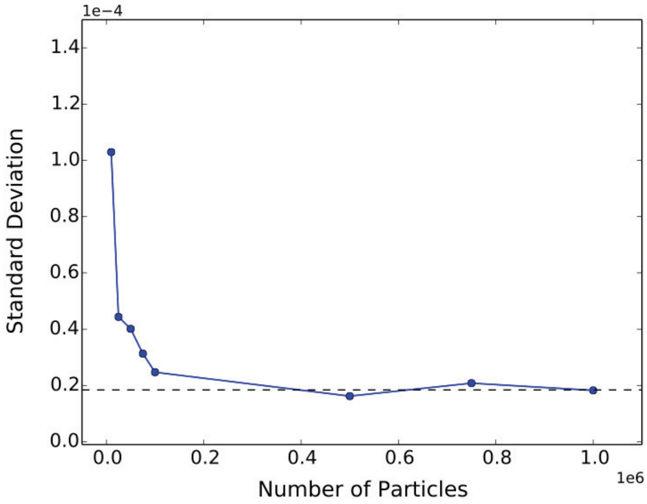

Figure 2.12 – Standard deviation from expectations of the stability diagram computed with the tracked particle distribution (quasi uniform case) as a function of the total number of particles.

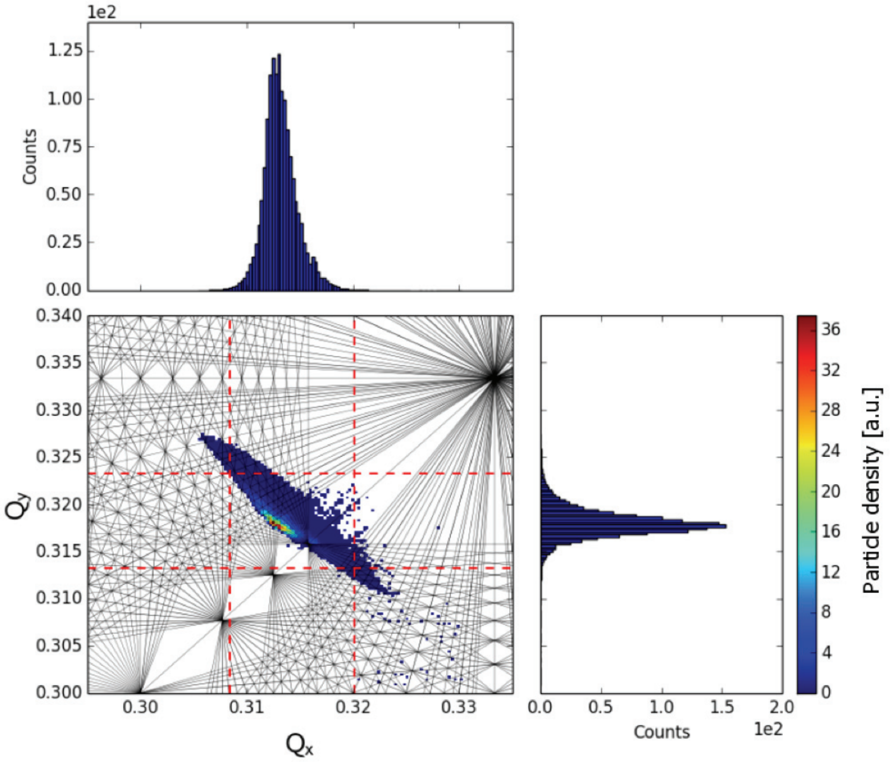

Figure 2.13 – Frequency distribution at injection energy for an octupole current of 35A up to 4 σ particles.

2.3 Summary

The extensions made to the numerical models were presented in this chapter. A new dedicated module was implemented in the COMBI code to simulate the transverse BTF response of the beam. A parametric study of the simulations settings was carried out to not affect the beam quality during the particle tracking keeping a good BTF signal to noise ratio. The reconstruction of the stability diagram is noisy in the opposite part compared to the beginning of the frequency sweep as shown in Fig. 2.6.

The BTF amplitude decreases as $1/\Delta\omega$ and it is proportional to the dispersion integral. A constant parameter was found to allow a direct comparison between the reconstructed stability diagram from the BTF response and the semi-analytical expectations in the presence of different tune spreads ($\Delta\omega$). The coupled synchro-betatron motion produces sidebands in the amplitude response and jumps in the phase response deforming the reconstructed stability diagram.

In the presence of strong machine non linearities, the beam particles may be subject to diffusive mechanisms under the effects of excited resonances. The tracked particle distribution for 10^6 turns by SixTrack simulations was included in the computation of the dispersion integral to evaluate the effects on the computed stability diagram. SixTrack simulations were performed for different octupole currents (6.5 A, 26 A, and 35 A) at the LHC injection energy (450 GeV) at collision tunes ($Q_x \sim 0.31$, $Q_y \sim 0.32$) for a normalized beam emittance of $\epsilon = 2.0\,\mu$m in both planes. Particle losses become more important for an increased octupole strength. At injection energy with a large octupole current (35 A) an effect from the tracked particle distribution on the computed stability diagram was observed, producing a deformation of the stability diagrams on the side of negative real tune shifts (Fig. 2.2.1). Increasing the tune spread in the beams is beneficial for the Landau damping properties of the beams as long as no diffusive mechanism is present. In this case a modification of the particle distribution can deteriorate the expected stability diagram.

3 Transverse beam stability at the Large Hadron Collider

The Large Hadron Collider (LHC) at CERN is a high-energy circular hadron collider designed to provide a maximum center of mass energy of 14 TeV and a peak luminosity of $\mathscr{L} = 10^{34}\,\mathrm{cm}^{-2}\,\mathrm{s}^{-1}$ determined by the machine parameters [29] when operating with protons. As previously introduced, the luminosity is proportional to the squared number of particles per bunch and inversely proportional to the squared transverse beam size at the collision point (round beams), therefore high density beams are required to produce a high luminosity. Traveling through the accelerator beam pipe, the particles induce electromagnetic fields in the accelerator environment (wake fields) that act back on the beam, altering the beam dynamics. The impedance is defined as the frequency Fourier transformation of the wake function and its effects are more important for high density beams. The impedance can affect both the transverse and the longitudinal dynamics compromising the beam stability. Coherent modes driven by the machine impedance are normally Landau damped by the use of octupole magnets [28] which are operationally powered to ensure enough detuning with amplitude to damp coherent modes within the range of the frequency distribution in the beams. Also beam-beam effects contribute to the detuning with amplitude [17]. As introduced in Sec. 1.2.3, the strength of Landau damping is represented by the so called stability diagram obtained by calculation of the dispersion integral for a certain frequency distribution [44]. If the coherent mode is contained within the stability diagram, the mode should not develop because Landau damped and the machine operates in a safe condition. Therefore, the interplay between impedance, Landau octupoles and beam-beam interactions defines the stability limits of the accelerator.

After a short introduction to the accelerator complex and a description of the latest machine operation conditions, the transverse beam stability at the LHC will be discussed in this chapter.

3.1 The LHC injection complex

The LHC is a circular accelerator running with protons and heavy ions, it is located at the Franco-Swiss border near Geneva, with a circumference of 27 km at a depth ranging from 50 to 175 m underground [46]. First, the protons are produced by the hydrogen source at about

50 keV, afterwords they enter in the 35 m long LINear ACcelerator (LINAC 2), where their energy is increased up to 50 MeV . Afterwords, the Proton Synchrotron Booster (PSB) accelerates them to an energy of 1.4 GeV and then they are transferred to the Proton Synchrotron (PS) where they are grouped into trains of bunches with 25 ns spacing reaching an energy of 26 GeV. The SPS (Super Proton Synchrotron), accelerates the protons up to 450 GeV and finally they are injected into the LHC split in two beams. The accelerator chain is illustrated in Fig.3.1.

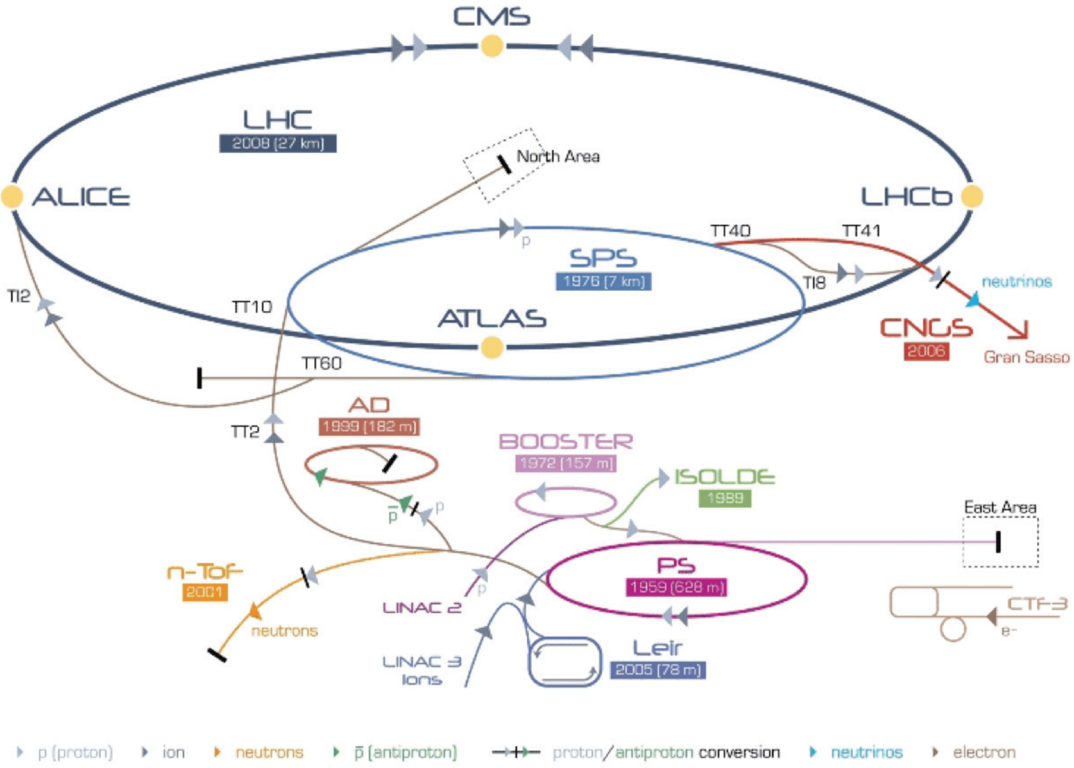
CMS
LHC
2008 (27 km)
North Area
ALICE
LHCb
TT40
TT41
SPS
1976 (7 km)
TI8
neutrinos
TI2
TT10
ATLAS
CNGS
2006
Gran Sasso
TT60
AD
1999 (182 m)
TT2
BOOSTER
1972 (157 m)
ISOLDE
1989
East Area
n-ToF
2001
PS
1959 (628 m)
CTF3
e–
LINAC 2
neutrons
LINAC 3
Ions
LEIR
2005 (78 m)
p (proton)
ion
neutrons
p̄ (antiproton)
proton/antiproton conversion
neutrinos
electron

Figure 3.1 – Accelerator complex at CERN [47].

The beams collide at four Interaction Points (IPs) where four experiments are located: ATLAS, ALICE, CMS, and LHC-b (in IP1, IP2, IP5 and IP8 respectively). The beams share a common beam pipe at the interaction Regions (IRs) around the IPs where the experiments are placed. Out of the IRs the two beams travel in two separated beam pipes.

3.2 LHC machine operations

During normal operations the LHC goes through different phases following a cycle. A typical operational cycle is illustrated in Fig. 3.2 during a physics run of the 2016. The beam energy, the total beam intensity and the β-function values at IP1 and IP5 (β^*) are plotted versus time.

The operational phases are also pointed out in the picture: during the *Setup* the beams are prepared in the injector chain. According to the filling scheme, the beams are injected in the LHC during the *Injection* phase at a constant beam energy of 450 GeV and $\beta^* = 11\,\mathrm{m}$. The beams are then accelerated to the maximum energy during the *Ramp* to a maximum value of $E_b = 6.5\,\mathrm{TeV}$. In order to reduce the cycle time, since the 2016, the β-functions at the IPs have been also reduced during this operational phase, renamed into *Ramp & Squeeze* [48]. From the injection value of $\beta^* = 11\,\mathrm{m}$, it is reduced to a value $\beta^* = 3\,\mathrm{m}$, in the 2016, characterizing the *Flat Top* mode of the accelerator together with the maximum beam energy (6.5 TeV in the 2015 and 2016). The β-functions at the IPs are then further reduced during the *Betatron Squeeze* after which the beams are brought into collision, with the collapse of the separation bumps at the IPs during the *Adjust* process. Then the luminosity in IP1 and IP5 are optimized to reach maximum values and subsequently IP2 and IP8 are also setted up to their target luminosity value by applying a transverse offset [30] between the two colliding beams. Once all the IPs have been optimized satisfying the specific requirements from the experiments, the mode *Stable Beams* is declared and the beams are kept into collision for many hours.
The main machine parameters in the 2015 and 2016 physics runs are summarized in Table 3.1 and compared to the 2012 physics run.

At the LHC the two beams can interact head-on (after the IP optimization) or with a separation d (transverse offset). As already described in Sec. 1.1.5 in order to avoid multiple head-on collisions, the LHC beams collide with a small crossing angle α_c leading to parasitic long range beam-beam interactions. The long range effects become important with the reduction of the β^* at the end of the betatron squeeze (Eq. 1.30). The collision configuration parameters in the 2015 and 2016 physics runs are summarized in Table 3.2 and compared to the 2012 collision

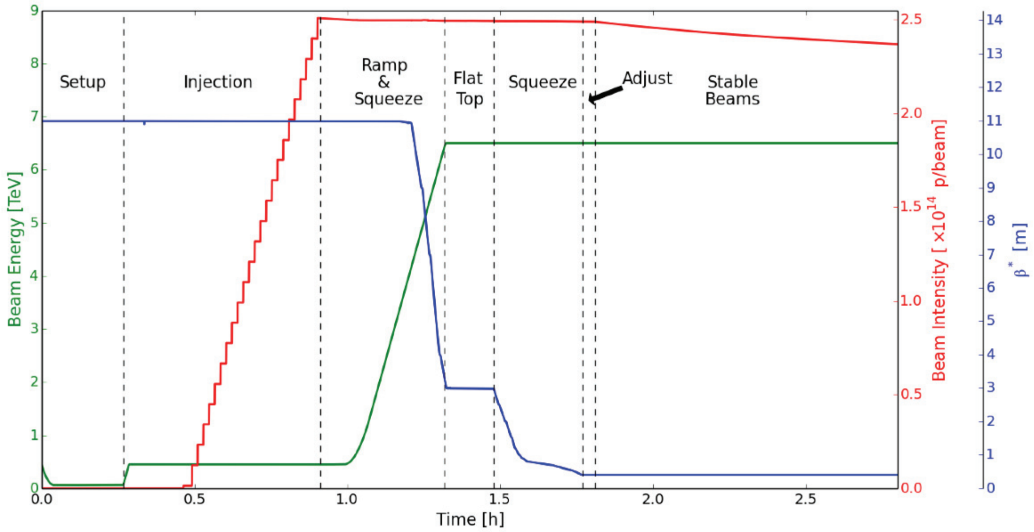

Figure 3.2 – Typical operational cycle in the LHC during a physics run of the 2016.

Table 3.1 – Main LHC machine parameters during the 2012, the 2015 and the 2016 physics runs.

Parameters	2016	2015	2012
Energy per beam [TeV]	6.5	6.5	4.0
Bunch spacing [ns]	25	25	50
β^* in IP1/5 [m]	0.40	0.80	0.60
Normalized Trans. Emittance [µm]	2.0	3.0	2.5
Max. Bunch population [10^{11}]	1.15	1.15	1.6
Max. number of bunches/colliding pairs IP1/5	2220/2208	2244/2232	1380
Max. stored energy [MJ]	265	270	140
ξ_{bb} per IP	0.007	0.005	0.008
Long range separation d_{bb} [σ]	10.4	12.5	9.3
Peak Luminosity in IP1/5 [$10^{34}\,\mathrm{cm}^{-2}\,\mathrm{s}^{-1}$]	1.4	0.5	<0.7

scheme. The listed values are divided by operational phase. The long range beam-beam separation d_{bb} at IP1 and IP5 are plotted in Fig. 3.3 for the 2012, 2015 and 2016 LHC physics runs with nominal beam parameters and optics.

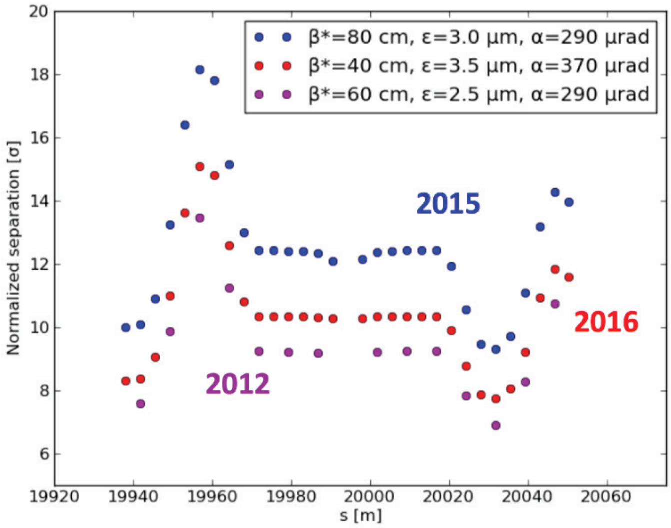

Figure 3.3 – Long range separations at the long range beam-beam encounters in IP1 and IP5 for the 2012, 2015 and 2016 LHC physics runs considering nominal beam parameters.

Injection			
Year	**2012**	**2015**	**2016**
β^* IP1&5 [m]	11	11	11
β^* IP2 [m]	10	10	10
β^* IP8 [m]	10	10	10
Crossing angle IP1&5 [µrad]	340	340	340
Crossing angle IP2 [µrad]	340	340	340
Crossing angle IP8 [µrad]	340	340	340
Separation IP1&5 [mm]	2	2.0	2.0
Separation IP2 [mm]	20	2.0	2.0
Separation IP8 [mm]	3.5	3.5	3.5
Flat top			
Year	**2012**	**2015**	**2016**
β^* IP1&5 [m]	11	11	3
β^* IP2 [m]	10	10	10
β^* IP8 [m]	10	10	6
Crossing angle IP1&5 [µrad]	290	290	370
Crossing angle IP2 [µrad]	290	240	400
Crossing angle IP8 [µrad]	360	460	500
Separation IP1&5 [mm]	0.65	0.55	0.55
Separation IP2 [mm]	0.7	2.0	2.0
Separation IP8 [mm]	0.7	1.0	1.0
End of Squeeze			
Year	**2012**	**2015**	**2016**
β^* IP1&5 [m]	0.6	0.80	0.40
β^* IP2 [m]	3	10	10
β^* IP8 [m]	3	3	3
Crossing angle IP1&5 [µrad]	290	290	370
Crossing angle IP2 [µrad]	290	240	400
Crossing angle IP8 [µrad]	360	500	500
Separation IP1&5 [mm]	0.65	0.55	0.55 / 0
Separation IP2 [mm]	0.65	2.0	2.0
Separation IP8 [mm]	0.7	1.0	1.0
Collisions			
Year	**2012**	**2015**	**2016**
β^* IP1&5 [m]	0.6	0.80	0.40
β^* IP2 [m]	3	10	10
β^* IP8 [m]	3	3	3
Crossing angle IP1&5 [µrad]	290	290	370 / 280[1]
Crossing angle IP2 [µrad]	290	240	400
Crossing angle IP8 [µrad]	360	500	500
Separation IP1&5 [σ]	0	0	0
Separation IP2 [σ]	0	6	6
Separation IP8 [σ]	0	3	3

Table 3.2 – LHC machine configurations for different operational phases.

[1] Crossing angle changed in IP1 and IP5 during the second part of the 2016 physics run with a normalized beam emittance $\epsilon = 2.5\,\mu\mathrm{m\,rad}$

3.3 Landau damping in the LHC

In the LHC the Landau octupoles provide the necessary tune spread to damp the impedance driven coherent instabilities. At flat top they are the main source of Landau damping for the beams. At the end of the betatron squeeze, when the tune spread given by long range beam-beam interactions becomes important, the tune spread provided by the octupole magnets can be modified by the interplay of these two effects [17].

The Landau octupole magnets can operate with positive octupole polarity (LOF > 0) for an octupole current $I_{oct} > 0$ and with negative octupole polarity (LOF < 0) for $I_{oct} < 0$.
The linear detuning coefficients defined in Eq. 2.6 are inversely proportional to the beam energy. In the 2012 the octupoles were more effective because of the reduced beam energy, $E_b = 4\,\text{TeV}$ at flat top, than the 2015 and 2016 physics runs where $E_b = 6.5\,\text{TeV}$ at flat top. Figure 3.4 shows the tune footprints in the presence of positive octupole polarity (Fig. 3.4a) and negative octupole polarity (Fig. 3.4b) for an octupole current of $I_{oct} = \pm 550\,\text{A}$ as during the machine operations in the 2012 and 2015 physics runs. The tune footprint for a beam energy of $E_b = 4\,\text{TeV}$ (pink line) is compared to the one for a beam energy of $E_b = 6.5\,\text{TeV}$ (blue line). As visible, the tune spread provided by the octupole magnets is enlarged when the beam energy is smaller. The change of the octupole polarity reverses the sign of the linear detuning coefficients resulting into a symmetric reflection of the tune footprint.

According to the octupole polarity the tune spread caused by long range beam-beam interactions can reduce or increase the overall tune spread of the beams, hence the Landau damping. As shown in Fig.3.5, including the long range beam-beam interactions in the model, the tune

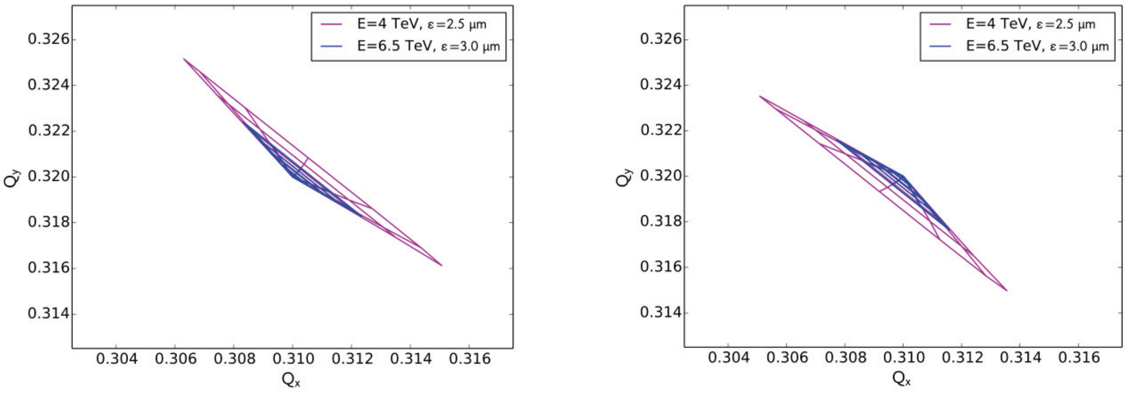

(a) Positive octupole polarity.

(b) Negative octupole polarity.

Figure 3.4 – Tune footprints in the presence of negative and positive octupole polarity ($I_{oct} \pm 550\,\text{A}$) at flat top energy $E_b = 4\,\text{TeV}$ as during the operations of the 2012 physics run (pink line) and at flat top energy of $E_b = 6.5\,\text{TeV}$ as during the operations of the 2016 and 2015 physics runs (blue line).

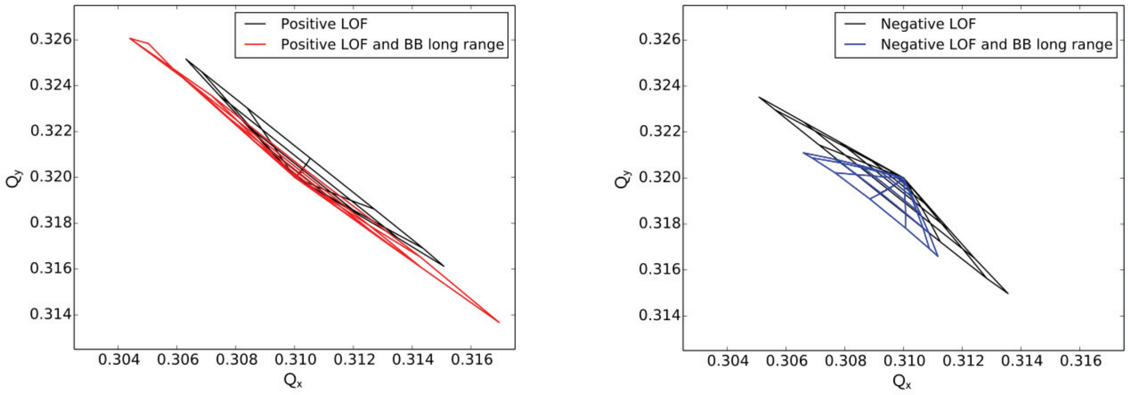

(a) Positive octupole polarity.

(b) Negative octupole polarity.

Figure 3.5 – Tune footprints in the presence of negative and positive octupole polarity ($I_{oct} \pm$ 550 A) at the end of the betatron squeeze for the 2012 machine configurations without long range beam-beam interactions (black lines) and with long range beam-beam interactions (blue line for negative octupole polarity and red line for positive octupole polarity).

footprint is reduced for the negative octupole polarity (blue line in Fig. 3.5b) and increased for the positive octupole polarity (red line in Fig. 3.5a) compared to the case with octupole magnets alone (black lines). These effects will directly result in a different Landau damping of the beams as shown in Fig. 3.6 [17] where the stability diagrams are plotted for negative and positive octupole polarity ($I_{oct} = \pm 500 A$) at the end of the betatron squeeze for the 2012 machine configurations with $\beta^* = 60\,\text{cm}$ for nominal bunches (blue lines) and PACMAN bunches (red line) and compared to the stability diagram at flat top without beam-beam interactions (black lines). The stability diagram is reduced in the presence of negative octupole polarity or it is increased in the presence of positive octupole polarity with a smaller impact for PACMAN bunches due to the missing long range beam-beam interactions.

The 2012 physics run of the LHC has shown losses and emittance blow up related to beam-beam effects [17, 44]. During the first part of the 2012 the Landau octupoles were set with negative octupole polarity, because more beneficial at flat top with single beam, and the chromaticity value was set $Q' \approx 2$ units. With this configuration several beam dumps were occurring during the 2012 Physics fills at the end of the betatron squeeze and several transverse coherent instabilities were observed for Beam 1 and beam 2 in both planes with sharp intensity particle losses (up to 70-60%). During the second part of the 2012 the Landau octupoles were set to positive polarity to increase the expected tune spread in the presence of long range beam-beam interactions at the end of the betatron squeeze (Fig. 3.6), brining a beneficial effect for the Landau damping. Together with an increase of the chromaticity to a value of $Q' \approx 15-20$ units [49], the instabilities were mitigated. The vertical plane of Beam 1 was still affected by coherent instabilities at the end of the betatron squeeze but with smaller beam losses (up to 3%) compared to the first part of the year. In the 2012 physics run the bunches were spaced by 50 ns. Due to the filling scheme used some bunches of the beams were colliding only in IP8. The luminosity was levelled with a transverse offset at IP8 and this process was critical for bunches without head-on collision in the other experiments [17]. During the luminosity levelling several minutes were spent at each separation, hence, if a minimum of stability would occur at that separation, a slow instability would have enough time to develop [17]. In the 2015 physics run, the bunch spacing was reduced from 50 ns to 25 ns and with the new filling scheme used the non colliding bunches were removed.

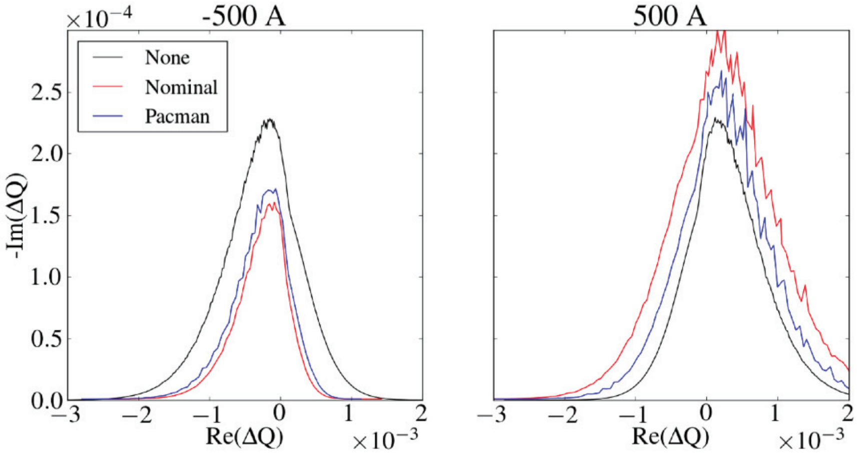

Figure 3.6 – Stability diagram at the end of the betatron squeeze for the LHC 2012 configuration with $\beta^* = 60$ cm for nominal (blue line) and PACMAN bunches (red line) as compared to the stability diagram at flat top (black lines) in the presence of negative and positive octupole polarity (from [17]).

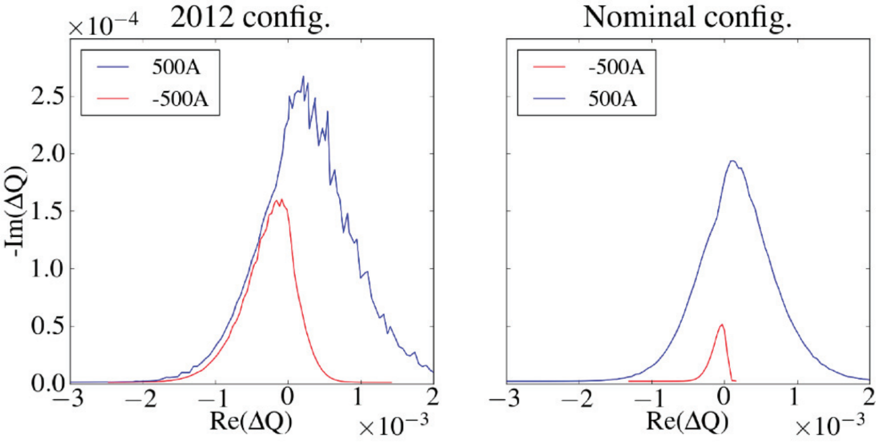

Figure 3.7 – Stability diagram at the end of the betatron squeeze for the LHC 2012 configuration with $\beta^* = 60$ cm (on the left) for negative (red line) and positive octupole polarity (blue line) as compared to the corresponding stability diagram for the 2015 LHC nominal machine configuration (on the right) (from [17]).

To ensure maximum transverse beam stability for the 2015 physics run several setup choices were proposed and operationally implemented in the LHC:

- reduce to negligible the beam-beam effects arising from IP2 and IP8 in order not to contribute to Landau damping and reduce to the possible minimum their effects on tunes and tune spread;
- setup of the octupole magnets with positive polarity due to the larger detuning with amplitude provided by them in the presence of long range beam-beam interactions at the end of the betatron squeeze compared to the negative octupole polarity (Fig. 3.7 [17]).

Considering these modifications and taking into account the new collision schemes, the transverse beam stability is studied for the 2015 and 2016 LHC configurations. The Landau damping of the beams is analysed in the presence of beam-beam interactions during different LHC operational phases.

3.3.1 Transverse stability at the end of the betatron squeeze

The instability thresholds are quantified by the computation of Eq. 1.37 during different LHC operational phases [44]. The stability diagrams for the optics and beam parameters of the 2015 physics run configuration ($\beta^* = 80\,\mathrm{cm}$) are summarized in Fig. 3.8 for different types of bunches at the end of the betatron squeeze and compared to the stability diagrams at flat top with positive (dashed black line) and negative (solid black line) octupole polarities ($I_{oct} = \pm 550\,\mathrm{A}$). The solid red line corresponds to the stability diagram at the end of the betatron squeeze for nominal bunches with positive octupole polarity while the dashed red line corresponds to the stability diagram at the end of the betatron squeeze for PACMAN bunches. The stability diagrams at the end of the betatron squeeze in the presence of negative octupole polarity are represented by the solid and dashed blue line for Nominal and PACMAN bunches respectively. At flat top, where the beams are still kept separated and the long range contribution is negligible, the negative octupole polarity gives a larger stability diagram compared to the positive polarity case. At the end of the betatron squeeze, where the long range beam-beam separation is $d_{bb} \approx 12\,\sigma$, the tune spread contribution given by long range beam-beam interactions adds up to the one provided by the Landau octupoles alone giving as expected a larger stability diagram than the corresponding case with negative octupole polarity. For PACMAN bunches, undergoing to a reduced number of long range interactions, the stability diagram for the case with positive polarity is smaller than the corresponding case with nominal bunches but it is still larger than the negative octupole polarity case at the end of the betatron squeeze.
In order to relate the stability diagram with the impedance driven coherent instabilities, the impedance coherent modes for chromaticity values of 2 units (black and blue crosses for the horizontal and the vertical plane respectively) and for chromaticity of 15 units (black and blue dots for the horizontal and the vertical plane respectively) are plotted in the com-

plex plane (Re(ΔQ_{coh}), Im(ΔQ_{coh})). The impedance modes are characterized by a real part, Re(ΔQ_{coh}) that gives the real coherent tune shift due to the coherent modes and by an imaginary part, Im(ΔQ_{coh}), linked to the time of the coherent instability to develop (rise time). With the present configuration all the impedance driven coherent instabilities should be Landau damped, however, transverse coherent instabilities at the end of the betatron squeeze were still occurring during the 2015 and 2016 LHC physics runs.

3.3.2 Transverse stability during the adjust process

During the collapse of the separation bumps to bring the beams in collision in IP1 and IP5 a minimum of stability is expected as shown in [44] for the LHC 2012 physics run. If the coherent modes are not lying anymore in the stability diagram and the time spent to cross this minimum is larger than the instability rise time of these modes, the beams can become unstable with consequent emittance blow up and beam losses. Therefore it is crucial to study the beam stability during this process and define the limitations to operate in safe conditions.

The evolution of the stability diagram during the adjust process is presented in Fig. 3.9 in the presence of positive octupole polarity as during the operations of the 2015 (Fig. 3.9a)

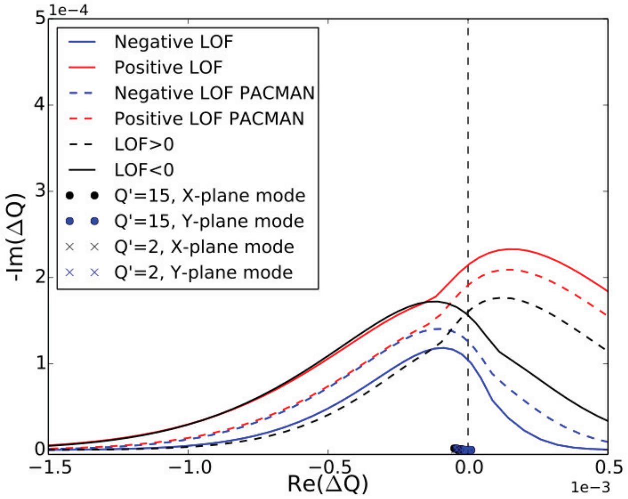

blow up

Figure 3.8 – Summary of the stability diagrams at the end of squeeze for the 2015 physics run and compared to the stability diagrams at flat top for negative (solid black line) and positive (dashed black line) octupole polarity with $I_{oct} = 550\,\mathrm{A}$. The red lines correspond to the stability diagrams with positive octupole polarity at the end of the betatron squeeze for Nominal (solid red line) and PACMAN bunches (dashed red line). The stability diagrams at the end of the betatron squeeze for negative octupole polarity are represented by the blue solid line (nominal bunches) and the dashed blue line (PACMAN bunches). The impedance coherent modes for chromaticity values of 2 units (black and blue crosses for the horizontal and the vertical plane respectively) and for chromaticity of 15 units (black and blue dots for the horizontal and the vertical plane respectively) are plotted.

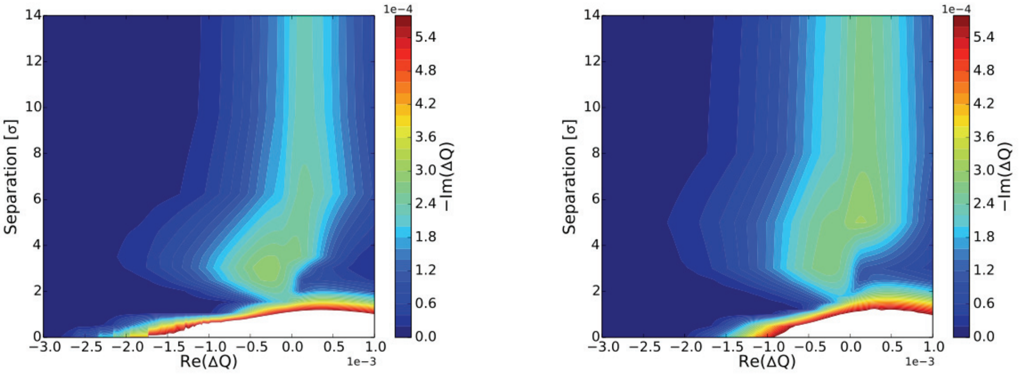

(a) LHC 2015 configuration.

(b) LHC 2016 configuration.

Figure 3.9 – Stability diagram evolution during the LHC collapse of the beam separation bumps in the presence of positive octupole polarity for the LHC 2015 and 2016 physics runs.

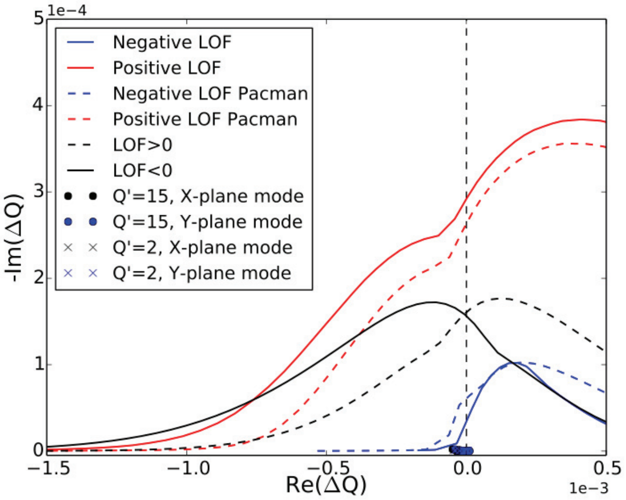

Figure 3.10 – Summary of the stability diagrams during the adjust process for the 2015 physics run. The red and blue solid lines are the stability diagrams for nominal bunches in the presence of positive and negative octupole polarity respectively. The red and blue dashed lines are the stability diagrams for PACMAN bunches in the presence of positive and negative octupole polarity respectively. For completeness the stability diagrams at flat top with negative (solid black line) and positive (dashed black line) are also plotted. The impedance coherent modes for chromaticity values of 2 units (black and blue crosses for the horizontal and the vertical plane respectively) and for chromaticity of 15 units (black and blue dots for the horizontal and the vertical plane respectively) are plotted.

and 2016 physics runs (Fig. 3.9b) with beam parameters and crossing angle presented in Tab. 3.1 and Tab. 3.2. Due to the smaller long range beam-beam separation at the end of the betatron squeeze for the LHC 2016 configuration ($d_{bb} \approx 10\ \sigma$) with respect to the LHC

2015 configuration where $d_{bb} \approx 12\ \sigma$, the stability diagram is larger at the end of the betatron squeeze for the LHC 2016 configuration. As shown in Fig. 3.9 the stability diagrams keep increasing with the reduction of the parallel separation at the IPs. However, a minimum of stability is present for both cases corresponding to a parallel separation of $d = 1 - 2\ \sigma$. Figure 3.10 shows the stability diagrams at the minimum of stability 1- 2 σ separation between the two beams for the 2015 physics run. As visible, the positive octupole polarity, represented in the plot by the red dashed line for PACMAN bunches and red solid line for nominal bunches, is preferred with respect to the negative polarity while crossing this minimum. With this polarity the Landau stability area is always larger than the expected one at flat top with $I_{oct} = 550\,\mathrm{A}$ (black dashed line) and the impedance coherent modes (black and blue dots for a chromaticity of 15 units and black and blue crossing for a chromaticity of 2 units in the horizontal and vertical plane respectively) are Landau damped since they are inside the stability diagram. In the presence of negative octupole at the minimum of stability the impedance coherent modes are at the edge of the stability limit, any errors on the impedance modes or variation on the stability diagram may lead to an instability.

In the 2015 during the so called OP scans, several instabilities were observed when the beams were separated from 0-3 σ. Observations of these instabilities will be discussed in the next section.

3.3.3 Instability during OP scans in the 2015 physics Run

During the 2015 several beam instabilities were observed. They were characterized by an emittance blow up of a factor ≈ 2. The instabilities were occurring during the so called OP scans [50, 51] used to provide emittance measurements. The OP scans consist in applying a parallel separation between the two colliding beams, from 0 σ to 3 σ in one IP at a time, to measure luminosity and the beam size at the IPs based on the S. Van Der Meer method [50, 51]. A reduction of the stability is expected in the presence of a small separation between the two colliding beams, therefore an analysis of the transverse stability during this process is discussed in this paragraph to give possible explanation to the observed instabilities. The instabilities were mostly affecting the horizontal plane of Beam 2 as shown by the bunch by bunch emittances in Fig. 3.11 for the Physics fill number 4363. This fill was taken as a case of study but many other fills were characterized by similar instabilities. The vertical black line defines the start of transverse scans which last few minutes and a transverse blow up is visible in the horizontal plane of Beam 2 correlated with the start of the separation scan. The emittance blow up in Beam 2 was caused by coherent oscillations observed in the same plane. The blow up in the vertical plane of Beam 2 was caused by a previous instability observed before collisions. Figure 3.12 shows the oscillation amplitudes for Beam 1 and Beam 2 in the horizontal plane together with the separations in IP1 and IP5 during the transverse scan. The parallel separation between the beams at the IPs was calculated from the published luminosity by the experiments, ATLAS (IP1) and CMS (IP5), during the scan by using Eq. 1.43. As visible, coherent oscillations are observed for a parallel separation between 1 - 2 σ in IP1 in the horizontal plane. The tune footprints computed with MAD-X up to 10 σ amplitude particles are shown in Fig. 3.13 for different parallel separations between the beams (from 0 σ to 3 σ) in IP1 (Fig. 3.13a) and in IP5 (Fig. 3.13b). The tune footprints were computed with beams in collision in all the IPs according to the crossing and collision schemes presented in Table 3.2 for the 2015 LHC configuration. The beam emittance was set to 3µm and the bunch intensity to 1.0×10^{11} p/bunch for the simulations. The asymmetric collisions due to the parallel separation in one of the two IPs, produces an asymmetric detuning with amplitude in the horizontal and vertical plane. The corresponding computed stability diagram are shown in Fig.3.14, for different horizontal separations in IP1 (Fig. 3.14a and Fig. 3.14b) and for different vertical separations in IP5 (Fig. 3.14c and Fig. 3.14d). As visible an important reduction of the stability diagram is expected in the plane of the parallel separation scan. The

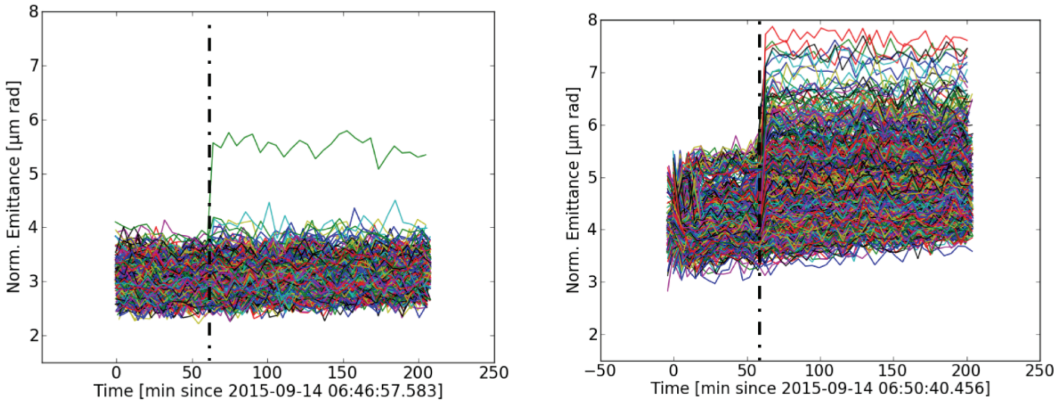

(a) Beam 1 horizontal plane.

(b) Beam 2 horizontal plane.

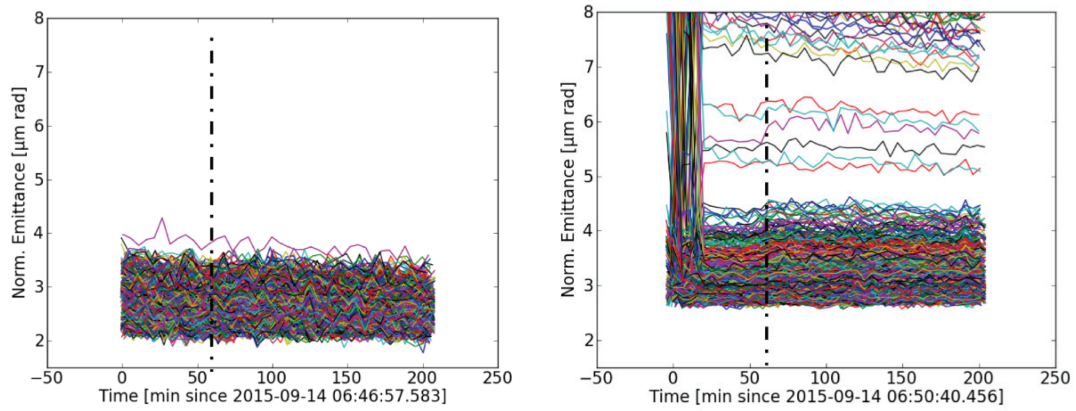

(c) Beam 1 vertical plane.

(d) Beam 2 vertical plane.

Figure 3.11 – Bunch by bunch emittance evolution during the Physics fill 4363. The vertical black line defines the start of transverse scans which last few minutes. Transverse blow up is visible in the horizontal plane of Beam 2 correlated with the start of the separation scan. The blow up in the vertical plane of Beam 2 was caused by a previous instability observed before collisions.

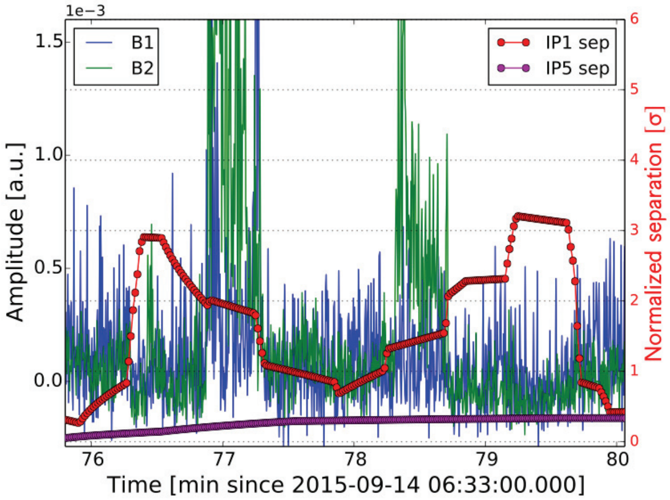

Figure 3.12 – Oscillation amplitude in the horizontal plane for Beam 1 and Beam 2 together with the parallel separations in IP1 and IP5 during the OP scan (fill 4363).

smallest reduction of the stability diagram is expected at a parallel separation of 2 σ and it is comparable to the stability diagram expected at flat top with positive octupole polarity for the case of the vertical separation scan in IP5 and the computed stability diagram in the same plane. The stability diagrams at this minimum in IP1 and in IP5 are compared in Fig. 3.15 for the computation of the dispersion integral in the horizontal and vertical planes. One separated plane of the two IPs does not guarantee a larger stability with respect to the stability diagram at flat top. The impedance coherent modes are plotted for a chromaticity of $Q' = 2$ units (black and blue crosses for the horizontal and vertical plane respectively) and for a chromaticity of $Q' = 15$ (black and blue dots for the horizontal and vertical plane respectively) for a transverse

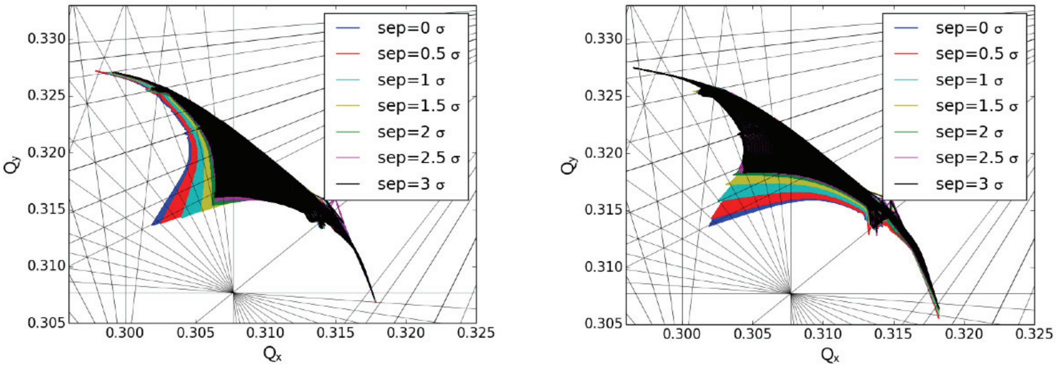

(a) Horizontal parallel separation scan in IP1.

(b) Vertical parallel separation scan in IP5.

Figure 3.13 – Tune footprints (up to 10 σ amplitude particles) for different parallel separation in IP1 (left plot) and in IP5 (right plot).

feedback gain of 100 turns. The vertical plane of IP5 shows a more important reduction at the minimum of the stability diagram ($d = 2\,\sigma$) compared to the corresponding stability diagram in the horizontal plane of IP1. However, the transverse instabilities during the OP scans were always affecting the horizontal plane (of Beam 2). From the model predictions all the coherent modes are contained in the expected stability diagrams and therefore no instabilities should develop during this process.

Therefore, a possible cause of the observed instability can be related to the mode coupling between the beam-beam coherent modes and impedance [52]. Later it was found indeed that a module of the transverse feedback was switched off in the horizontal plane of Beam 2 until the 30th of September 2015 when a full setup and re-configuration of the transverse feedback system took place. After the new setup of the ADT no instabilities were observed

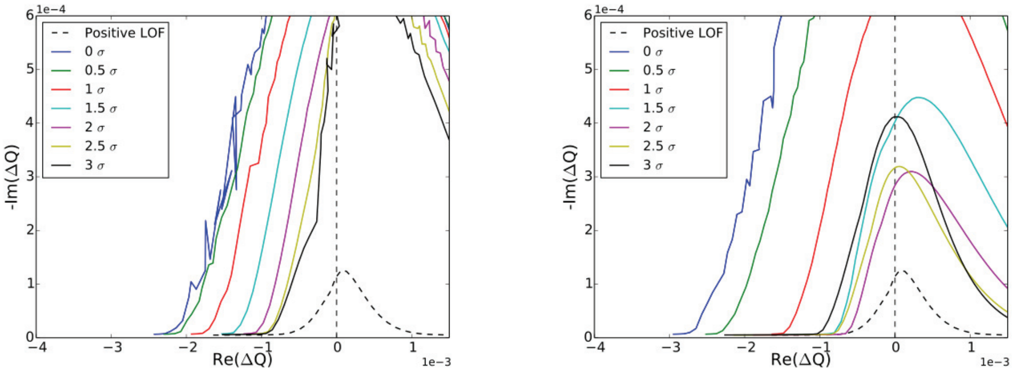

(a) Parallel separation in IP1, stability diagrams computed in the horizontal plane.

(b) Parallel separation in IP1, stability diagrams computed in the vertical plane.

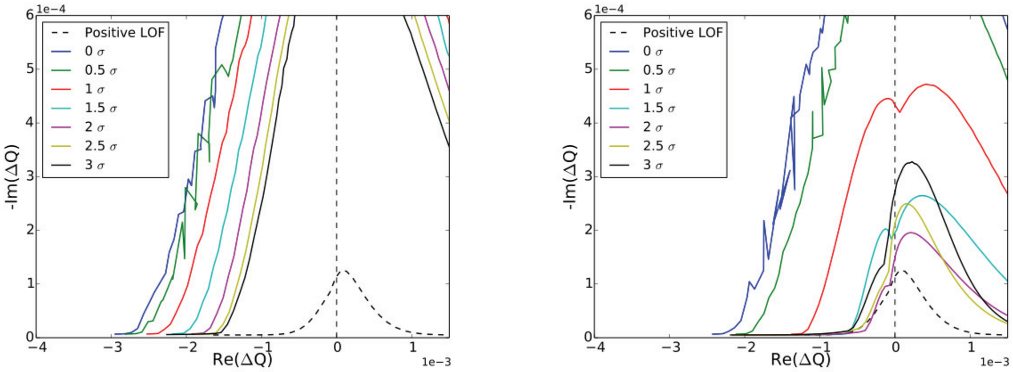

(c) Parallel separation in IP5, stability diagrams computed in the horizontal plane.

(d) Parallel separation in IP5, stability diagrams computed in the vertical plane

Figure 3.14 – Computed stability diagrams for different parallel separations in IP1 (top) and in IP5 (bottom). The stability diagrams are computed both in the horizontal and the vertical plane.

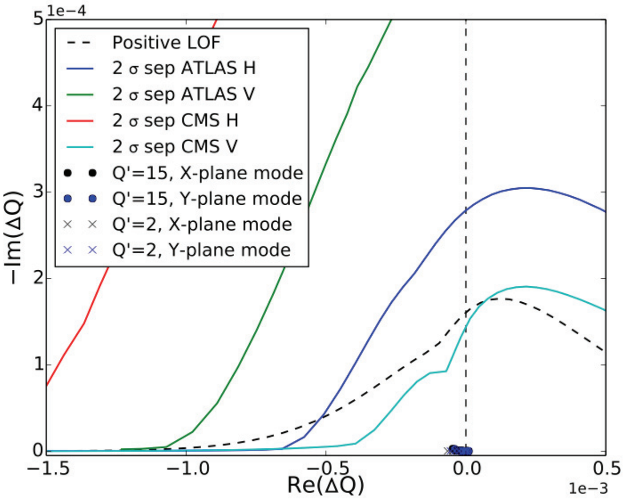

Figure 3.15 – Stability diagrams at the minimum of stability with a parallel separation $d \approx 2\ \sigma$ in the horizontal and vertical plane of IP1 (blue line and green line respectively) and in the horizontal and vertical plane of IP5 (red line and light blue line respectively) compared to the stability diagram expected at flat top with positive octupole polarity ($I_{oct} = 550\text{A}$). The impedance coherent modes are plotted for a chromaticity of $Q' = 2$ units (black and blue crosses for the horizontal and vertical plane respectively) and for a chromaticity of $Q' = 15$ (black and blue dots for the horizontal and vertical plane respectively) for a transverse feedback gain of 100 turns.

during the OP scans, therefore a reduced ADT strength could explain the observed instability in the horizontal plane. In the 2012 it was proved that the ADT can damp the mode coupling between the beam-beam coherent modes and impedance [52]. In addition at 1-2 σ beam parallel separation π-modes become strongest [53]. From these assumptions the observed instability in the horizontal plane of Beam 2 was likely related with the weaker feedback strength in this plane.

3.3.4 Beam stability during luminosity leveling with a transverse beam offset

In the August 2016 the two experiments ATLAS and CMS requested a reduction of the peak luminosity of ≈20% in order to reduced the pile-up effects in their experiment detectors. A way to decrease the luminosity consists to collide the beams with a small transverse separation at the IP as described in Eq. 1.43. Since a reduction of the stability diagram is expected with a small separation between the colliding beams, a preliminary test was carried out in August 2016 for fill 5229 to ensure the beam stability during this process. As discussed in Sec. 3.3.2, when a long time is spent at the minimum of stability (2 σ separation between the beams) transverse beam instabilities may occur at this minimum. The beams were brought into collisions and after the optimization of the IPs a parallel beam separation of $\approx 2.0\,\sigma$ both in IP1 and IP5 was applied to reduce the luminosity of a ≈20%, considering the experimental beam conditions with a normalized beam emittance $\epsilon = 2.5\mu$m. The beams were brought in head-on collision again in steps of $\approx 0.25\,\sigma$, waiting 15-20 min at each step. This process is shown in Fig. 3.16 where the normalized luminosities in IP1 and IP5 are plotted during the parallel separation scan together with the corresponding parallel separation between the beams. No evidence of instability was observed at each separation step. The measured luminosity reduction in IP1 and IP5 as a function of the separation steps is shown in Fig.3.17 and compared to the analytical expectation given by Eq. 1.43. Before the conclusion of the experiment, the beams were again separated by $\approx 2.0\,\sigma$ in IP1 and IP5 and the octupole current was reduced from 470 A to 340 A. Also in this configuration, with a reduced tune spread in the beams, no evidence of instability was observed as expected (Fig. 3.15).

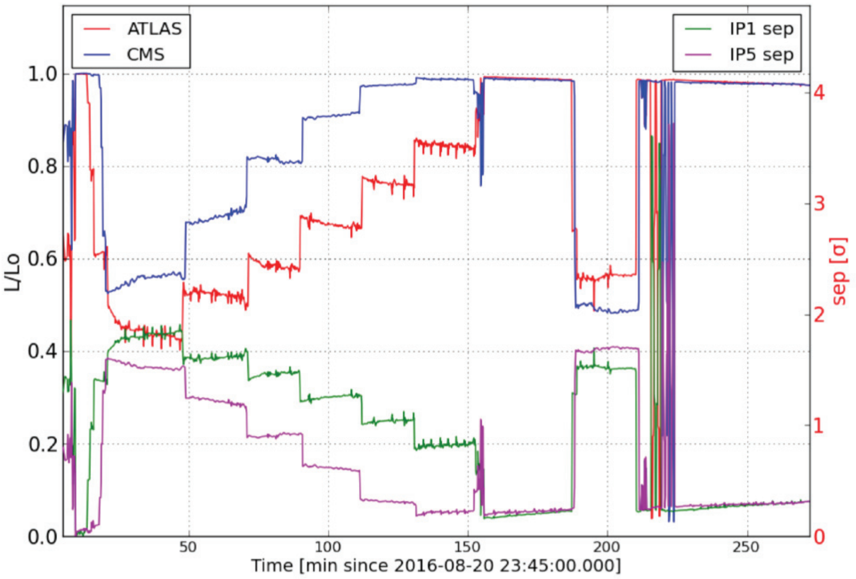

Figure 3.16 – Normalized luminosity in IP1 and IP5 during luminosity leveling with a transverse beam offset in IP1 and IP5 together with the corresponding beam parallel separation in IP1 and IP5.

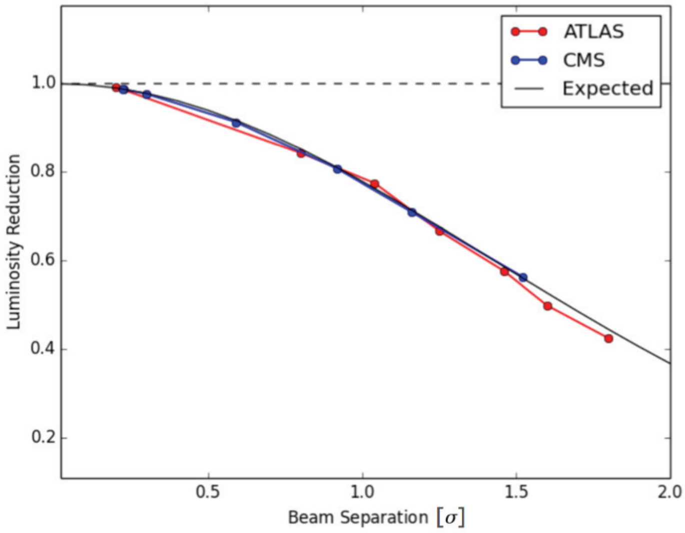

Figure 3.17 – Measured luminosity reduction with a transverse offset in IP1(red dotted line) and IP5 (blue dotted line) compared to model expectations (black solid line).

3.3.5 Set up of the collisions for the 2015 and 2016 physics runs

Due to the several beam instabilities observed at the end of the betatron squeeze in the 2012, a strict control on the tune shifts produced by the beam-beam interactions from IP2 and IP8 was required in order to minimize the beam-beam effects from these two IPs. In the presence of tune shifts of the order of 10^{-3} the dynamic aperture can be reduced up to 2 σ [54] in addition tune shifts below 10^{-3} produce a negligible tune spread [55]. The setup of the crossing angles in IP2 and IP8 was planned to keep the tune spread and tune shifts below 10^{-4} to be in the shadow in IP1 and IP5. The analysis of the settings of the crossing angles is presented in the following sections.

Set-up of the crossing angle for the 2015 physics run

The ALICE and LHCb experiments, in IP2 and IP8 respectively, are both equipped with an inner spectrometer that, according to its polarity, leads to a reduction of the the total crossing angle at the IP, hence a reduction of the long range beam-beam separations with an enhancement of their effects.

The long range beam-beam separations are plotted in Fig. 3.18 for different external crossing angles in IP8 for positive (left) and negative (right) polarities of the LHCb spectrometer at the end of betatron squeeze ($\beta^* = 3\,\text{m}$). As shown in Fig. 3.18a, at the first long range encounter a reduction of the long range beam-beam separations at the different encounters is visible possibly leading to detrimental effects such as unwanted tune shifts. An external crossing angle $\alpha_c = 500\,\mu\text{rad}$ ensures long range beam-beam separations above 26 σ all around the IP8. For the case of negative spectrometer polarity (Fig. 3.18b) the contribution of the inner

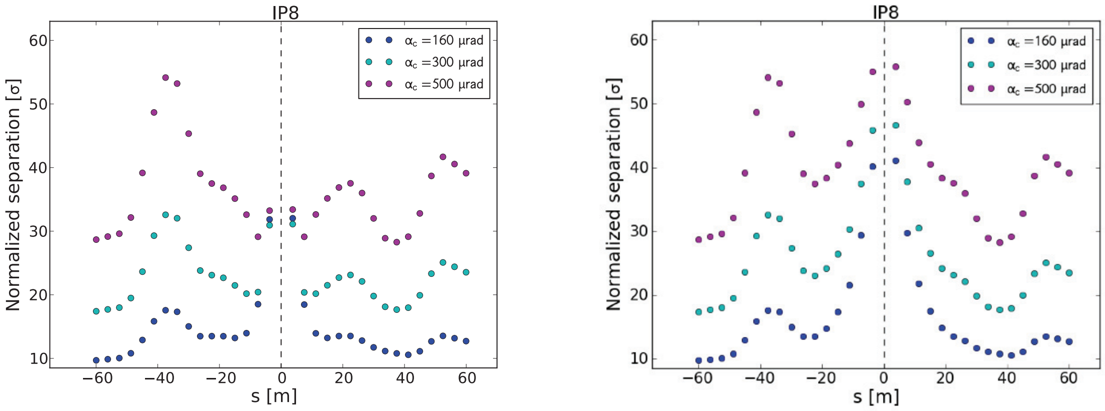

(a) Positive polarity of the LHCb spectrometer.

(b) Negative polarity of the LHCb spectrometer.

Figure 3.18 – Long range separations in IP8 at the end of the betatron squeeze for positive (left) and negative (right) polarities of the LHCb spectrometer.

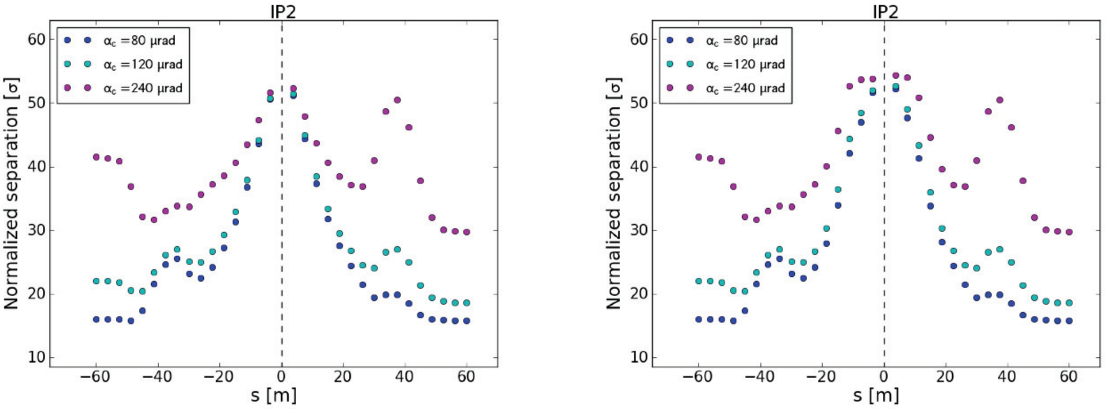

(a) ALICE spectrometer switched off.

(b) ALICE spectrometer switched on.

Figure 3.19 – Long range separations in IP2 at the end of the betatron squeeze for the ALICE spectrometer switched off (left) and for the ALICE spectrometer switched on (right).

spectrometer and the external crossing angle add-up to each other giving larger beam-beam separations, compared to the case with positive spectrometer polarity, for the long range encounters closer to the IP where the inner spectrometer is located.

In the 2015 physics run the ALICE spectrometer was switched off or switched on during operations with a fixed polarity. Fig. 3.19 shows the long range beam-beam separations for different external crossing angles in IP2, for the case of the ALICE spectrometer switched off (Fig. 3.19a) and for the case of the ALICE spectrometer switched on (Fig. 3.19b). The two cases produce very similar long range beam-beam separations all around the IP. A crossing angle $\alpha_c = 240\,\mu\text{rad}$ in IP2 ensures long range beam-beam separations above 30 σ for both the cases.

For tune shifts of $\Delta Q_{x,y} \approx 2 \times 10^{-3}$ the dynamic aperture may easily drop by a value of 2 σ, therefore it is important to keep the tune shifts neglegible.

The horizontal (left) and vertical (right) tune shifts as a function of the crossing angle in IP8 at the end of the betatron squeeze are shown in Fig. 3.20, for negative LHCb spectrometer polarity (black and red lines for the horizontal and the vertical plane respectively) and for positive LHCb spectrometer polarity (dashed black and dashed red lines for the horizontal plane and vertical plane respectively). Positive tune shifts are produced in the horizontal plane and negative tune shifts in the vertical plane while reducing the crossing angle in IP8. As shown, a crossing angle $\alpha_c = 500\,\mu\text{rad}$ (green line) keeps the long range tune shifts below 10^{-4} for both the spectrometer polarities. Figure 3.21 shows the horizontal (left) and vertical (right) tune shifts as a function of the crossing angle in IP2 at the end of the betatron squeeze with the ALICE spectrometer switched on (black and red lines for the horizontal and the vertical plane respectively) and for the ALICE spectrometer switched off (dashed black and dashed red lines for the horizontal plane and vertical plane respectively). Positive tune shifts are produced in the vertical plane and negative tune shift in the horizontal plane while reducing the crossing angle in IP2. For both cases a crossing angle $\alpha_c = 240\,\mu\text{rad}$ keeps the long range tune shifts below 10^{-4} (green line). The tune footprints with the new crossing angle scheme are shown in Fig.3.22 for the 2015 configuration with beams in collision in IP1 and IP5 with $\beta^* = 0.80\,\text{m}$ and crossing angle $\alpha_c = 290\,\mu\text{rad}$ (light blue line). The long range beam-beam contributions at the end of the betatron squeeze is added in IP2 with a crossing angle $\alpha_c = 240\,\mu\text{rad}$ (blue line) and in IP8 with a crossing angle $\alpha_c = 500\,\mu\text{rad}$ (red line). The tune shifts are very small (below 10^{-4}) and the contribution of IP2 and IP8 stay in the shadow of the beam-beam effects produced in IP1 and IP5.

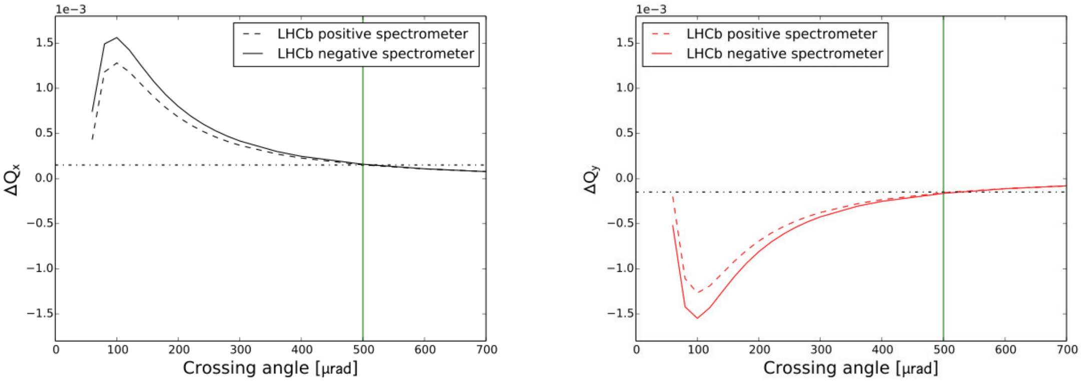

(a) Horizontal tune shifts.

(b) Vertical tune shifts.

Figure 3.20 – Horizontal and vertical tune shifts induced by long range beam-beam interactions at the end of the betatron squeeze as a function of the crossing angle in IP8. The dashed line represents a tune variation of 10^{-4} and the green line corresponds the crossing angle implemented in this IP during the 2015 physics run.

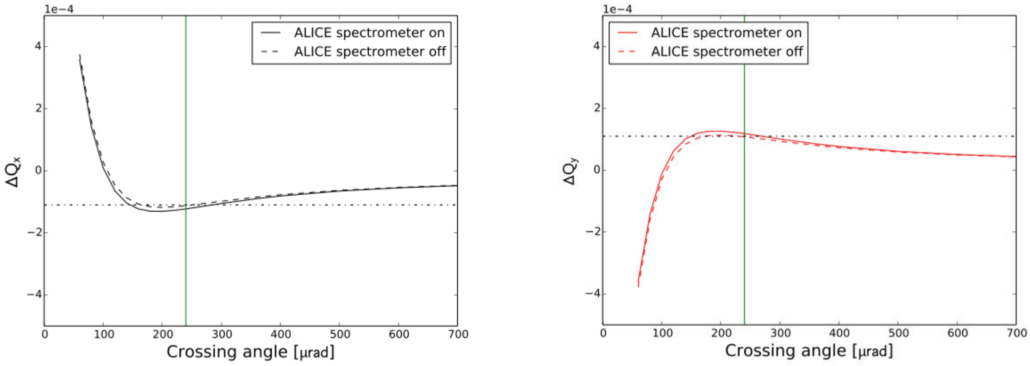

(a) Horizontal tune shifts.

(b) Vertical tune shifts.

Figure 3.21 – Horizontal and vertical tune shifts induced by long range beam-beam interactions at the end of the betatron squeeze as a function of the crossing angle in IP2. The dashed line represents a tune variation of 10^{-4} and the green line corresponds the crossing angle implemented in this IP during the 2015 physics run.

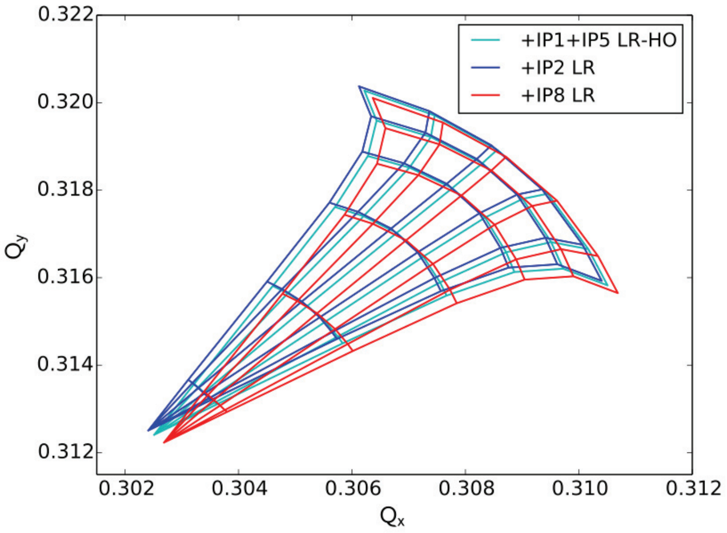

Figure 3.22 – Tune footprints for the 2015 configuration with beams in collision in IP1 and IP5 with $\beta^* = 0.80\,\mathrm{m}$ and crossing angle $\alpha_c = 290\,\mu\mathrm{rad}$ (light blue line). The long range beam-beam contributions at the end of the betatron squeeze configuration is added in IP2 with a crossing angle $\alpha_c = 240\,\mu\mathrm{rad}$ (blue line) and in IP8 with a crossing angle $\alpha_c = 500\,\mu\mathrm{rad}$ (red line).

Set-up of the crossing angle for the 2016 physics run

The 2016 physics run was characterized by a reduction of the β^* value in IP1 and IP5 from 80 cm to 40 cm. Therefore, the crossing angles in these two IPs were enlarged from a total crossing angle $\alpha_c = 290\,\mu\mathrm{rad}$ to $\alpha_c = 370\,\mu\mathrm{rad}$ in order to keep the long range beam-beam

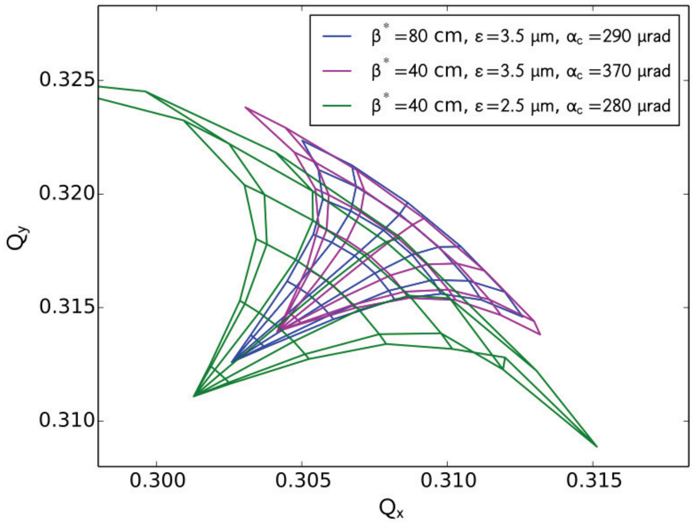

Figure 3.23 – Footprint in collision for the 2015 Run and 2016 Run with nominal beam parameters (normalized emittance $\epsilon = 3.75 \mu\text{m}$ and bunch intensity $I = 1.15\,\text{p/bunch}$.

separation at the first long range encounter above 10 σ for a normalized beam emittance $\epsilon = 3.5 \mu\text{m}$. During the second part of the 2016 physics run the nominal beam emittance was reduced to a value of $\epsilon = 2.5 \mu\text{m}$ to increase the luminosity reach. Therefore, the crossing angles in IP1 and IP5 were reduced from $\alpha_c = 370 \mu\text{rad}$ to $\alpha_c = 280 \mu\text{rad}$ corresponding to a long range beam-beam separation at the first long range encounter of $d_{sep} = 9.3\,\sigma$. The angle correction was applied at the beginning of the adjust process.

A comparison between the tune footprints with beams in collision for the 2015 Physics (blue line) and the first part of the 2016 physics run (pink line) is presented in Fig. 3.23 considering the nominal beam parameters (normalized beam emittance $\epsilon = 3.5 \mu\text{m}$ and a bunch intensity $I = 1.15\,\text{p/bunch}$). As visible, the 2016 case is characterized by a smaller head-on tune shift with respect to the 2015 case due to the larger crossing angle at the IPs. However, the long range beam-beam interactions are stronger due to the smaller separations with respect to the 2015 case and their impact on the tune spread is larger. The tune footprint with the reduced crossing angle (green line) for a normalized beam emittance $\epsilon = 2.5 \mu\text{m}$ is also plotted. Due to the smaller emittance and the smaller crossing angle the head-on interaction is stronger compared to the previous cases. Due to the smaller long range separation at the first encounter ($d_{sep} = 9.3\,\sigma$) the long range beam-beam interactions are stronger than the other cases. The evolution of the stability diagram during the collapse of the beam separation bumps is shown in Fig. 3.24 for the nominal machine configuration with a crossing angle $\alpha_c = 370 \mu\text{rad}$ (Fig. 3.24a) and for a reduced crossing angle $\alpha_c = 280 \mu\text{rad}$ (Fig. 3.24b). The beam intensity was set to $I = 1.2 \times 10^{11}$ p/bunch for the simualations. For the case with reduced crossing angle and beam emittance a larger stability is expected throughout the adjust process because of the stronger head-on interactions in IP1 and IP5.

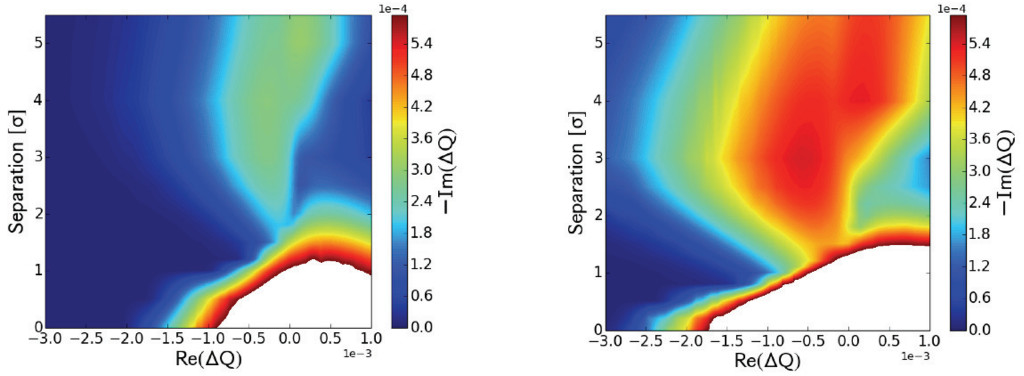

(a) LHC 2016 configuration for a normalized beam emittance $\epsilon = 3.5\mu m$ and a nominal crossing angle of $\alpha_c = 370\mu rad$.

(b) LHC 2016 configuration for a normalized beam emittance $\epsilon = 2.5\mu m$ and a reduced crossing angle of $\alpha_c = 280\mu rad$

Figure 3.24 – Stability diagram evolution during the adjust process in the presence of positive octupole polarity for the 2016 physics run configuration, for the first part of the year with a normalized beam emittance $\epsilon = 3.5\mu m$ and a nominal crossing angle of $\alpha_c = 370\mu rad$ and for the second part of the year with a normalized beam emittance $\epsilon = 2.5\mu m$ and a reduced crossing angle of $\alpha_c = 280\mu rad$.

A study of the impact of the long range effects was carried out for the setup of the crossing angles in IP2 and IP8. For the 2016 physics run, a swap of the ALICE spectrometer polarity was requested, therefore the analysis of the tune shifts and spread produced by long range beam-beam interactions was extended considering the new requirement. Fig. 3.25 shows the long range beam-beam separations for different external crossing angles in IP2 with the swapped polarity of the ALICE spectrometer. A reduction from 30 σ to 15 σ long range beam-beam separation is observed for a reduced crossing angle $\alpha_c = 80\mu rad$ in IP2. The tune shifts induced by long range beam-beam interactions as a function of the crossing angle in IP2 with the beams in collision in all the IPs are shown in Fig. 3.26, in the horizontal plane (left) and in the vertical plane (right). The black line corresponds to the ALICE spectrometer turned on and the black dashed line to the ALICE spectrometer with opposite polarity. The blue line corresponds to the case with the ALICE spectrometer turned off. Figure 3.27 shows the tune spread as a function of the crossing angle in IP2 with all the IPs in collisions. The tune spread was considered as the maximum tune shift up to the 6 σ amplitude particle. In order to keep the tune shifts and the tune spread from IP2 below 10^{-4} (green shadow in the plots) for all the configurations of the ALICE spectrometer, an increase of the total crossing angle in IP2 from $\alpha_c = 240\mu rad$ to $\alpha_c = 400\mu rad$ was required (green line).

Despite the new settings, transverse instabilities were still observed at the end of the betatron squeeze in the 2015 and 2016 physics runs, excluding the possibility that the observed instabilities were provoked by the beam-beam effects from IP2 and IP8.

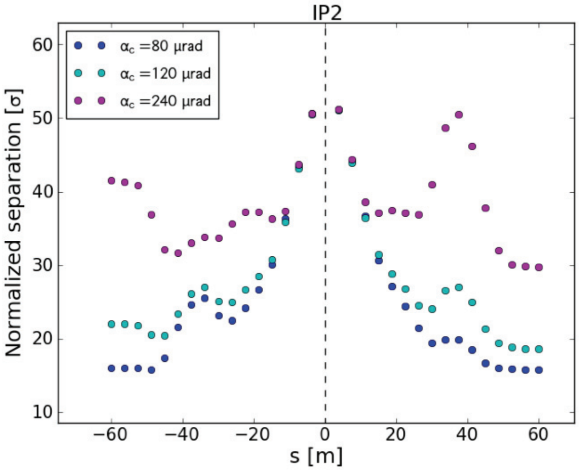

Figure 3.25 – Long range separations in IR2 at the end of the betatron squeeze for the ALICE spectrometer with swapped polarity.

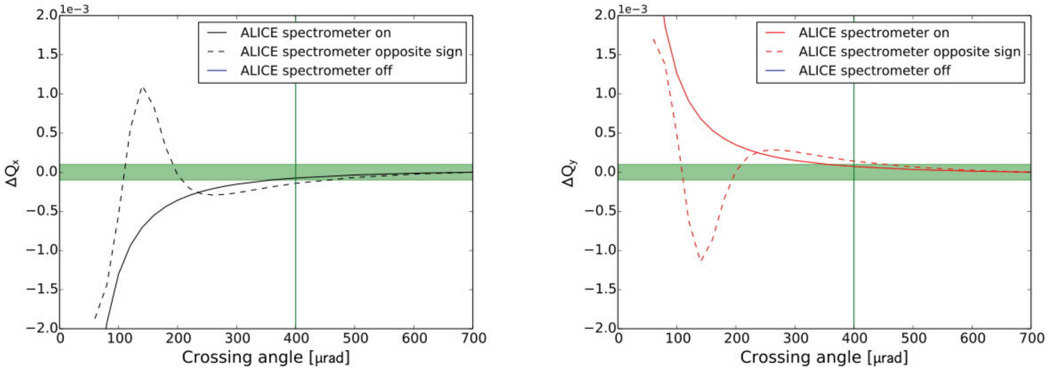

(a) Horizontal tune shifts.

(b) Vertical tune shifts.

Figure 3.26 – Long range beam-beam tune shifts as a function of the crossing angle in IP2 for the 2016 LHC configuration with beams in collision in all the IPs. The green shadow corresponds to a tune variation of $\pm 10^{-4}$ and the green line corresponds the new crossing angle implemented in this IP.

3.4 Summary

During the 2012 physics run several instabilities were affecting the beams. They were observed mostly in the vertical plane of Beam 1, at the end of the betatron squeeze, despite the stabilizing effects from the favorable interplay of positive octupole polarity and long range beam-beam interactions and the increased chromaticity value in the beams. Therefore, the stability for the 2015 and 2016 LHC configurations was studied and maximized during the different operational phases. A detailed analysis for the setup of the crossing angles for the 2015 and 2016 LHC physics runs was presented and operationally implemented to keep the tune shift and the tune

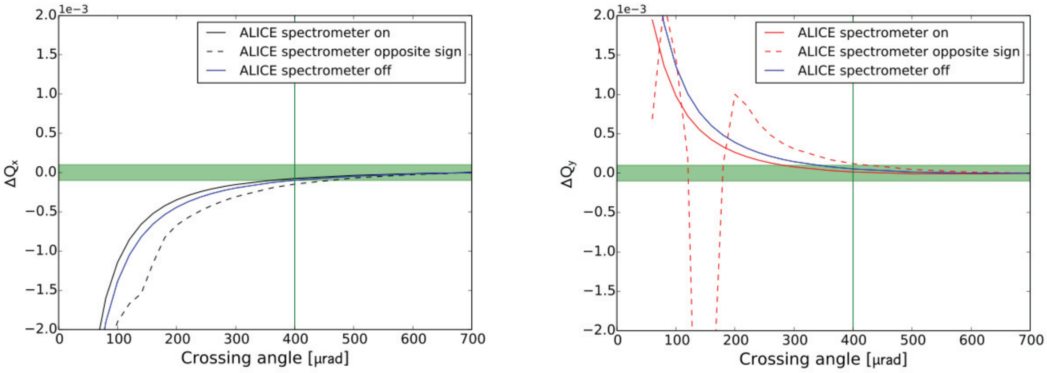

(a) Horizontal tune spread.

(b) Vertical tune spread.

Figure 3.27 – Long range beam-beam tune spread as a function of the crossing angle in IP2 for the 2016 LHC configuration with beams in collision in all the IPs. The green shadow corresponds to a tune spread variation of $\pm 10^{-4}$ and the green line corresponds the new crossing angle implemented in this IP.

spread caused by the beam-beam interactions in IP2 and IP8 below 10^{-4}. The use of positive octupole polarity ensures maximum stability at the end of the betatron squeeze where all the impedance coherent instabilities should be Landau damped according to the models (Fig. 3.8), even at the minimum of stability during the adjust beam process (Fig. 3.10). However, several instabilities were still observed both in the 2015 and in the 2016 physics runs at the end of the betatron squeeze, mostly affecting the vertical plane. This led to experimental studies of Landau damping by means of BTF measurements in the LHC in order to understand the limitations of the models. The first BTF measurements in the LHC are presented in Chapter 5.

4 Transverse beam stability studies for the High-Luminosity LHC upgrade

The LHC has been successfully operating since the 2010 pushing the exploration of new physics frontiers beyond the Standard Model. In order to extend its discovery potential, the LHC will be upgraded in the 2020s to increase the design (leveled) luminosity by a factor 5 and the integrated luminosity by a factor 10. For this purpose the High Luminosity LHC (HL-LHC) project was approved in the 2013 [56].
The HL-LHC project [56, 57] aims to reach a leveled luminosity of $5 \times 10^{34}\,\mathrm{cm}^{-2}\,\mathrm{s}^{-1}$ and an integrated luminosity of 250 fb per year. In order to achieve these targets the beam parameters, as well as the hardware configurations, will be determined taking into account the performance limitations related to several aspects: injector chain, beam-beam interactions, beam impedance, cryogenics, collimation system and machine protection. The HL-LHC Baseline operational parameters are listed in Table 4.1 and compared to the LHC design choices.

4.1 Collision configurations and optics

The luminosity upgrade of the LHC requires the development of challenging technologies and new equipments such as the new inner triplet quadrupoles in the low-β insertions and RF crab cavities devices. The HL-LHC project also implies new techniques for the luminosity leveling and involves a new optics scheme to achieve extremely small values of the β^* at the IPs (until 15-10 cm) [57]. Some of these new methods and technologies will be shortly described in the next paragraphs of this section.

4.1.1 Luminosity leveling

To limit the peak pile-up in the experimental detectors and avoid an overload of energy deposition due to collision debris on the interaction region magnets, the instantaneous luminosity has to be limited. As a consequence of this limitation the HL-LHC operations rely on luminosity leveling, i.e. operations with a constant luminosity value of $5 \times 10^{34}\,\mathrm{cm}^{-2}\,\mathrm{s}^{-1}$, kept as long as possible during the length of the Physics fills in order to increase the integrated luminosity.

Table 4.1 – Beam parameters for the HL-LHC compared to the LHC nominal parameters.

Parameters	HL-LHC	LHC (Nominal)
Energy [TeV]	7	7
Bunch spacing [ns]	25	25
Number of bunches	2808	2808
Bunch intensity [10^{11}]	2.2	1.15
Total beam current [A]	1.11	0.58
Bunch length [cm]	7.50	7.50
Long. Emittance [eVs]	2.50	2.50
Energy spread [10^{-4}]	1.20	1.20
Normalized Trans. Emittance [μm]	2.5	3.75
β^* [m]	0.15	0.55
Crossing angle [μrad]	590	300
Peak Luminosity [$\mathrm{cm^{-2}\,s^{-1}}$]	7.4	1.0
Leveled Luminosity [$\mathrm{cm^{-2}\,s^{-1}}$]	5.0	NA

Figure 4.1 shows an example of the HL-LHC luminosity evolution during a Physics fill. The red line corresponds to a run without leveling, the blue line represents a run with luminosity leveling while the black line is the LHC designed luminosity. The leveled luminosity suppresses the decay for several hours with a smaller luminosity peak. However, since the maximum achievable peak luminosity is limited, the integrated luminosity needs to be maximized by increasing the time length and the beam current. As shown in Table 4.1, a doubled beam current compared to the LHC nominal value, together with a high brightness of the beams, represents a challenge for collective effect mitigations [58].

By recalling the luminosity expression in Eq.1.40, it can be seen that the luminosity leveling can be achieved in several ways: controlled reduction of the β^*, reduction of the transverse distance between the colliding beams, crossing angle variation and controlled variation of the bunch length. All these options were analyzed and discussed and they are still debated, however changing the β^* remains the most likely approach [59–61] for luminosity leveling.

The HL-LHC Baseline and Ultimate scenarios foresee collisions in IP1 and IP5 at $\beta^* = 70\,\mathrm{cm}$ and $\beta^* = 40\,\mathrm{cm}$ respectively [62]. Both of them rely on the luminosity leveling by reducing the β^* up to 15 cm, with a leveled luminosity of $5 \times 10^{34}\,\mathrm{cm^{-2}\,s^{-1}}$ for the Baseline scenario and $7.5 \times 10^{34}\,\mathrm{cm^{-2}\,s^{-1}}$ for the Ultimate scenario.

4.1.2 The Achromatic Telescopic Squeezing optics

To reduce the beam size at the IP and increase the luminosity, the β^* value at the IPs has to be reduced. Both the Baseline and Ultimate scenarios rely on luminosity leveling with a reduction of the β^* up to 15 cm. However, dealing with very small β^* is a real optics challenge that gives rise to a series of limitations. One of them is the mechanical acceptance of the inner triplet, others are related with linear and non linear chromaticity, spurious dispersion and β-beating [56]. In order to overcome these limitations, ensuring chromatic correction with very

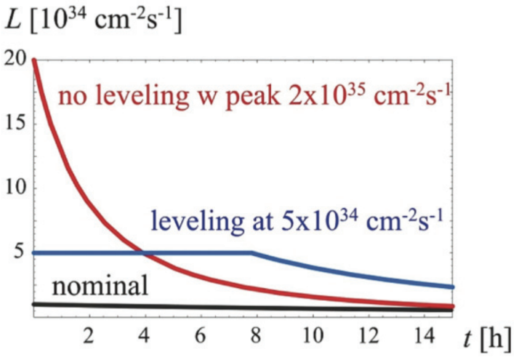

Figure 4.1 – HL-LHC luminosity evolution during a physics fill without leveling (red line) and with luminosity leveling (blue line) compared to the LHC case (black line) [56].

small β^* values (15-10 cm) a new optics scheme called the Achromatic Telescopic Squeezing (ATS) was developed [63, 64]. This new optics scheme is based on two-stage telescopic modes. The first one is the so called *pre-squeeze*, a standard squeeze optics with some additional constraints to limit the strength of the matching quadrupoles of the low-β insertions and of the sextupoles in the arcs. The second stage is the *telescopic squeeze* that acts only on the matching strength of the quadrupoles located beside the IPs insertions, keeping a constant strength for the sextupole magnets in the arcs. This procedure leads to an increase of the β-function in the arcs in oder to maximize, with a constant magnetic field, the efficiency of the lattice sextupoles devoted to the chromatic correction [63, 64]. Therefore, a typical signature of the ATS optics are the β-beating waves created in the four sector near by the low-β insertion of ATLAS (IP1) and CMS (IP5). This is shown in Fig. 4.2 for the β-functions in the arcs beside IP1 and IP5. The red and blue lines correspond to the β-functions in the horizontal and vertical plane respectively for the ATS optics with $\beta^* = 15\,\text{cm}$, while the green and cyan lines correspond to the β-functions in the horizontal and vertical plane respectively for the LHC optics with $\beta^* = 80\,\text{cm}$.

4.1.3 Crossing angle and crab cavities

The reduction of the β^* at the IPs implies not only a beam size increase in the low-β triplet quadrupoles but also a larger crossing angle at the IPs in order to ensure a sufficient normalized long range beam-beam separation $d_{bb} \approx 12.5\,\sigma$, considering the HL-LHC parameters, with a $\beta^* = 15\,\text{cm}$ and the nominal HL-LHC full crossing angle $\alpha_c = 590\,\mu\text{rad}$. Such a large crossing angle yields to a reduction of the geometrical factor R (Eq.1.40) of about 70% compared to the LHC value. The superconducting RF crab cavities can compensate the luminosity reduction by means of a transverse electric field that deflects each bunch by a rotation of $\frac{\alpha_c}{2}$. Thanks to these devices the bunches will collide fully head-on at the IPs with $R = 1$, maximizing the luminosity reach. Figure 4.3 is an illustration of the bunch rotation induced by the deflecting kicks of the crab cavities.

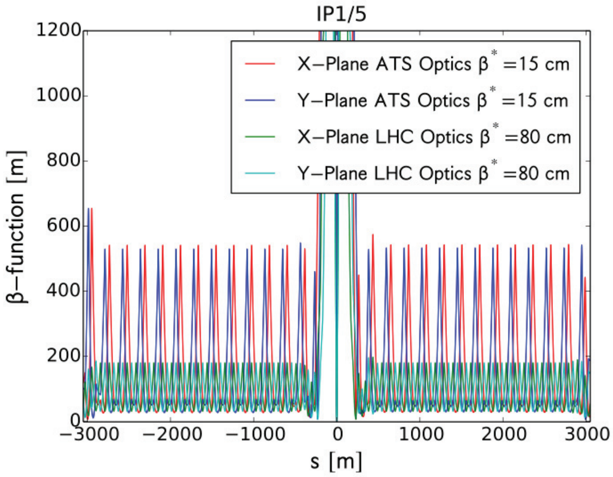

Figure 4.2 – β-functions in the arcs beside IP1 and IP5 for the ATS optics with $\beta^* = 15\,\text{cm}$ (red and blue lines are the β-functions in the horizontal and vertical plane respectively) compared to the LHC optics with $\beta^* = 80\,\text{cm}$ (green and cyan lines are the β-functions in the horizontal and vertical plane respectively).

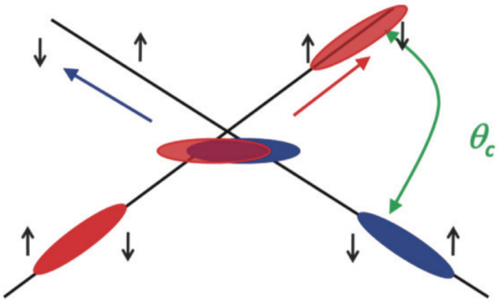

Figure 4.3 – Schematic view of collisions with the crab cavities rotation of the bunches at the IP (from [56]).

4.2 Transverse beam stability during the HL-LHC operational cycle

In this section the transverse stability of the beams is analyzed for the operational cycle of the HL-LHC [62]. All the presented studies take into account the nominal beam parameters listed in Table 4.1 and aim to propose safe configurations in terms of transverse beam stability for the LHC upgrade with and without beam-beam interaction.

4.2.1 Stability diagram with single beam

After the acceleration up to 7 TeV reached at flat top, the β-function value both in IP1 and IP5 is $\beta^* = 6\,\text{m}$. At this stage the beams are still kept separated at the IPs (d_{bb}=50 σ) and the long range beam-beam contribution is negligible due to the large β^* value at the IPs. In this configuration the main source of Landau damping for the impedance coherent modes arises from the tune spread provided by the Landau octupole magnets [25]. Figure 4.4 shows the computed stability diagram at flat top for both negative (black solid line) and positive (black dashed line) octupole polarities powered with the nominal current of ±570 A. An inductive impedance as the one for HL-LHC and LHC [28] causes negative real coherent tune shifts. The negative octupole polarity provides a larger Landau damping to damp coherent instabilities, hence it is preferred to the positive polarity in terms of transverse beam stability with single beam at flat top.

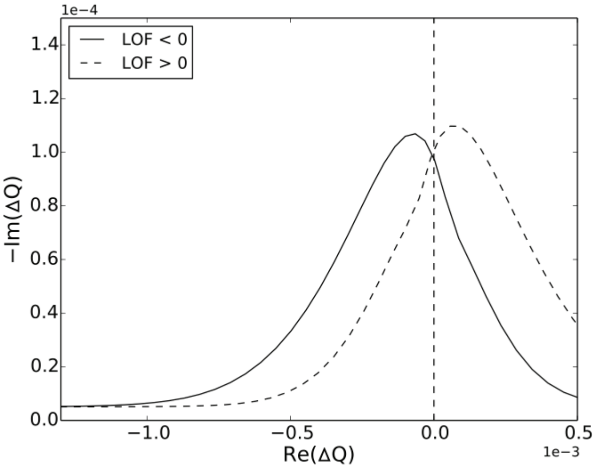

Figure 4.4 – Stability diagrams at flat top for the HL-LHC in the presence of negative (solid line) and positive (dashed line) octupole polarities.

4.2.2 Effects of non linearities induced by ATS optics

Some introductory studies were carried out in order to assess the impact of the non linearities introduced by the ATS optics on the beam tune spread without including the long range beam-beam contribution. As previously mentioned it provides the size of the computed stability diagram. Figure 4.5 shows a comparison between the tune footprints for the nominal LHC optics used in the 2015 physics run with $\beta^* = 80\,\mathrm{cm}$ (blue line) and the ATS optics with $\beta^* = 15\,\mathrm{cm}$ (red line) with no long range beam-beam contribution. Both tune footprints were computed for a normalized emittance of $\epsilon = 2.5\,\mu\mathrm{m}$ and a nominal octupole current $I_{oct} = 550\,\mathrm{A}$. The case with positive octupole polarity is shown in Fig. 4.5a while the case with negative octupole polarity is shown in Fig. 4.5b. The larger β-functions in the arcs for the ATS optics, presented in Fig. 4.2, have a strong impact on the footprint sizes that reflects on the Landau damping of the beams. To quantify this effect the corresponding stability diagrams were computed and plotted in Fig. 4.6 with positive octupole polarity (Fig. 4.6a), and negative octupole polarity (Fig. 4.6b). Since the octupole detuning is proportional to the squared β-function value in the arcs where Landau octupoles are placed [28], the ATS optics with $\beta^* = 15\,\mathrm{cm}$ gives an additional Landau damping of factor ≈ 2.5 as visible in Fig. 4.6.

An asymmetry between the stability diagrams computed with negative and positive octupole polarities was observed by comparing the two cases. This is shown in Fig. 4.7 where both the footprints with positive (red line) and negative (blue line) octupole polarities are shown together with the corresponding stability diagrams.

The symmetry between the two cases was recovered by subtracting the detuning with amplitude produced by the sextupole magnets from the overall tune spread in the beams. A not negligible detuning with amplitude was produced by the sextupole magnets used in the ATS optics for the chromatic correction with the reduction of the β-functions at the IPs. The tune spread produced by the sextupole magnets is shown in Fig. 4.8 for $\beta^* = 15\,\text{cm}$. By removing

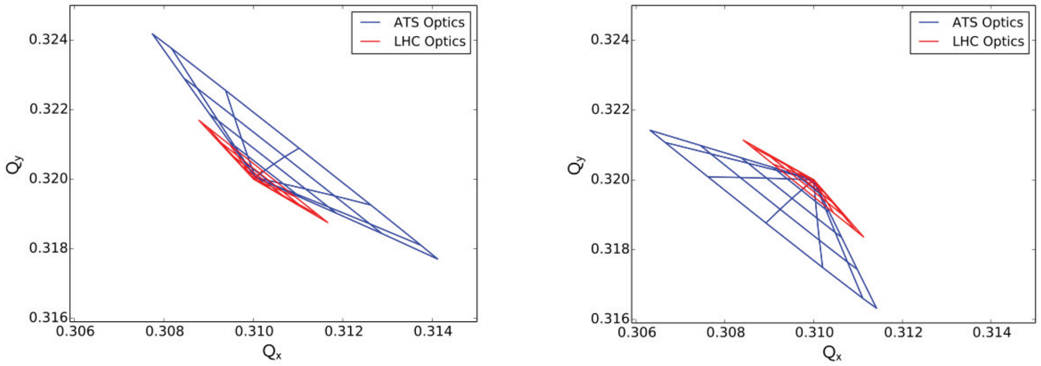

(a) Positive octupole polarity.

(b) Negative octupole polarity.

Figure 4.5 – Tune footprint comparison between the nominal LHC 2015 optics with $\beta^* = 80\,\text{cm}$ (blue line) and the ATS optics with $\beta^* = 15\,\text{cm}$ (red line). A normalized emittance of $\epsilon = 2.5\,\mu\text{m}$ was used for both cases.

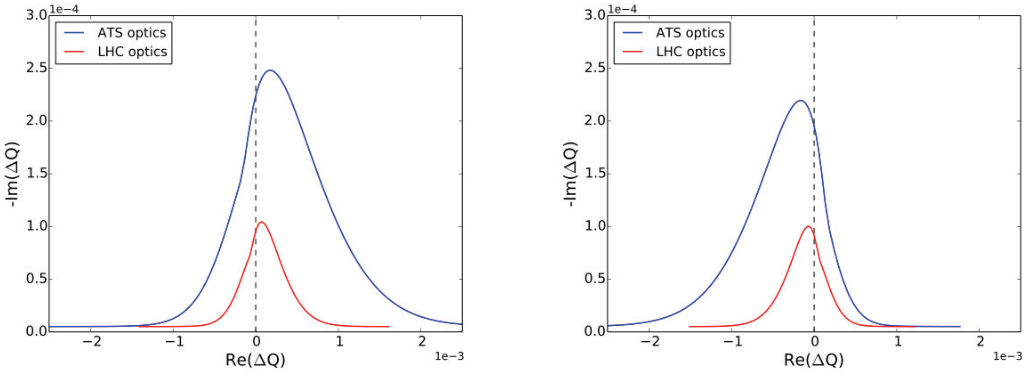

(a) Positive octupole polarity.

(b) Negative octupole polarity.

Figure 4.6 – Stability diagrams with nominal LHC 2015 optics with $\beta^* = 80\,\text{cm}$ (red line) and ATS optics ($\beta^* = 15\,\text{cm}$) (blue line). A normalized emittance of $\epsilon = 2.5\,\mu\text{m}$ was used for both cases.

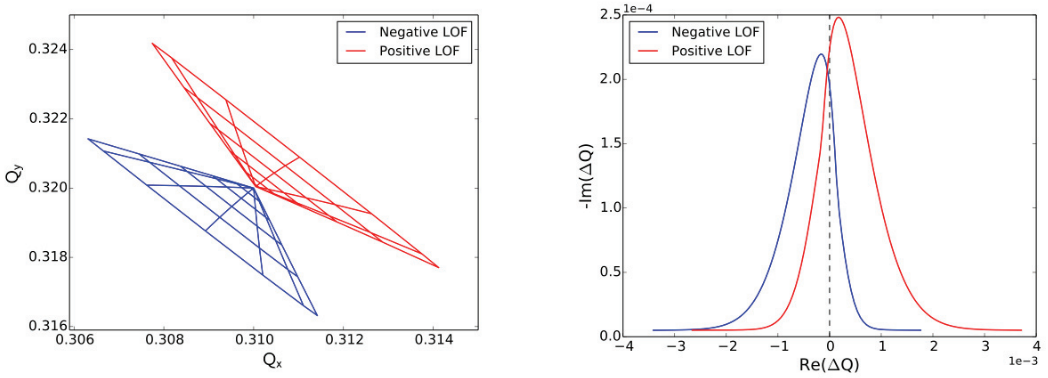

Figure 4.7 – Tune footprint with negative and octupole polarities and corresponding stability diagram for the ATS optics with $\beta^* = 15\,\text{cm}$.

this contribution, the symmetry of the detuning with amplitude between negative and positive octupole polarity is fully recovered as shown in Fig. 4.9 together with the corresponding stability diagrams.

4.2.3 Stability diagram during the Betatron squeeze

During the betatron squeeze the transverse beam size at the IPs is reduced by decreasing the β^* value. For the Baseline scenario that aims to reach a leveled luminosity $5 \times 10^{34}\,\text{cm}^{-2}\,\text{s}^{-1}$, the β^* target is 70 cm, while for the Ultimate scenario the β^* target is $\beta^* = 40\,\text{cm}$ with a leveled luminosity $7.5 \times 10^{34}\,\text{cm}^{-2}\,\text{s}^{-1}$. Throughout this process the long range beam-beam separation at the first encounter reduces together with the $\sqrt{\beta^*}$ (Eq.1.30). The impact of long

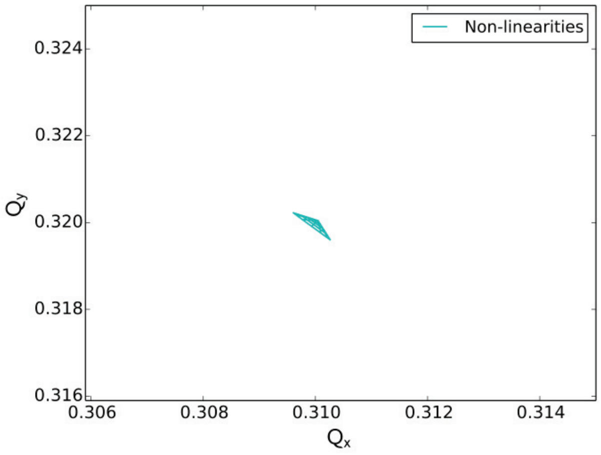

Figure 4.8 – Tune footprint produced by the tune spread due to machine sextupole magnets with the ATS optics ($\beta^* = 15\,\text{cm}$)).

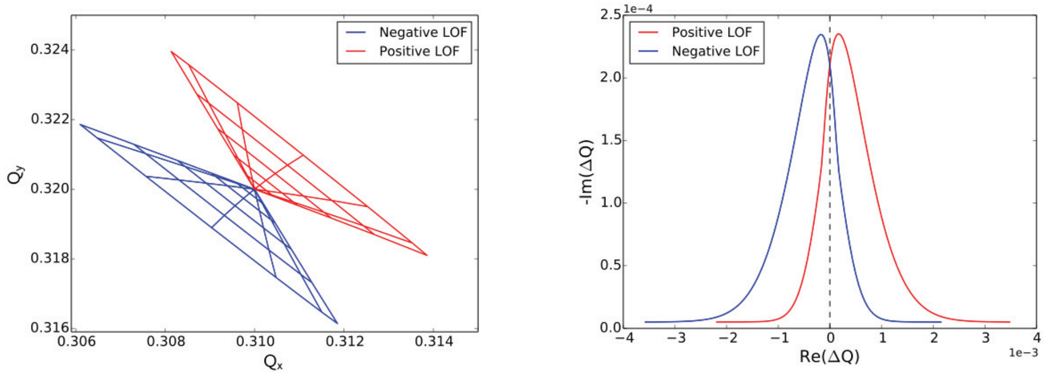

Figure 4.9 – Tune footprint with negative and octupole polarities and corresponding stability diagrams for the ATS optics ($\beta^* = 15\,\text{cm}$) without machine non linearities contribution in the tune spread.

range beam-beam interactions on the beam dynamics therefore increases while reducing the β^* and the detuning with amplitude caused by the long range beam-beam interactions affects the Landau damping provided by the octupoles magnets. For $\beta^* < 30$ cm because of the β-beating caused by the ATS optics, the transverse beam size at the location of the Landau octupole magnets increases and their contribution on the tune spread becomes more important. The interplay between beam-beam interactions and octupole magnets is not always favorable in terms of transverse beam stability and a careful analysis of the Landau damping of the beams is necessary during this process. In the case of negative octupole polarity the effects of the long range beam-beam interactions can lead to a reduction of the tune spread provided by the octupole magnets resulting in a smaller stability diagram with respect to the initial one at flat top as shown in Fig. 4.4. The stability diagram evolution as

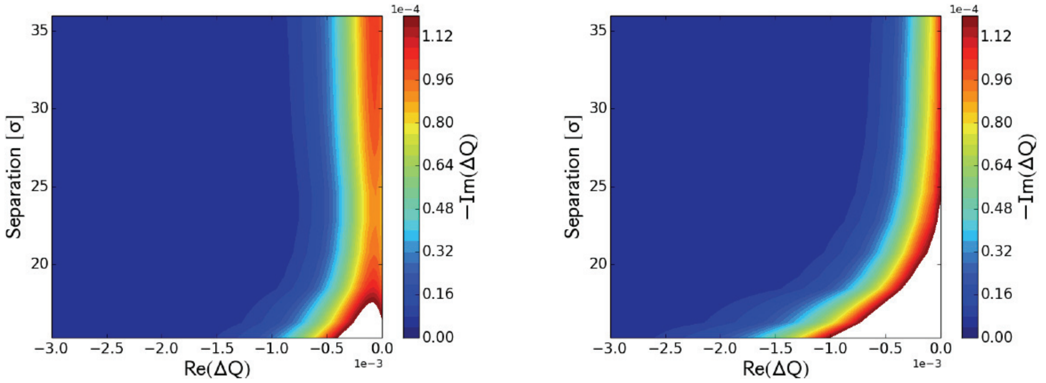

(a) Negative octupole polarity.

(b) Positive octupole polarity.

Figure 4.10 – Stability diagram evolution during the HL-LHC betatron squeeze for both octupole polarities powered with the nominal current $I_{oct} = \pm 570\,\text{A}$.

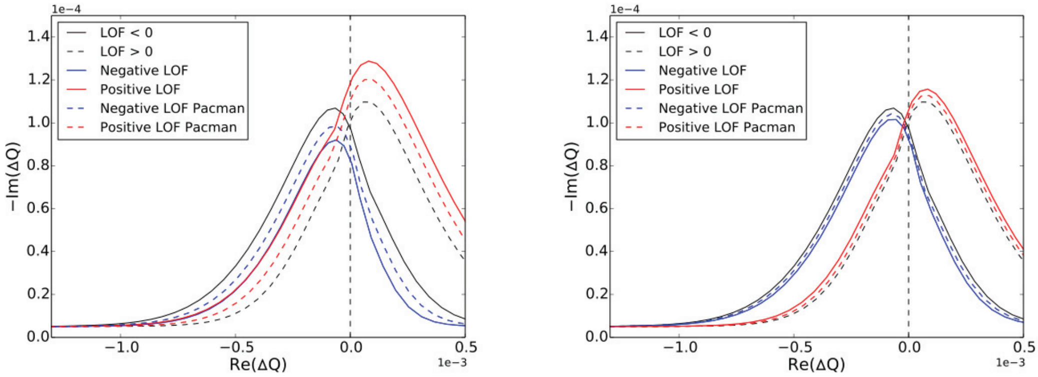

(a) Ultimate scenario end of squeeze, collisions with $\beta^* = 40\,\text{cm}$.

(b) Baseline scenario end of squeeze collisions with $\beta^* = 70\,\text{cm}$.

Figure 4.11 – Stability diagrams at the end of the betatron squeeze for the Ultimate and Baseline scenarios for nominal and PACMAN bunches. The solid and dashed red lines are the stability diagrams with positive octupole polarity for nominal and PACMAN bunches respectively. The solid and dashed blue lines are the stability diagrams with negative octupole polarity for nominal and PACMAN bunches respectively. The solid black line is the stability diagram at flat top with negative octupole polarity while the black dashed line for positive octupole polarity.

a function of the normalized long range beam-beam separation in IP1 and IP5 during the betatron squeeze is presented in Fig. 4.10 for both negative (Fig. 4.10a) and positive (Fig. 4.10b) octupole polarity, with an octupole current of $I_{oct} = \pm 570\,\text{A}$. Before starting the squeeze, the beams are still kept separated (d=0.55 cm). Focusing the attention on the negative real coherent tune shifts only, the stability area continuously grows in the case of positive polarity (Fig.4.10b), while it decreases for the negative octupole polarity with a maximum reduction at $\beta^* \approx 40\,\text{cm}$, corresponding to a normalized long range beam-beam separation $d_{bb} \approx 20\,\sigma$. However, at this separation the stability area results to be larger compared to the one at flat top for the positive octupole polarity case. This is summarized in Fig. 4.11 where the stability diagrams at the end of the betatron squeeze are presented for both the Ultimate scenario (Fig. 4.11a) and for the Baseline scenario (Fig. 4.11b). The red lines, dashed for PACMAN bunches and solid for nominal bunches, correspond to the positive octupole polarity case while the blue lines to the negative octupole polarity for PACMAN bunches (dashed blue line) and nominal bunches (solid blue line). For comparison, the stability diagrams at flat top are also plotted: the black solid line represents the negative octupole polarity case while the black dashed line represents the positive octupole polarity case.

For the Baseline scenario, in the case of negative octupole polarity the expected stability area slightly decreases compared to the one at flat top, while a non-negligible reduction is observed for the positive polarity. For the Ultimate scenario the stability diagram for the negative octupole polarity reduces at the $\beta^* = 40\,\text{cm}$, but it still results to be larger than the positive polarity case. For all the cases the PACMAN bunches have a very similar behavior to the nominal bunches. The further reduction of the β^*, associated with the telescopic part

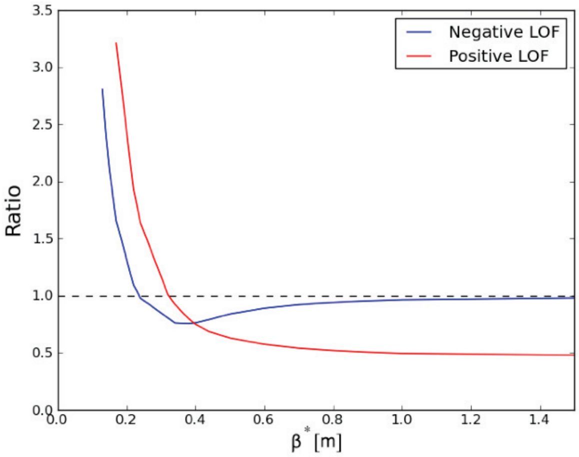

Figure 4.12 – Comparison between the stability diagram at flat top with negative octupole polarity ($I_{oct} = -570\,\mathrm{A}$) and the stability diagrams during the squeeze with negative (blue line) and positive (red line) octupole polarity. The value at half height of the stability diagram at flat top with negative octupole polarity was chosen as a reference. The ratio between the value at half height of the stability diagram and the reference value is plotted as a function of the β^* during the betatron squeeze.

of the squeeze, results to be beneficial in terms of stability area due to the larger β-function values in the arcs, as shown in Fig. 4.10. The β-beating caused by the ATS optics, increases the transverse beam size at the location of the Landau octupole magnets enhancing their effects on the tune spread of the beams. In this configuration the overall impact on the tune spread is dominated by the contribution of the octupole magnets. Figure 4.12 shows a comparison between the stability diagrams at flat top with negative octupole polarity ($I_{oct} = -570\,\mathrm{A}$) and the stability diagrams during the squeeze with negative (blue line) and positive (red line) octupole polarity. Considering a reference value at the half height of the stability diagram at flat top with negative octupole polarity ($I_{oct} = -570\,\mathrm{A}$) it is possible to compare the stability diagrams for different β^* during the squeeze with respect to it. The ratio between the corresponding value of the stability diagram and the reference value is plotted as a function of the β^* during the betatron squeeze. This ratio defines a stability factor: when it is ≈1 the two stability diagrams are similar, when it is smaller (or larger) than one the stability diagram is reduced (or increased) with respect to the case with negative octupole polarity at flat top. With negative octupole polarity reducing the β^*, the stability factor decreases because of the unfavorable long range beam-beam interactions and octupole interplay in terms of the overall tune spread in the beams. The maximum reduction is observed for a value of $\beta^* \simeq 30\,\mathrm{cm}$. Below this value the tune spread is dominated by the octupole magnets whose strength is increased due to the β-beating caused by the ATS optics. For the case of positive octupole polarity the stability diagrams are always smaller than the reference case and they only increase for $\beta^* < 30$ cm because of the ATS optics effects: a stronger β-beating in the arcs, where the octupole magnets are placed, is expected and this effect increases their

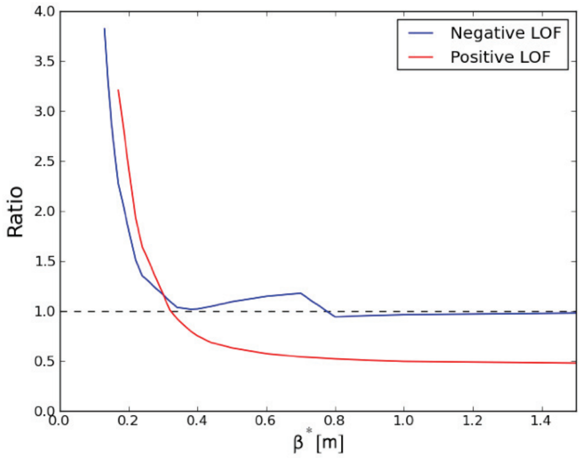

Figure 4.13 – Comparison between the stability diagram at flat top with negative octupole polarity ($I_{oct} = -570\,\mathrm{A}$) and the stability diagrams during the squeeze with negative (blue line) and positive (red line) octupole polarity. The value at half height of the stability diagram at flat top with negative octupole polarity has been chosen as a reference. The ratio between the value at half height of the stability diagram and the reference value is plotted as a function of the β^* during the betatron squeeze where an increase of ≈ 8% of the β-function at the locations of the octupole magnets has been introduced at $\beta^* = 70\,\mathrm{cm}$.

effectiveness on the beams. As a result of this analysis, it can be deduced that the negative octupole polarity is preferred to the positive octupole polarity at flat top with single beam and also in the presence of long range beam-beam interactions during the betatron squeeze for both the Baseline and Ultimate scenario. The negative octupole polarity is also preferred to the positive one in terms of dynamic aperture studies [65], thus based on this analysis, an operational scenario with the negative octupole polarity was proposed and accepted to become the baseline scenario for the HL-LHC operations [62].

However, the choice of negative octupole polarity shows a reduction of the stability diagram at lower β^* as shown in Fig. 4.12. A proposal was made to compensate this reduction by using the ATS optics beating starting from larger β^* values. An octupole current of −650 A would fully recover the reduction of the stability diagram at $\beta^* = 40\,\mathrm{cm}$ making it comparable with the one expected at flat top with negative octupole polarity. However, due to hardware limitations it is not possible to reach such a current in the octupole magnets with the present configurations. The detuning with amplitude produced by the Landau octupoles is proportional to the squared β-function value at the locations of the octupole magnets in the arcs [28], therefore an increase of the 14% in the octupole current with respect to the nominal value of −570 A turns into an increase of the 8% of the β-function at the octupole magnets. A gradual application of this correction, since the beginning of the betatron squeeze, will compensate the reduction due to the long range beam-beam interactions during the betatron squeeze. Figure 4.13 shows the stability factor during the betatron squeeze introducing the optics correction at $\beta^* = 70\,\mathrm{cm}$. In

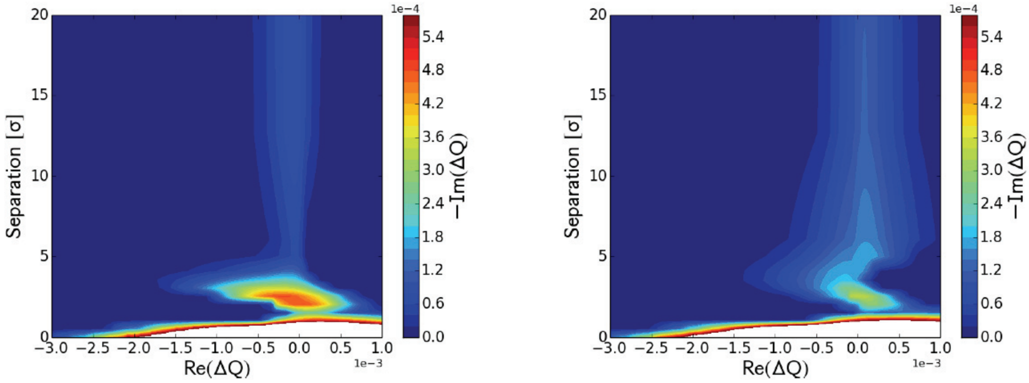

(a) Collapse of the beams with negative octupole polarity.

(b) Collapse of the beams with positive octupole polarity.

Figure 4.14 – Evolution of the stability diagrams during the adjust beam process for the HL-LHC case without crab crossing for the Baseline scenario with $\beta^* = 70\,\text{cm}$.

this case, the stability diagram for negative octupole polarity will never be smaller than the stability diagram at flat top with negative octupole polarity during the full betatron squeeze.

4.2.4 Stability diagram during the adjust beam process

At the end of the betatron squeeze, the beams are brought into collision collapsing the separation bumps at the IPs. The RF crab cavities can act on the beams since the beginning of the collapse process or at the end of the collapse when the beams are already colliding head-on. Predictions of the transverse beam stability of the beams are presented in the next sections during the collapse process with and without RF crab cavities acting on the beams in order to identifying critical reductions of the Landau damping for both configurations.

During the collapse of the separation between the two beams, it is possible to keep the RF crab cavities switched off. The evolution of the stability diagram as a function of the transverse normalized beam separation in IP1 and in IP5 during the adjust beam process without crab-crossing is shown in Fig. 4.14 for both negative (Fig. 4.14a) and positive polarity (Fig. 4.15b). The stability diagrams were computed considering both the beam-beam head-on and long range interactions in IP1 and IP5. The stability area increases with the positive octupole polarity during the collapse, but there is a reduction at a transverse beam-beam separation $d \approx 1.5\,\sigma$. For the negative octupole polarity two minima are identified at $d \approx 6\,\sigma$ and $d \approx 1.5\,\sigma$. Similar conclusions can be drawn for the Ultimate scenario with collision at $\beta^* = 40\,\text{cm}$.

By switching on the crab-crossing during the adjust process of the beams, a larger stability area than the case without crab crossing is expected with almost zero transverse beam separation due to the fully head-on collision that increases the tune spread in the beams. Figure 4.15 shows the evolution of the stability diagram during the collapse process with the RF crab cavities acting on the beams. In the case of positive octupole polarity (Fig.4.15b), the stability diagram keeps increasing with the reduction of the transverse beam separation, while for the negative octupole polarity (Fig.4.15a) two minima are identified at $d \approx 6\,\sigma$ and $d \approx 1.5\,\sigma$. However, these two minima are characterized by a larger stability area compared to the previous case without crab crossing. A similar behavior is expected for the Ultimate scenario and it is presented in the next paragraph.

4.2.5 Analysis of the stability minima

As discussed in the previous section, two minima of stability are expected during the collapse process for the negative octupole polarity. Figure 4.16 summarizes the stability diagrams at the first minimum expected at $d = 6\,\sigma$ for both positive and negative octupole polarities during the collapse process for the Ultimate scenario (Fig. 4.16a) and for the Baseline scenario (Fig 4.16b). For the negative octupole polarity case the correction of $I_{oct} = -650\,\mathrm{A}$ was applied in oder to compensate the reduction of the stability diagram during the betatron squeeze at $\beta^* = 40\,\mathrm{cm}$. The blue dashed line represents the case for negative octupole polarity without crab-crossing and the blue solid line represents the case for negative octupole polarity with crab-crossing. The red lines represent the positive octupole polarity case for the nominal octupole current ($I_{oct} = 570\,\mathrm{A}$) without crab-crossing (red dashed line) and with full crab-crossing (red solid line). As a reference, the stability diagrams at flat top with negative (black solid line) and positive (black dashed line) octupole polarity are shown in the same plot. From this picture it is possible to conclude that in the presence of this minimum, for the negative octupole polarity the stability diagram without crab-crossing is similar to the one with positive polarity for single beam at flat top, while there is a reduction with full crab-crossing. Same considerations for the Ultimate scenario case can be deduced from the stability diagrams

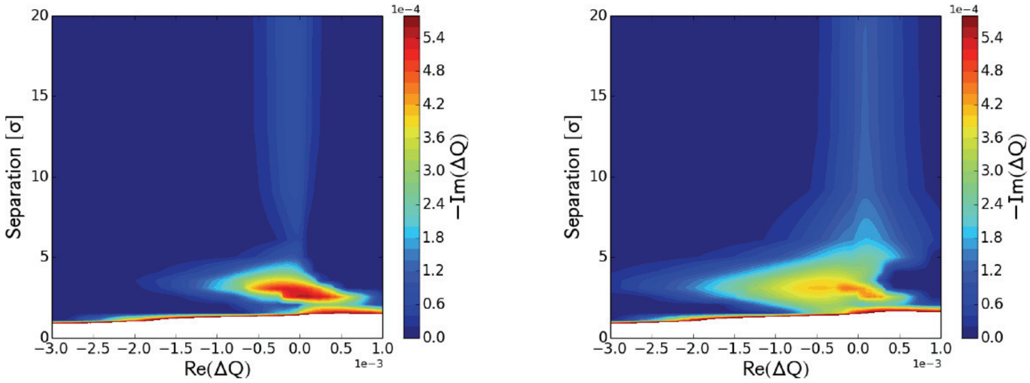

(a) Collapse of the beams with negative octupole polarity.

(b) Collapse of the beams with positive octupole polarity.

Figure 4.15 – Evolution of the stability diagrams during the adjust beam process for the HL-LHC case with full crab-crossing turned on for the Baseline scenario with $\beta^* = 70\,\mathrm{cm}$.

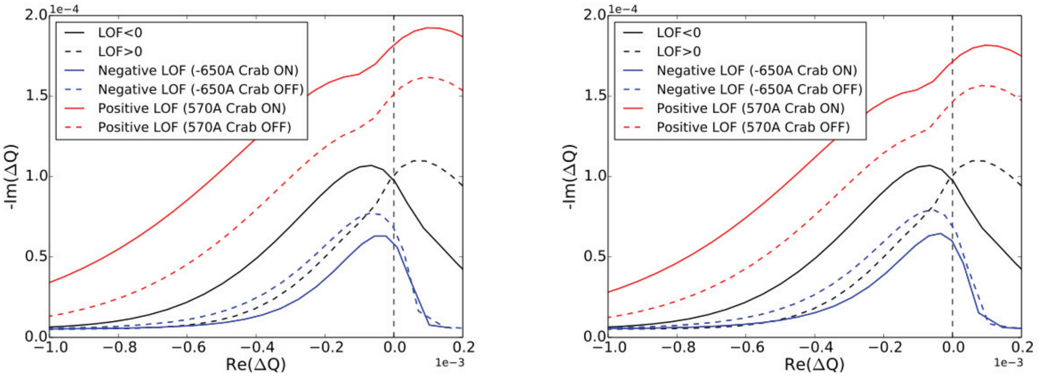

(a) Ultimate scenario.

(b) Baseline scenario.

Figure 4.16 – Stability diagrams at the reduction of $d = 6\ \sigma$ during the adjust beam process.

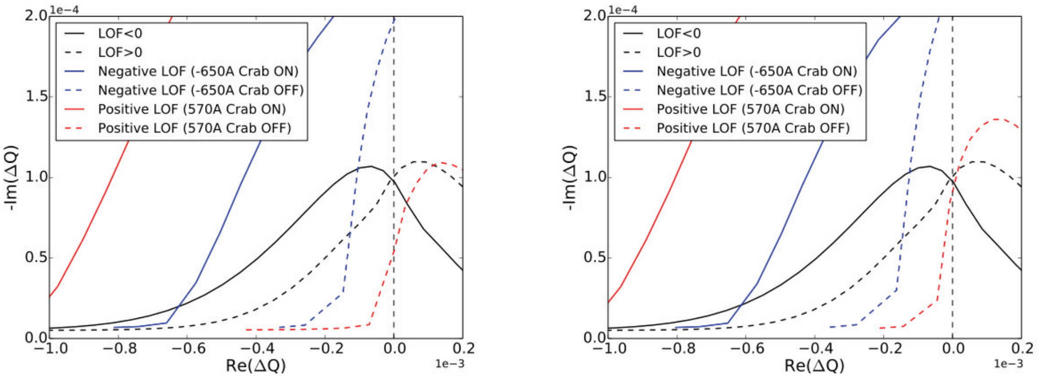

(a) Ultimate scenario.

(b) Baseline scenario.

Figure 4.17 – Stability diagrams at the reduction of $d = 1.5\ \sigma$ during the adjust beam process.

plotted in Fig. 4.16a. For the minimum at $d = 1.5\ \sigma$, the corresponding stability diagrams are shown in Fig.4.17, with the same color legend as in the previous plot. With crab-crossing on, a larger stability diagram is expected for positive octupole polarity. Also in the case of negative octupole polarity a much larger stability diagram is expected with respect to the case without crab-crossing. Without crab-crossing the negative polarity case exhibits a larger stability diagram than the corresponding positive octupole polarity case that is characterized by an important minimum at $d = 1.5\ \sigma$. Similar conclusions can be drawn for the Ultimate scenario (Fig. 4.16a).

Figure 4.18 shows the stability diagrams for negative octupole polarity expected at the two minima of stability at a normalized transverse beam separation $d = 1.5\ \sigma$ with the full crab crossing (blue solid line) and without crab crossing (blue dashed line) and at $d = 6\ \sigma$ normalized transverse beam separations (green solid line) with the crab crossing on and without crab crossing (green dashed line). The red and green dots correspond to single bunch impedance coherent modes in the horizontal and vertical plane respectively. The blue and yellow dots correspond to the multi bunch impedance coherent modes (2748 bunches in total) in the horizontal and vertical plane, respectively. Some coherent impedance modes results to be unstable at the 1.5 σ minimum for the case with full crab crossing. The minimum at 6 σ for the case with the crab crossing on results to be worse than the case without crab crossing.

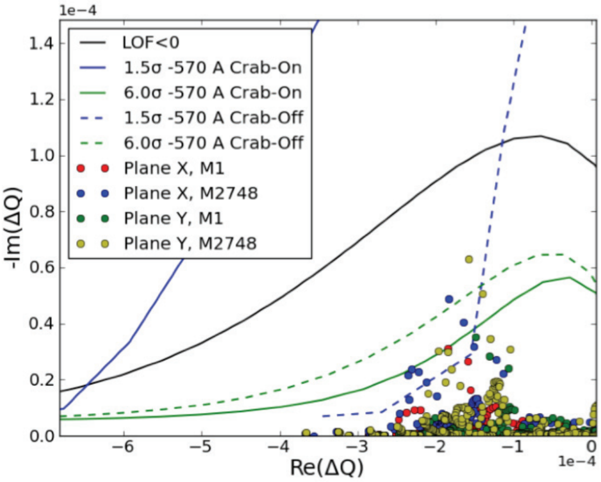

Figure 4.18 – Stability diagrams at the minima of stability during the adjust beam process together with the impedance coherent modes expected at the end of the squeeze for the HL-LHC Baseline scenario. The red and green dots are the single bunch impedance modes in the horizontal and vertical plane respectively while the blue and yellow dots are the multi-bunches impedance modes in the horizontal and vertical plane respectively.

If the Landau damping of a coherent mode is not ensured anymore, because of the reduced stability diagram as it happens at the two minima of stability identified before, the rise time of the coherent mode has to be slower than the crossing speed of the critical region. In this way the associated instability has not enough time to develop. During the 2012 LHC physics run, no transverse beam instabilities were observed during the adjust beam process. Only the bunches colliding only in IP8 at a beam separation $d \approx 1.5\ \sigma$ with positive and negative octupole polarities have shown instabilities for all the physics fills of the 2012 [44]. However, it has to be remarked that in the 2012 the adjust process was quite long, with a duration of ≈ 200 s and both the transverse feedback (ADT) settings and chromaticity values were not entirely controlled during machine operations. During the LHC Machine Development (MD) studies on the offset leveling carried out in the 2012, the fastest transverse instability, with a reduced ADT gain acting on the beams, was characterized by a rise time of 2 s at a transverse beam separation $d \approx 1.5\ \sigma$ [52] and the beam dumps were prevented by increasing the ADT efficiency.

In the 2015 and 2016 the adjust beam process was characterized by a duration of ≈ 40 s, much

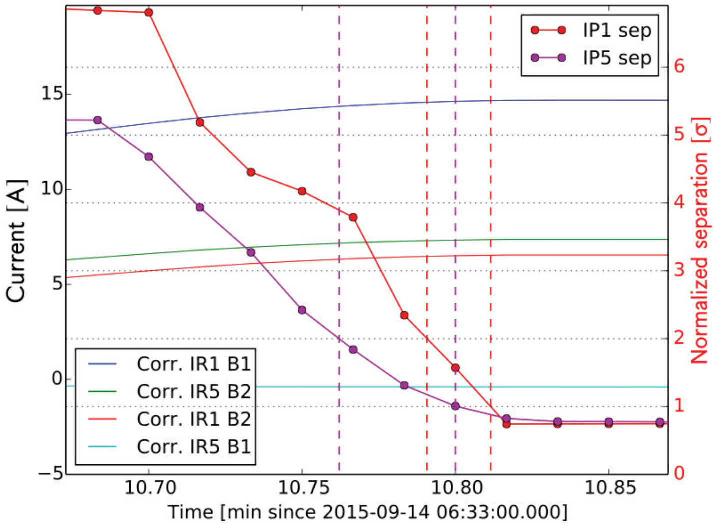

Figure 4.19 – Beam separation in IP1 (red line) and IP5 (pink line) during the adjust beam process compared to the current of some corrector magnets of the beam orbit in IP1 and IP5. The dashed red and pink lines show the time to go from 1 σ to 2σ beam separation at IP1 and IP5 respectively.

faster than the same process in the 2012. During the collapse of the beam separation bumps no sign of transverse instabilities was observed in the 2015 physics runs, except while separating the beams during the OP scans with a less effective ADT, or lower chromaticity, at transverse beam separation $d \approx 1.5\,\sigma - 2.0\,\sigma$, as presented in Sec. 3.3.3.

From the luminosity values published by the experiments, it is possible to estimate the transverse beam separation at the IPs during the adjust process by using Eq.1.43. The luminosity values were normalized to the beam intensities. The collapsing speed of the separation bumps is associated with the current flowing in the corrector magnets of the beam orbit. Figure 4.19 shows the normalize transverse beam separation in IP1 (red line) and IP5 (pink line) derived from the luminosity during the adjust beam process for a typical Physics fill. In the same plot the currents of some corrector magnets of the beam orbit in IP1 and IP5 are also shown. The dashed red lines and the dashed pink lines correspond to the moments for which the value of the beam separation goes from $d = 2.0\,\sigma$ to $d = 1.0\,\sigma$ in IP1 and in IP5 respectively. It is possible to observe that for both IPs, in the range of $d = 1.0 - 2.0\,\sigma$, the corrector magnet currents are already in the deceleration part of the current ramp, therefore a further increase of the ramp rate of the corrector magnet current during the collapse of the separation bumps would not be effective in these regions. The time spent in the range of $1.0 - 2.0\,\sigma$ beam separation for several physics fills during the 2015 are presented in Table 4.2 for both IP1 and IP5. The averaged time spent while crossing the minimum of Landau damping results to be $\bar{\tau}_{IP1} \approx 1.6$ [s/σ] in IP1 and $\bar{\tau}_{IP5} \approx 2.5$ [s/σ] in IP5. For the Baseline scenario with collision starting at $\beta^* = 60\,\text{cm}$, the most critical coherent impedance modes are characterized by a

rise time of (1.5-2.5) s comparable with the averaged time spent at the minimum of Landau damping in IP1 and IP5 (Tab. 4.2). As shown in Fig. 4.18, some coherent impedance modes results to be unstable at the 1.5 σ minimum for the case without crab crossing. The minimum at 6 σ for the case with the crab crossing on results to be worse than the one for the case with the crab crossing off. However, for this case the collapsing speed of the separation bumps is less than 1 s from 2 σ to 1 σ, as also visible in Fig. 4.19.
In general it would be beneficial to cross the two minima of stability as fast as possible, preferably in less than 1 s faster than the fastest observed instability in the LHC characterized by a rise time of $1.5\,\mathrm{s} - 2.5\,\mathrm{s}$.

Table 4.2 – Time spent while crossing the minimum of Landau damping during the adjust beam process in IP1 and IP5 for several physics fills of the 2015 LHC physics run.

Fill Number	IP1 [s/σ]	IP5 [s/σ]
4332	1.428	3.822
4337	1.368	4.152
4363	1.248	2.280
4364	1.860	1.962
4384	2.016	1.836
4391	1.774	1.670
4398	1.417	1.787
4555	1.458	2.226
Average	1.571	2.467

4.3 Collision beam process

If the transverse separation crosses the critical separation $d = 1.5\ \sigma$ the reduction of the stabilizing area can lead to strong beam-beam impedance coupled instability with consequent emittance blow-up and/or beam losses. However, during the luminosity production with full crab crossing a larger stability diagram is expected compared to the case with negative octupole polarity at flat top.

It would be helpful to relax the constraints on the transverse beam separation during the luminosity production since keeping the orbit control in within 1 σ of the rms beams size is very challenging during operations. This can be achieved turning off the Landau octupoles with beams in collisions. By removing the interplay between the detuning from the Landau octupole with negative polarity and the detuning arising from the long range beam-beam interactions, the stability diagram, represented by the red line in Fig. 4.20, is larger compared to the one with negative octupole polarity at the minimum of Landau damping at 1.5 σ (blu line). This configuration allows to relax the orbit control constraints during the β^* leveling between (0-4) σ transverse beam separation at the IPs for an operational scenario with negative octupole polarity.

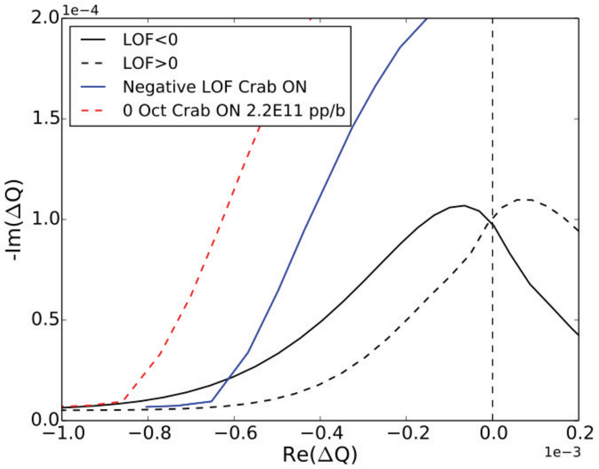

Figure 4.20 – Stability diagrams at the minimum of stability with beam in collisions and crab-crossing with Landau octupole switched off (red dashed line) compared to the negative octupole polarity at the minimum of 1.5 σ (blue solid line).

4.4 Summary

A detailed analysis of the Landau damping properties during the different operational phases of the HL-LHC was carried out for both the Baseline and Ultimate scenario. The transverse beam stability in the presence of the beam-beam interaction was studied during the betatron squeeze, during the adjust beam process and during collisions. The operational scenario with the octupoles magnets set with negative polarity was proposed and accepted to became the baseline scenario for the HL-LHC [57]. As a results of this studies to avoid the reduction of Landau damping during the betatron squeeze, an increase of the 8% of the β-function at the octupole magnets gradually applied at the beginning of the betatron squeeze was proposed to compensate the reduction.

The evolution of stability during a possible β^* leveling scenario with and without crab crossing was also studied and presented in this chapter. The analysis aimed to define the tolerances in terms of maximum offset allowed during physics production to guarantee the stability of the beams. Thanks to the strong head-on, the large detuning with amplitude allows to relax the constraints on orbit control during the β^* from 1 σ to 4 σ separation with full crab-crossing. This is a fundamental result since keeping the orbit control in within 1 σ of the rms beam size is very challenging during operations.

The stability evolution during the collapse of the beam separation bumps was presented to evaluate how the speed of this process could affect the beam stability. The minima of stability during the collapse process were identified for both the cases with full crab-crossing and without crab-crossing: they occur around 6 σ and 1.5 σ beam separation. The speed to pass through these minima plays an important role in terms of beam stability. Past observations at the LHC during the adjust beam process were taken into account as well as during OP scans for the cases when beams became unstable. Based on the rise times of the observed instabilities a recommendation was made to go from 2 σ to 1 σ beam separation in less than 1 s (i.e. faster than the fastest instability measured at the LHC).

5 Beam based experimental study of Landau damping at the LHC

Motivated by multiple observations of coherent instabilities in the LHC during 2012, 2015 and 2016 physics runs, the knowledge of the Landau damping of the beams was doubted. Studies of the stability diagram computed by evaluating the dispersion integral for different tune spread and machine configurations could not explain the observed instabilities [17]. The Beam Transfer Function (BTF) measurements are proportional to the dispersion integral and therefore they are the best direct measurements of the stability diagram [66]. Beam Transfer Functions are also powerful beam diagnostic tools, for example they can be applied to monitor tunes [67] or to recover the tune spread in presence of coherent beam-beam modes in colliders [68]. They also contain information about the transverse and longitudinal impedance [69, 70] and can detect excited coherent modes in the beams [66, 71]. Measuring the cross talk between two colliding beams gives information about the beam-beam coupling [72].

The methodology of a BTF consists of the excitation of the beam with a sinusoidal wave and measuring the complex response of the beam characterized by an amplitude and a phase. The frequency excitation is changed in steps and the harmonic excitation can be adjusted as the beam oscillations are kept within an acceptable amplitude range to avoid emittance blow-up. From the complex response of the beam to the external excitation it is possible to reconstruct the stability diagram [25, 28] for different configurations of the LHC and analyse the beam stability. Transverse BTF measurements were performed in the LHC for the first time during the 2015 physics run. The safety of the system was assessed and measurements were acquired for several machine configurations. This chapter details the BTF system and describes the results of the measurements acquired over several experiments [73–76]. Comparisons to expectations are presented throughout.

5.1 The transverse BTF system in the LHC

A constant collaboration with the Beam Instrumentation team of the LHC made possible the development and the installation of the transverse BTF system during the first part of the 2015 physics run [73, 74].

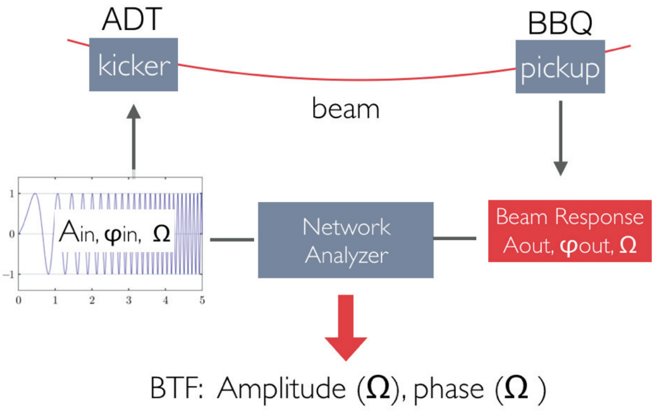

Figure 5.1 – Schematic view of the BTF system. The beam is excited by the ADT kickers with a sinusoidal wave, the complex response of the beam is given by the BBQ BPM.

Measurements were acquired on single bunches of both nominal ($\sim 1.15\times10^{11}$ p/b) and lower intensity at injection and at flat top energy, 450 GeV and 6.5 TeV respectively. Transverse BTF measurements are presented for different machine settings and configurations. All the measurements were acquired on single bunch with the LHC transverse feedback (ADT) [77] turned off in order to avoid the transfer function contribution of the ADT in the BTF signal. During a BTF acquisition the chosen beam is safely excited, i. e. without causing losses or emittance blow up, within a frequency range of interest for betatron motion. The beam is excited by the kickers of the ADT at a certain frequency Ω, while the beam response is recorded by the Beam Position Monitors (BPM) of the Base Band Q (BBQ) measurements system [78]. A schematic view of the BTF system is shown in Fig. 5.1. A typical BTF measurement is shown in Fig. 5.2 for Beam 1 (B1) in the horizontal plane at injection energy. The blue line represents the amplitude response while the red line is the phase response of the beam. The coherent peak is centered at the value of the fractional part of the horizontal betatron tune ($Q_x = 0.28$ at injection) and the first order synchrotron sidebands are also visible at $\pm Q_s = 5\times10^{-3}$ (at injection energy) from the bare betatron tune corresponding to jumps in the phase response. The synchrotron sidebands are due to non-zero chromaticity $Q^{'}\approx 5.0$ during the measurements, as discussed in 2.1.3. At the betatron tune the amplitude response reaches its maximum value, while the phase response its maximum slope. The phase response changes from 0 to π when the excitation is applied through the resonance. At the betatron frequency the phase value is $\pi/2$. The set-up of the system was performed at injection energy on low intensity bunches in order to be as transparent as possible to the beams, without causing neither emittance growth nor losses during the excitation. To find an optimum BTF excitation amplitude value, an empirical approach was chosen keeping a sufficient signal to noise ratio in the amplitude and phase response. Since the calibration of the system has not been performed yet, the excitation amplitudes can not be expressed in units of transverse rms

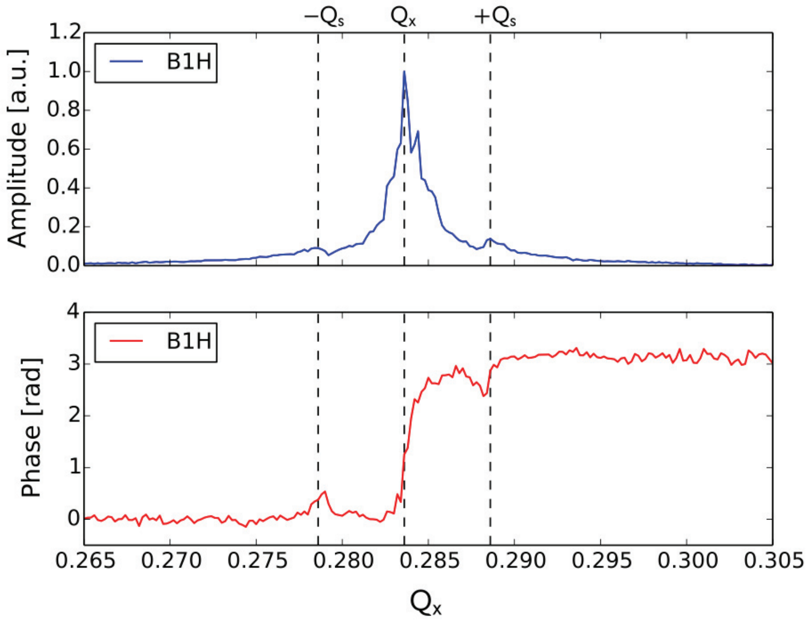

Figure 5.2 – Example of a BTF a measurement: amplitude and phase response for B1 at the LHC injection energy.

beam size. Beam 1 was excited in the vertical plane with different amplitudes: 1.0, 1.8, 3.6, 5.8 [a.u.] until an emittance blow up was observed in the Beam Synchrotron Radiation Telescopes (BSRT) [79]. The vertical normalized emittance of B1 during the set-up is shown in Fig. 5.3, where the black dashed lines correspond to each excitation amplitude change.

5.1.1 Fitting function for the BTF data analysis

The BTF system in the LHC has not been calibrated yet due to the complex procedure required to perform a full calibration and the limited time available for the Machine Development (MD) studies. This means that the excitation amplitude as well as the amplitude response of the beam are expressed in relative units only. Due to this circumstance, the reconstructed stability diagram from the measurements does not reflect the correct size of the Landau stability area, and therefore the actual imaginary and real coherent tune shifts. In order to evaluate the measured tune spread and compare it to expectations, the experimental data will be analyzed by using a fitting function that takes as input the semi-analytical amplitude and the phase of the computed dispersion integral and fit the measurements to analytical expectations by using the following parameterization:

$$\begin{cases} \varphi(Q_{meas}) = \varphi\left[p_0 + p_1 \cdot (Q_{model} - Q_0)\right] \\ A(Q_{meas}) = p_2 / p_1 \cdot A_{model}(Q_{model}) \end{cases} \tag{5.1}$$

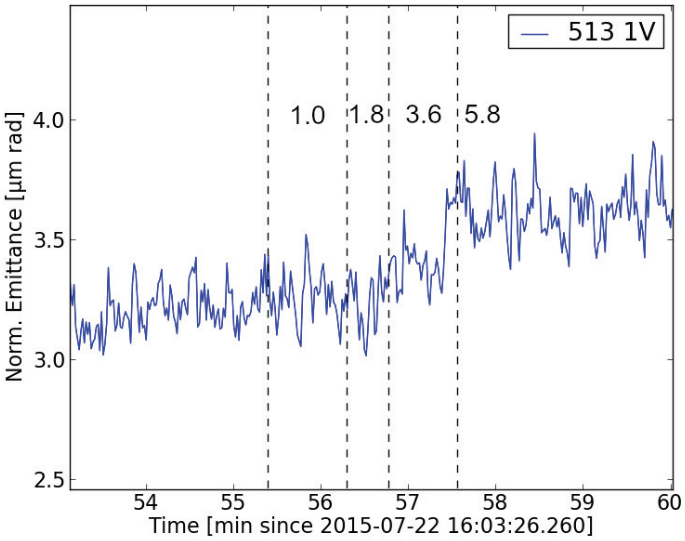

Figure 5.3 – Normalized beam emittance in the vertical of Beam 1 while scanning the excitation amplitude of the BTF.

where the parameter p_0 gives the tune shifts with respect to the frequencies of the analytical detuning ($Q_{model} - Q_0$) with Q_0 the model bare tune, p_1 is a factor related to the tune spread with respect to the expected one. It is important to underline that this parameter does not depend on the amplitude response, therefore it is not related with the unknown calibration factors of the BTF amplitude. It is independently calculated from the slope of the measured phase response. The factor p_2 is a scaling factor of the amplitude response with respect to the reference case (A_{model}) and it needs to be divided by the tune spread factor p_1 in order to take into account the amplitude height dependency on the tune spread discussed in section 2.1.4. Such a parameterization allows to correlate the measured amplitude and phase to a known case and compare the measurements with the analytical models currently used to predict the stability thresholds limits in the LHC. This parameterization provides a method of overcoming the unknown excitation amplitude and measure the amplitude calibration at the cost of relying on an approximation of the amplitude detuning and the beam distribution. An example of this method is shown in Fig. 5.4 where the black lines represents the fitting function and the blue lines are the measured BTF amplitude and phase responses in the horizontal plane. Measurements were taken at injection energy with an octupole current of $I_{oct} = 6.5$A. The corresponding stability diagram is shown in Fig. 5.5. In this case the tune spread parameter is $p_1 = 1.05$, indicating a difference with respect to the analytical case of $\approx 5\%$, the red shadow in the plot represents this difference between measurements and expectations. The computation of the semi-analytical dispersion integral was performed for a Gaussian particle distribution and a normalized beam emittance of 2.5µm corresponding to the experimental conditions of the beams. During the data taking of the BTF, the beams are kicked with a fixed excitation amplitude. Due to this, the BTF signal is affected by significant

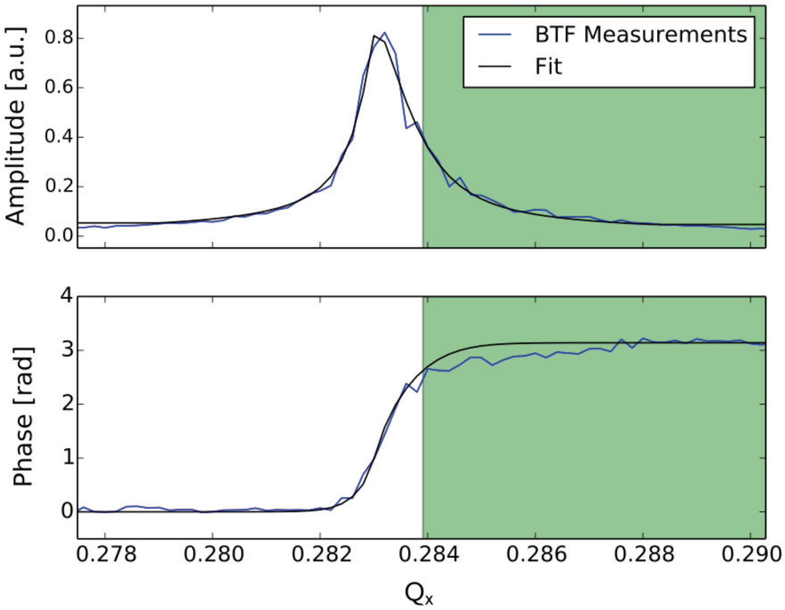

Figure 5.4 – Measured amplitude and phase response of the beam during a BTF measurement (blue line) in presence of detuning with amplitude given by octupole magnets at injection energy ($I_{oct} = 6.5$A) compared to analytical expectations (black line). The green shadow represent the data points excluded from the fit because of the artifact signal in the BTF response for the frequency above the betatron tune.

noise in the measurements, especially away from the resonant frequency range of the beams. In some cases it makes the reconstruction of the stability diagram difficult. Kicking the beams with a fixed excitation amplitude translates into an artifact signal after the coherent betatron tune excitation. Since the frequency swept is performed from lower to higher frequencies, this can produce some fake spread beyond the betatron tune frequency that requires a smaller excitation amplitude to perturb less the beam motion during the BTF frequency swept. This is visible in the phase response in Fig. 5.4 where there is a certain remaining slope in the phase before approaching the π value (green shadow). This effect suggests that after the excitation of the coherent betatron tune the beams require additional time to damp the oscillations between one excitation and the other. Due to this, the corresponding measurements are always affected by an artifact signal that is also found in simulations (Fig. 2.5). For this reason the measurements corresponding to the excitation frequencies above the coherent tune are usually excluded from the fit (green shadow in Fig. 5.4 and in Fig. 5.5). As visible, the measured points corresponding to the coherent positive real tune shifts of the reconstructed stability diagram turn out to be artifacts because of the remaining slope in the phase before approaching the π value. Thus, only the negative real tune shifts of the measured stability diagrams will be plotted in the complex plane without losing critical information since the LHC impedance is inductive and produces negative real coherent tune shifts [28], therefore the beam stability can still be evaluated from the measurements.

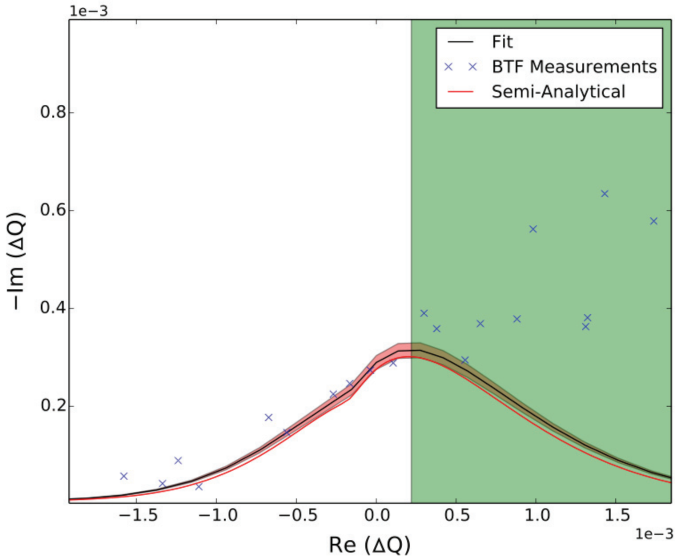

Figure 5.5 – Reconstructed stability diagram from measured BTF (blue crosses) in presence of detuning with amplitude given by octupole magnets at injection energy (I_{oct} = 6.5 A), compared to analytical estimation (black line) and with the semi-analytical model (red line). The green shadow represent data points excluded from the fit because of the artifact signal in the BTF response for frequencies above the betatron tune.

5.2 LHC stability at injection energy

Octupoles magnets are operationally used in the LHC to provide sufficient detuning with amplitude to damp the impedance driven coherent instabilities through the Landau damping mechanism [25, 28]. Transverse BTF measurements have been acquired for different octupole currents: 0 A, 6.5 A, 13 A, 26 A at injection energy on a single bunch with intensity of 1.1×10^{11} p/bunch at collision tunes ($Q_x \sim 64.31$, $Q_y \sim 59.32$). The corresponding amplitude detuning coefficients for each octupole current can be calculated by using Eq. 2.4. Figure 5.6 shows both the amplitude and the phase response as a function of different octupole currents for Beam 1 (B1) excited both in the horizontal (Fig. 5.6a) and in the vertical plane (Fig. 5.6b). For comparison, each BTF amplitude response was normalized to its maximum value. By increasing the octupole strength, the width of the amplitude response increases while the slope of the linear part of the phase decreases due to the largest tune spread. For a current of 26 A, the width of the amplitude response in the vertical plane is reduced with respect to the horizontal plane as shown in Fig. 5.7, where the amplitude beam response in the horizontal and vertical plane are compared. The normalized beam emittance was $\epsilon = 2.0$µm in both planes therefore it is not the cause for the strong asymmetry observed in the BTF amplitude response. However, losses were observed for B1 in the vertical plane while increasing the octupole current.

The losses of B1 recorded by the Beam Loss Monitors (BLMs) [80] positioned at the primary collimators (TCPs) in IR7 [81] are shown in Fig. 5.8. The blue line represents the losses at the horizontal primary collimator, the green line at the skew primary collimator and the yellow line at the vertical collimator. The red dashed line represents the octupole current changes during the experiment. Beam losses are already visible for an octupole current of 13 A, they increase by one order of magnitude when the octupole current $I_{oct} = 26$A. In Fig. 5.8 losses at the horizontal and skew collimators are higher with respect to the signal at the vertical

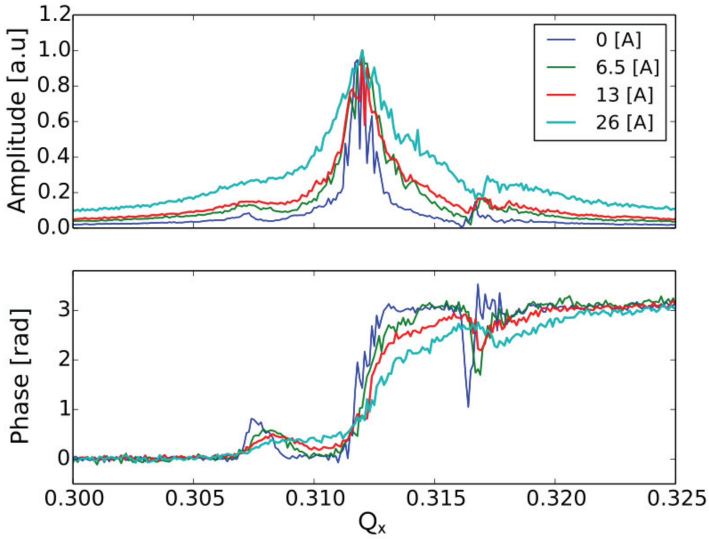

(a) Measured BTF amplitude and phase in the horizontal plane.

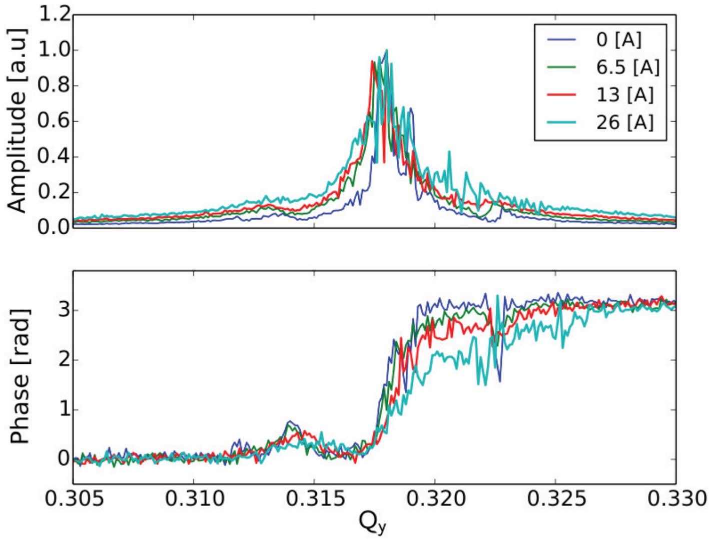

(b) Measured BTF amplitude and phase in the vertical plane.

Figure 5.6 – Measured BTF amplitude and phase for Beam 1 for different octupole currents at injection energy.

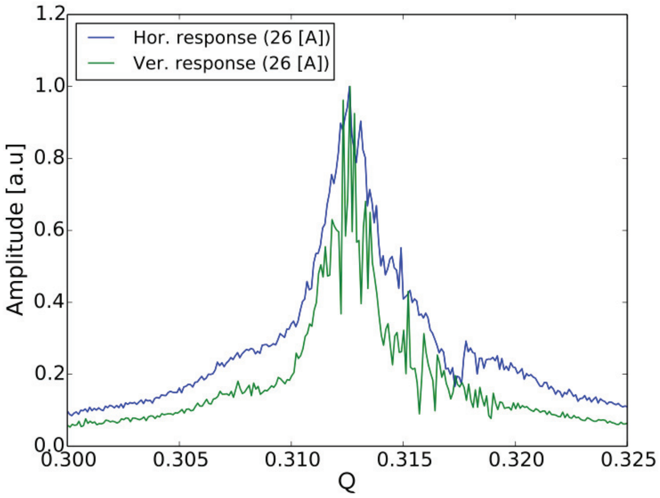

Figure 5.7 – Vertical and horizontal BTF amplitude at injection energy in presence of 26A octupole current.

collimator. This is a typical signature of vertical losses since the hadronic shower produced by the protons lost at the vertical collimator are recorded by the BLM of the horizontal and skew TCPs, which are located downstream of the vertical TCP collimators [81]. Due to the collision tunes at injection, $Q_x \sim 0.312$ and $Q_y \sim 0.318$, during the experiment an octupole current of 26A was already sufficient to bring the 5-6 σ particles on the 3rd order resonance. This effect is visible in the tune diagram in Fig. 5.9 computed using the MAD-X tracking module. However, such large amplitude particles cannot lead to a drastic reduction of the spread observed in a frequency range of $Q_y = (0.315 - 0.323)$. These frequencies correspond, instead, to the 0-3 σ particles in the vertical plane as shown in Fig. 5.10 where the dashed red lines display the betatron frequencies up to 3 σ particles. In addition, the observed tune spread reduction is only present in the vertical plane and not in both planes as may be expected from the tune footprint in Fig. 5.9. To find an explanation of this asymmetry in the BTF response, simulations with SixTrack tracking were carried out in order to evaluate the effects of the particle distribution that may lead to deformations in the BTF response.

The corresponding tune footprint from SixTrack is shown in Fig. 5.10 at injection energy, for an octupole current of 26A and a normalized beam emittance $\epsilon_{x,y} = 2.0\mu$m together with the projections of the frequency distributions in the horizontal and in the vertical plane. In this case, no asymmetry is visible between the two planes. As suggested by the non zero measured BTF response of the cross talk between the horizontal and vertical plane (Fig. 5.11), the linear coupling was not negligible at the moment of the measurements. Therefore, some linear coupling was included in the model. The SixTrack footprint including a linear global coupling in the simulated machine corresponding to a $|C^-| \approx 1.5 \times 10^{-3}$ is shown in Fig. 5.12 where a strong reduction of the frequency distribution in the vertical plane is then visible. The corresponding particle distribution in normalized action variables is shown in Fig. 5.13.

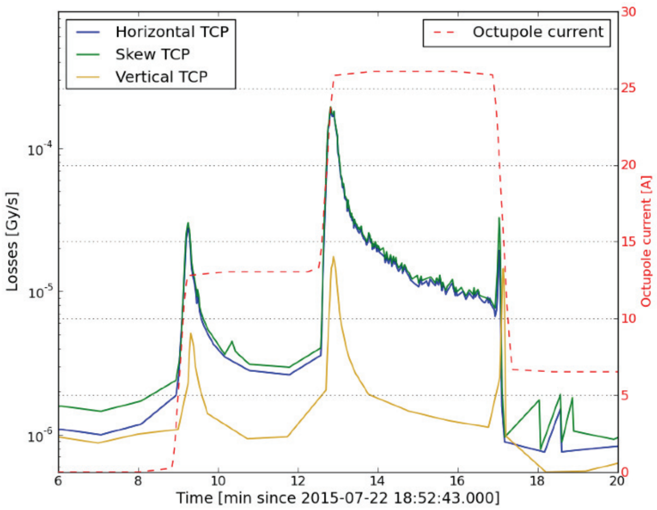

Figure 5.8 – Measured B1 losses at the primary collimators in IR7 during the octupole current scan at injection energy.

To evaluate the effect of the distribution on the computed dispersion integral, the tracked distribution in presence of linear coupling has been used in the computation of the stability diagram. The amplitude of the the complex dispersion integral is shown in Fig. 5.14 for the horizontal (red line) and the vertical plane (blue line) and an asymmetry between the two

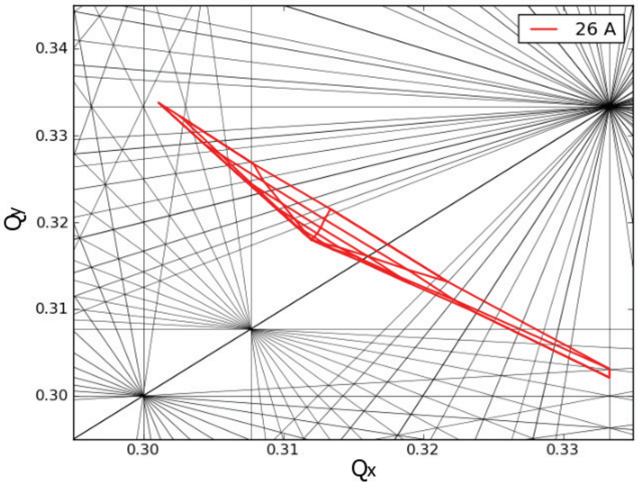

Figure 5.9 – Two dimensional detuning with amplitude (tune footprint) due to octupole magnets powered with a current of 26 A at injection energy (450 GeV) and a normalized beam emittance of $\epsilon = 2.0\,\mu\mathrm{m\,rad}$. Machine fractional tunes are set to $(Q_x = 0.312, Q_y = 0.318)$ as experimental conditions during the octupole scan at injection energy.

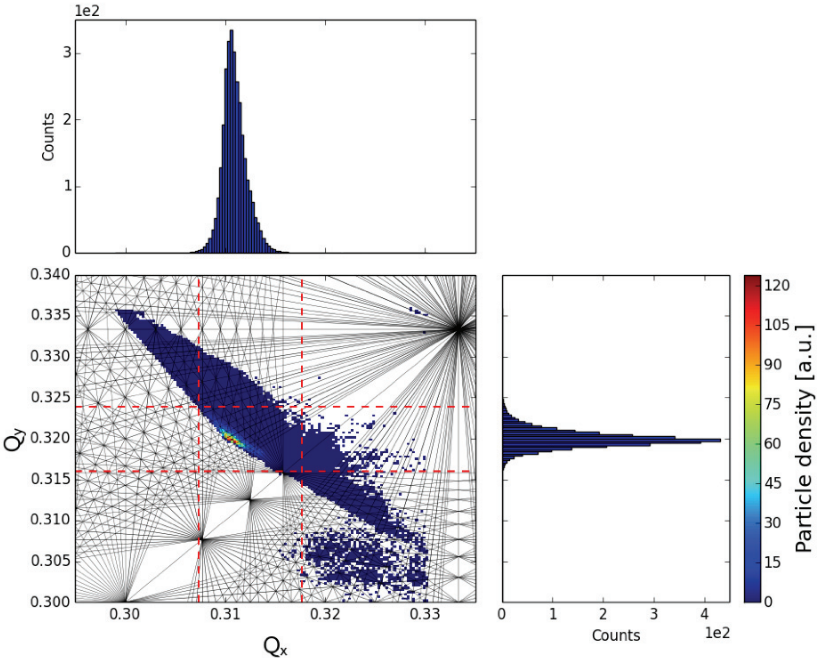

Figure 5.10 – Two dimensional detuning with amplitude (up to 6 σ particles) due to octupole magnets powered with 26A. Projections of the vertical and horizontal plane are shown. The dashed red lines display the extremum betatron frequencies up to 3 σ particles.

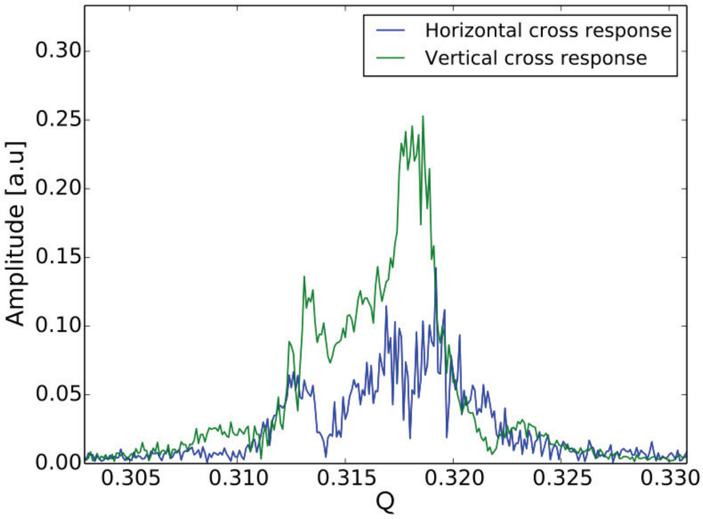

Figure 5.11 – Cross amplitude between the horizontal and the vertical BTF at injection in presence of 26A octupole current.

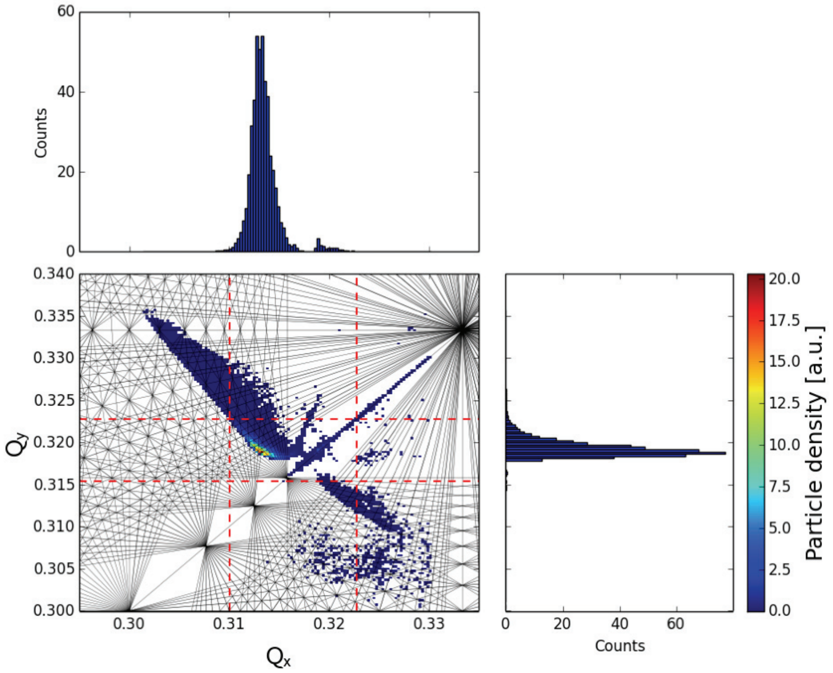

Figure 5.12 – Two dimensional detuning with amplitude (up to 6 σ particles) due to octupole magnets powered with 26A and linear coupling ($C^{-} \approx 1.5 \times 10^{-3}$). Projections of the vertical and horizontal plane are shown. The dashed red lines display the extremum betatron frequencies up to 3 σ particles.

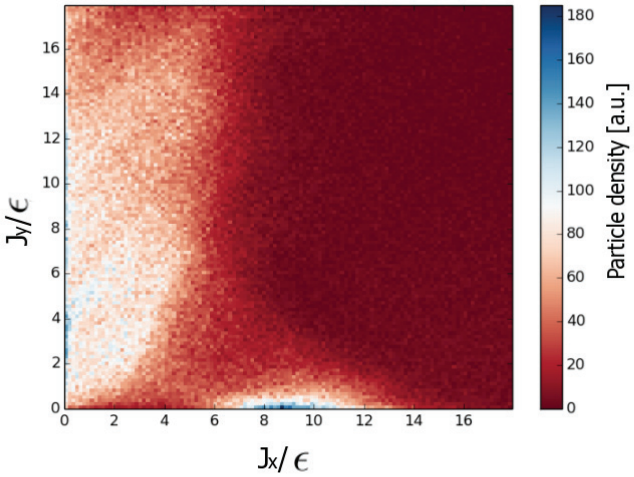

Figure 5.13 – Particle distribution tracked for 10^6 turns in presence of linear coupling and octupole detuning with amplitude, the color bar represents the particle density.

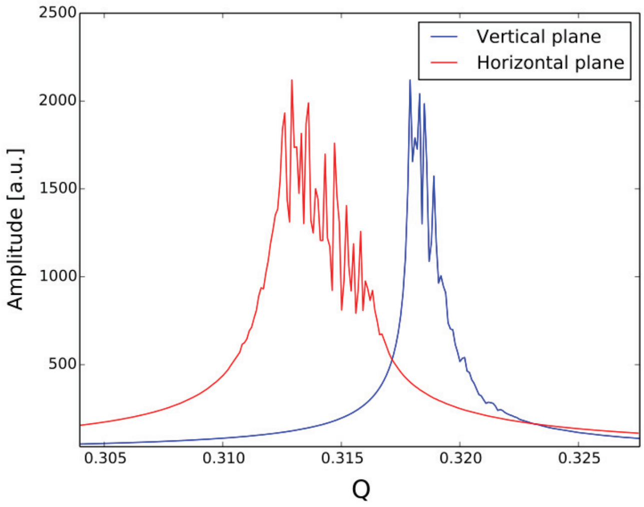

Figure 5.14 – Amplitude of the complex dispersion integral as a function of the frequency obtained by tracked distributions in presence of linear coupling ($C^- \approx 1.5 \times 10^{-3}$) and octupole magnets powered with 26 A at injection energy.

planes is now visible. By applying the fitting parameterization in Eq. 5.1, it is possible to compare the measured tune spread to the analytical expectations by using the tune spread factor p_1. Table 5.1 summarizes the results of the comparison with respect to the analytical reference case with an octupole current of $I_{oct} = 6.5$A. By looking at the results given by the fit of the data in Tab. 5.1, a larger spread was measured both in the horizontal and vertical plane with respect to expectations. For the case with an octupole current of 0 A an equivalent octupole currents of ≈ 5.72 A and ≈ 5.23 A in the horizontal and vertical plane respectively was found. The discrepancy between the measured spread with 0 A octupole current and the predicted one is consistent with expectations of non linear errors from the magnets [82]. Octupole currents of ≈ 11.8 A and ≈ 12.0 A were found for the 6.5 A case, while for the case of 26 A the asymmetric response between the vertical and the horizontal plane is also reflected by the results of the fitting function. Figure 5.15 shows the fitted tune spread factors as a function of the octupole current. The blue dots represent the BTF measurements in the horizontal plane while the green dots are the measurements in the vertical plane. The solid black line represents the tune spread factor expected from the models with respect to the analytical reference case with an octupole current of $I_{oct} = 6.5$A. The red shadow represents the model expectations where an additional spread of ≈ 5.5 A, corresponding to the case for an octupole current $I_{oct} = 0$A, was applied with an uncertainty of ±10% on the emittance value. For a current $I_{oct} = 0$A and $I_{oct} = 6.5$A the behavior in the horizontal and vertical plane is very similar and comparable to expectations (red shadow). For a current $I_{oct} = 13$A the measured tune spread in the vertical plane starts to deviate from expectations and for a current $I_{oct} = 26$A a larger spread is observed in the horizontal plane and a smaller one in the vertical plane for which losses were observed during the experiment (Fig. 5.8). Because of the diffusive mechanisms in the vertical plane, together with the cut of the frequency distribution in the

Table 5.1 – Tune spread factors for different octupole currents at injection energy. The tune spread factors are evaluated with respect to the semi-analytical reference case with an octupole current of $I_{oct} = 6.5$A.

I_{oct}[A]	B1 H p_1	B1 V p_1
0	0.88	0.82
6.5	1.81	1.85
13	2.68	2.37
26	5.3	3.61

same plane (Fig. 5.13) due to effect of the linear coupling, the increase of the octupole current (and therefore the increase of the tune spread in the beams) does not provide a larger Landau damping in this plane, that is actually reduced compared to the expectations.

5.2.1 Effect of chromaticity on the reconstructed stability diagram

For the case with the octupole current of 6.5 A, the stability diagram from BTF measurements was reconstructed from the amplitude and phase response shown in Fig. 5.16. The corre-

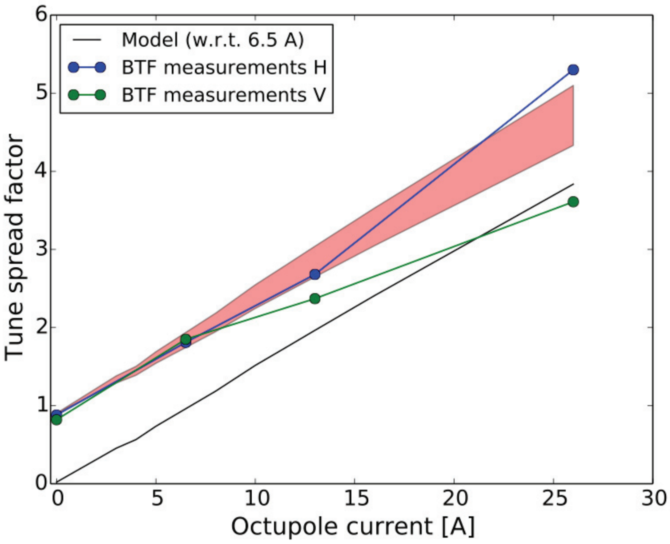

Figure 5.15 – Tune spread factors evaluated from the fitting function applied to the BTF measurements at injection energy for different octupole currents. The blue dots represent the BTF measurements in the horizontal plane while the green dots are the measurements in the vertical plane. The solid black line represents the factors expected from the model with respect to the reference case with an octupole current of $I_{oct} = 6.5$A. The red shadow represents the model expectations where an additional spread of ≈ 5.5 A (corresponding to the case for an octupole current of 0 A), was applied with an uncertainty of ±10% on the emittance value.

sponding stability diagram is plotted in Fig. 5.17. The blue dots correspond to measurements, the black line is the fit computed from Eq. 5.1 using as analytical reference case the dispersion integral computed by the PySSD code for an octupole current of 6.5 A. The measurements are compared with COMBI simulations for an octupole current of ≈ 11.8A as suggested by the corresponding tune spread factor $p1 = 1.81$ in Tab. 5.1. The loop appearing in the measured stability diagram due to the chromaticity is reproduced in COMBI with a chromaticity $Q' \approx 5$

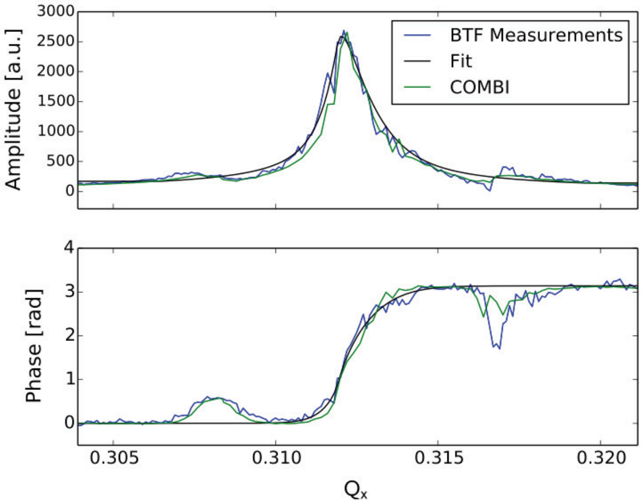

Figure 5.16 – Measured amplitude and phase (blue line) and simulated BTF (green line) at injection energy in presence of 6.5A octupole current and a chromaticity $Q' \approx 5$ units.

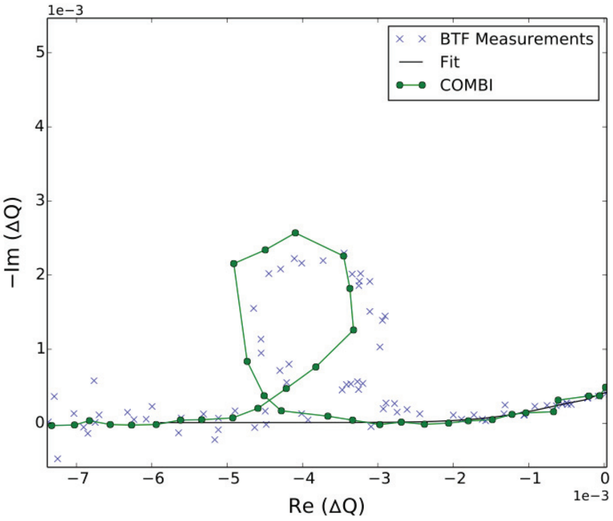

Figure 5.17 – Reconstructed stability diagram from BTF measurements (blue crosses) compared to semi-analytical 2D dispersion integral (black line) and multi-particle 3D model (green line) at injection energy in presence of 6.5 A octupole current and a chromaticity $Q' \approx 5$ units.

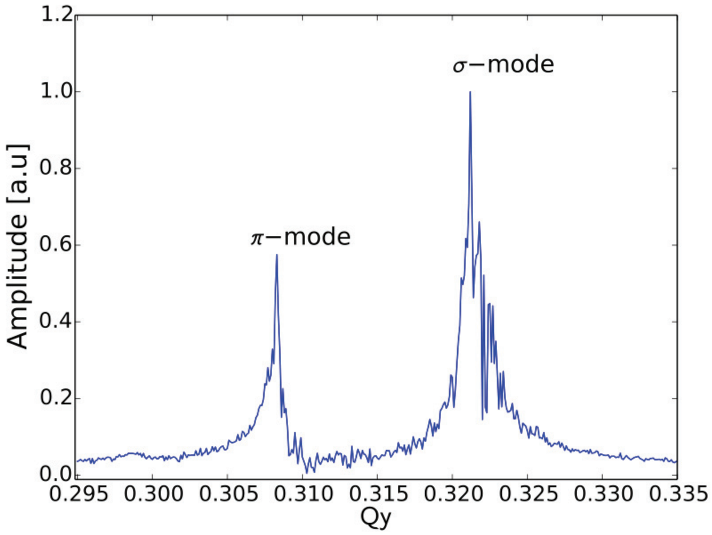

Figure 5.18 – Measured BTF amplitude in the vertical plane of Beam 1 with colliding beams. The coherent beam-beam σ and π modes are visible in the amplitude response.

units corresponding to the experimental conditions during the BTF measurements. This observation opens future perspectives on possible estimates of chromaticity for the COMBI to BTF comparisons.

5.3 Beam stability in presence of beam-beam interactions

Beam Transfer Function measurements were acquired at the end of the betatron squeeze for different values of the crossing angles in IP1 and IP5 and for different transverse beam separations at the two IPs. In the next paragraphs the experimental observations will be shown and the interpretation of the experimental results will be given, supported by the model expectations.

5.3.1 Measurements with head-on collision

Beam Transfer Function measurements were acquired with beams in head-on collision at injection and at top energy. Figure 5.18 shows the BTF amplitude response for colliding beams in IP1 and IP5. A single bunch per beam of nominal intensity was injected. Measurements were taken at injection energy with collision tunes. Table 5.2 summarizes the beam parameters at the moment of the BTF acquisitions together with the corresponding beam-beam tune shift of the coherent π-mode calculated by the beam-beam parameter, ξ_{bb} as: $\Delta Q \simeq 2 \cdot Y \cdot \xi$ where Y is the Yokoya factor and for Gaussian beams it is equal to $Y = 1.21$ [24]. The expected beam-beam tune shift for B1 in the vertical plane was $\Delta Q \approx -0.0131$, which corresponds to the measured distance between the π-mode and σ-mode, both visible in the vertical BTF

Table 5.2 – Beam parameters during BTF measurements on colliding beams at injection energy.

Beam	**Intensity** 10^{11} [p/b]	**H. Emit.** [μm rad]	**V. Emit.** [μm rad]	ΔQ ($\simeq 2\cdot Y\cdot\xi$)	ΔQ_{meas} (B1 V BTF)
B2	0.991	2.01	2.23	$-1.31\cdot 10^{-2}$	$-1.29\cdot 10^{-2}$

response (Fig. 5.18) giving $\Delta Q_{meas} = -1.29\cdot 10^{-2}$. After few minutes since the BTF excitation, an instability occurred, first in B1 and afterwards in B2, characterized by a fast emittance blow up in both planes. The emittances increased by a factor 1.4 and 1.5 in the horizontal plane of B1 and B2 respectively and by a factor 3.2 and 3.18 in the vertical plane of B1 and B2 respectively.

The instability was most probably due to the excitation of the coherent π-mode through the BTF excitation since the transverse feedback was switched off on both beams during the measurements. The coherent π-mode excitation is well visible in the spectrum of B1 in Fig. 5.19 at the betatron frequency ≈ 0.308 corresponding to the frequency of the π-mode visible in the BTF amplitude response in the vertical plane of B1 shown in Fig. 5.18. The presence of the coherent beam-beam modes may lead to beam instabilities during the BTF excitations with colliding beams and in addition they make difficult the reconstruction of the stability diagrams from the measurements. For these reasons when taking BTF measurements with beams in collision the experimental setup was adjusted in order to suppress these modes. This was achieved by keeping on the transverse feedback for the beam not used for BTF

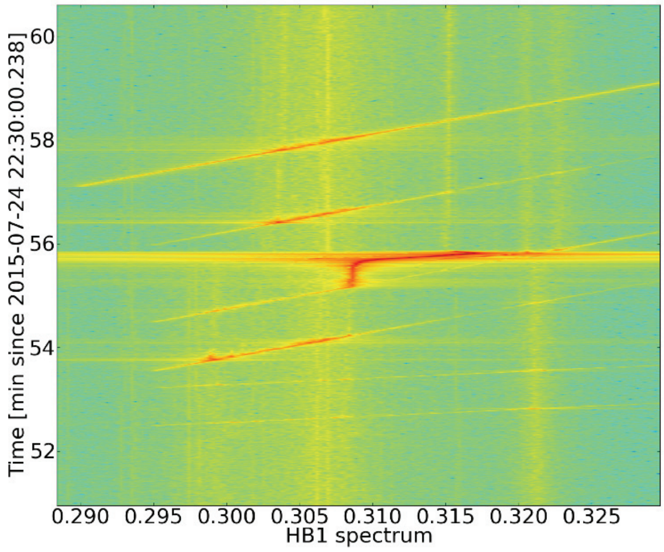

Figure 5.19 – BBQ spectrogram for Beam 1 in the horizontal plane with beams in collisions. The BTF excitations correspond to the diagonal red lines in the spectrogram.

Table 5.3 – Normalized full parallel separation in IP1 and IP5 during parallel separation scan with beams in collision.

Sep IP1 [σ]	**Sep IP5** [σ]
0.3	0.086
0.87	0.52
1.2	0.76
1.37	1.0
1.6	1.26
1.83	1.52
2.16	2.0
3.96	4.7

measurements and by breaking the symmetry of the intensities of the colliding bunches (weak-strong regime) [83]. Beam Transfer Function measurements in presence of head-on collisions with a transverse beam separation will be discussed in the next section.

5.3.2 Separation scan at the IPs

BTF measurements were acquired with beams in collisions during a parallel separation scan at the IPs. During the experiment, a train of 48 nominal bunches was injected in B1 while a single lower intensity bunch was injected in B2 to suppress the coherent beam-beam modes in the BTF response [83]. In this configuration the single bunch in B2 experiences 48 long range beam-beam interactions and two head-on collisions as during the operations. The transverse feedback was turned off for the single bunch in B2 for which BTF measurements were acquired. First, the two beams were put into collision in IP1 and IP5 and after the optimization of the IPs, the beams were separated in steps with a maximum parallel separation of $d \approx 5.0\ \sigma$. From the luminosity values published by ATLAS in IP1 an CMS in IP5 it was possible to estimate the parallel separation in the two IPs in units of r.m.s. beam size using Eq. 1.43. Figure 5.20 shows the normalized luminosity recorded by ATLAS and CMS during the separation scan together with the full parallel separation d at both IPs, also summarized in Tab. 5.3 for each separation step during the experiment. The normalized emittances during the experiment are summarized in Tab. 5.4 both for B1 and B2.

BTF measurements with different parallel separations at the IPs are presented in Fig. 5.21 both in the horizontal plane (left plot) and in the vertical plane (right plot). The beam-

Table 5.4 – Normalized beam emittances at the end of squeeze for Fill 1 and Fill 2 .

	Beam 1 (H) [µm rad]	Beam 1 (V) [µm rad]	Beam 2 (H) [µm rad]	Beam 2 (V) [µm rad]
Fill 2	2.6	2.4	3.3	1.9

beam parameters in the horizontal and the vertical plane, calculated by using Eq. 1.29, are $\xi_x = 6.77 \times 10^{-3}$ and $\xi_y = 7.33 \times 10^{-3}$ respectively, considering the experimental conditions for the partner bunch of the head-on collision in B1 with a normalized emittances of $\epsilon_x = 2.6\mu$m and $\epsilon_y = 2.4\mu$m and a bunch intensity of $I_b = 1.4 \times 10^{11}$ p/bunch. During the experiment, the pilots bunches were unwillingly left in the beams. In this case the BTF response is the sum of the two complex signals from both bunches and the extrapolation of the signal for a single bunch to reconstruct the stability diagram is therefore complicated. From the fixed coherent

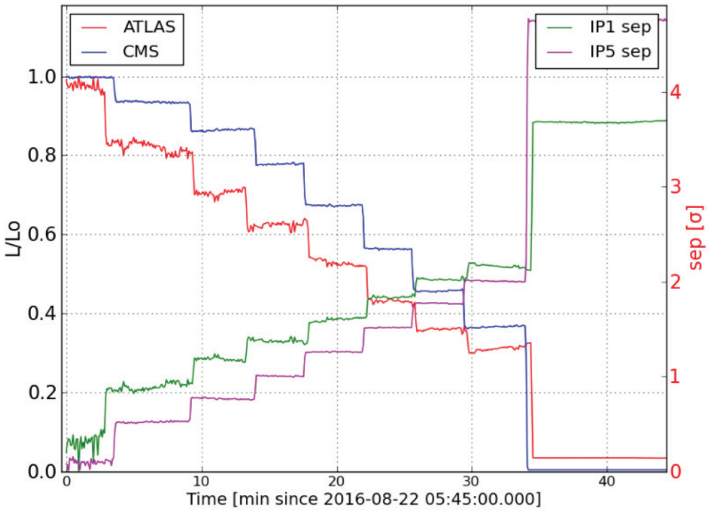

Figure 5.20 – Normalized luminosity recorded by ATLAS and CMS during the separation scan in IP1 and IP5.

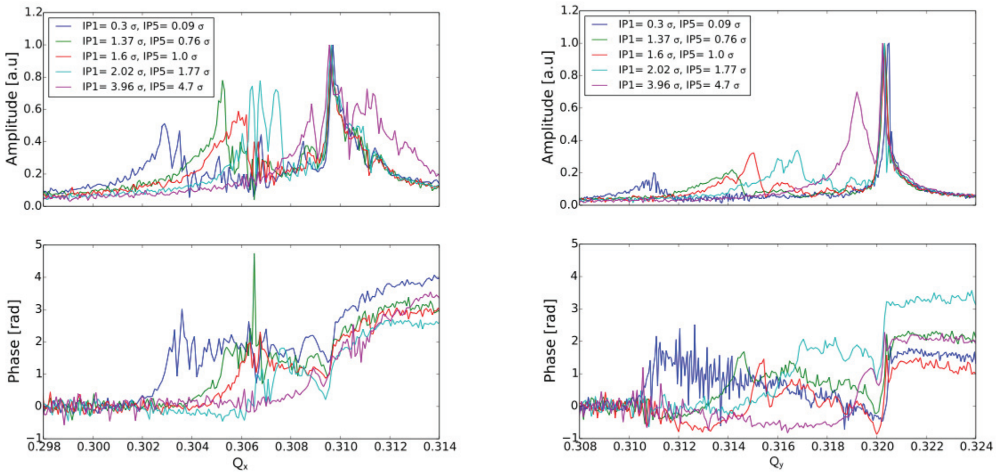

(a) BTF response in the horizontal plane.

(b) BTF response in the vertical plane.

Figure 5.21 – Measured BTF for Beam 2 for different parallel separations in IP1 and IP5.

tune of the pilot bunch that was not colliding, we measured the tune shift of the colliding bunch of B2. The measured tune shift at each step, normalized to the the maximum tune shift after the IP optimizations, are shown in Fig.5.22 for both the horizontal (left) and the vertical plane (right).The solid black lines correspond to the expected luminosity reduction due to a parallel offset at the IPs and in presence of a crossing angle ($\alpha_c = 370\,\mu\text{rad}$) [30].

The measurements are compared to COMBI simulations (red dashed line for the horizontal plane and blue dashed line for the vertical plane) showing good agreement with expectations. The separations left after the IP optimizations, (0.3 σ in the horizontal plane of IP1 and 0.086 σ in the vertical plane of IP5) ware considered as an error on the measured separation.The resolution of the BTF measurements was used as the error on the measured normalized tune shift.

The measured stability diagrams with full head-on collisions (dotted blue line) and with separated beams (dotted red line) with $d = 3.96\,\sigma$ in IP1 and $d = 4.7\,\sigma$ in IP5, are shown in Fig. 5.23 where the Savitzky-Golay [84] filter was applied to the amplitude and phase responses in order to remove the signal noise. The measured BTF amplitude and phase are shown in Fig. 5.24 with full head-on (blue line) and with separated beams (red line), the black lines corresponds to the smoothed data after the application of the filter during the post processing. The value of the stability diagrams are in arbitrary units due to the missing BTF calibration factor. A reduction of the stability area is observed with separated beams with respect to the fully head-one case. However the noise of the signal and the presence of the pilot bunches unwillingly left in the beams makes difficult the interpretation of the measurements and the comparison with the models by means of the fitting function in Eq. 5.1. With a full head-on collision, an increase of a factor 5 on the stability diagram is expected from the models with respect to the case with separated beams, while from measurements only an increase by a factor 2.2 is observed.

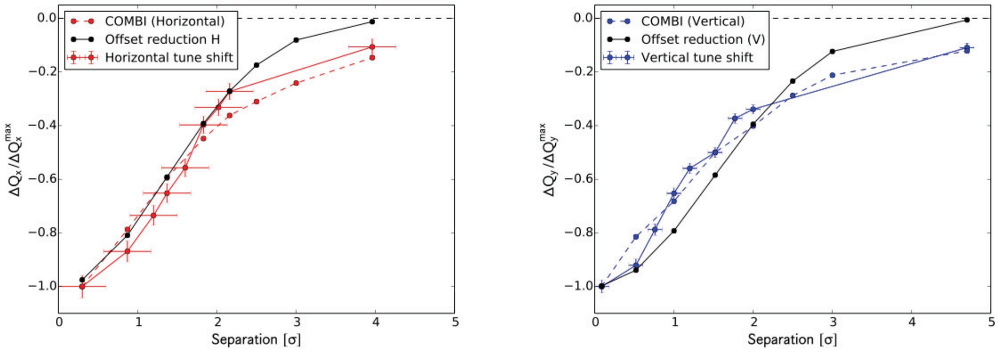

(a) Horizontal plane.

(b) Vertical plane.

Figure 5.22 – Measured tune shifts from BTF measurements during the parallel separation scan in IP1 and IP5. The tune shifts are normalized to the maximum tune shift observed in each plane.

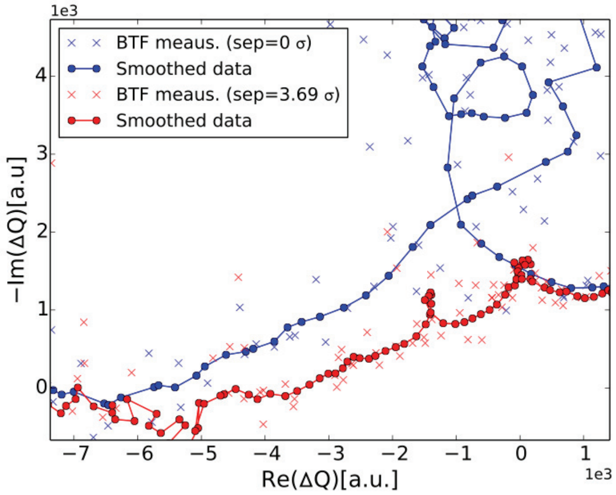

Figure 5.23 – Stability diagrams reconstructed from BTF measurements in the horizontal plane with full head-on collision (blue crosses) and with a parallel separation of 3.69 σ (red crosses). For the reconstruction of the stability diagram the Savitzky-Golay filter was applied to the data to remove signal noise in the measurements (dotted lines).

5.3.3 Crossing angle scan at the end of the betatron squeeze

In order to investigate the effects of long range beam-beam interactions on the transverse beam stability, a crossing angle scan in IP1 and IP5 was performed at the end of the betatron squeeze for the LHC 2016 configuration with $\beta^* = 40\,\text{cm}$ and Landau octupole magnets powered with a current $I_{\text{oct}} = 470\,\text{A}$ and positive polarity. Table 5.5 summarizes the normalized long range beam-beam separation at the first encounter Eq. 1.30 for the angular steps used during the experiment. The long range beam-beam separation was calculated considering a normalized beam emittance of $\epsilon \approx 1.8\,\mu\text{m}\,\text{rad}$ in both planes, corresponding to the experimental conditions of the beams. Measurements were acquired on the single bunch injected in Beam 1 with an intensity of $I_{B1} = 6.22 \times 10^{10}\,\text{p/bunch}$ while no BTF measurements were acquired on Beam 2, where a train of 48 bunches of nominal intensity $I_{B2} = 1.2 \times 10^{11}\,\text{p/bunch}$ was injected. In this configuration the low intensity bunch will undergo the whole set of beam-beam interactions as during Physics fills (36 long range beam-beam interactions and 2 head-on collisions), while the train stays unperturbed. The transverse feedback is switched off on the single measured bunch. The weak-strong configuration between the bunches avoids coherent beam-beam responses [83]. Figure 5.25 shows the measured amplitude and phase in the horizontal (Fig. 5.25a) and in the vertical plane (Fig. 5.25b) for the different crossing angles in IP1 and IP5. The angular changes occurred simultaneously at both IPs. An unexpected asymmetric beam response was observed between the horizontal and vertical planes. In particular, the vertical plane seems to be less affected by the long range beam-beam interactions in terms of tune spread with respect to the horizontal plane while decreasing the crossing angle as can be seen from the different amplitude widths and the phase slopes between the two planes. Figure 5.26

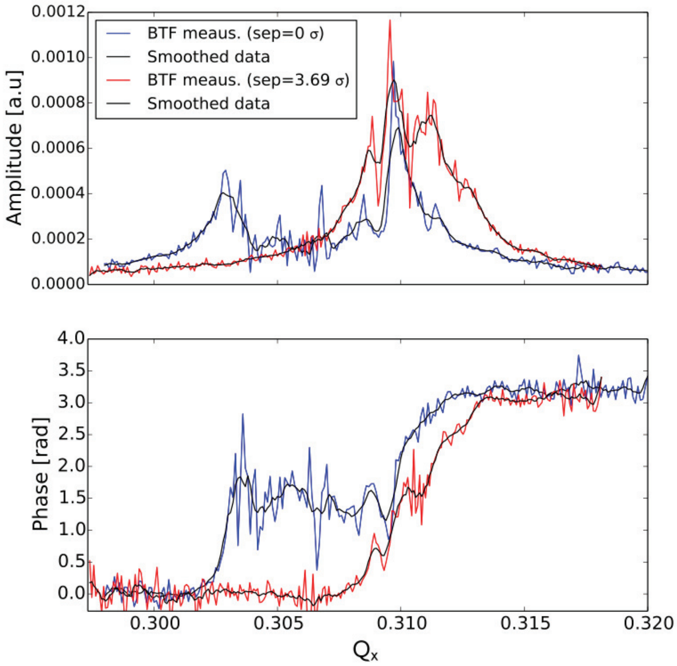

Figure 5.24 – Measured amplitude and phase in the horizontal plane with full head-on collision (blue line) and with a parallel separation of 3.69 σ (red line). The corresponding stability diagrams are presented in Fig. 5.23 where the Savitzky-Golay filter was applied to the data to remove signal noise from measurements (black solid line).

shows the measured beam response at the end of the squeeze (the long range beam-beam separation is $d_{bb} \approx 14.5\,\sigma$) and with a reduced crossing angle $\alpha_c = 370\,\mu\text{m}$ ($d_{bb} \approx 10.6\,\text{sigma}$) compared both to the model expectations given by the computed amplitude and phase of the

Table 5.5 – Normalized long range beam-beam separation at the first encounter in units of the rms beam size for different crossing angles at the IPs during the experiment. Normalized beam emittance $\epsilon \approx 1.8\,\mu\text{m}\,\text{rad}$ in both planes.

Angle (α_c) [μrad]	**BB Long Range separation** [σ]
370	14.5
340	13.3
310	12.2
290	11.4
270	10.6
250	9.8
230	9.0
210	8.2

complex dispersion integral. As visible, a larger tune spread than predicted is measured in the horizontal plane and a smaller spread than predictions is measured in the vertical plane. An important increase in the vertical tune spread is observed for the crossing angle of 230 µrad (Fig. 5.25) that, is smaller than the beam response in the horizontal plane. This increase in the vertical tune spread exhibits a dependency on the tune frequency as revealed by the vertical tune scan performed during the experiment and shown in Fig. 5.27. The amplitude response is plotted for different values of the vertical tunes, keeping a constant crossing angle of 230 µrad. The blue line corresponds to the first acquisition of the BTF while the green line correspond to

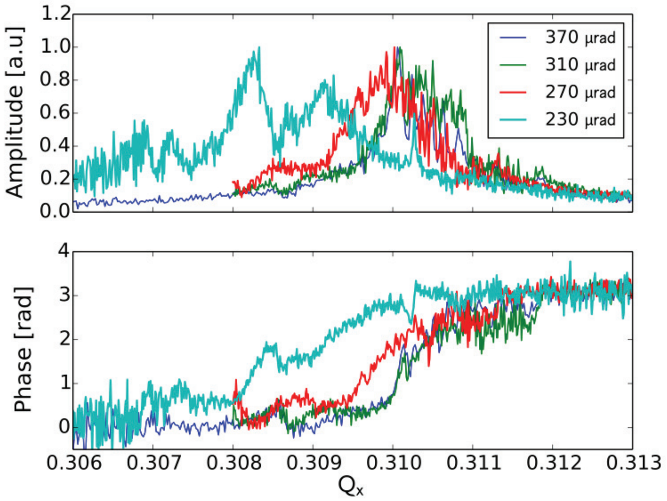

(a) BTF amplitude and phase response for B1 in the horizontal plane.

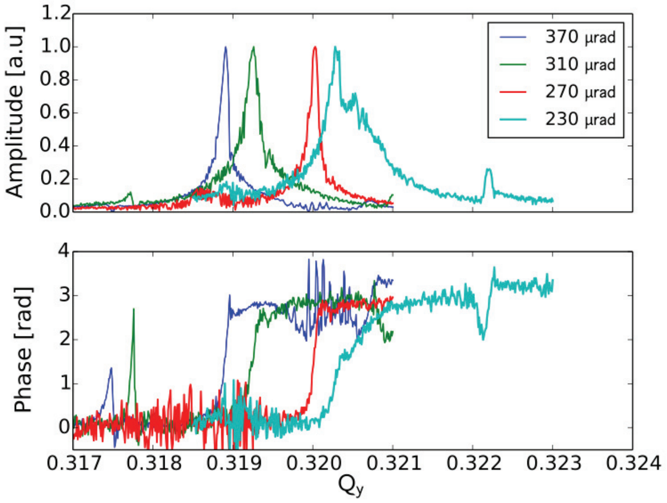

(b) BTF amplitude and phase response for B1 in the vertical plane.

Figure 5.25 – Measured BTF for Beam 1 for different crossing angles in IP1 and IP5 simultaneously changed in both the IPs.

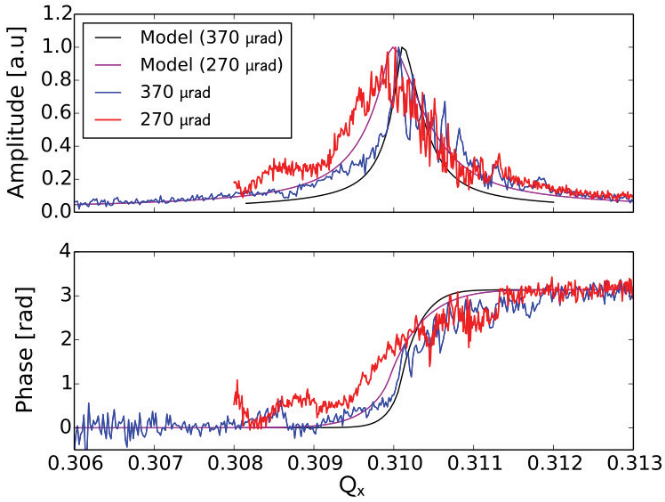

(a) BTF amplitude and phase response for B1 in the horizontal plane and compared to model expectations.

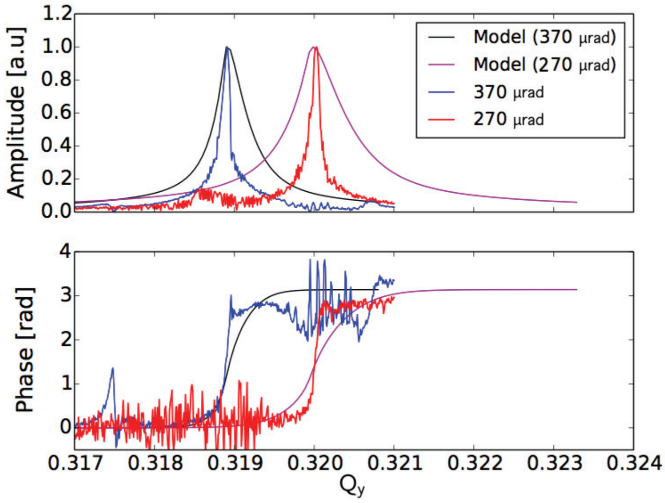

(b) BTF amplitude and phase response for B1 in the vertical plane and compared to model expectations.

Figure 5.26 – Measured BTF amplitude and phase response for Beam 1 at the end of the squeeze ($\alpha_c = 370\mu\text{m}$) and for a reduced crossing angle ($\alpha_c = 270\mu\text{m}$) in IP1 and IP5. The BTF response is compared to the model expectations (black and pink lines) for both the angles used.

the BTF amplitude with a shift of the vertical tune of $\Delta Q = -0.001$. For this case, a reduction of the vertical tune spread is observed in the BTF response. The initial BTF amplitude shape is fully recovered by restoring back the vertical tune value with a shift of $\Delta Q = +0.001$ (red line). During the crossing angle scan an unexpected tune shift as a function of the crossing angle was observed in both planes in opposite directions, larger in the vertical plane than the

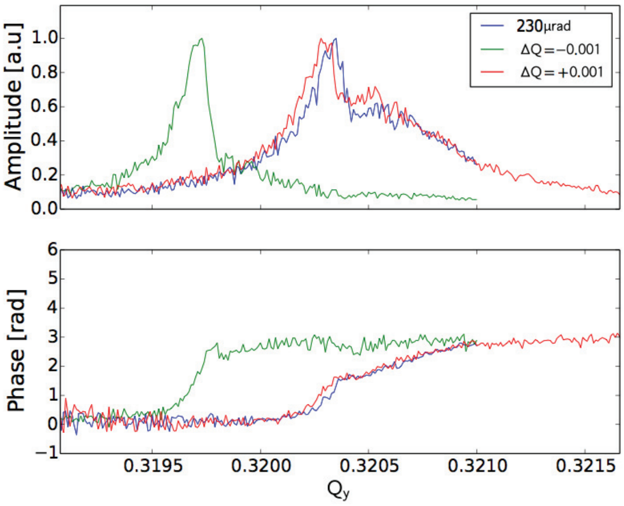

Figure 5.27 – BTF response in the vertical plane of B1 for a crossing angle of 230 μrad for different vertical tune values. The blue line corresponds to the first acquisition of the BTF while the green line corresponds to the BTF amplitude with a shift of the vertical tune of $\Delta Q = -0.001$. The initial BTF amplitude shape is fully recovered by restoring the initial vertical tune value (red line).

horizontal plane. In order to evaluate the spread in the machine and compare measurements with expectations, some fits of the data were performed following the parameterization in Eq.5.1. As reference, the analytical form of the amplitude and phase responses was computed by using the PySSD where the tune spread only for Landau octupole was considered. An octupole current of $I_{oct} = 470\,\mathrm{A}$ with positive octupole polarity (as during the experiment and operations) was used, considering a normalized beam emittance of $\epsilon = 1.8\,\mu\mathrm{m\,rad}$. An example of the fit from the measured BTF response is shown in 5.28, where the blue line represents the BTF data at the end of the betatron squeeze ($\alpha_c = 370\,\mu\mathrm{m}$) for Beam 1 in the horizontal plane while the black one is the result of the fit (Eq.5.1). From the fitting function it is possible to obtain an information on the tune shift and on the tune spread in the beams during the crossing angle reduction. The vertical BTF measured response with the corresponding fit function are shown in Fig.5.29. In this case the fit function overestimates the vertical tune spread: a sharp peak is observed in the measured amplitude response and the slope of the phase response is steeper than the fitted one. Thus, in order to reproduce the correct detuning with amplitude in the vertical plane other mechanisms should be included in the model.

The results of the parameterization for all the crossing angles taken during the experiment are summarized in Fig. 5.30. In the horizontal plane, at the end of the betatron squeeze with a crossing angle of 370 μrad, the BTF measures a tune spread larger by a factor 5 compared to the reference case. The horizontal tune spread increases as a function of the crossing angle up to a factor ≈10 for the smallest crossing angle used of 210 μrad. In the vertical plane the information of the tune spread is overestimated but it is still smaller compared to the

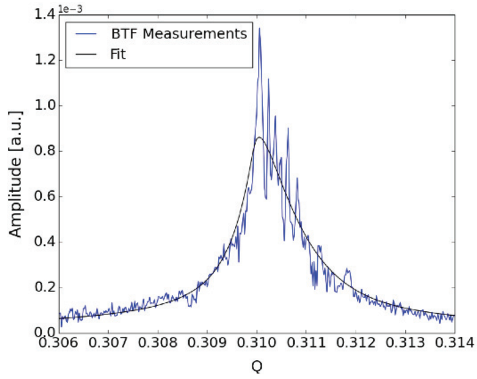

(a) Amplitude.

(b) Phase.

Figure 5.28 – Measured BTF for Beam 1 at the end of the betatron squeeze in the horizontal plane.

expectations (as already shown in Fig. 5.29) and to the tune spread measured in the horizontal plane. In addition, the vertical tune spread is shown to be less sensitive to the crossing angle reduction. Possible explanations of this asymmetric behavior between the horizontal and vertical planes will now be discussed.

A larger tune shift is observed in the vertical plane compared to the horizontal plane (Fig. 5.30). A maximum tune shift $\Delta Q_y \approx 2.4 \times 10^{-3}$ is observed in the vertical plane while $\Delta Q_x \approx 2.0 \times 10^{-3}$ in the horizontal plane for the smallest crossing angle used ($\alpha_c = 230\,\mu\text{rad}$). A possible explanation of the observed tune shift as a function of the crossing angle is the breaking of the horizontal-vertical passive compensation of the long range beam-beam tune shifts [14]. If the strength of long range beam-beam interactions is different in one of the two IPs, it will result in a tune shift in the plane of the long range beam-beam interactions. For this case we compare the expected tune shifts as a function of the crossing angle where an asymmetry in

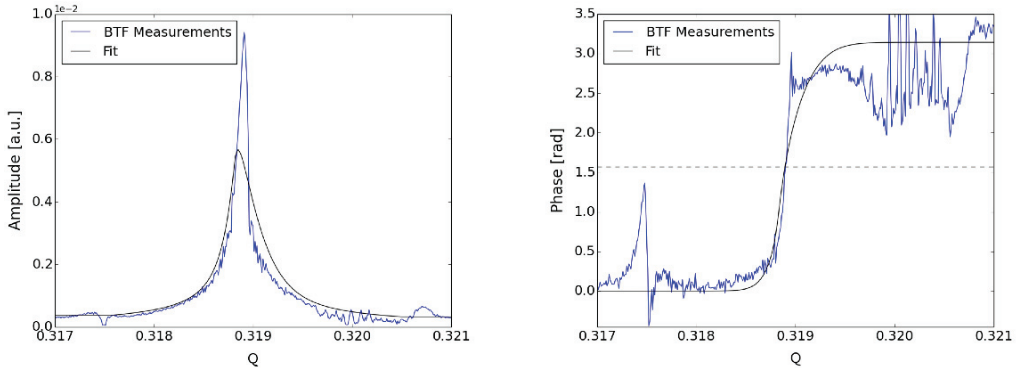

(a) Amplitude.

(b) Phase.

Figure 5.29 – Measured BTF for Beam 1 at the end of the betatron squeeze in the vertical plane.

the IP1 and IP5 crossing angle of 30% was applied (black solid line).

Figure 5.31 shows the measured long range beam-beam contribution factor (as a percentage with respect to the end of the betatron squeeze with $\alpha_c = 370\,\mu\text{rad}$) as a function of the long range beam-beam separation for each crossing angle used. The long range beam-beam contribution factor was deduced by applying the parameterization to the BTF measurements in the horizontal plane (blue line) and in the vertical plane (red line), through which the stability diagram was reconstructed for each angle. The measured long range beam-beam contribution was expressed as the ratio of the half height of the reconstructed stability diagram for each angle change with respect to the half height of the stability diagram reconstructed at the end of the betatron squeeze. The black line represents the model expectations as a function of the crossing angle. For long range beam-beam separations larger than 11.5 σ, a larger impact of the long range beam-beam contribution in terms of stability diagram is observed in the horizontal plane compared to the expectations. For long range beam-beam separation smaller than 11.5 σ, the expectations are larger compared to the measured long range beam-beam contribution. An increase of the long range beam-beam contribution of $\approx$ 90% is observed in the horizontal plane at the smallest beam-beam separation. In the vertical plane the tune spread increases reaching a value of $\approx$ 130% with respect to the initial case at the end of the betatron squeeze. As shown in Fig. 5.27, where the vertical BTF response is plotted during a tune scan in the vertical plane for a fixed crossing angle of $\alpha_c = 230\,\mu\text{rad}$, there is a strong dependency of the measured tune spread on the tune values. A variation of the tune $\Delta Q_y = -0.001$ reduces the tune spread in the vertical plane by a factor $\approx$ 3.25%

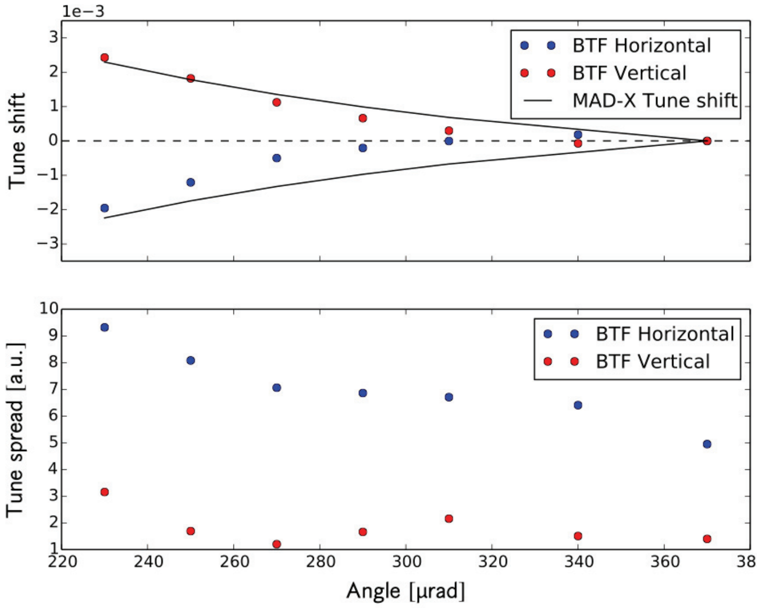

Figure 5.30 – Horizontal and vertical tune spread and tune shifts during the crossing angle scan at the end of squeeze for Beam 1 from fitted BTF data.

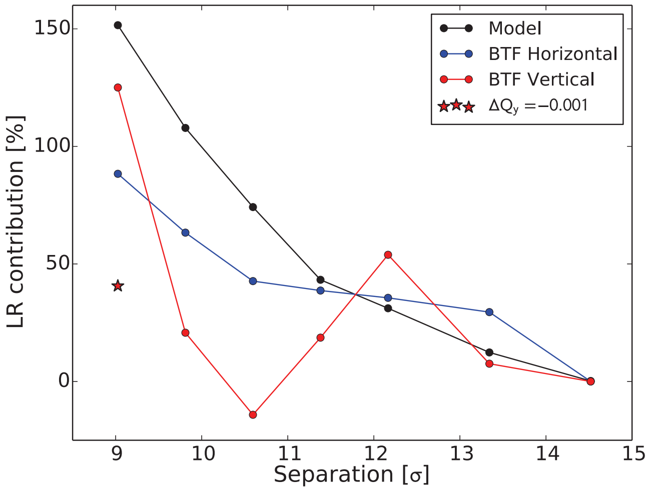

Figure 5.31 – Measured long range beam-beam contribution to the stability diagram as function of the crossing angle (blue line) compared to the model expectations (black line). The long range beam-beam contribution is expressed (as a percentage) as the ratio between the half height of the stability diagram for each angle and the half height of the stability diagram at the end of the betatron squeeze.

(red star in Fig. 5.31) with respect to the crossing angle case with $\Delta Q_y = +0.001$, represented by the last point of the dotted red line in Fig. 5.31. In order to investigate the effects of the crossing angle changes on the particle distribution, and consequently on the stability diagram, particle distribution of $5 \times 10^5 - 10^6$ were tracked for 10^6 turns. Figure 5.32 shows the tracked distributions in normalized action variables (J_x, J_y) as a function of the crossing angle α_c (left plots) and the corresponding stability diagrams (right plots) computed from the extended PySSD code using the tracked distributions in presence of the accelerator lattice elements, beam-beam elements and Landau octupole for different crossing angle configurations. The blue lines correspond to the computed stability diagram in the horizontal plane from the tracked distribution while the red lines represent the vertical plane. For comparison the computed stability diagrams using an unperturbed Gaussian distribution in the horizontal (solid black line) and in the vertical plane (dashed black line) are shown in the same picture. With the reduction of the crossing angle the overall tune spread increases giving as result a larger stability area. However, any evident modifications in the computed stability diagrams from the tracked distribution are visible compared to the corresponding Gaussian cases. The effects of an asymmetric crossing angle in IP1 and IP5 were investigated to interpret the asymmetric BTF response between the horizontal and the vertical plane possibly due to an asymmetric distribution in the two planes arising from particle losses. The stability diagrams were computed from the tracked particle distribution reducing the crossing angle in IP1 (IP5) by 30% considering the following angles in IP5: 370 µrad (260 µrad), 270 µrad (189 µrad) and 230 µrad (161 µrad), used during experiment. The beams collide in IP1 in the vertical plane, therefore a reduction of the crossing angle in this IP increases the strength of the long

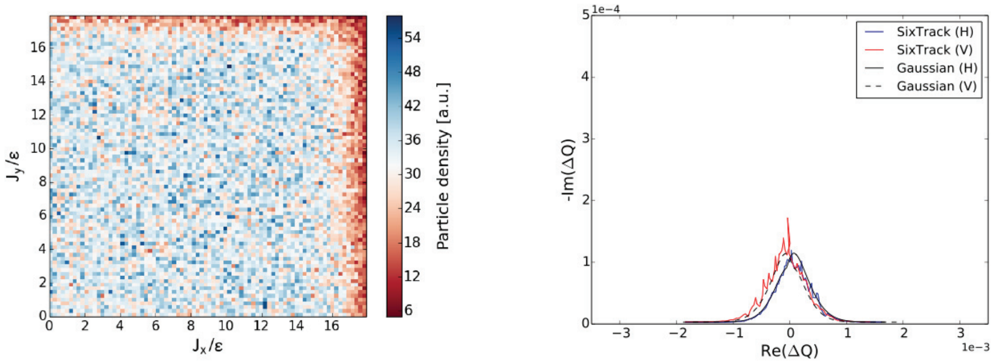

(a) Tracked particle distribution with $\alpha_c = 370\,\mu\text{rad}$ in IP1 and IP5.

(b) Stability diagram from tracked distribution with $\alpha_c = 370\,\mu\text{rad}$ in IP1 and IP5.

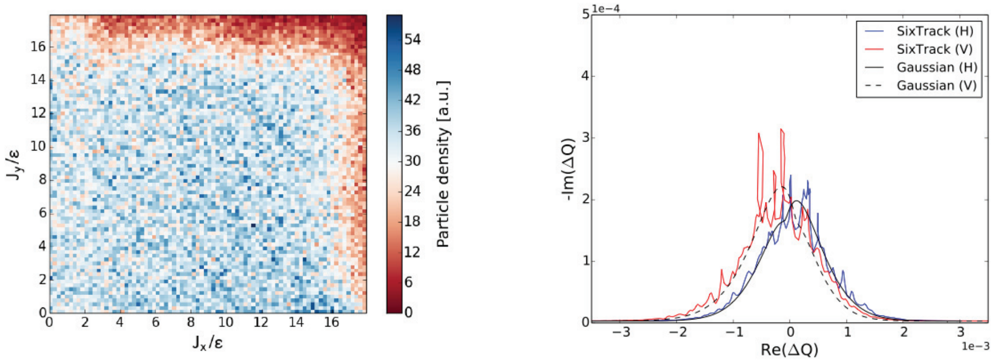

(c) Tracked particle distribution with $\alpha_c = 270\,\mu\text{rad}$ in IP1 and IP5.

(d) Stability diagram from tracked distribution with $\alpha_c = 210\,\mu\text{rad}$ in IP1 and IP5.

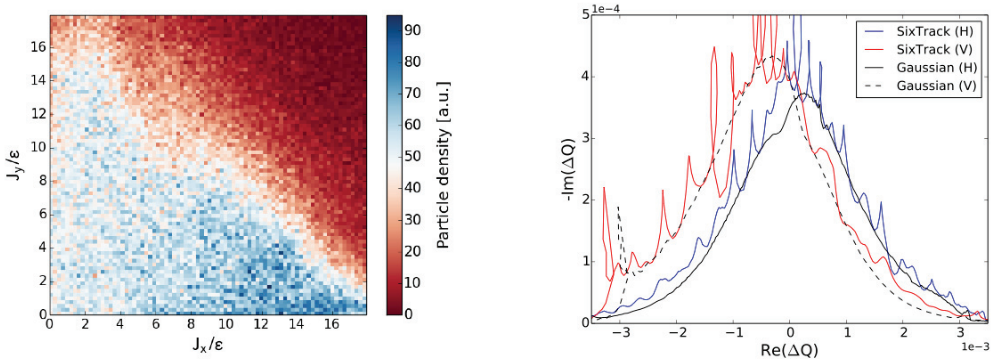

(e) Tracked particle distribution with $\alpha_c = 210\,\mu\text{rad}$ in IP1 and IP5.

(f) Stability diagram from tracked distribution with $\alpha_c = 210\,\mu\text{rad}$ in IP1 and IP5.

Figure 5.32 – Particle distribution from SixTrack tracking and corresponding stability diagrams for different crossing angles in IP1 and IP5 at the end of the betatron squeeze.

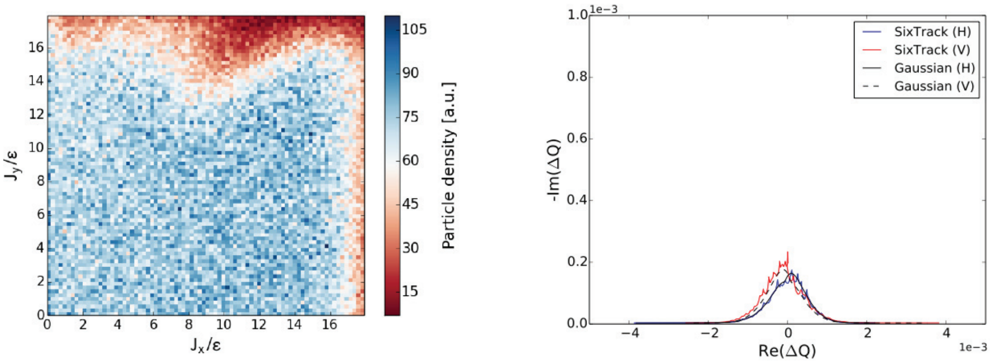

(a) Tracked particle distribution with $\alpha_c = 270\,\mu$rad in IP1 and $\alpha_c = 370\,\mu$rad in IP5.

(b) Stability diagram from tracked distribution with $\alpha_c = 270\,\mu$rad in IP1 and $\alpha_c = 370\,\mu$rad in IP5.

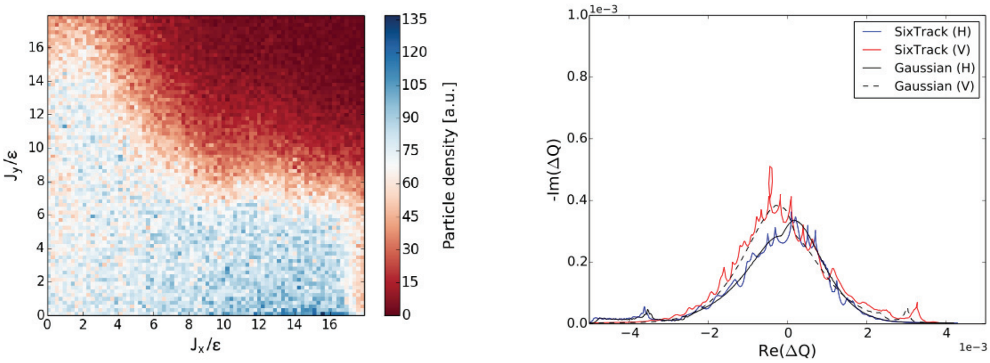

(c) Tracked particle distribution with $\alpha_c = 189\,\mu$rad in IP1 and $\alpha_c = 270\,\mu$rad in IP5.

(d) Stability diagram from tracked distribution with $\alpha_c = 180\,\mu$rad in IP1 and $\alpha_c = 270\,\mu$rad in IP5.

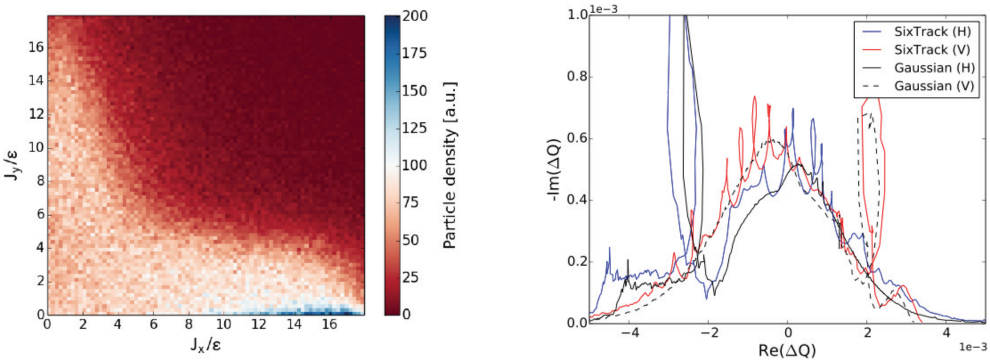

(e) Tracked particle distribution with $\alpha_c = 161\,\mu$rad in IP1 and $\alpha_c = 230\,\mu$rad in IP5.

(f) Stability diagram from tracked distribution with $\alpha_c = 161\,\mu$rad in IP1 and $\alpha_c = 230\,\mu$rad in IP5.

Figure 5.33 – Particle distribution from SixTrack tracking and corresponding stability diagrams at the end of the betatron squeeze for asymmetric crossing angles in IP1 (reduced crossing angle) and IP5.

range beam-beam interactions with likely consequent of particle losses in the corresponding plane because of the provoked tune shifts. This phenomena may affect the stability diagram, causing an asymmetry between the horizontal and the vertical plane in terms of stability area. Figure 5.33 shows the tracked particle distribution as a function of the different crossing angle in IP1 and IP5 together with the corresponding stability diagram. The reduction of the crossing angle in IP1 results in particle losses in the vertical plane that become more important with the progressive reduction of the crossing angle in IP1. However, this mechanism does not turn to any remarkable modifications on the stability diagrams from the tracked distribution compared to the Gaussian distribution cases. Significant losses (≈ 50%) were observed for the case with $\alpha_c = 189\,\mu\text{rad}$ in IP1 and $\alpha_c = 230\,\mu\text{rad}$ in IP5 in simulations. The closed loops created in the computed stability diagram (Fig. 5.33f) are not ascribable to any physical effects, they are mainly due to the deformation of the tune footprint itself since they are also present for the Gaussian distribution case. However, as visible from the distribution evolution, the particles are gradually lost in both planes. Therefore this mechanism is not sufficient to explain the asymmetric BTF response in the horizontal and vertical plane observed during the experiment. Other mechanisms might explain the observations and they have to been taken into account in the models. One of these mechanisms may be the linear coupling as discussed in the next section.

5.3.4 Observations with linear coupling

During the angular scan at the end of the betatron squeeze, an asymmetric behavior between the horizontal and the vertical plane was observed in the BTF response. As shown in the previous section, a larger tune spread in the horizontal plane was observed with respect to expectations. A smaller spread was observed in the vertical plane with respect to the horizontal plane. A correction of the linear coupling was performed by modifying the skew quadrupole

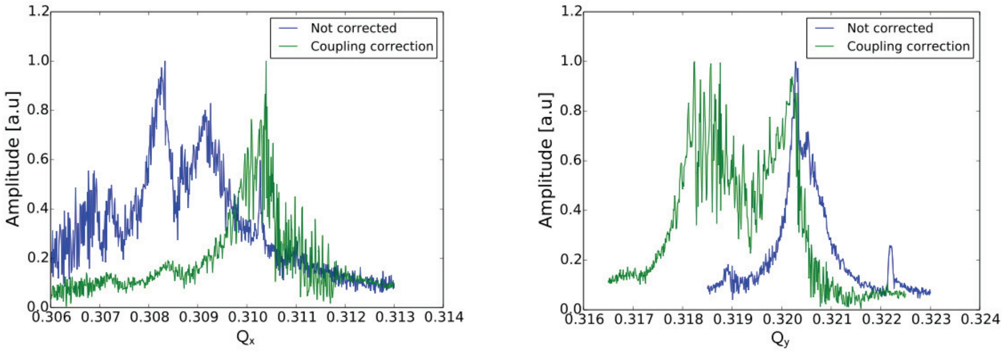

(a) BTF response H-Plane.

(b) BTF response V-Plane.

Figure 5.34 – Measured BTF amplitude response for Beam 1 before and after linear coupling correction.

strengths before applying the last step in angle of 210 µrad. The corresponding measurements before and after the correction are shown in Fig.5.34 for B1 both in the horizontal and in the vertical plane. The total crossing angle in IP1 and IP5 was set to 230 µrad during the BTF measurements. For comparison purposes, the BTF amplitude response was normalized by the maximum values in each case. In the horizontal plane a tune shift is observed together with a reduction of the horizontal tune spread after the linear coupling correction. On the other hand, an increase of the vertical tune spread is observed in the vertical BTF response. The effects of the linear coupling on the tune spread and particle distribution were therefore investigated.

Some footprints for different values of linear coupling are shown in Fig. 5.35 in presence of long range beam-beam interactions at the end of the betatron squeeze. The global linear coupling is applied in MAD-X by means of a knob which controls the strength of the skew quadrupoles in the model. The knob is characterized by a real ($\Re_{knob}$) and imaginary part ($\Im_{knob}$) linked to the amplitude and phase of the f_{1001} difference driving resonance in Eq. 1.22 [5]. The values of the knobs are normalized such that: $|C^{-}| = \sqrt{\Re_{knob}^2 + \Im_{knob}^2}$. As illustrated by Fig. 5.35, by changing the coupling value $|C^{-}|$, the footprint is distorted and the overall tune spread is reduced. These effects are reflected in the shape and the size of the stability diagram. Figure 5.36 shows the computed stability diagrams for a Gaussian distribution at the end of the betatron squeeze for the LHC 2016 configuration ($\beta^* = 0.4\,\mathrm{m}$ and $\alpha_c = 370\,\mu\mathrm{rad}$) without coupling (red line) and in presence of linear coupling ($|C^{-}| = 0.0035$) and Landau octupoles powered with a current of 470 A. A normalized beam emittance $\epsilon = 1.8\,\mu\mathrm{m\,rad}$ was considered both in the horizontal and the vertical plane, as during the experiment, corresponding to a long range beam-beam separation $d_{bb} = 14.5\ \sigma$ at the first encounter, therefore the long range beam-

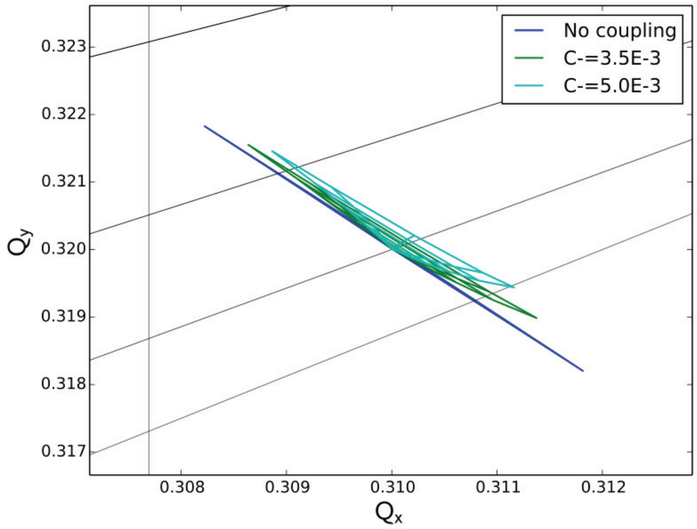

Figure 5.35 – Tune footprints at the end of the betatron squeeze for different linear coupling ($|C^{-}|$) values.

beam contribution is negligible. The solid black line corresponds to the stability diagram computed in the horizontal plane while the dashed black line corresponds to the stability diagram computed in the vertical plane. As expected from the reduction of the footprint in presence of linear coupling, an overall reduction of the stability diagram is observed compared to the one expected at the end of squeeze without linear coupling. In order to investigate the effects of the linear coupling on the particle distribution, the SixTrack code was used to track the particles for a large number of turns. The particle distributions in normalized action variables J_x, J_y after the SixTrack tracking for different values of the linear coupling are shown in Fig. 5.37 together with the corresponding frequency distribution, still computed from the SixTrack tracking. A reduction of the tune spread is observed by increasing the linear coupling. As described in Section 2.1.5, the initial distribution is uniform at the first turn (usually 10^6 particles are generated). After the tracking, the particle distribution is saved and weighted with a bi-dimensional Gaussian function before the computation of the stability diagram. By increasing the value of the $|C^-|$, the particle are clustered towards the horizontal direction as observed in the tracked distribution. The corresponding computed stability diagrams from the tracked particle distribution are shown in Fig.5.38 and compared to the stability diagrams for a Gaussian distribution both in the horizontal (solid black line) and vertical direction (dashed black line). The accumulation of the particles in a preferential direction, the horizontal plane in this case, produces a large value of the derivative $d\Psi/dJ_x$ giving a larger stability diagram in that direction (blue line) with respect to the Gaussian distribution case. In the vertical plane (red line) a larger stability diagram is observed on the side of positive coherent real tune shift than the Gaussian distribution case but much smaller compared to the stability diagram from

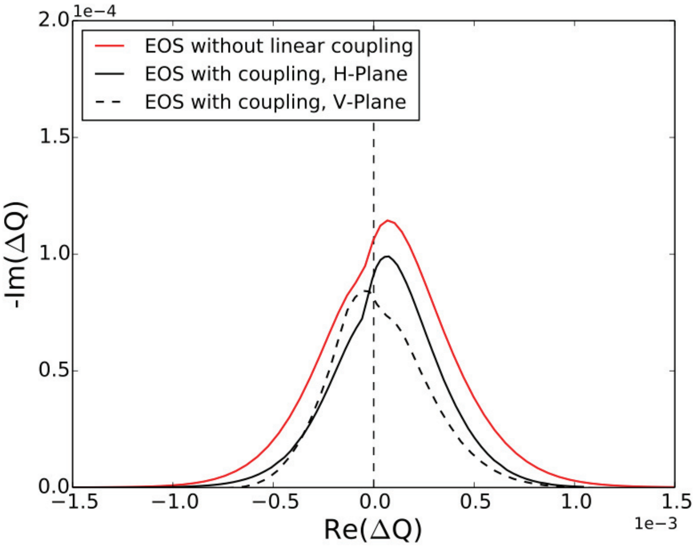

Figure 5.36 – Stability diagrams at the end of the betatron squeeze for a Gaussian particle distribution without linear coupling (red line) and with linear coupling (solid and dashed black lines).

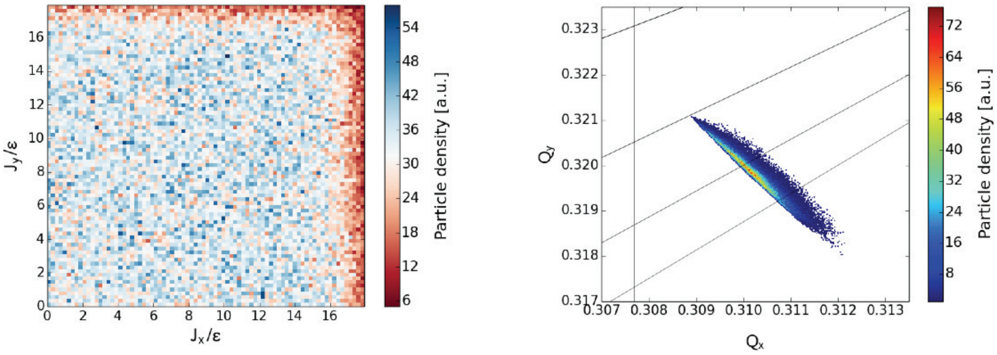

(a) Particle distribution without linear coupling.

(b) Tune diagram computed from SixTrack tracking without linear coupling.

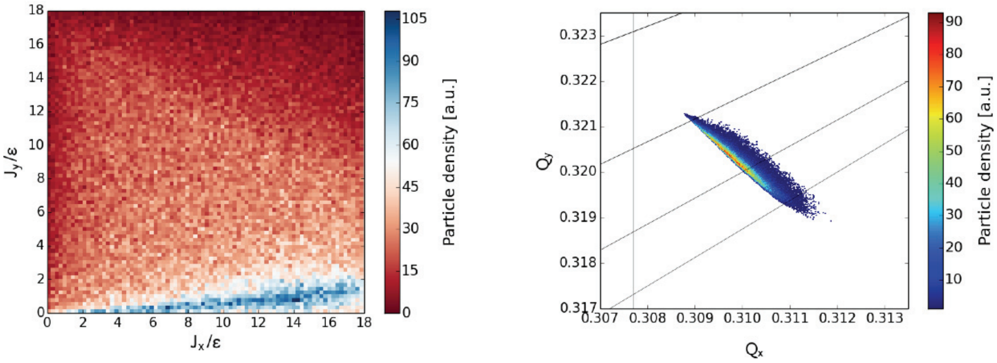

(c) Particle distribution including linear coupling in the models: $|C^{-}| = 3.5\mathrm{e}-3$.

(d) Tune footprint computed from SixTrack tracking without linear coupling for $|C^{-}| = 3.5\mathrm{e}-3$.

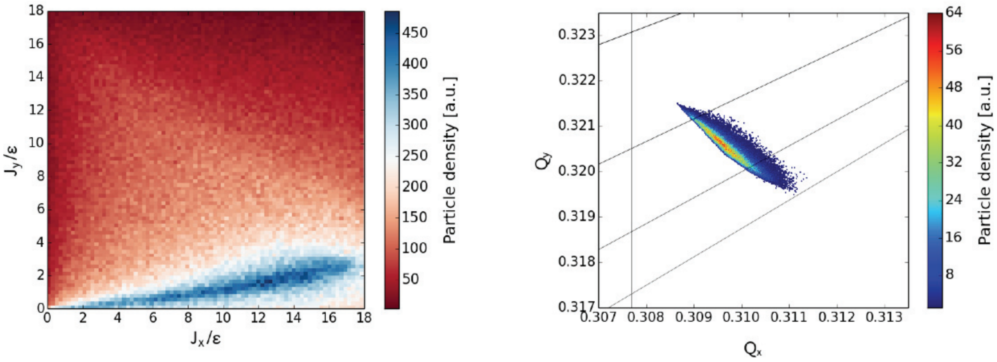

(e) Particle distribution including linear coupling in the models: $|C^{-}| = 5.0\mathrm{e}-3$.

(f) Tune footprint computed from SixTrack tracking without linear coupling for $|C^{-}| = 5.0\mathrm{e}-3$.

Figure 5.37 – Particle and frequency distributions after long particle tracking at end of the betatron squeeze (LHC 2016 configuration) for a normalized beam emittance $\epsilon = 1.8\,\mu\mathrm{m\,rad}$ in both planes, as during the experiment, with positive octupole polarity (I_{oct}= of 470 A) for different C^{-} values. Due to the small emittance, the long range beam-beam contribution is negligible ($d_{bb} = 14.5\sigma$.)

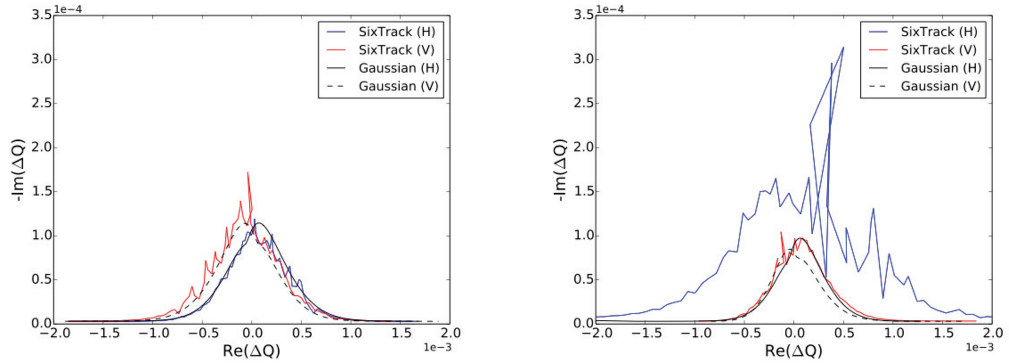

(a) Stability diagram at the end of squeeze without linear coupling in the models

(b) Stability diagram from tracked distribution with linear coupling in the models ($|C^{-}| = 3.5\text{e}-3$)

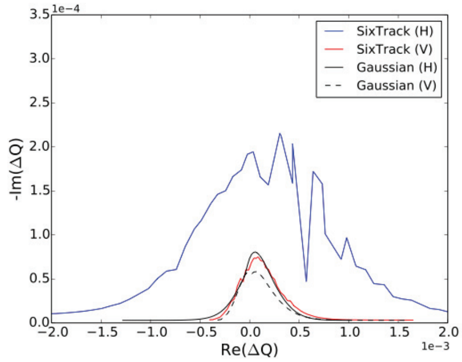

(c) Stability diagram from tracked distribution with linear coupling in the models ($|C^{-}| = 5.0\text{e}-3$)

Figure 5.38 – Stability diagrams from tracked particle distribution for different values of $|C^{-}|$ at the end of the betatron squeeze for the LHC 2016 configuration ($\beta^{*} = 0.4\,\text{m}$ and $\alpha_c = 370\,\mu\text{rad}$). Due to the small emittance used, $\epsilon = 1.8\,\mu\text{m rad}$ in both planes as during the experimental conditions, the long range effects are negligible ($d_{bb} = 14.5\,\sigma$).

the tracked distribution computed in the horizontal plane.

It was observed that the use of negative or positive skew quadrupole knobs to control the global linear coupling in the model produces a different impact on the particle distribution: with positive skew quadrupole knobs, the particles are clustered along the horizontal direction while with negative skew quadrupole knobs the particles are clustered along the vertical direction. These effects give rise to an asymmetric Landau damping: for the case with positive skew quadrupole knobs (Fig. 5.39f) a larger stability diagram in the horizontal plane (blue line) is observed with respect to the Gaussian particle distribution case in the same plane (solid black line), and compared to the vertical plane both for the Gaussian distribution (dashed black line) and the tracked distribution (red line). A smaller stability area in the horizontal plane for the case with negative skew quadrupole knobs is observed (blue line in Fig. 5.39d)

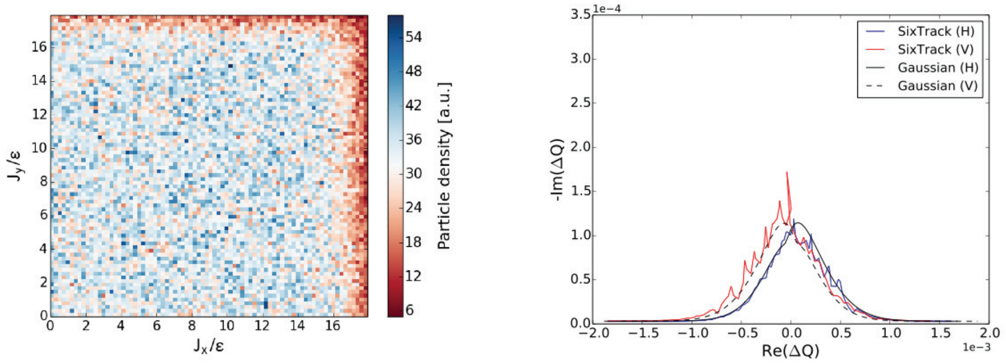

(a) Particle distribution without linear coupling.

(b) Stability diagram from tracked distribution without linear coupling

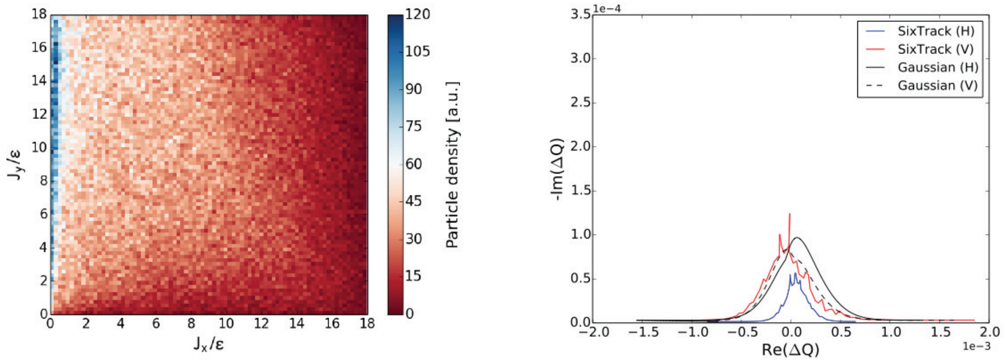

(c) Particle distribution with linear coupling: $C^{-} = 0.0035$ (negative coupling knobs).

(d) Stability diagram from tracked distribution with linear coupling: $C^{-} = 0.0035$ (negative coupling knobs)

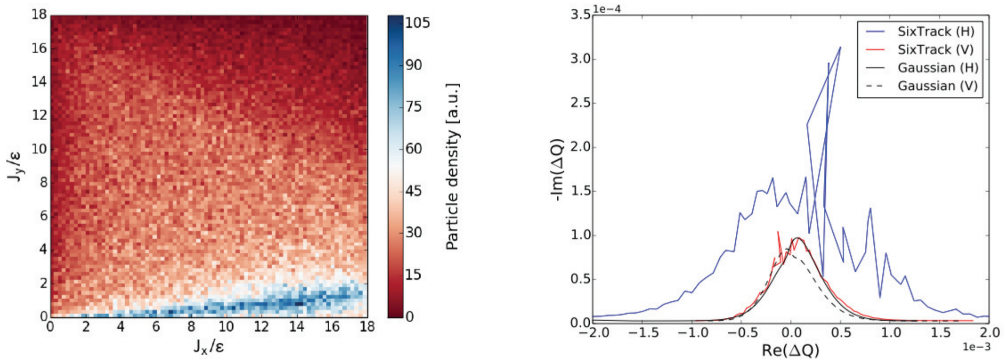

(e) Particle distribution with linear coupling: $C^{-} = 0.0035$ (positive coupling knobs).

(f) Stability diagram from tracked distribution with linear coupling: $C^{-} = 0.0035$ (positive coupling knobs)

Figure 5.39 – Particle distribution after SixTrack tracking at end of the betatron squeeze, with positive octupole polarity (current of 470 A) without linear coupling and with linear coupling ($|C^{-}| = 0.0035$) introduced in the model by using positive and negative skew quadrupole knobs.

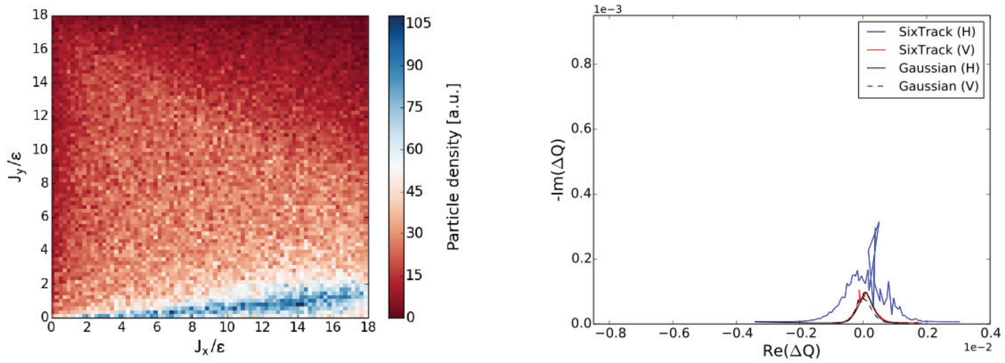

(a) Particle distribution with linear coupling and $\alpha_c = 370\mu\text{rad}$ in IP1 and IP5.

(b) Stability diagram from tracked distribution with linear coupling and $\alpha_c = 370\mu\text{rad}$ in IP1 and IP5.

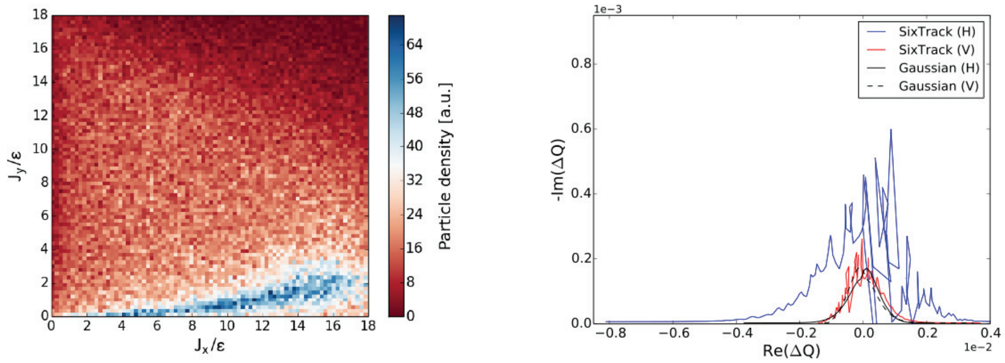

(c) Particle distribution with linear coupling and $\alpha_c = 270\mu\text{rad}$ in IP1 and IP5.

(d) Stability diagram from tracked distribution with linear coupling $\alpha_c = 270\mu\text{rad}$ in IP1 and IP5.

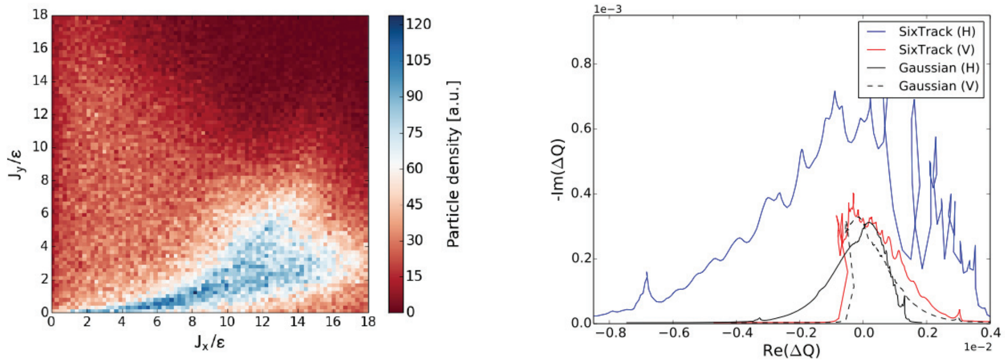

(e) Particle distribution with linear coupling and $\alpha_c = 210\mu\text{rad}$ in IP1 and IP5.

(f) Stability diagram from tracked distribution with linear coupling $\alpha_c = 210\mu\text{rad}$ in IP1 and IP5.

Figure 5.40 – Tracked particle distribution and corresponding stability diagrams at end of the betatron squeeze with positive octupole polarity (current of 470 A) and linear coupling, $|C^{-}| = 0.0035$ (positive skew quadrupole knobs), for different crossing angle in IP1 and IP5.

compared both to the corresponding Gaussian distribution case (black line) and to the the tracked particle distribution case in the vertical plane (red line). This last case is very similar to the Gaussian distribution case in the same plane (dashed black line).

The tracked particle distributions during the reduction of the crossing angle in IP1 and IP5 in presence of linear coupling in the models ($|C^{-}| = 0.0035$) are shown in Fig.5.40 for positive skew quadrupole knobs together with the corresponding computed stability diagrams. Some of the angles used during the angular scan of the experiment were considered: 370 µrad, 270 µrad and 210 µrad. The angles are reduced in both the IPs. The particles are clustered towards the horizontal direction and larger stability diagrams in the horizontal plane (blue line) is observed with respect to the vertical plane (red line) and with respect to the Gaussian distribution case in the horizontal plane (solid black line). The stability area increases in both planes while reducing the crossing angle. This effect is due to the stronger long range beam-beam interaction that adds up to the tune spread provided by the Landau octupole current with positive polarity producing a larger tune spread in the beams. In Fig. 5.41 the tracked distributions as a function of the crossing angles are shown for negative skew quadrupole knobs (Fig. 5.39f). In this configuration, the stability diagram in the horizontal plane (blue line) is smaller compared to the Gaussian distribution case in the same plane (black solid line). In the vertical plane the stability diagram from the tracked distribution (red line) remains similar to the Gaussian distribution case in the same plane (dashed black line).

As observed, in presence of linear coupling with positive skew quadrupole knobs, for the reduced crossing angle of $\alpha_c = 210\,\mu\text{rad}$ in IP1 and IP5 a sharp cut is visible in the stability digram in the vertical plane. The cut is visible both for the tracked distribution case and for the Gaussian distribution case. This observation suggests that this cut is produced by the deformation of the amplitude detuning itself that dominates the shape of the stability diagram in the vertical plane rather than the particle distribution. However, the clustering towards the horizontal direction results in a larger stability diagram in this plane compared both to the Gaussian distribution case and the stability diagram in the vertical plane. For the configuration used ($\beta^{*} = 0.4\,\text{m}$, $\alpha_c = 370\,\mu\text{rad}$ and a normalized rms beam emittance $\epsilon = 1.8\,\mu\text{m}\,\text{rad}$), this effect on the vertical stability diagram is observed only in presence of a reduced long range beam-beam separation of $d_{bb} = 8.2\,\text{m}$ and therefore in presence of enhanced long range beam-beam interactions (and tune spread).

In 2012 several instabilities were observed at the end of the betatron squeeze in the vertical plane with positive octupole polarity ($I_{oct} = 550\,\text{A}$). The crossing angle in IP1 and IP5 in the 2012 was $\alpha_c = 290\,\mu\text{rad}$, corresponding to a long range beam-beam separation of $\approx 9\ \sigma$ with $\beta^{*} = 60\,\text{cm}$ considering a beam emittance of $2.5\,\mu\text{m}\,\text{rad}$. In the 2012 physics run the nominal beam intensity was $I_b = 1.8\,\text{p/bunch}$, therefore the long range beam-beam interactions were stronger compared to the 2016 LHC physics run. Including a linear coupling of $|C^{-}| = 0.0035$, the tune footprint for the 2012 configuration at the end of the betatron squeeze with (red line) and without (blue line) linear coupling is shown in Fig. 5.42 where for completeness both the polarities of the octupole magnets were included. In the 2012 LHC configuration at the end

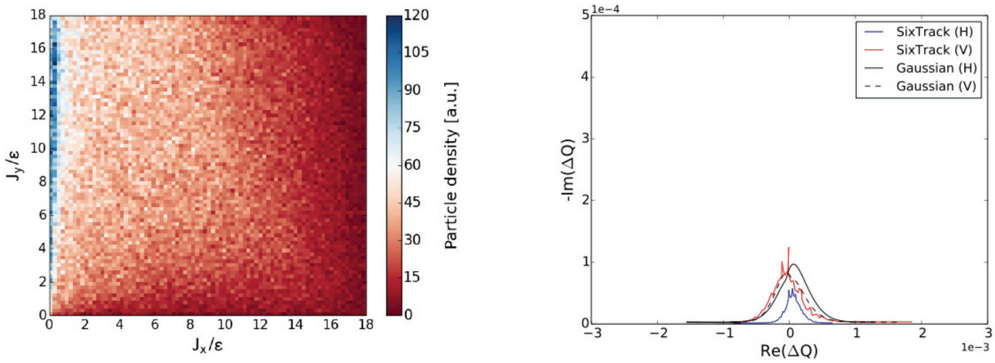

(a) Particle distribution with linear coupling and $\alpha_c = 370\mu\text{rad}$ in IP1 and IP5.

(b) Stability diagram from tracked distribution with linear coupling and $\alpha_c = 370\mu\text{rad}$ in IP1 and IP5.

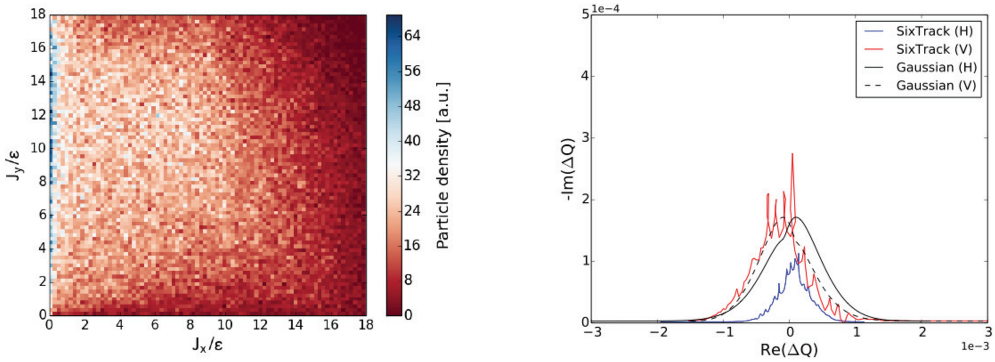

(c) Particle distribution with linear coupling and $\alpha_c = 270\mu\text{rad}$ in IP1 and IP5.

(d) Stability diagram from tracked distribution with linear coupling and $\alpha_c = 270\mu\text{rad}$ in IP1 and IP5.

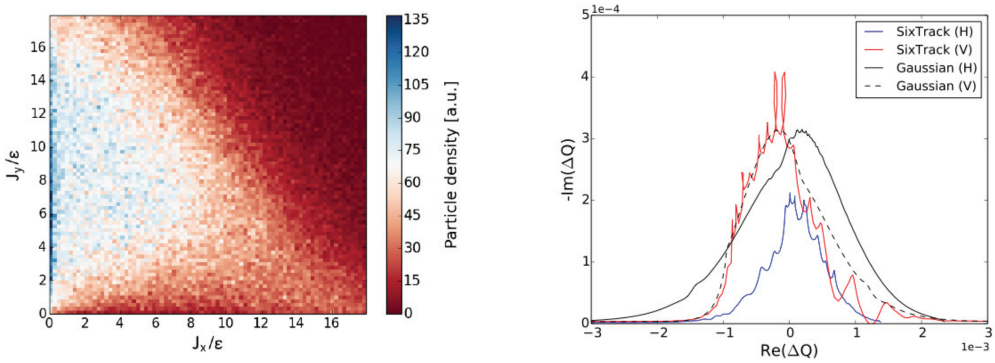

(e) Particle distribution with linear coupling and $\alpha_c = 210\mu\text{rad}$ in IP1 and IP5.

(f) Stability diagram from tracked distribution with linear coupling and $\alpha_c = 210\mu\text{rad}$ in IP1 and IP5.

Figure 5.41 – Tracked particle distribution and corresponding stability diagrams at end of the betatron squeeze with positive octupole polarity (current of 470 A) and linear coupling, $|C^{-}| = 0.0035$ (negative skew quadrupole knobs), for different crossing angle in IP1 and IP5.

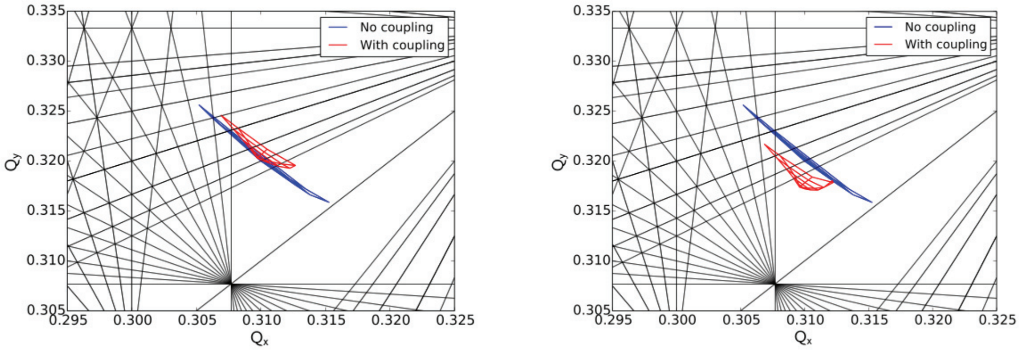

(a) End of the betatron squeeze with positive octupole polarity.

(b) End of the betatron squeeze with positive octupole polarity and reduced vertical tune ($Q_y = 0.317$).

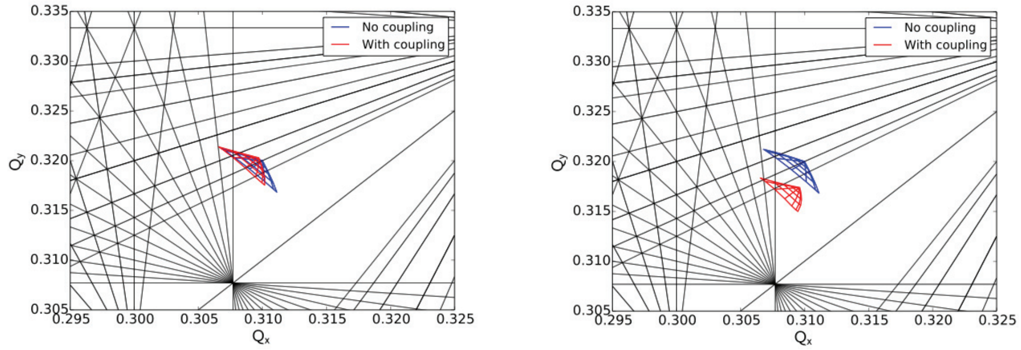

(c) End of the betatron squeeze with negative octupole polarity.

(d) End of the betatron squeeze with negative octupole polarity and reduced vertical tune ($Q_y = 0.317$).

Figure 5.42 – Tune footprint at the end of the betatron squeeze (2012 configuration) with positive and negative octupole polarity ($I_{oct} = 550\,\mathrm{A}$) in presence of linear coupling (red line) and without linear coupling (blue line).

of the betatron squeeze a larger tune spread was expected compared to the one for the 2016 configuration (Fig. 5.35). A cut in the vertical tune spread is observed in presence of the linear coupling with positive octupole polarity (red line). The particles towards the diagonal are pushed away from having $Q_y \approx Q_x$ and an asymmetry is visible between the horizontal and the vertical detuning. The tune footprint folds on itself while the vertical tune approaches the horizontal tune (Fig. 5.42b). This effect is still present with negative octupole polarity but the deformation on the footprint is less important than the case with positive octupole polarity, and only the large amplitude particles are influenced. The computed stability diagrams from the tracked particle distribution are shown in Fig. 5.43 with and without linear coupling in the models and for positive octupole polarity. Without linear coupling no important effects are visible compared to the Gaussian distribution case. In the presence of linear coupling due to the footprint deformation, a sharp cut in the stability diagram is observed (Fig. 5.43d) in

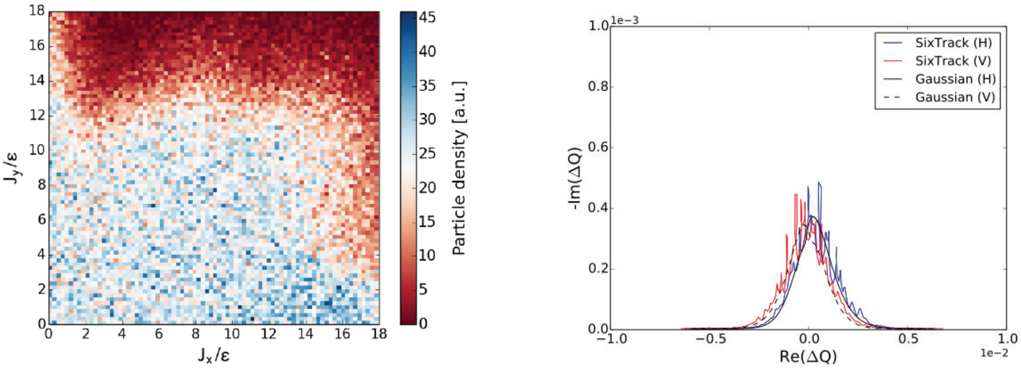

(a) Particle distribution without linear coupling.

(b) Stability diagram from tracked distribution without linear coupling.

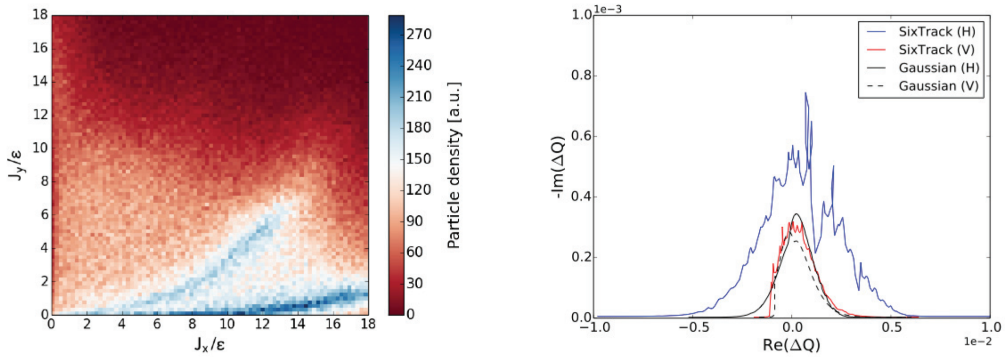

(c) Particle distribution with linear coupling.

(d) Stability diagram from tracked distribution with linear coupling.

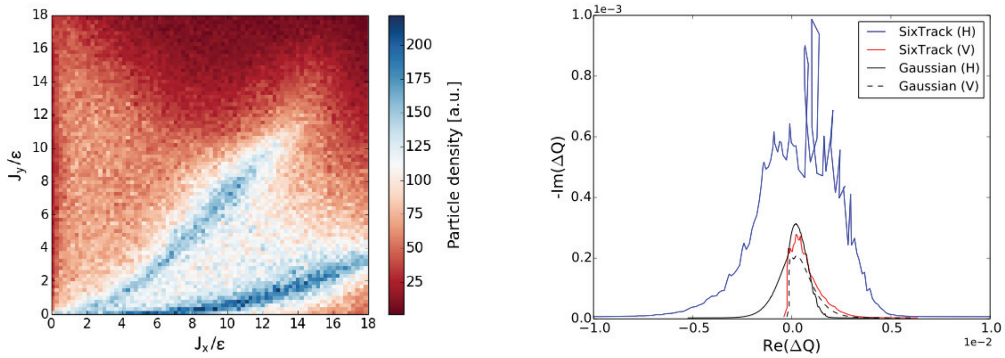

(e) Particle distribution with linear coupling and reduced tune in the vertical plane.

(f) Stability diagram from tracked distribution with linear coupling and reduced tune in the vertical plane.

Figure 5.43 – Particle distribution from SixTrack tracking and corresponding stability diagrams at end of the betatron squeeze (2012 configuration) for positive octupole polarity (current of 550 A) with linear coupling ($|C^{-}| = 0.0035$ and positive coupling knobs) and without linear coupling, and for a reduced vertical tune ($\Delta Q_y = 3 \times 10^{-3}$).

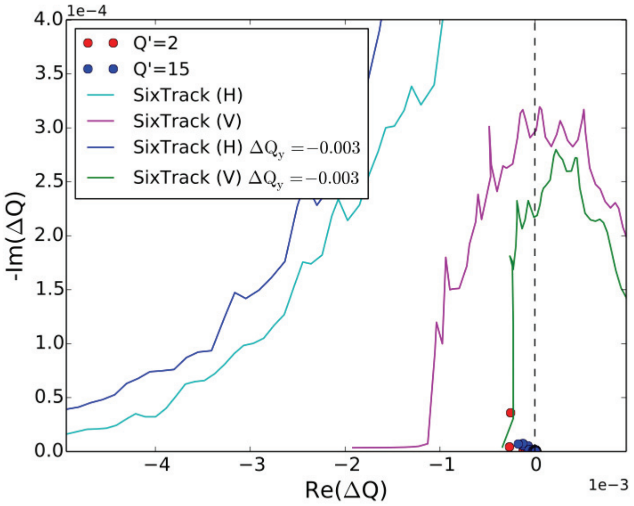

Figure 5.44 – Stability diagrams in presence of long range beam-beam interactions at end of the betatron squeeze for the 2012 configuration, positive octupole polarity ($I_{oct} = 550\,\mathrm{A}$) with transverse linear coupling, $|C^{-}| = 0.0035$ (positive skew quadrupole knobs). The light blue line and the pink line represent the stability diagram in the horizontal and vertical plane respectively, for nominal collision tunes ($Q_x = 0.31, Q_y = 0.32$). The blue line and the green line represent the stability diagram in the horizontal and vertical plane respectively, for a reduced tune in the vertical plane ($Q_y = 0.317$). The impedance coherent modes were included in the plot for a chromaticity of 2 units (red dots) and 10 units (blue dots).

the vertical plane both for the tracked particle distribution (red line) and the corresponding Gaussian distribution (dashed black line), while an increase of the stability diagram in the horizontal plane is visible for the tracked particle distribution (blue line) in presence of linear coupling compared to the Gaussian particle distribution case (black solid line). The cut is sharper in Fig. 5.43f, where the vertical tune is decreased. Figure 5.44 shows the stability diagrams at end of the betatron squeeze for the 2012 configuration, positive octupole polarity (the nominal current of 550 A was used) with a linear coupling $|C^{-}| = 0.0035$ (positive skew quadrupole knobs). The light blue line and the pink line represent the stability diagram in the horizontal and vertical plane respectively with nominal collision tunes ($Q_x = 0.31, Q_y = 0.32$). The blue line and the green line represent the stability diagram in the horizontal and vertical plane respectively with a reduced tune in the vertical plane of $Q_y = 0.317$ with respect to the nominal value. The impedance coherent modes were included in the plot for a chromaticity of 2 units (red dots) and 10 units (blue dots). Some impedance coherent modes are at the edge of the stability in the vertical plane in presence of a reduced vertical tune $Q_y = 0.317$. In the horizontal plane (blue and light blue lines) the stability diagrams are always larger compared to the vertical plane due to the clustering of the particles towards this direction. For the case with a reduced tune in the vertical plane the stability diagram in the horizontal plane (light blue line) is also larger compared to the one in the same plane with nominal collision tunes (blue line). This observation is consistent with the 2012 physics run where the instabilities were always affecting the vertical plane at the end of the betatron squeeze. In the 2016 a larger tune spread was observed in the horizontal plane with BTF measurements and a smaller one in the vertical plane at the end of the squeeze. A different value of the working point and a stronger linear coupling could explain the observed instabilities at the end of the betatron squeeze mostly affecting the vertical plane. Further experimental studies to investigate the effects of the linear coupling on the Landau damping will be carried out and more BTF experiments will be proposed for the 2017 LHC Machine Developments. Studies on destabilizing effects of the transverse linear coupling have already shown a significant increase of the octupole stability thresholds [85].

5.3.5 BTF limitations and improvements

As discussed in the previous paragraph, the LHC BTF system presents some limitations (unknown calibration factor, measurement noise and artifact signal due to the fixed excitation amplitude) resulting in a challenging data analysis. Some actions are planned for the 2017 in order to improve the measuring system and for possible operational use:

- improve the signal to noise ratio with an adaptive excitation amplitude as a function of the excitation frequency;
- introduce a delay to the excitations and/or damp coherent oscillations before exciting beyond the betatron tune frequency ;
- where possible calibrate the excitation amplitude of the system and measure oscillation amplitude at the BBQ;
- gate the system to individual 25 ns bunches to allow single bunch measurements.

Despite the challenges and limitations, important results were achieved with this measurement system together with the development of numerical tools to reproduce the observations.

5.4 Summary

The transverse BTF system was installed in the LHC in order to experimentally explore the Landau damping of the beams over the LHC operational cycle to understand the observations of coherent instabilities. Beam Transfer Function measurements were acquired at injection energy for different octupole currents (0 A, 6.5 A, 13 A and 26 A) and compared to expectations. An analysis making use of a fitting function was developed to overcome the limitations of the uncalibrated system. The evolution of tune shift and tune spread and therefore of the stability diagram at various stages of the operations was quantified. The tune spread factors evaluated from the fitting function applied to the BTF measurements at injection energy are summarized in Tab. 5.1. A larger tune spread than predicted was measured. An additional tune spread corresponding to ≈ 5 A is needed to well reproduce the expectations (Fig. 5.15). This tune spread is consistent with expectations of non linear errors from the magnets. With an octupole current of 26 A a smaller tune spread is observed in the vertical plane compared to the horizontal plane. In addition, beam losses were observed in the vertical plane. The diffusive mechanisms due to excited resonances together with the presence of transverse linear coupling during the measurements can explain the reduced tune spread in the vertical plane due to the strong beam losses observed. For the case with the octupole current of 6.5 A the stability diagram from BTF measurements was reconstructed and it is consistent with expectations (Fig. 5.17). The longitudinal contribution in the measured stability diagram in the transverse plane was fully characterized by means of multi-particle simulations. Model and measurements show a good agreement for a chromaticity $Q' \approx 5$ units in accordance with the experimental conditions during the BTF measurements.

Beam Transfer Function measurements were acquired at the end of the betatron squeeze where long range beam-beam contributions are more significant. A crossing angle scan in IP1 and IP5 was performed. An unexpected and non negligible asymmetry in terms of tune spread and tune shift between the horizontal and the vertical plane was observed. The long range beam-beam interactions alone cannot produce any evident deformation on the particle distribution that can explain the observations, even for a reduced long range beam-beam separation $d_{bb} = 8.24\,\sigma$ (Fig. 5.32). The measured spread in the LHC seems to be dominated by effects other than long range beam-beam interactions. This asymmetry was proved to be linked to the non-zero transverse linear coupling which leads to two main effects as shown with simulations:

- different detuning with amplitude between the horizontal and vertical plane. As shown in Fig. 5.35 the particles towards the diagonal in the tune diagram are pushed away and an asymmetry is visible between the horizontal and the vertical detuning. This effect becomes more important for a large tune spread in the beams as at the end of the betatron squeeze for the 2012 machine configuration. In the presence of linear coupling, increasing the tune spread in the beams by using stronger octupoles or stronger beam-beam interactions is not beneficial to the Landau damping. If the small amplitude particles approach the diagonal, a sharp cut in the computed stability diagram is produced (Fig. 5.43). A considerable dependency on the working point was observed: reducing the vertical tune produces a more pronounced deformation of the amplitude detuning;
- clustering of the particles towards the horizontal direction. In this case the derivative of the particle distribution contributes to an enlargement of the stability diagram creating a very large asymmetry between the stability diagrams of the two planes, otherwise unexplainable from measurements.

6 Conclusions

During the 2012, 2015 and 2016 LHC physics runs the beams were affected by transverse instabilities at top energy during different phases of the operational cycle. These instabilities caused beam dumps, emittance blow-up and particle losses compromising the luminosity reach of the collider. At the LHC, predictions of instability thresholds of coherent modes driven by the impedance are based on computations of the dispersion integral. Such studies of the Landau damping, considering a Gaussian distribution inside the beams, were performed for different tune spreads and machine configurations. These studies could not explain the observed instabilities since predictions show the impedance coherent modes lay within the stability diagram [17] during the full operational cycle. However, the tune spread is not the only ingredient playing a role in the evaluation of the stability diagram. The tune spread in the beams provides the size of the stability diagram in the complex plane, where the coherent tune shifts ΔQ_{coh} correspond to stable modes. The shape of the stability diagram is defined by the particle distribution inside the beams and its derivative. In the presence of diffusive mechanisms, caused by excited resonances or noise, the particle distributions inside the beams can be modified. Together with the modifications of the particle distributions, the diffusive mechanisms can produce changes of the frequency distribution and alter the tune spread in the beams. As a consequence of these two combined effects, the stability diagram can be reduced or deformed, potentially leading to a possible loss of Landau damping for coherent modes which were previously damped by lying within the unperturbed stability diagram. To guarantee luminosity reach of future projects which aim to surpass the performance of conventional LHC, such as the High-Luminosity upgrade or the Future Circular Collider (FCC), it is crucial to understand the limitations deriving from coherent instabilities.

The transverse stability of the LHC beams was analysed for different operational phases and machine configurations during setup of the 2015 and 2016 physics runs, to ensure the maximum of stability over all stages of the cycle. In addition, the setup of the crossing angles in IP2 and IP8 was adjusted to control the beam-beam effects from these two IPs and cancel their contributions to the Landau damping. In this configuration good margins of stability are guaranteed during the different operational stages and the impedance coherent modes should be Landau damped according to the predictions. Parallel studies on transverse beam stability were carried out for the HL-LHC in order to ensure maximum stability during the full operational cycle for the foreseen scenaria. From the results of these studies, a proposal to operate with negative octupole polarity was approved and included in the HL-LHC TDR [57]. In addition, a solution to compensate the reduction of the stability diagram during the betatron squeeze due to beam-beam long range interactions was proposed. The solution was based on the gradual application of 8% larger β-function in the arcs from $\beta^* = 70\,\text{cm}$.

According to predictions the impedance modes should be Landau damped during the full LHC operational cycle, however transverse beam instabilities were still present during the 2015 and 2016 LHC physics runs. This demonstrates a clear limitation on the predictive power of existing models. These observations motivated the experimental and numerical studies of this thesis. Numerical models were updated to take into account the particle distribution changes under the effects of realistic lattice configurations and the related impact on the stability diagram when strong diffusive mechanism are present. In parallel, Beam Transfer Function (BTF) system was installed and BTF measurements were performed in the LHC to experimentally explore the Landau damping of the beams and understand the limitations of the models. The BTF provides a direct measurement of the stability diagram and is sensitive to detuning with amplitude as well as to the particle distribution changes. The models were extended to reproduce numerically and parametrically the measurements and characterize the BTF response in the presence of beam-beam interaction. Since the system was not calibrated, a fitting function was parameterized and implemented to quantify the tune spread, hence the beam stability, and compare the measurements with expectations for the first time at the LHC.

At flat top, where the beams are still kept separated, the stability of the beam is dominated by the tune spread produced by the octupole magnets. In order to investigate the effects of the octupoles and the impact of diffusive mechanisms, an octupole scan was performed at injection energy to investigate the impact of machine non linearities, stronger at injection, on the particle distributions and therefore on the expected stability.

Beam Transfer Function measurements at injection energy were acquired for different octupole currents (0 A, 6.5 A, 13 A and 26 A). The tune spread factors evaluated from the fitting function applied to the BTF measurements at injection energy (summarized in Tab. 5.1) revealed a larger tune spread than the expected one. For the case with an octupole current of 0 A, an equivalent octupole currents of ≈ 5.72 A and ≈ 5.23 A in the horizontal and vertical plane respectively was found in agreement with the expected non linear errors from the lattice [82]; this observation proves the BTFs to provide a good measure of the tune spread in the beams.

Upon increasing the octupole current to 26 A a larger tune spread was observed in the horizontal plane and a smaller one in the vertical plane, for which beam losses were observed during the experiment. Diffusive mechanisms due to excited resonances together with the presence of transverse linear coupling during the measurements reduced the amount of tune spread in the beams leading to a reduction of Landu damping. From this observation, it is concluded for the first time that, in the presence of reduced dynamic aperture, the actual Landau damping in the beams is reduced. The simulated dynamic aperture was ≈ 3 σ and it could be further reduced due to multipolar errors.

For the case of 6.5 A octupole current, the stability diagram from BTF measurements was reconstructed and showed an agreement with expectations (Fig. 5.17). The longitudinal contribution to the measured stability diagram in the transverse plane was fully characterized by means of multi-particle simulations including a chromaticity $Q' \approx 5$ units as was present during the BTF measurements.

A parametric study of the beam-beam long range contribution to stability was performed at the end of the betatron squeeze in the 2016 LHC configuration (with $\beta^* = 40$ cm). The BTF measurements were acquired for different crossing angles of IP1 and IP5, hence for different beam-beam long range separations. The BTF measurements revealed an unexpected asymmetric behavior in terms of tune spread and tune shift between the horizontal and the vertical plane. A maximum tune shift $\Delta Q_y \approx 2.4 \times 10^{-3}$ was observed in the vertical plane while $\Delta Q_x \approx 2.0 \times 10^{-3}$ in the horizontal plane for the smallest crossing angle of 230 µrad. A possible explanation of the observed tune shift as a function of the crossing angle is the breaking of the horizontal-vertical passive compensation of the beam-beam long range tune shifts given by the alternating crossing scheme in IP1 and IP5. A different strength of the long range interactions in one of the two IPs would result in a tune shift in the plane of the long range interactions. The measured tune shift was reproduced with an asymmetry between the crossing angles in IP1 and IP5 of 30%, but it could be also due to asymmetric β^* values at the two IPs. In 2016, the crossing angle in both IP1 and IP5 was reduced in operation from 370 µrad to 280 µrad to increase the luminosity reach. With the new crossing angle, if beam lifetimes are guaranteed above 10 hours, a corresponding increase of 10% of the integrated luminosity is foreseen. However, vertical beam losses were observed for Beam 1. They were caused by the tune shift in the vertical plane that was induced by the reduction of the crossing angle [86]. The tune shift affected the bunches experiencing long range beam-beam interactions, reducing the beam lifetimes to below 10 hours [86]. The observation of the vertical tune shift due to beam-beam long range interactions was also confirmed by BTF measurements presented in this thesis for different crossing angles at the end of the betatron squeeze. The tune shift measured by the BTF for the angle of 280 µrad was applied as a correction to compensate the tune shift observed in the vertical plane of Beam 1. After the correction, the beam lifetimes increased to above 10 hours [86] with a corresponding 10% increase of the integrated luminosity, as predicted.

As a function of the crossing angle (Fig. 5.31), the impact of the beam-beam long range contribution to the measured stability diagrams was very different between the horizontal and vertical planes. For beam-beam long range separations larger than 11.5 σ a larger contribution to the stability diagram was observed in the horizontal plane with respect to expectation by a factor of ≈ 1.3. For beam-beam long range separations smaller than 11.5 σ the expected contributions are larger than the measured by up to a factor ≈ 2 for the smallest crossing angle used. An increase of the long range contribution of ≈ 90% is observed in the horizontal plane at the smallest beam-beam separation with respect to the initial case at the end of the betatron squeeze. In the vertical plane the beam-beam long range contribution to the stability diagram is smaller than expected and smaller compared to the large spread observed in the horizontal plane. This finding shows for the first time an asymmetry of the stability of the two planes consistent with the observations in the LHC for which the vertical plane is more often affected by transverse instabilities. A strong dependence of tune spread on tune values was observed: a negative tune shift of $\Delta Q_y = -0.001$ reduces the tune spread by a factor 3 (Fig. 5.27 and Fig. 5.31). This dependency is confirmed by the reproducibility of the BTF response upon restoring the initial tune value in the vertical plane. (Fig. 5.27).

Simulations with different tracked particle distributions as a function of the crossing angle could not explain the observed asymmetry between the two planes (Fig. 5.32). Therefore, other mechanisms had to be included in the models; a possible candidate may be the transverse linear coupling. The choice of this mechanism was mainly dictated by BTF observations where a coupling correction ended up in a reversed situation in terms of horizontal and vertical tune spread. Hence, the linear coupling was included in the models and an asymmetric behavior between the two transverse planes was then reproduced (Fig. 5.40). By using the extended models it is possible to evince that the observed asymmetry can be related to two different effects. The first is the different detuning with amplitude in the two planes: in the presence of linear coupling and large tune footprint, as the case of the LHC 2012 physics run at the end of the betatron squeeze, where the beam-beam long range contribution was very strong, the particles towards the diagonal are pushed away. In this case a sharp cut on the stability diagram is visible due to the tune footprint deformation (Fig. 5.44) and some coherent modes are at the edge of stability. The second is related to the clustering of particles towards the horizontal direction of the distribution, for which the derivative of the particle distribution contributes to the enlargement of the stability diagram (Fig. 5.44) in the horizontal plane. For the first time the incoherent effects of the particle distribution modifications due to realistic lattice configurations were included in the computation of the stability diagram giving compatible explanations of the observed instabilities in the LHC.

Further studies are already planned at the LHC in order to explore the behaviour of the beams in presence of interplay of linear coupling, octupoles and long range beam-beam interactions. Given the satisfactory results, improvements of the BTF system are being applied in order to improve the signal quality and use a gated BTF system on few bunches during Physics fills. Analysis of BTF measurements by means of extended numerical tools and the results presented in this thesis allow better understanding of the Landau damping of the beams, and therefore the transverse beam stability at the LHC, helping to improve accelerator performance.

Bibliography

[1] H. Wiedemann, *Particle Accelerator Physics*, 3rd ed. (Springer, 2007).

[2] K. Wille, *The Physics of Particle Accelerators, an introduction*, 1st ed. (OXFORD University Press, 1996).

[3] W. Herr, in *CAS - CERN Accelerator School: Advanced Accelerator Physics Course, Warsaw, Poland, 2015* (CERN, 2015).

[4] S. Y. Lee, *Accelerator Physics* (World Scientific, 1999).

[5] T. Persson and R. Tomàs, Phys. Rev. ST Accel. Beams **17**, 051004 (2014).

[6] Y. Alexahin and E. Gianfelice-Wendt, Journal of Instrumentation **6**, P10006 (2011).

[7] W. Herr and T. Pieloni, in *CAS - CERN Accelerator School: Advanced Accelerator Physics Course* (Aug 2013).

[8] T. Pieloni, *A study of beam-beam effects in hadron colliders with a large number of bunches*, Ph.D. thesis, Ecole Polytechnique Federale de Lausanne (EPFL) (2008).

[9] "MAD - Methodical Accelerator Design," http://madx.web.cern.ch.

[10] W. Herr, *Particle tracking with MAD-X including LHC beam-beam interactions*, LHC Project Note 344 (CERN, 2004).

[11] "DYNAP: Tunes, Tune Footprints, Smear and Lyapunov Exponent, MAD-X user's guide," http://madx.web.cern.ch/madx/madX/doc/usrguide/dynap/dynap.html.

[12] M. Ferro-Luzzi, *LHC bunch filling schemes for commissioning and initial luminosity optimization*, LHC Project Note 415 (CERN, 2008).

[13] W. Herr, *Features and implications of different LHC crossing schemes*, LHC Project Report 628 (CERN, 2003).

[14] W. Herr, *Effect of PACMAN bunches in the LHC*, LHC Project Report 39 (CERN, 1996).

[15] W. Herr *et al.*, *Observations of beam-beam effects at the high intensities in the LHC*, CERN-ATS-2011-154 (CERN, 2011).

[16] V. Vaccaro, *Longitudinal instability of a coasting beam above transition, due to the action of lumped discontinuities*, CERN-ISR-RF-66-35 (CERN, 1966).

[17] X. Buffat, *Transverse beams stability studies at the Large Hadron Collider*, Ph.D. thesis, Ecole Polytechnique Federale de Lausanne (EPFL) (2015).

[18] A. W. Chao, *Physics of Collective Beams Instabilities in High Energy Accelerators*, edited by I. J. W. . Sons (Wiley series and Beam Physics and Accelerator Techonology, 1993).

[19] N. Mounet, "DELPHI: an analytic vlasov solver for impedance-driven modes," CERN HSC meeting (2014).

[20] G. Rumolo and F. Zimmermann, *Practical user guide for HEADTAIL*, CERN-SL-Note-2002-036-AP (CERN, 2002).

[21] Y. Alexahin, Nucl. Instrum.Methods Phys.Res. **480**, 253 (2002).

[22] K. Hirata, Nucl. Instrum.Methods Phys.Res. **269**, 253 (1988).

[23] K. Hirata and E. Keil, Nucl. Instrum.Methods Phys.Res. **292**, 156 (1990).

[24] K. Yokoya and H.Koiso, Paticle Acceleratos **27**, 181 (1990).

[25] J. S. Berg and F. Ruggero, *Landau damping with two-dimensional betatron tune spread*, CERN SL-AP-96-71 (1996).

[26] W. Herr, in *CAS-CERN Accelerator School: Advanced Accelerator Physics, Trondheim, Norway, 19–29 August 2013*, CERN-2014-009, edited by W. Herr (CERN, 2014).

[27] L. Landau, J. Phys. USSR **10**, 25 (1946).

[28] J. Gareyte, J. Koutchouk, and F. Ruggero, *Landau damping, Dynamic Aperture and Octupoles in the LHC*, LHC Project Report 91 (CERN, Geneva, Switzerland, 1997).

[29] O. S. Brüning, P. Collier, P. Lebrun, S. Myers, R. Ostojic, J. Poole, and P. Proudlock (editors), CERN-2004-003-V1 (2004).

[30] W. Herr and B. Muratori, in *CAS - CERN Accelerator School: Intermediate Course on Accelerator Physics* (Zeuthen, Germany, Sep 2003).

[31] F. Antoniou *et al.*, in *Proceedings of IPAC 2015* (Richmond, VA, USA, 2015).

[32] R. Jacobsson, in *Proceedings of the ICFA Mini-workshop on beam-beam effects in hadron colliders* (CERN, Geneva, Switzerland, 2014).

[33] http://sixtrack.web.cern.ch/SixTrack/ (2016).

[34] W. Herr and T. Pieloni, http://lhc-beam-beam.web.cern.ch/lhc-beam-beam/combi_welcome.html.

[35] T. Pieloni and W. Herr, *Models to study multi bunch coupling through head-on and long-range beam-beam interactions*, CERN LHC Project Report 937 and Proceedings of EPAC06, Edinburgh, United Kindom, 2006 (CERN, 2006).

[36] F. Jones, W. Herr, and T. Pieloni, *Parallel Beam-Beam simulation Incorporating Multiple Bunches and Multiple Interaction Regions*, CERN LHC Project Report 1038 and Proceedings of Particle Accelerator Conference 2007, Albuquerque, New Mexico, USA 2007 (CERN, 2007).

[37] T. Pieloni and W. Herr, in *Proceedings of 2005 Particle Accelerator Conference* (2005).

[38] E.Keil, *Coherent beam-beam effect in machines with unequal betatron phase advances between crossing points*, LEP Note 226 (CERN, 1980).

[39] W. Herr, *Consequences of Periodicity and Symmetry for the Beam-Beam Effects in the LHC*, LHC Project Report 49 (CERN, 1996).

[40] https://www.open-mpi.org.

[41] F. Schmidt, *SixTrack User's Reference Manual*, (CERN, 1994).

[42] G. Robert-Demolaize, *Design and Performance Optimization of the LHC Collimation System*, Ph.D. thesis, Universite Joseph Fourier, Grenoble (2006).

[43] W. Herr and L. Vos, *Tune distributions and effective tune spread from beam-beam interactions and the consequences for Landau damping in the LHC*, LHC Project Note 316 (CERN, 2013).

[44] X. Buffat *et al.*, Phys. Rev. ST Accel. Beams **17**, 111002 (2014).

[45] E. Mètral, *Coupled Landau damping of transverse coherent instabilities in particle accelerators*, Ph.D. thesis, Université Joseph Fourrier (1999).

[46] M. Benedikt, P. Collier, V. Mertens, J. Poole, and K. Schindl (editors), CERN-2004-003-V3 (2004).

[47] https://espace.cern.ch/liu-project/LIU_images/Forms/DispForm.aspx?ID=11.

[48] S. Redaelli *et al.*, in *Proceedings of HB2010* (2010).

[49] E. Mètral *et al.*, IEEE Transactions on Nuclear Science **63**, 1001 (2016).

[50] S. V. D. Meer, ISR-PO/68-31,KEK68-64 (CERN, 1968).

[51] S. M. White *et al.*, in *Proceedings of IPAC'10, Kyoto, Japan* (2010).

[52] S. White *et al.*, Phys. Rev. ST Accel. Beams **17**, 041002 (2014).

[53] Y. Alexahin, "Possible beam-beam effect involvement in the end-of-squeeze instability," Beam-Beam and Luminosity Studies meeting (2015).

[54] T. Pieloni *et al.*, in *6th Evian Workshop on LHC beam operation*, CERN-ACC-2015-376, edited by S. D. amd B. Goddard (2016).

[55] D. Neuffer and S. G. Peggs, *Beam-Beam Tune Shifts and Spreads in the SSC – Head On, Long Range, and PACMAN Conditions*, SSC-063 (1986).

[56] O. Brüning and L. Rossi, *The High Luminosity Large Hadron Collider* (World Scientific, 2015).

[57] G. Apollinari, I. B. Alonso, O. Brüning, M. Lamont, and L. Rossi, *High-Luminosity Large Hadron Collider (HL-LHC). Preliminary Design Report*, CERN-2015-005 (CERN, 2015).

[58] S. Fartoukh and F. Zimmermann, in *The High Luminosity Large Hadron Collider* (World Scientific, CERN, Geneve, Switzerland 2015) Chap. 4.

[59] F. Zimmermann, Presentation at CERN-PAF/POFPA meeting on 13-02-2007.

[60] B. Muratori and T. Pieloni, in *Proceedings of the ICFA Mini-workshop on beam-beam effects in Hadron Colliders*, CERN-2014-004, edited by W. Herr and G. Papotti (CERN, 2014).

[61] D. Banfi *et al.*, in *Proceedings of IPAC'14, Dresden, Germany*, THPRO83 (2014).

[62] E. Mètral *et al.*, *HL-LHC Operational scenarios*, CERN-ACC-NOTE-2015-0009 (CERN, 2015).

[63] *Chamonix 2011 Workshop on LHC Performance*, CERN-ATS-2011-005 (Chamonix, France, 24-28Jan 2011).

[64] S. Fartoukh, Phys. Rev. ST Accel. Beams **16**, 111002 (2013).

[65] T. Pieloni *et al.*, in *Proceedings of IPAC 2017, Copenhagen, Denmark, 2017*, TUPVA027 (2017).

[66] J. Borer *et al.*, IEEE Transactions of Nuclear Science **NS-26**, 3405 (1979).

[67] M. G. Minty and F. Zimmermann, *Measurement and Control of Charged Particle Beams* (Springer, 2003).

[68] P. Gorgen *et al.*, Nuclear Instruments and Methods in Physics Research Section A: Accelerators, Spectrometers, Detectors and Associated Equipment **777**, 43 (2014).

[69] P. Chou and G. Jackson, in *Proceedings of the 1995 Particle Accelerator Conference*, Vol. 5 (1995).

[70] H. Damerau *et al.*, *Evaluation of the broadband longitudinal impedance of the CERN PS*, CERN-ATS-2012-064 MD (CERN, 2012).

[71] J.-Y. Hemery *et al.*, IEEE Transactions of Nuclear Science **NS-28**, 2497 (1981).

[72] A. Hofmann, *The beam-beam transfer function*, ISR Performance Report (CERN, 1981).

[73] C. Tambasco *et al.*, *First Beam Transfer Function measurements in the LHC,* CERN-ACC-NOTE-2016-0012 (CERN, Geneva, Switzerland, 2016).

[74] C. Tambasco *et al.*, *MD 382: Beam Transfer Function and diffusion mechanisms,* CERN-ACC-NOTE-2016-0016 (CERN, 2016).

[75] C. Tambasco *et al.*, *MD 1856 - Landau Damping: Beam Transfer Functions and diffusion mechanisms,* (CERN, Geneva, Switzerland, 2017).

[76] C. Tambasco *et al.*, *MD 1407 - Landau Damping: Beam Transfer Functions and diffusion mechanisms,* (CERN, Geneva, Switzerland, 2017).

[77] E. Gorbachev *et al.*, *LHC transverse feedback system: first results of commisioning,* LHC Project Report 1165 (CERN, 2008).

[78] M. Gasior and R. Jones, CERN-AB-2005-060 BDI (2005).

[79] G. Trad *et al.*, in *Proceedings of IPAC 2016* (2016).

[80] B. Dehning *et al.*, in *Proceedings of PAC07, Albuquerque, New Mexico, USA* (2007).

[81] R. Bruce *et al.*, Phys. Rev. ST Accel. Beams **17**, 081004 (2014).

[82] R. Tomás, *Collecting amplitude detuning measurements from 2012,* CERN-ACC-NOTE-2014-0027 (CERN, 2014).

[83] Y. Alexahin, Part. Accel. **59**, 43 (1998).

[84] W. H. Press, S. A. Teukolsky, W. T. Vetterling, and B. P. Flannery, *Numerical Recipes in C: the Art of Scientific Computing,* second edition ed. (Cambridge university press, 1992).

[85] L. Carver *et al.*, in *Proceedings of IPAC 2017, Copenhagen, Denmark*, THPAB040 (2017).

[86] B. Salvachua *et al.*, in *Proceedings of IPAC 2017, Copenhagen, Denmark*, TUPVA025 (2017).

Claudia Tambasco

Physicist

Nationality: *Italian*
☎ *+41766090544*
✉ *claudia.tambasco@cern.ch*
Rue de Genève 34,
01210 Ferney-Voltaire (FR)

Experience

Mar 2014 to June 2017

Doctoral student at CERN, *(Geneva, Switzerland).*
Beam Transfer Function measurements and transverse beam stability studies for the Large Hadron Collider and its High Luminosity upgrade
Thesis directors: Dr. T. Pieloni and Prof. L. Rivkin.

- Investigation of Landau damping and transverse beam stability studies during the full operational cycle for HL-LHC and LHC. Proposition of operational scenarios in the presence of beam-beam interactions.
- Physics fill analysis affected by transverse beam instabilities.
- Contribution in the design, execution and data analysis of several experimental studies on beam-beam effects in the LHC by means also of Beam Transfer Function (BTF) meausurements.
- Analysis and modeling of the transverse BTF measurements in the LHC in the presence of Landau octupole, beam-beam interactions and chromaticity.
- Adapting simulation tools including new features in relation to the carried out studies.

Sep 2014 to Present

Teaching assistant, École Polytechnique Fédérale de Lausanne.

- Tutoring sessions for Master students in Physics and Engineering for the course: "*Introduction to particle accelerators*" by Prof. L. Rivkin.

March 2015

Invited student at Brookhaven National Laboratory Upton, USA.
Experimental studies on BTF measurements during the electron-lens commissioning of RHIC (Dr. W. Fischer).

Jul 2013 to Jan 2014

Intern Student at CERN for master thesis project, (Geneva, Switzerland).
Improvements on the physics model of the SixTrack scattering collimator routine.
Under the supervision of Dr. S. Redaelli and Dr. B. Salvachua.

- Review of the scattering processes between high energetic protons and the collimator jaw material of the SixTrack scattering routine.
- Implementation in the SixTrack code of a new function for calculating the ionization losses.
- Development of reference plots for SixTrack collimation studies and comparisons with the Merlin model.

Jul - Aug 2012

Intern Student at CERN, (Geneva, Switzerland).
Data analysis for UA9 Crystal collimation project.
Under the supervision of Dr. W. Scandale.

- Development of C routines for ROOT data analysis on collimation procedures with crystals.
- Online data analysis during Machine Development session on the SPS machine during crystal collimation experiments.

Education

June 2017

Ph.D. in Physics, *École Polytechnique Fédérale de Lausanne (Lausanne, Switzerland).*
Thesis title: *Beam Transfer Function measurements and transverse beam stability studies for the Large Hadron Collider and its High Luminosity upgrade.*

Jan 2014

Master's degree in Physics, *Sapienza University of Rome (Rome, Italy).*
Specialization: Nuclear and Subnuclear Physics
Thesis title: *An improved scattering routine for collimation tracking studies at LHC.*

Jul 2011	**Bachelor's degree in Physics**, *Sapienza University of Rome (Rome, Italy)*, **Thesis title:** *The structure of nucleons.*

Computer skills

Operating Systems	**Microsoft Windows** and **Unix based** systems (Scientific Linux CERN 4,5,6, Ubuntu), **Mac OSX**
Programming Languages	**C, Python** Fortran77,C++
Tools	**Python Matplotlib, Mathematica, Timber, ROOT, Gnuplot**, LaTeX, MS Office and Open Office, Apple pages, Origin 8.6, PSpice.
Simulation Tools	**MAD-X, SixTrack**, COMBI, PySSD.

Conferences and Workshops

May 2017	**International Particle Accelerator Conference 2017 (IPAC'17)**, *Impact of incoherent effects on the Landau Stability Diagram at the LHC*, C. Tambasco *et al.*, Copenaghen, Denmark.
May 2016	**International Particle Accelerator Conference 2016 (IPAC'16)**, Student Grant winner, *First BTF Measurements at the Large hadron Collider*, C. Tambasco *et al.*, Busan, Korea.
December 2015	**The 6th Evian Workshop**, *Beam-beam effects: long range and head-on*, T. Pieloni *et al.*, Evian, France.
October 2015	**Joint HiLumi LHC-LARP Annual Meeting 2015**, *Beam-beam effects and Stability of the beams during the operational cycle*, C. Tambasco *et al.*, CERN, Geneva, Switzerland.

Attended lectures

July 2016	**Using Mathematica to analyse and model experimental data**, École Polytechnique Fédérale de Lausanne, Prof. P. Stadelmann
Nov 2015	**Intensity limitation in particle beams**, CERN Accelerator school, CERN, Geneva, Switzerland.
Sep 2015	**Advanced accelerator physics**, CERN Accelerator school, Warsaw, Poland.
Sep 2014	**Introduction to accelerator physics**, CERN Accelerator school, Prague, Czech Republic.

Languages

Italian	Native
English	Fluent (C1)
French	Intermediate (B1)

Claudia Tambasco

List of Publications

Thesis:

PhD Thesis: "*Beam Transfer Function measurements and transverse beam stability studies for the Large Hadron Collider and its High Luminosity upgrade*", École polytechnique fédérale de Lausanne, (Lausanne, Switzerland), 2017. Supervision of: Prof. L. Rivkin, EPFL/IPHYS LPAP, Dr. T. Pieloni, EPFL /IPHYS LPAP and CERN.

Master thesis: "*An improved scattering routine for collimation tracking studies at LHC*", Sapienza University of Rome (Rome, Italy), 2014. Supervision of: Dr. G. Cavoto, INFN, Dr. B. Salvachua and Dr. S. Redaelli, CERN.

Bachelor thesis: "*The structure of nucleons*", Sapienza University of Rome (Rome, Italy), 2011. Supervision of: Prof. E. Longo, INFN.

Articles:

- C. Tambasco *et al.*, *"Impact of incoherent effects on the Landau Stability Diagram at the LHC*", Proceedings of IPAC 2017 - TUPVA031, Copenhagen, Denmark, 2017.
- J. Wenninger *et al.*, *"Observations of Beam Losses at the LHC during reduction of crossing angle*", Proceedings of IPAC 2017 - TUPVA025, Copenhagen, Denmark, 2017.
- T. Pieloni *et al.*, *"Beam-Beam Studies for FCC-hh*" , Proceedings of IPAC 2017 - TUPVA026, Copenhagen, Denmark, 2017.
- T. Pieloni *et al.*, *"Study of Beam-Beam Long Range Compensation with Octupoles*", Proceedings of IPAC 2017 - TUPVA027, Copenhagen, Denmark, 2017.
- X. Buffat *et al.*, *"Observations of Emittance Growth in the Presence of External Noise in the LHC*" , Proceedings of IPAC 2017 - TUPVA029, Copenhagen, Denmark, 2017.
- T. Pieloni *et al.*, *"Dynamic Aperture Studies of the Long-Range Beam-Beam Interaction at the LHC*" , Proceedings of IPAC 2017 - THPAB056, Copenhagen, Denmark, 2017.
- X. Buffat *et al.*, *"Observations of emittance growth in the presence of external noise in the LHC*" , Proceedings of IPAC 2017 -TUPVA029, Copenhagen, Denmark, 2017.
- C. Tambasco *et al.*, *"First BTF measurements at the Large Hadron Collider"*, Proceedings of IPAC 2016, Busan, Korea, 2016.
- G. Arduini *et al.*, *"High Luminosity LHC: challenges and plans", FERMILAB-CONF-16-621-AD-APC, November 2016*

- E. Métral *et al.*, *“Beam Instabilities in Hadron Synchrotrons”,* IEEE Transactions on Nuclear Science*,* Volume: 63, April 2016
- T. Pieloni *et al.*, *“Dynamic beta and beta-beating effects in the presence of the beam-beam interactions”,* Proceedings of HB 2016, Malmö, Sweden, 2016.
- E. Métral *et al.*, *“Measurement and interpretation of the transverse beam instabilities in the CERN Large Hadron Collider (LHC) and extrapolations to HL-LHC”,* Proceedings of HB 2016, Malmö, Sweden, 2016.
- F. Zimmermann *et al.*, *“Beam dynamics issues in the FCC”,* Proceedings of HB 2016, Malmö, Sweden, 2016.
- M. Crouch *et al.*, *“Impact of long range beam-beam effects on intensity and luminosity lifetimes from the 2015 LHC run”*, Proceedings of IPAC 2016, Busan, Korea, 2016.
- X. Buffat *et al.*, *“Simulation of the Head-On beam-beam limitations in Future High Energy Colliders”,* Proceedings of IPAC 2016, Busan, Korea, 2016.
- L.R. Carver *et al., “Current status of instability threshold measurements in the LHC at 6.5 TeV”,* Proceedings of IPAC 2016, Busan, Korea, 2016.
- T. Pieloni *et al., “Beam-beam effects: long range and head-on”,* Proceedings of the 6th Evian Workshop, Evian, France, 2015.
- R. Bruce *et al., “Simulations and measurements of beam loss patterns at the CERN Large Hadron Collider”,* Phys. Rev. ST Accel. Beams 17, August 2014.
- M. Serluca *et al., “ Comparison of Merlin/SixTrack for LHC collimation studies”,* Proceedings of IPAC 2014, Dresden, Germany, 2014.
- R. Bruce *et al., “ Integrated simulations tools for collimation cleaning in HL-LHC”,* Proceedings of IPAC 2014, Dresden, Germany, 2014.

Conferences and Workshops:

- **International Particle Accelerator Conference 2016 (IPAC’16)**, Student Grant winner, “*First BTF Measurements at the Large Hadron Collider*”, C. Tambasco et al., Busan, Korea.
- **The 6th Evian Workshop**, “*Beam-beam effects: long range and head-on*”, T. Pieloni et al., Evian, France.
- **Joint HiLumi LHC-LARP Annual Meeting 2015**, “*Beam-beam effects and Stability of the beams during the operational cycle*”, C. Tambasco et al., CERN, Geneva, Switzerland.

Internal notes:

- C. Tambasco *et al., “MD 1856 - Landau Damping: Beam Transfer Functions and diffusion mechanisms”,* CERN-ACC-NOTE-2017- 0027, CERN, Switzerland, 2017.

- C. Tambasco *et al., "MD 1407 - Landau Damping: Beam Transfer Functions and diffusion mechanisms",* CERN-ACC-NOTE-2017- 0026, CERN, Switzerland, 2017.
- C. Tambasco *et al., "MD 382: Beam Transfer Function and diffusion mechanisms",* CERN-ACC-NOTE-2016-0016, CERN, 2016.
- C. Tambasco *et al., "First Beam Transfer Function measurements at LHC",* CERN-ACC-NOTE-2016-0012, CERN, 2016.
- X. Buffat *et al., "Probing the behaviour of high brightness bunches in collision at 6.5 TeV and the interplay with an external source of noise (MD1433)",* CERN-ACC-NOTE-2017-0030, CERN, Switzerland, 2017.
- L. Carver *et al., "MD1228: Validation of Single Bunch Stability Threshold & MD1751: Instability Studies with a Single Beam",* CERN-ACC-NOTE-2017-0013, CERN, Switzerland, 2017.
- E. Métral *et al., "Summary of the half-day internal review of LHC performance limitations (linked to transverse collective effects) during run II (CERN, 29/11/2016) ",* CERN-ACC-NOTE-2017-0005, CERN, Switzerland, 2017.
- M. Crouch *et al., "Long range beam-beam interaction and the effect on the beam and luminosity lifetimes",* CERN-ACC-NOTE-2016-0019, CERN, 2016.
- L. R. Carver *et al., "MD 346: Summary of single bunch instability threshold measurements",* CERN-ACC-NOTE-2016-0002, CERN, 2016.
- E. Métral *et al*., *"HL-LHC Operational Scenarios",* FP7 High Luminosity Large Hadron Collider Design Study, CERN-ACC-NOTE-2015-0009, 2015.
- C. Tambasco, T. Pieloni, X. Buffat*, "HL-LHC Stability Diagrams: octupoles and beam-beam long range",* CERN-ACC-SLIDES-2014-0089, CERN, 2014.